Tourmaline geochemistry and cassiterite geochronology of highly evolved tin granites and their hydrothermal systems in eastern Australia

Patrick Andrew Carr

July 2018

A thesis submitted for the degree of Doctor of Philosophy of The Australian National University.

THE AUSTRALIAN NATIONAL UNIVERSITY

The work in this thesis is my own except where otherwise acknowledged.

Patrick Andrew Carr

July 2018

Acknowledgments

My foremost acknowledgement is to my primary supervisors, Vickie Bennett and Marc Norman, who have provided me with a world-class education. Their support has been comprehensive, and as a result, I finish my PhD with the same excitement and enthusiasm that I started with.

My advisory panel has contributed to many aspects of this work. Firstly, Phil Blevin of the Geological Survey of NSW has been instrumental in facilitating field work and access to samples. He is a leading expert in granite genesis and mineralisation processes, and his council has greatly improved this thesis. Contributions from Ian Williams have greatly improved the science within this thesis, in particular with his expert knowledge of granite genesis, SIMS and isotope systematics. Guidance from Trevor Ireland and John Mavrogenes at the mid-point of the project provided new methods and concepts to explore that are incorporated into the final version.

The clean laboratory and TIMS component of this thesis would not be possible without the incredible support of Yuri Amelin and Sonja Zink. Technical support was skilfully provided by Shane Paxton, Peter Holden, Peter Lanc, Janaina Avila, Les Kinsley and Harri Kokkennen.

The Geological Survey of NSW has funded and assisted with field work (Phil Blevin, Bradley Williams and Michael Nelson) and provided access to samples. Geoscience Australia also provided access to samples. In particular, Simon Bodorkos and Andrew Cross are thanked for their assistance in SIMS geochronology.

This thesis was improved by many conversations with Gordon Lister, Antonio Acosta-Virgil, John Walshe, Antony Burnham, Morgan Williams, Oscar Branson and Dave Heslop.

I am fortunate enough to have two parents, who are not only isotope geochemists, but have both worked on the deposits studied here, and one who is active editor of a geological journal. Their editing, scientific and financial

support has been crucial to the publication and quality of this thesis, and the overall PhD experience.

The RSES community have contributed to an excellent environment for learning and, importantly, enjoying scientific research.

My remaining family and friends are thanked for their support, patience and distractions. Most notably, my partner Claire, who in a short time has given me the knowledge of a lifetime.

Abstract

Three models have been proposed for cassiterite (SnO_2) mineralisation in magmatic–hydrothermal environments: (1) magmatic crystallisation from a granitic melt, (2) late-stage magmatic partition of Sn into a fluid or vapour phase and subsequent cassiterite deposition, and (3) hydrothermal leaching of Sn from granite and/or country rocks and subsequent deposition. The complex chemistry of the 'tin' granites, and the large and pervasive hydrothermal systems which can overprint and destroy primary features make understanding the processes responsible for Sn enrichment difficult.

Two new analytical methods were developed. Firstly, a method for the determination of Rb–Sr and Sm–Nd isotopic compositions of magmatic and hydrothermal tourmalines, which can record the compositional evolution of magmas and their hydrothermal fluids. Secondly, cassiterite U–Pb geochronology to constrain the absolute age and duration of magmatic–hydrothermal Sn systems. These data, together with major and trace element compositions of tourmaline, whole-rock geochemistry, quartz $\delta^{18}O$ values and zircon U–Pb geochronology are applied to two Sn deposits associated with the Ardlethan and Mole granites of eastern Australia.

The geochemical and isotope data of tourmaline show large compositional changes across the magmatic–hydrothermal transition. In the Ardlethan Granite, tourmaline ^{87}Rb–^{86}Sr isotope compositions, which provide robust estimates of $^{87}Sr/^{86}Sr_{(i)}$ because of their low $^{87}Rb/^{86}Sr$, are used to model the assimilation and fractional crystallisation processes that lead to a 30-times enrichment of Sn in residual melts relative to the source rocks. However, caution must be taken with interpreting $^{87}Sr/^{86}Sr_{(i)}$ tourmaline data as high $^{87}Rb/^{86}Sr$ of parental melts and fluids can lead to significant *in-situ* decay of ^{87}Rb prior to tourmaline precipitation. This phenomon is hypothesised for the parental melts of the Mole Granite which due toextreme fractional crystallisation have extreme $^{87}Rb/^{86}Sr$ of ~900. Subsequently $^{87}Sr/^{86}Sr_{(i)}$ tourmaline compositions are more evolved the the whole rock composition.

The Sn concentration of tourmaline increases from magmatic to hydrothermal settings within the Ardlethan and Mole granites, recording the exsolution of a fluid from a silicate melt. The enrichment of Sn during fluid fractionation, recorded by tourmaline, agrees with experimentally determined melt–fluid partitioning coefficients. Fluid fractionation is the dominant enrichment process for greisen deposits of the Ardlethan Granite, and all deposits of the Mole Granite.

Fluid leaching of host rocks is evidenced by convergence of Fe/(Fe+Mg), Sr, $^{87}Sr/^{86}Sr_{(i)}$ and $\varepsilon Nd_{(i)}$ in hydrothermal tourmaline from the original source rock composition to the host rock composition. At Ardlethan, the host rock of mineralised breccia pipes is enriched in Sn (~50 ppm) and fluid leaching results in an increase of Sn in the mineralising fluids. Although fluid leaching occurs around the Mole Granite, the low Sn concentrations in the host rocks limits Sn enrichment.

Melt/fluid-mineral partitioning is a major uncertainty in the interpretation of tourmaline trace element geochemistry. Natural studies performed here provide some constraints, however, more targeted experimental work is required.

A new method for U–Pb characterisation of cassiterite by ID-TIMS has provided a matrix-matched reference material for *in-situ* techniques. However, common-Pb corrections of *in-situ* techniques remain a large uncertainty in cassiterite geochronology. At Ardlethan, the common-Pb compositions are appropriately estimated by terrestrial Earth models and are more precise than isochron ages. Conversely, the common-Pb associated with the Mole Granite appears variable between a terrestrial Earth composition and a highly evolved composition.

Cassiterite U–Pb geochronology of both the Ardlethan and Mole granite mineralisation systems indicate precipitation synchronous with emplacement. The method does not have sufficient precision (~4 % absolute) to distinguish the age of cassiterite precipitation from that of zircon, however, the magmatic–hydrothermal systems of the Ardlethan and Mole granites persisted for a maximum of 4.2 Ma.

Table of Contents

Chapter 1: Introduction to magmatic-hydrothermal mineral deposits

1.1 Introduction

Magmatic-hydrothermal Sn deposits are commonly associated with highly evolved, leucocratic granites emplaced at shallow crustal depths and characterised by enrichment in F, Li, Rb, Ga, Sn and Nb (Tischendorf, 1977). The geochemical compositions of these 'tin' granites, being enriched in elements incompatible in silicate melts, is attributed to extended fractional crystallisation (e.g. Ishihara, 1978; Štemprok, 1990) or small degree partial melts (Tischendorf and Förster, 1990; Wolf *et al.*, 2018). However, magmatic crystallisation of cassiterite (SnO_2), the major Sn ore, is rare (Linnen *et al.*, 1992) due to its high solubility in silicate melts (> 1000 ppm SnO_2; Štemprok, 1990; Taylor and Wall, 1992). Extensive research has shown that during fluid or vapour separation from a cooling silicate melt, Sn will strongly partition into the fluid phase, primarily as a function Cl molarity (Eadington, 1983; Kovalenko *et al.*, 1986; Wilson and Eugster, 1990; Keppler & Wyllie, 1991; Rankin *et al.*, 1992; Linnen, 1998; Duc-Tin *et al.*, 2007; Schmidt, 2018). Fluid fractionation from these 'tin' granites is thought to be the dominant enrichment process leading to mineralisation in greisen, quartz veins, skarn, porphyry-style and pegmatites (e.g. Plimer, 1987; Ren *et al.*, 1995; Audétat, 1998). On rare occasions, further enrichment of Sn within these magmatic fluids is attributed to scavenging from host rocks (Lehmann and Harmanto, 1990). Despite the potential mechanisms for Sn enrichment in magmatic-hydrothermal environments being known, genetic models differ in the contribution of each mechanism to the formation of a deposit.

1.1.1 Melting and magmatic processes of 'tin' granites

Significant debate on the origins of 'tin' granites has been concerned with the role of particular source rocks (e.g. Schuling, 1967; Wolf *et al.*, 2018), conditions and degree of partial melting (e.g. Tischendorf and Förster, 1990; Romer and Kroner, 2016), geodynamic setting (e.g. Sillitoe *et al.*, 1975) and degree and species of fractional crystallisation (Ishihara, 1977; Štemprok, 1990). However, a major difficulty in defining such parameters is that as

granites become more evolved, the geochemistry converges towards minimum temperature melt compositions that are no longer diagnostic of parental magmas (Tuttle and Brown, 1958). The major element composition of a haplogranite is approximated by equal amounts of normative quartz, albite and orthoclase. In contrast, the concentrations of trace elements that do not substitute into these rock-forming minerals vary widely depending on when their host accessory phases become saturated in the melt.

The distribution of primary Sn deposits worldwide is confined dominantly to areas of thickened continental crust, either within orogenic belts (e.g. eastern Australia; Blevin, 2004; western Thai belt, Thailand; Linnen, 1998) or within intra-cratonic settings (e.g. central and northern Africa, Goodenough *et al.*, 2014; central Brazil, Payolla *et al.*, 2002) (Figure 1). Tin is enriched in magmatic melts relative to their source rocks during the creation of continental crust leading to distinct concentration differences between the depleted mantle (0.1 ppm; Salters and Stracke, 2004), lower crust (1.7) and upper crust (2.1 ppm) (Rudnick and Gao, 2004). As such, 'tin' granites were assumed historically to be related to melting of continental crust (Schuiling, 1967; Lehmann, 1982). Schuling (1967) inferred that 'tin' granites were derived from discrete Sn-rich sources, that could be melted periodically to produce multiple Sn deposits of different ages (e.g. Precambrian, Jurassic, and Cenozoic Sn

Figure 1: Global tectonic map (USGS 2014) with distribution of tin provinces and occurrences (modified after Sainsbury, 1969).

deposits of the Pan African belt). Romer and Kroner (2016) suggest the source rocks of ‘tin’ granites are enriched in Sn during extreme chemical weathering on passive margins. Wolf *et al.* (2018) show that source rocks can be enriched at depth during repeated episodes of low temperature melting that will enrich Sn in the residual phases. Subsequent high temperature melting of these residual phases will be more enriched in Sn. A comparable model of high temperature melting of refractory, anhydrous source rocks also been applied more generally to A-type granites that can be associated with tin deposits (e.g. Landenberger and Collins, 1996; King *et al.*, 1997).

The geodynamic setting of magmatic-hydrothermal Sn deposits includes continent–continent orogens (e.g. Alpine–Himalayas; Kerrich *et al.*, 2005), far back-arc (e.g. Tasman Orogen; Solomon and Groves, 2000), and accretionary orogens (e.g. Bolivia; Sillitoe *et al.*, 1975). Lehmann (1990) suggest that Sn deposits are focussed above thickened crustal zones because they provide extra space and time for extended granite differentiation and Sn enrichment (e.g. Bolivia, Andes). Within continental collision belts, ‘tin’ granites are emplaced predominantly during post orogenic magmatism (e.g. SE Asia and Variscan; Mitchell, 1977). Cheng *et al.* (2018) recently proposed a new model to explain the relationship between highly evolved ‘tin’ granites and their crystal-rich, less evolved, volcanic equivalents. Those authors infer a favourable extensional geodynamic setting leading of emplacement of ‘tin’ granites. In their model, melts associated with barren felsic volcanics are trapped in the upper crust during transient compressional tectonics and allows the melts to undergo extreme fractional crystallisation. Despite magmatic-hydrothermal Sn deposits only occurring in zones of thickened continental crust, in rare cases mantle-derived fluids or melts have been implicated in magmatic-hydrothermal Sn deposits (Sillitoe, 1974; Walshe *et al.*, 1995, 2011; Zhao *et al.*, 2002; Goodenough *et al.*, 2014).

1.1.2 Magmatic to hydrothermal transition

A rising magma will reach a point when it is volatile components (e.g. H_2O, CO_2, F, B and Cl) reach saturation exsolving a magmatic volatile phase (MVP; fluid and/or vapour; see Candela, 1997 for summary) from the silicate melt. Numerous studies indicate that the MVP is enriched by up to 2–3 orders of

magnitude in the concentration of metals (e.g. Cu, Au, Sn) relative to the host silicate rock (e.g. Audétat *et al.* 1998) and is therefore regarded as an important processes in metal enrichment in magmatic-hydrothermal mineral deposits. Extensive experimental studies have addressed the partitioning of elements between silicate melts and an MVP to quantify Sn enrichment (Nekrasov *et al.*, 1980; Eadington, 1983; Kovalenko *et al.*, 1988; Wilson and Eugster, 1990; Keppler & Wyllie, 1991; Rankin *et al.*, 1992; Linnen, 1998; Duc-Tin *et al.*, 2007; Schmidt, 2018). These studies have focussed on partitioning of Sn, and other associated elements (e.g. W, Cu, Mo, Zn, U and Th) between a haplogranitic melt and a MVP under variable conditions including pressure, temperature, oxygen fugacity, alkalinity and ligand (e.g. F^- and Cl^-) concentration. Overwhelmingly, Sn partitioning into a fluid is favoured by high Cl^- molarity (Eadington, 1983; Kovalenko *et al.*, 1986; Wilson and Eugster, 1990; Keppler & Wyllie, 1991; Rankin *et al.*, 1992; Linnen, 1998; Duc-Tin *et al.*, 2007; Schmidt, 2018). Oxygen fugacity is shown to be a second-order effect (Duc-Tin *et al.*, 2007), or even insignificant (Schmidt, 2018). Experimentally determined partitioning coefficients ($^{Sn}D_{MVP-melt} = \frac{concentration\ in\ MVP}{concentration\ in\ melt}$) for Sn between a haplogranite melt and a MVP vary significantly ($^{Sn}D_{MVP-melt}$ = 0.002–12; Nekrasov *et al.*, 1980; Keppler and Wyllie, 1991; Duc-Tin *et al.*, 2007). Natural studies on Sn partitioning into a MVP are sparse because the preservation of primary fluid compositions is rare and fluid inclusions are difficult to analyse. Audétat (1998) and Zajacz *et al.* (2008) provided initial estimates by analysing fluid inclusions by LA-ICP-MS and confirmed the preference of Sn into a MVP, however the extremely small volumes of fluid analysed within inclusions do not allow for precise $^{Sn}D_{MVP-melt}$ to be determined.

The formation of economic magmatic-hydrothermal deposits also requires that the metal-rich MVP is extracted from the bulk silicate melt and concentrated in a confined zone. The MVP is 4–5 times less dense than the surrounding melt (Lemmon *et al. 2003*) and this contrast is the primary driver for MVP migration towards the apical zone of the granite (see Sillitoe 2010 for review of the physical processes of fluid migration in silicate melts). The formation of bubbles, or bubble plumes is invoked as the main mechanism of MVP migration through silicate melts (e.g. Ruprecht *et al.,* 2008; Huber *et al.* 2012). Huber *et al.* (2012)

indicate that high crystallinity silicate melts are most efficient at extracting an MVP because they facilitate connected volatile pathways that are not disturbed by convection currents or physical pertubations in the magma reservoir (e.g. Candela and Blevin 1995; Parmigiani *et al.,* 2011).

1.1.3 Hydrothermal circulation

Following MVP separation and migration and sufficient cooling of the granite (~<350^{o}C), continued circulation of hydrothermal fluids is channelled into master cracks formed during from the contraction of the cooling granite] Previous studies infer widespread metasomatism, particularly of the host granite, leading to remobilisation of several elements including Sn (Lehmann and Harmanto, 1990). Within 'tin' granites, the Sn is occurring as Sn^{4+} that has substituted for Ti^{4+} or Fe^{3+} (by coupled substitution) into oxides (magnetite, ilmenite or rutile) or silicates (biotite, titanite or amphibole) (Taylor, 1979; Lehman, 1990). Contrary to earlier beliefs that Sn is only mobile as a chloride in fluids when reduced (Sn^{2+}) (Heinrich, 1990), the recent experimental study of Schmidt (2018) documented several oxidised Sn^{4+}–chloride species indicating its hydrothermal mobility. Hydrothermal fluids have been shown to dramatically alter the primary chemistry of 'tin' granites (Lehmann and Harmanto, 1990; Dostal *et al.*, 2004), however the extent to which they enrich Sn relative to the melt is unknown.

1.1.4 Timescales of magmatic-hydrothermal processes

Understanding the absolute age and duration of magmatic-hydrothermal processes is fundamental to genetic models. 'Tin' granites commonly form in large batholiths with long and complex granite emplacement histories (e.g. 35 Ma; Cheng et al., 2018). Precise knowledge of the age of cassiterite mineralisation can help identify source granites of mineralising fluids or long-term hydrothermal fluid circulation. In these locations, determining the absolute ages of cassiterite mineralisation can be essential in identifying the magmatic source of mineralisation.

High-precision geochronology and thermal modelling indicates that individual plutons can form from the accumulation of multiple magmatic injections over timescale of 10^{4}–10^{6} years (Clemens & Mawer, 1992; Petford et al., 2000; Coleman et al., 2004; Glazner et al., 2004; Annen et al., 2006; Miller et al., 2007; Michel et

al., 2008; Schlattegger et al., 2009; de Saint Blanquat et al., 2011; Caricchi et al., 2012; Leuthold et al., 2012; Floess and Baumgartner, 2015). This style of granitic plutonism can have considerable effects on ore-forming processes including the duration of mineralising events (Vigneresse, 2007). Significant progress in understanding the duration of magmatic-hydrothermal mineralisation processes in this dynamic environment has been made on large porphyry Cu systems (see review paper of Chiaradia *et al.* 2013). Constraining the rate of this emplacement is limited by our internal analytical precision (2σ) of the radioisotope systems (for U-Pb this is approaching 0.1% and for the Re-Os, and $^{40}Ar/^{39}Ar$ 0.2 %; Chiaradia *et al.* 2013). Recent high precision U-Pb zircon (CA-ID-TIMS) and Re-Os molybdenite dating from the El Salvador and El Teniente porphyry Cu-Mo deposits indicate that mineralisation occurred during periods of 0.6 Ma and 1.7 Ma, respectively, and were emplaced in multiple short-lived (<100 ky) mineralisation pulses (Zimmerman *et al.* 2014; Spencer *et al.* 2015). Conversely, estimates for the duration of emplacement of magmatic-hydrothermal Sn systems from the emplacement of the granite and cooling of hydrothermal fluids vary between instantaneous (e.g. Yuan *et al.*, 2008) to 1 Ga (McNaughton *et al.*, 1993).

1.2 Scope and structure of this study

Although the mechanisms for Sn enrichment in magmatic-hydrothermal environments are well known, the degree to which each mechanism contributes to the overall enrichment within a system is more poorly understood. Studies that attempt to quantify Sn enrichment processes have tended to focus on either the magmatic (e.g. Wolf *et al.*, 2018) or hydrothermal (e.g. Audétat, 1998) environments separately, and a whole of system understanding is lacking. A major contribution of this thesis is the description of two methods for isotopic determination of tourmaline and cassiterite ages that will provide fundamental constraints on the compositional and temporal evolution of magmatic-hydrothermal Sn deposits, respectively. These methods are presented in conjunction with more traditional techniques (e.g. whole rock Rb–Sr and Sm–Nd, zircon U–Pb), to better constrain the source rocks and geodynamic setting of Sn granites, and magmatic and hydrothermal processes that enrich Sn.

Chapter 2.1 details the development of a new method for Rb–Sr and Sm–Nd isotopic determination in tourmaline. In Chapters 2.2 and 2.3 this new method is applied to two major magmatic-hydrothermal Sn systems in eastern Australia to better constrain the compositional evolution of melts and hydrothermal fluids leading to cassiterite mineralisation.

In Chapter 3, the timescales of magmatic-hydrothermal processes are constrained with the presentation of new LA-ICP-MS cassiterite U–Pb data. These data are presented in conjunction with new age constraints from more traditional geochronometers (e.g. U–Pb in zircon and Rb–Sr whole-rock isochrons). LA-ICP-MS U–Pb cassiterite data was generated following significant technique development that is included in Appendix 1 and 2.

Chapter 2 – Tourmaline geochemistry of magmatic-hydrothermal Sn deposits of eastern Australia

2.1 Introduction to tourmaline geochemistry

Magmatic to hydrothermal Sn deposits are associated predominantly with highly evolved and high-heat producing granites that are part of large igneous systems (Taylor, 1979; Lehman, 1990). These systems can have complex intrusion histories whereby the genetic relationship between units and deposits is ambiguous. Similarly, the large heat flux associated with radiogenic, high-heat producing granites can produce extensive and pervasive hydrothermal systems that can modify the mineralising fluids, overprint primary mineralising processes and disguise the original magmatic source (Tischendorf, 1977).

Tracing mineralising fluid sources and their subsequent chemical evolution in magmatic-hydrothermal systems (e.g. mixing/leaching with host rocks) is difficult to do due to poor preservation of the primary fluid. Whilst fluid and/or melt inclusions provide direct access to primary fluids, the small amount of fluids (10^{-11} to 10^{-8} g total mass) preserved makes analysing the trace element composition challenging and isotopic determination near impossible. Furthermore, the petrogenetic context of the inclusion, whether it be primary or secondary is not always clear (e.g. Heinrich *et al.*, 2004; Lerchbaumer and Audétat, 2012). Laser ablation ICP-MS studies (Audétat *et al.*, 1998, 2000a, 2000b, 2008) have provided some estimates of the composition of fluid and melt inclusions but such data have inherently large uncertainties. Mineral proxies of melt and fluid compositions such as tourmaline are advantageous due to better preservation, relative ease of analysis (e.g. EMP and LA-ICP-MS), ability to concentrate elements for greater analytical sensitivity, and the ability to more easily determine their petrogenetic context. However, mineral proxies require an understanding of element partitioning between the mineral of interest and its parental melt or fluid.

The chemical and isotopic composition of tourmaline has been assessed in numerous geological environments: igneous (Jiang *et al.* 2002; this study),

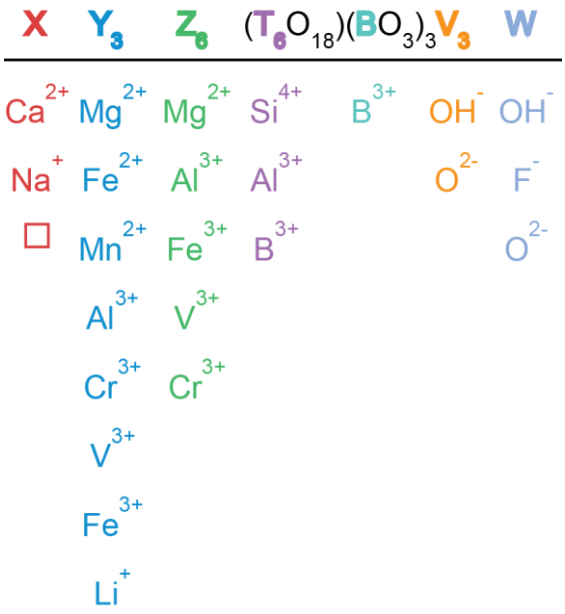

Figure 2: Chemical structure of tourmaline (above line) with the major element substitutions for each site shown below the line. □ represents a vacancy in the site. Formula presented in Henry et al. 2011.

sedimentary (Henry and Dutrow, 1992), and low- (Henry and Dutrow, 1996) and high-grade metamorphics (e.g. Dutrow *et al.*, 1999). Increasing use of tourmaline in these environments has culminated in the publication of an Elements edition (Dutrow and Henry, 2011). Tourmaline has several advantages for use as a passive fluid and melt monitor in magmatic to hydrothermal systems: 1) its complex chemical structure can accommodate a variety of elements depending on the composition of a parental melt or fluid, 2) tourmaline precipitates over a wide pressure and temperature range (e.g. Holtz and Johannes, 1991), 3) tourmaline displays negligible diffusion at temperatures below 600°C (Desbois and Ingrin, 2007), and 4) tourmaline is moderately resistant to physical and chemical abrasion (e.g. Slack and Trumbull, 2011). All of these characteristics indicate that tourmaline has the potential to record the parental melt and fluid composition, and preserve that record over geological timescales.

The chemical sensitivity of tourmaline to changing fluid and melt composition is granted by a complex chemical structure and major element substitutions outlined in Figure 2. The complexity led Bragg (1937) to label tourmaline as the "garbage can mineral" due to its wide chemical diversity. Similarly, Marschall and Jiang (2011) suggest that tourmaline incorporates over "half the periodic table" into its structure. The large chemical variability means that tourmaline has 33 species that are classified primarily by small variations in major element composition on the X, Y, Z, W and V sites (Figure 3; see Dutrow and Henry 2018). However, partitioning of non-major elements into tourmaline from a melt or fluid is unconstrained. Tourmaline-melt partition coefficients have only been published in a single paper for a single major element composition (Van Hinsberg 2011) whilst tourmaline-fluid partition coefficients have not yet been published. Therefore, large uncertainties remain in the interpretation of

tourmaline data as a proxy for melt or fluid compositions. Tourmaline associated with granites is typically of the alkali group, between schorl and dravite, however in moderately fractionated granites and pegmatites, tourmaline can be between schorl and foitite or elbaite.

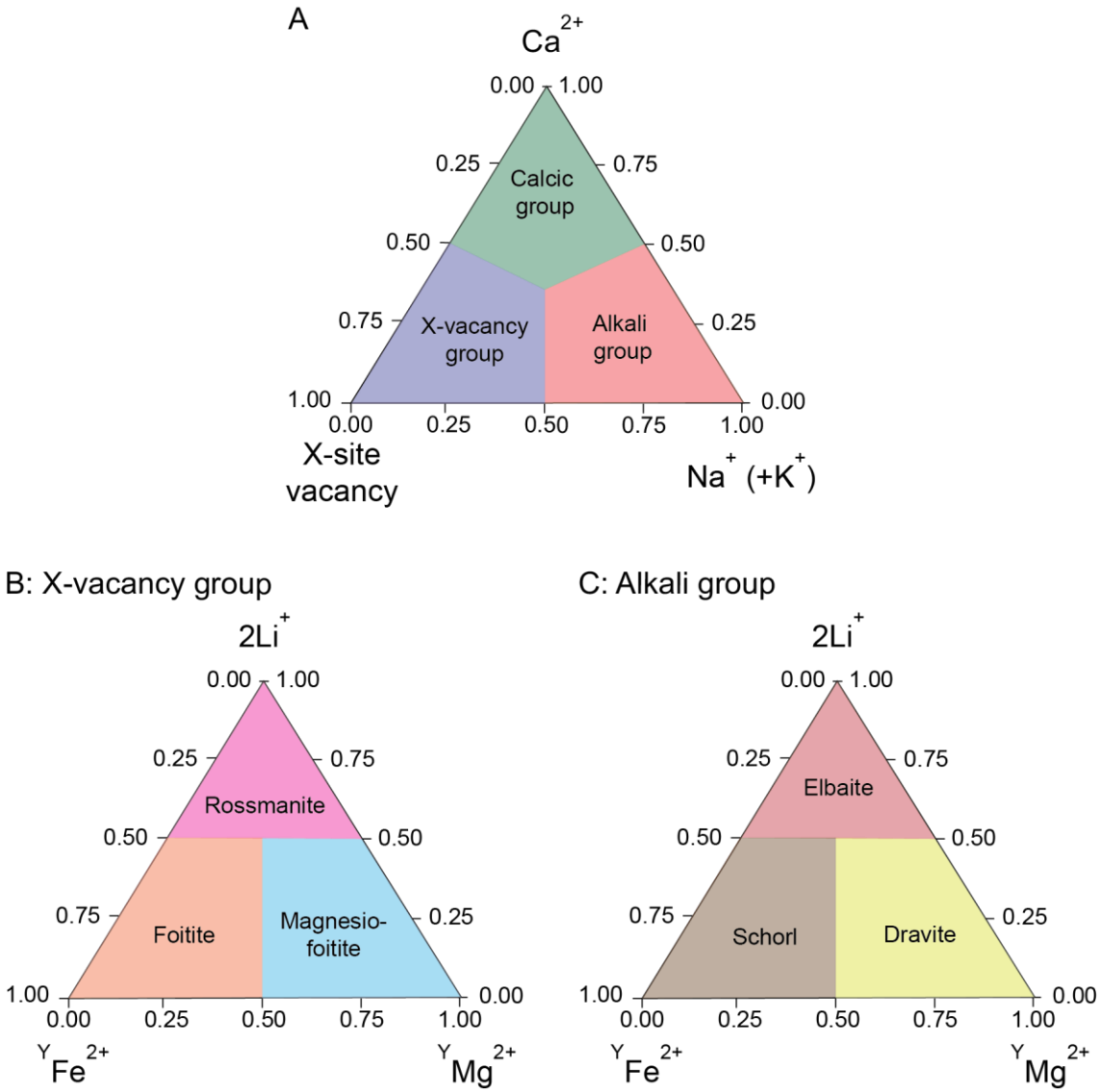

Figure 3: Classification diagrams of tourmaline determined by major element compositions. The first classification is based off the major element composition of the X-site (A). X-vacancy group (B) and alkali group (C), most common in magmatic environments, are then subdivided dependent on the major element composition of the Y site. Classification of tourmaline and figure is derived from Henry et al. 2011.

Sparse experimental data indicates that tourmaline has a wide pressure and temperature stability field (Figure 4). The stability of tourmaline is related primarily to the availability of B, and then pressure and temperature conditions, however, the chemical composition of tourmaline also effects its stability (van

Hinsberg, 2011). The broad pressure and temperature field of shallow magmatic-hydrothermal Sn deposits of eastern Australia is shown in Figure 4. Schorl and dravite, the most common tourmaline compositions associated with granite are stable predominantly throughout this field. The stability of foitite and elbaite in this context has not been assessed.

2.1.1 Tourmaline in magmatic-hydrothermal environments

Tourmaline is a common mineral occurring within igneous bodies and mineralised zones of magmatic to hydrothermal Sn deposits (e.g. Taylor, 1979; Lehmann, 1990). The incompatibility of B in the primary minerals associated with granitic rocks (e.g. quartz, feldspars and micas) mean that it is commonly saturated in the upper zones of the granite body, as a late magmatic phase, and adjacent to these granites in hydrothermal greisen, vein and breccia environments (e.g. London *et al.*, 1996).

Numerous studies have utilised the chemical composition of tourmaline to understand the primary compositions of melts and fluids. These studies have analysed the major, minor and trace element composition (London and Manning, 1995; Rozendaal and Bruwer, 1995; Griffin *et al.*, 1996; Jiang *et al.*, 1998, 2004; Mlynarczyk and William-Jones, 2006; Marks *et al.*, 2013; Yang *et al.*, 2015; Hazarika *et al.*, 2015; Redler *et al.*, 2016), the stable isotope (primarily boron and oxygen) composition (Smith and Yardley, 1996; Tonarini *et al.*, 1998; Jiang *et al.*, 2002; Zachariáš *et al.*, 2005; Trumbull *et al.*, 2008; Sushchevskaya, 2011; Yavuz *et al.*, 2011; Duncan *et al.*, 2014; Baksheev *et al.*, 2015; Driveness *et al.*, 2015; Huang *et al.*, 2016), and the Sm–Nd and Rb–Sr isotopic composition (Mueller *et al.,* 1991; Anglin *et al.*, 1996, Jiang *et al.*, 1999, 2000) of tourmaline from a variety of environments.

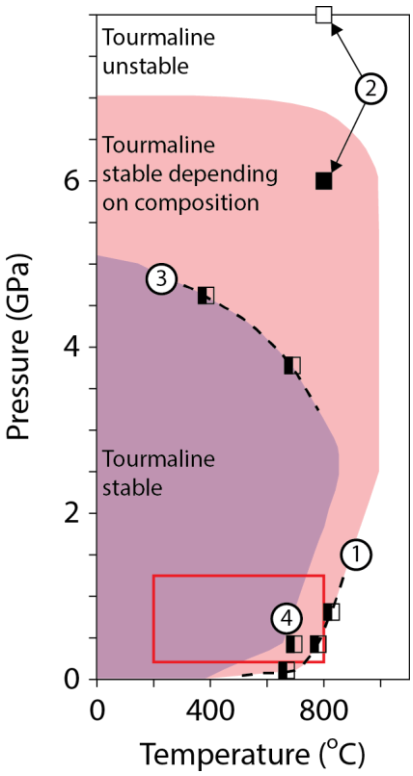

Figure 4: Temperature and pressure stability field for tourmaline derived from limited natural and experimental data (squares). Black squares indicate tourmaline is stable and white unstable. Black and white squares indicate the transition. Dravite stability experiments are shown from Robbins and Yoder (1962) (1), Krosse (1995) (2) and Ota et al. (2008) (3). Natural schorl stability of Holtz and Johannes (1991) is shown in 4. The region of interest to this study in shown in the red box.

$^{143}Nd/^{144}Nd_{(i)}$ and $^{87}Sr/^{86}Sr_{(i)}$ isotopic compositions of tourmaline have the potential to identify the provenance of melts and fluids and are insensitive to age corrections due to low Sm/Nd and Rb/Sr ratios, respectively. The $^{87}Sr/^{86}Sr_{(i)}$ is calculated from the measured $^{87}Sr/^{86}Sr_{(m)}$ and $^{87}Rb/^{86}Sr$, the decay constant of ^{87}Rb (λ) (Villa *et al.,* 2015) and the time (t in millions of years) since closure of the Rb-Sr decay system in a rock, according to Equation 1:

$$\left.{}^{87}Sr\right/_{{}^{86}Sr_{(i)}} = \left.{}^{87}Sr\right/_{{}^{86}Sr_{(m)}} - \left.{}^{87}Rb\right/_{{}^{86}Sr}(e^{\lambda t} - 1) \qquad \text{Equation 1}$$

Highly fractionated granites associated with Sn deposits ubiquitously have extreme bulk rock $^{87}Rb/^{86}Sr$ values (>20) and therefore the calculated $^{87}Sr/^{86}Sr_{(i)}$ is highly sensitive to t (Equation 1). The effect of these age corrections between

a low Rb/Sr mineral such as tourmaline and a high Rb/Sr whole-rock or mica composition from the same $^{87}Sr/^{86}Sr_{(i)}$ (0.7) is shown in Figure 5. After 500 Ma of ^{87}Rb decay in an isotopically closed system, the $^{87}Sr/^{86}Sr$ will have increased to 0.706 by the time the sample is measured. Conversely, a highly fractionated granite with a $^{87}Rb/^{86}Sr$ of 70 will have increased to ~1.2, or ~0.5 more evolved than the low $^{87}Rb/^{87}Sr$ sample from the same system. Both of these $^{87}Sr/^{86}Sr_{(m)}$ values require age corrections to determine $^{87}Sr/^{86}Sr_{(i)}$ (Equation 1) that are significantly greater than the typical analytical uncertainty (2SE = 0.000009). Uncertainty in t from Equation 1 for a high $^{87}Rb/^{86}Sr$ sample (e.g. age error on U–Pb zircon dating ~1%) can lead to large variability in estimated $^{87}Sr/^{86}Sr_{(i)}$ compositions. In the example of Figure 5, an age uncertainty of ±5 Ma (1%) yields calculated $^{87}Sr/^{86}Sr_{(i)}$ between 0.6950 and 0.7049, or 0.7 ± 0.05.

The small variations in $^{143}Nd/^{144}Nd$ render the εNd notation useful, and it is defined by the following equation:

$$\varepsilon Nd = \frac{\left(^{143}Nd/^{144}Nd\right)_m - \left(^{143}Nd/^{144}Nd\right)_{chon}}{\left(^{143}Nd/^{144}Nd\right)_{chon}} * 10^4 \qquad \text{Equation 2}$$

where $^{143}Nd/^{144}Nd_{(m)}$ is the measured Nd value and $^{143}Nd/^{144}Nd_{(chon)}$ is the present-day chondritic value of 0.512638.

Anglin *et al.* (1996) and Jiang *et al.* (2000) utilised the Sm–Nd isotopic decay system to date tourmaline crystallisation associated with mineralisation. Only Jiang *et al.* (1999) have attempted to use initial Sr and Nd compositions of tourmaline to fingerprint fluid sources and tentatively infer mixing with isotopically poorly constrained country rocks.

These new techniques are applied to two Sn deposits in eastern Australia associated with the Ardlethan and Mole granites. These granites are associated with large deposits of cassiterite. Tourmaline is a common gangue mineral within these deposits and occurs in both magmatic and hydrothermal settings.

Granites of the Lachlan and New England orogens are an ideal location for study as they have been subject to extensive Rb-Sr and Sm-Nd isotopic study

since the inception of the I- and S-type granite classification nomenclature by Chappell and White (1974). Therefore, the $^{87}Sr/^{86}Sr_{(i)}$ and $\varepsilon Nd_{(i)}$ variability within these orogens is well defined.

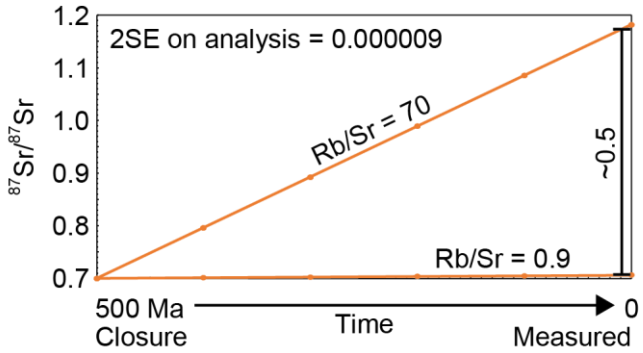

Figure 5: Modelled evolution of $^{87}Sr/^{86}Sr$ from a single reservoir with different Rb/Sr. Granites associated with Sn deposits typically have extremely enriched Rb/Sr (e.g. 70) leading to rapidly evolving $^{87}Sr/^{86}Sr_{(i)}$. Calculation of the $^{87}Sr/^{86}Sr_{(i)}$ requires knowledge of the time since closure of the isotopic system. With the elevated Rb/Sr associated with these granites, even the ~1% uncertainty in U–Pb zircon ages determined by in-situ methods can introduce large errors in the calculation of $^{87}Sr/^{86}Sr_{(i)}$. Conversely, tourmaline has low Rb/Sr (~0.9) and requires very little age correction to determine $^{87}Sr/^{86}Sr_{(i)}$. See text for discussion.

2.2. Analytical methods for tourmaline, whole-rock and quartz samples

2.2.1 Tourmaline geochemistry

Major and trace element analysis

Major element concentrations within tourmaline were determined by EMP at the RSES on a Cameca SX100. A 20 nA primary electron beam was accelerated at 15 KeV onto a spot size of approximately 10 µm. The elements measured (and count times in parentheses) include Na (30 s), F (90 s), Mg (10 s), Al (10 s), Si (10 s), K (30 s), Ca (30 s), Ti (60 s), Mn (30 s). While analysing F the beam was defocussed slightly to excite a larger area. Background intensities were measured on both sides of each peak for a combined time equal to the analysis time. The calibration materials for each element were as follows: Na – Amelia Albinte, F – F-phlogopite, Mg and Fe – San Carlos Olivine, Al – corundum, Si – quartz, K – sanidine, Ca – Wollastonite, Mn – rhodonte andTi – rutile and P – apatite. Data were reduced using the X-phi matrix correction program and analytical precision was monitored with analyses of the Kakanui augite for all elements and topaz for F. The approximate detection limit of each element during EMP analyses is 200 ppm for Na, K, Ca, Mn and Ti, 1500 ppm for F, 300 ppm for Mg and Al, 500 ppm for Si and 350 ppm. The detection limit for P was ~400 ppm, however it was never measured in tourmaline and is therefore not included in this thesis.

Trace element concentrations within tourmaline were determined by LA-ICP-MS at the RSES on an Agilent 7700 quadrupole ICP-MS. This system is equipped with an ArF excimer laser with a wavelength of 193 nm and a repetition rate of 5 Hz. The laser system was coupled to the mass spectrometer with a custom-built ANU ‘He1Ex’ two volume vortex laser ablation cell (Eggins *et al.,* 1998). Ablation was performed in a He environment and combined with an argon and hydrogen carrier gas. Spot diameters of 71, 93 and 157 µm were used depending on crystal sizes. The dwell time was 0.01 seconds for all measured elements except the REE that were 0.05 seconds. A total of 70 integrations were analysed for a total analysis time of 64 seconds. An additional 25 seconds prior to and following ablation was performed to allow background counts to minimise.

The data were reduced using Iolite 2.5 (Paton *et al.,* 2011) with NIST612 (Jochum *et al.,* 2011) as the reference and Si, determined for each spot by EMP, as the internal standard. Detection limits were determined using the equation of Longerich *et al.* (1996) and are included in data tables for each element. Analytical accuracy and precision were monitored using the USGS BCR-2G and BHVO-2G glasses for quality control. For LA-ICP-MS data of the Ardlethan Granite case study, absolute analytical precision was 5–10% for Li, Mg, Ca, Sc, Ti, V, Mn, Co, Rb, Sr, Nb, Sn, LREE (La–Eu), Hf, W, Pb, Th and U and 10–20% for Cu, Y, Zr, In, MREE and HREE (Gd–Lu) and Ta. For the Mole Granite analytical precision was <5% for Li, Mg, Mn, Co, Rb, Mo, Sn, La, Ce and U, 5–10% Sc, Zn, Sr, Y, Zr, Nb, In, REE (excluding La and Ce), Hf, Ta, W, Pb, Th and 10–15% for Cu (1SD).

A new method for Rb–Sr and Sm–Nd isotopic analysis of tourmaline

Sparse studies on the determination of the Rb–Sr and Sm–Nd isotopic composition of tourmaline (Ansdell and Keyser, 1992; Anglin *et al.,* 1996; Jiang *et al.,* 1999) motivated the development of a program to optimise the method for this study. This process is briefly documented chronologically below.

Tourmaline concentrates

Samples containing tourmaline as identified in hand specimen or thin section were crushed and sieved to 80–250 µm size fraction. Tourmaline was then concentrated from this fraction using gravimetric separations with tetrabromoethane (TBE) and methyl iodide (MEI) heavy liquids followed by magnetic separations using a Franz magnetic separator. Final purification of the tourmaline fraction was handpicked under binocular microscope. Between 30 and 200 mg of tourmaline concentrates per sample were then powdered in an agate mortar and pestle. The minimum sample size was determined to have >10 ng of Nd isotopic TIMS analysis.

Washing and digestion

All subsequent work was carried out in the ANU SPID^{2}ER clean laboratory in HEPA filtered work stations. All acids used were purified using Savillex Teflon

sub-boiling stills. For the initial experiments the samples were weighed into precleaned 15 ml Savillex Teflon screw-cap beakers. Powders were then washed in 3 M HCl, 5 M HNO_3 and Milli Q 18 MΩ water before column chemistry. For each washing step the clean reagent was added, the sample was cleaned in an ultrasonic bath for 10 minutes and centrifuged at 3000 rpm for 10 minutes and the supernatant was removed by pipetting. The final step was two washes in Milli-Q H_2O followed by spike addition and dissolution using HF and HNO_3. However, this method produced measured Rb/Sr ratios higher than that predicted by LA-ICP-MS analysis of splits of the same tourmaline and highly evolved measured $^{87}Sr/^{86}Sr$ (Table 1). This was postulated to be the due to the presence of micaceous micro-inclusions (also noted by Jiang *et al.,* 1999). Following this observation, a more aggressive washing/leaching routine was employed that included two washes in 5 M HNO_3, followed by Milli Q water and ultrasonic washes and centrifuges between each step. This cleaning method produced lower $^{87}Rb/^{86}Sr$ that were similar to LA-ICP-MS data (Table 1). The samples then underwent a partial leach in concentrated HF and HCl in the proportions of 3:1. The acid mixture and powder were heated at 95^{o}C for one hour. After cooling, an ultrasonic bath and centrifuge, the acids were removed by pipetting and the samples were rinsed in Milli Q water. To redissolve any fluorides precipitating from the HF solution, concentrated HCl was added to the samples and heated at 95^{o}C for an hour. Following washing and leaching, the samples were spiked with mixed ^{150}Nd–^{147}Sm (ANU1), and ^{85}Rb–^{84}Sr (Lo RbSr) spikes prior to digestion. Samples were then digested with 1 mL of concentrated HNO_3 and 2 mL of concentrated HF and refluxed on a hotplate in a clean air hood at 140^{o}C for up to six days. The samples were periodically agitated in an ultrasonic bath to facilitate dissolution. For some samples with high Sr/Nd ratios the samples were initially spiked with only ANU1 Sm–Nd spike and then, after complete dissolution, an aliquot of the dissolved solution (typically 10%) was taken for Rb–Sr analysis. This enabled optimum spiking without the need for excessive spike quantities. After complete dissolution, when no undissolved material was apparent on visual inspection, the samples were dried at 95^{o}C, refluxed in 6 M HCl, dried again, at 95^{o}C the brought up in 2 M HNO_3 prior to chemical separation.

Table 1: Rb-Sr isotopic data for tourmaline from Ardlethan. The occurrence of micaceous micro-inclusions in tourmaline lead to overestimated $^{87}Rb/^{86}Sr$ and $^{87}Sr/^{86}Sr_{(0)}$ compared to LA-ICP-MS data. A more aggressive wash removed these inclusions.

	ID-TIMS – Non-aggressive wash		ID-TIMS – Aggressive wash		LA-ICP-MS
Sample	$^{87}Rb/^{86}Sr$	$^{87}Sr/^{86}Sr_{(0)}$	$^{87}Rb/^{86}Sr$	$^{87}Sr/^{86}Sr_{(0)}$	$^{87}Rb/^{86}Sr$
ARD06	1.27	0.71739	0.076	0.71041	0.053–0.255
ARD17	2.32	0.72514	0.0249	0.70920	<0.1
ARD19	2.39	0.73078	0.048	0.71091	<0.1

Initially elements were purified through a 4-column process. Solutions were passed through small Teflon columns containing 200 µL of TRU-Spec resin (Horwitz *et al.,* 1993) above 100 µL of prefilter (inert) resin. All resins were batch cleaned prior to use, and then further acid cleaned before sample elution. TRU-Spec resin columns separated the REE from the remaining matrix. The REE fraction was dried, taken up in 0.25 M HCl and then passed through calibrated 75 mm long Teflon Ln-spec columns to isolate Sm and Nd. The fraction from TRU-Spec columns containing Rb and Sr was passed through small columns containing 200 µL of Sr-Spec resin above 100 µL of prefilter resin to isolate Sr from the matrix from Sr. Rb containing fractions were then purified through cation (Bio-Rad AG50-WX8 200 mesh) columns.

For Nd analysis, the fraction was dried and loaded using 2 µL of 1 M HNO_3 in a filtered air hood, onto an outgassed zone refined evaporation filament as part of a double filament assembly and was run on Triton Plus TIMS using 10^{11} ohm resistors in static mode. Sample loads for the tourmaline ranged from 5 ng to 50 ng. For the first set of samples Nd did not emit until elevated currents (in some cases >2200 mA on the evaporation filament and 4500 mA on the ionisation filament compared to the 'normal' 1300 mA on the evaporation filament and 3800 mA on the ionisation filament). This apparent filament poisoning causing ion suppression was most prominent in the larger samples (>100 mg of dissolved tourmaline). To investigate the problem, after removal of the sample from the Triton, the filament was cut from the holder block and the remaining

material on the filament was analysed by LA-ICP-MS. This analysis showed the presence of high amounts of Al on the filament, which was likely hindering Nd ionisation. Horwitz *et al.* (1993) indicate that after loading the sample onto TRU-Spec resin and passing 10 reservoir volumes of 2 M HNO_3 through the columns <2.9% of the original Al remains within the resin. Although in the early experiments 15 reservoir volumes of 2 M HNO_3 were eluted, the large sample sizes and high concentration of aluminium in tourmaline (~35 wt% Al_2O_3) meant that even these small fractions of Al remaining in the resin after washing were still effective at prohibiting ionisation.

To combat this, two methods were tested: 1) samples were passed through large Teflon columns containing cation resin (Bio-Rad AG50-WX8 200 mesh) prior to the methods outlined above, and 2) use of additional washes with 2 M HNO_3 through the TRU resin prior to collection of the REE. The second method proved most effective at removing remaining Al and thus preventing ionisation inhibition and was also more time efficient. The modified elution scheme for a tourmaline matrix in TRU resin is outlined in Table 2. A schematic of entire column chemistry is outlined in Figure 6.

Table 2: Elution scheme for tourmaline in TRU-Spec resin (50–100 µm)

Column volume = 0.3 mL
Reservoir volume = 1 mL

Step	**Eluent**	**Volume**
Cleaning	3 M HCl	5 x 1 mL
Conditioning	2 M HNO_3	5 x 0.3 mL
Load sample	2 M HNO_3	<4 mL
Collect Rb/Sr	2 M HNO_3	2 x 1 mL
Rinse	2 M HNO_3	7 x 1 mL
Collect Sm/Nd	3 M HCl	4 x 1 mL

Rb–Sr and Sm–Nd isotopic analysis

The purified Rb solutions were dried and then loaded onto Re filaments with silica gel similar to Pb loading procedures (Huyskens *et al.*, 2012) to provide more stable emission and decrease the rate of fractionation. The $^{87}Rb/^{85}Rb$ ratio of tourmaline was measured on a MAT261 multicollector Thermal Ionisation

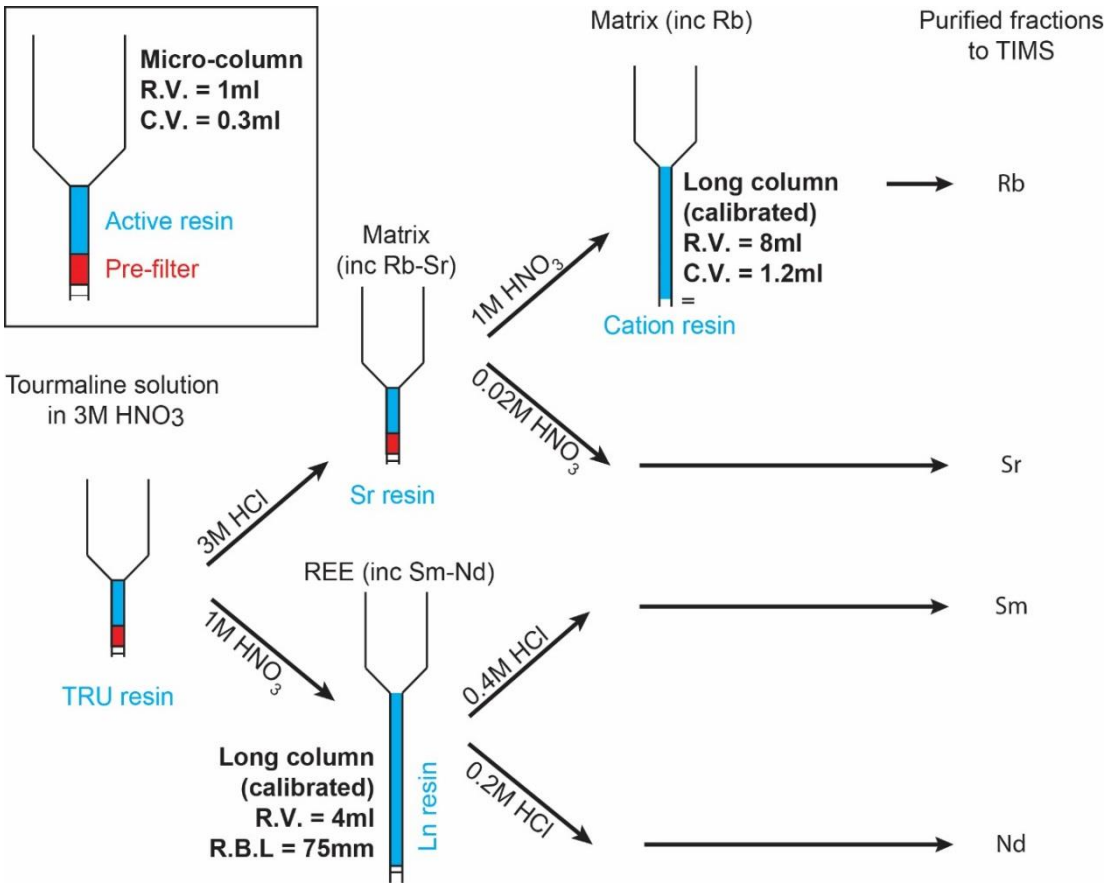

Figure 6: Method flow chart for Rb-Sr and Sm-Nd isotopic analysis of tourmaline developed during this study. R.V. = reservoir volume; CV = column volume; R.B.L. = Resin Bed Length.

Mass Spectrometer (TIMS) at the ANU using either an ion counter or Faraday cups. Each analysis of Rb consisted of 6 blocks of 10 scans with 8 second periods. A 30 second baseline measurement and a peak centre and focus was

done at the beginning of each analysis. As Rb has only two stable isotopes, a internal correction is not possible, so a mass fractionation correction was applied by bracketing sample analyses with Rb extracted from a mica reference material and run under identical conditions.

Purified Sm and Nd solutions were dried down with HNO_3 onto Re filaments and loaded into a TRITON multicollector TIMS with a second, ionisation filament to enhance ionisation. To increase sensitivity, liquid nitrogen was added to the cold trap in the source chamber to freeze water vapour and lower the source pressure to prevent formation of oxides. Sr was loaded onto single Re filaments with a TaF activator. Isotopic ratios were determined by static collection on Faraday cups and corrected for mass fractionation using the following stable isotopic ratios in each analysis; $^{149}Sm/^{152}Sm$ = (0.5168), $^{146}Nd/^{144}Nd$ = 0.7219

(O'Nions *et al.*, 1979), and $^{86}Sr/^{88}Sr = 0.1194$ (Steiger & Jaeger, 1977). Each analysis of Sr and Nd consisted of 15 blocks of 12 scans that were 8 second periods. A 30 second baseline was measured every 3 blocks and a peak centre and focus at the beginning and after 8 blocks. Mass interference of ^{87}Sr by ^{87}Rb was monitored using ^{85}Rb. Sm inferences on Nd isotopes (^{144}Sm, ^{148}Sm and ^{150}Sm) were monitored on ^{147}Sm. Each analysis of Sm consisted of 6 blocks of 12 scans that were 8 second periods, a 30 second baseline measurement every 3 blocks and a peak centre and focus at the beginning of each analysis. Offline Excel data reduction spreadsheets were used for iterative spike-subtraction and mass fractionation calculations to produce final data.
Total procedural blanks were run with every batch of samples. Blanks run in association with tourmalines from the Ardlethan Granite blank were for Nd <30 pg, Sm <10 pg, Sr 300–600 pg with a single batch of 8000 pg of Sr, and Rb 7–35 pg. The single batch of Sr with a high blank was attributed to a contaminated digital pipettor. However, even the high Sr blank were in most cases insignificant compared to the 100–500 ng of Sr from the sample (0.08–0.016 % of the total weight). For the samples associated with the high Sr blank, the associated increased uncertainty of $^{87}Sr/^{86}Sr$ is included. Procedural blanks run concurrently with the Mole Granite tourmalines were generally <30 pg of Nd and <50 pg of Sr.

Over the period of this study the external precision of Triton multicollector TIMS was monitored with the in-house Nd-1 (Nd) (originally prepared from an AMES metal) and NBS987 (Sr) standards. Fifteen analyses of Nd-1 over 3 years yielded an average value of 0.512142 ± 0.0000138 (2SD). La Jolla (0.5118503 ± 0.0000051, 2SE; n = 1) and JNd1 (0.5120986 ± 0.0000047, 2SE; n = 1) were analysed as secondary standards. Twenty-eight analyses of NBS987 yielded an average $^{87}Sr/^{86}Sr$ of 0.710263 ± 0.000019 (2SD).

2.2.2 Whole rocks

Determination of the major, minor and trace element concentrations and Rb–Sr and Sm–Nd isotopic compositions were by traditional methods summarised here. Major element compositions were determined by XRF by Bodorkos *et al.* (2013) at the Ardlethan Granite and Laker (2017) at the Mole Granite. For the trace element concentrations whole-rock powders were fused with lithium

metaborate to form a glass and analysed by LA-ICP-MS. A 10 Hz and ~150 µm diameter spot was traversed over ~1 mm of sample and standard at a rate of 10 µm/s. Each value is the average of three traverses. The data were reduced with the NIST612 as a primary reference material and SCO1, GSP2 and AGV2 as secondary reference materials. Si was used as an internal standard, determined by XRF, to correct for variations in ablation yield. The absolute analytical precision was <5% for Mg, Ca, Ti, V, Mn, Co, Rb, Sr, Zr, Sn, LREE, Th and U, <10% for Zn, Y, HREE, Nb, Pb and <20% for Cu, Ga.

Rb–Sr and Sm–Nd isotopic compositions of the whole-rock powders were determined by ID-TIMS. Approximately 50 mg of powdered rock was weighed into a Teflon container and placed in a steel jacketed Parr bomb along with weighed aliquots of 'ANU1' (^{150}Nd–^{147}Sm) and 'HiRbSr' (^{85}Rb–^{84}Sr) mixed spikes. These pressure vessels were heated at 190^{o}C for 2 days in a laboratory oven, or until complete dissolution of the powder. Rb, Sr, Sm and Nd were then isolated through a 3-stage column chemistry involving TRU resin, Sr resin and Ln resin, comparable to the tourmaline method (Figure 6). Measurement of the isotopic compositions was the same as described for tourmaline.

2.2.3 Oxygen isotopes in quartz and whole-rocks

The oxygen isotopic composition of individual quartz grains was determined on the SHRIMP II ion microprobe at the Research School of Earth Sciences, ANU using methods detailed in Ickert *et al.* (2008) and summarised here. Quartz grains were handpicked from mineral separates under a binocular microscope and mounted in epoxy. Epoxy mounts were polished initially with 800 grit paper and 9 µm, 3 µm and a 1 µm diamond paste. After SEM imaging, the mount was cleaned and coated with approximately 20 nm of Au and left in a vacuum oven overnight prior to analysis. Measurements were taken after a primary Cs^{+} ion beam operating between 2 and 3 uA was focussed onto a 25-um spot. The production of negative secondary ions is increased by focussing an electron gun on the sample surface. Secondary ions are accelerated from the sample chamber and into the mass spectrometer at 10 KeV. ^{16}O and ^{18}O are measured simultaneously on two collectors for 6 scans of 20 seconds each. To correct for the effect of background desorption in the area of the detector (electron-induced secondary ion emission; EISIE), the primary beam was turned off periodically

during the analytical session and the EISIE was measured (Ickert *et al.,* 2008). The EISIE correction assumes a $^{16}O/^{18}O$ of ~600.

To monitor instrument bias, drift and accuracy the UWQ (Kelly *et al.*, 2007) and NBS28 (Gonfiantini *et al.*, 1995) quartz grains were used for primary calibration and quality control, respectively. The reproducibility of 85 analyses of UWQ1 bracketing unknowns of the Ardlethan Granite was 0.48 ‰ (2SE). Drift-corrected analyses of the NBS28 quartz had an average value of $\delta^{18}O$ = 9.61 ± 0.86 ‰, within error of reported values (9.58 ± 0.09). The reproducibility of 89 analyses of UWQ1 bracketing unknowns of the Mole Granite was +0.52 ‰ (2SD). Eleven analyses of the NBS28 reference material had an average value of +9.35 ± 0.64 ‰ (2SD), within error of reported values (+9.58 ± 0.09).

Whole-rock fines (>40 µm) of the Dundee Rhyodacite, Emmaville Volcanics, the Mole Granite and Bondonga Beds (Table 18) were analysed commercially by GNS by the laser-fluorination method (Sharp, 1990). Bulk rock samples were crushed and sieved to 150 µm in a W-carbide mill. Oxygen isotopes were determined by GNS as follows; "Oxygen was extracted from sample powders for isotope analyses using a CO_2-laser and BrF_5 (Sharp, 1990). Four analyses of NBS-28 analysed [varied] by less than 0.15 ‰. Samples and standards were heated overnight to 200°C prior to loading into the vacuum extraction line. These were then evacuated for approximately 6 hours. Blank BrF_5 runs were done until yield was less than 0.2 µmoles oxygen. Oxygen yields were recorded, and CO_2 gas analysed on a Geo20-20 mass spectrometer."

$\delta^{18}O$ is reported in per mil (‰) variations relative to the standard Vienna Standard Mean Ocean Water (VSMOW) according to the formula:

$$\delta^{18}O = 1000 \text{ x } \frac{([^{18}O/^{16}O]_{sample} - [^{18}O/^{16}O]_{standard})}{(^{18}O/^{16}O)_{standard}} \qquad \text{Equation 3}$$

2.3. Composition of magmatic melts and the transition to hydrothermal fluids of the Ardlethan porphyry and greisen Sn system

2.3.1 Introduction

In this Chapter the major and trace element concentrations and Rb–Sr and Sm–Nd isotopic concentrations from tourmaline from within the Ardlethan Sn deposit in the Lachlan Orogen of eastern Australia are presented. Granites of the Lachlan Orogen have been subject to extensive Rb–Sr and Sm–Nd isotopic study since the inception of the I- and S-type granite classification nomenclature by Chappell and White (1974) (Nelson *et al.*, 1984; McCulloch and Woodhead, 1993; McDonough and McCulloch, 1993; Keay *et al.*, 1997). Subsequently the regional temporal and compositional evolution of the orogen has been well defined (Kemp *et al.*, 2009) including most possible end-member igneous and sedimentary units occurring at Ardlethan.

2.3.2 Geology

The Ardlethan Granite is associated with breccia and greisen cassiterite mineralisation. The majority of mineralisation occurs within a series of bifurcating breccia pipes hosted by the Mine Granite (Figure 7). Between 1912 and 1986 these pipes produced approximately 30,000 tonnes of tin (Paterson, 1990). The greisen mineralisation is concentrated within the eastern margin of the Ardlethan Granite and north of the breccia pipes (Figure 7). Greisen mineralisation is significantly smaller, with only shallow workings, although recent exploration is ongoing (Thomson Resources).

Initially, the Ardlethan and Mine granites were assigned to the *ca* 430 Ma Koetong Supersuite, also known as the Wagga Tin Belt due to its association with numerous Sn deposits, of which the mineralisation at Ardlethan is the largest (Richards *et. al.,* 1982; Chappell *et. al.,* 1991; Blevin and Chappell, 1995; Carr *et. al.,* 1995; Ren *et. al.,* 1995; White *et al.,* 2001). However, recent geochronology has identified the Ardlethan Granite and other granite and volcanic units to be *ca* 415 Ma (Bodorkos *et. al.,* 2013). It remains unclear whether the Koetong Supersuite was emplaced over a *ca* 15 Ma period

(between 430 and 415 Ma), or if *ca* 415 Ma represents a new period of magma generation.

The Koetong Supersuite is a prominent north-northwest-trending belt of mafic to felsic (SiO_2 = 45.34–77.32 wt%) granites in the central Lachlan Orogen (White *et al.*, 2001). The supersuite has an inferred sedimentary source based on the abundant meta-sedimentary enclaves in the mafic components, peraluminous chemistry (Chappell, 1996; White *et al.*, 2001) and radiogenic $^{87}Sr/^{86}Sr_{(i)}$, $\varepsilon Nd_{(i)}$ and Pb isotopic compositions (McCulloch and Chappell, 1982; McCulloch and Woodhead, 1993; Carr *et al.*, 1995). The supersuite is inferred to have undergone extensive fractional crystallisation due to a large range in SiO_2 composition and inflections of elements on variation diagrams (e.g. increasing Rb and decreasing Ba at SiO_2 >70 wt%; Figure 8; Chappell, 1996). By contrast, the adjacent Bullenbalong Supersuite did not undergo extensive fractional crystallisation and thus is not associated with Sn mineralisation (Figure 8). Sn is expected to be enriched in residual melts during fractional crystallisation due to its general incompatibility felsic minerals (Blevin and Chappell, 1995;

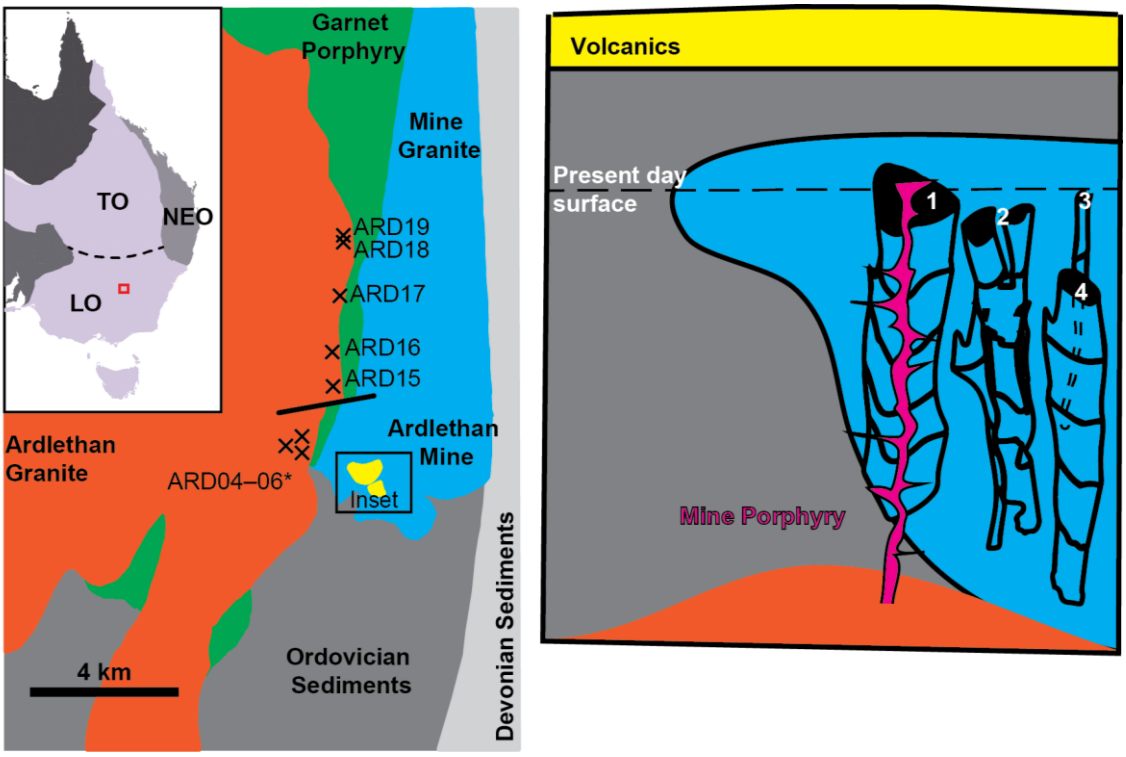

Figure 7: Geological map of the Ardlethan region (left) including sample locations for isotopic analysis (edited from Ren et al., 1995). Schematic cross-section (right) of the breccia pipes occurring within the Mine Granite but inferred to converge on the Ardlethan Granite. 1) Mine Breccia pipe; 2) Carpathia-Blackreef Breccia pipe; 3) Stackpool-Godfrey Breccia pipe; 4) White Crystal Breccia pipe. The Mine Porphyry occurs within these breccia pipes and contemporaneous with the brecciation event. Schematic cross-section edited from Ren et al., 1995.

Ren *et al.*, 1995; Walshe *et al.*, 1995; White *et al.*, 2001; Walshe *et al.*, 2011), however, Sn concentrations are comparable in the Koetong and Bullenbalong supersuites over a wide range of SiO_2.

Two major plutonic phases are located within the Ardlethan region: The Mine Granite and the Ardlethan Granite, as well as two minor plutonic phases: the microgranite (not mapped) and the Mine Porphyry (Figure 7). The garnet-bearing quartz–feldspar porphyry (GQFP) was originally classified as a plutonic fractionated end-member of the Ardlethan Granite, but it was recently reclassified as a pyroclastic flow sitting above the Ardlethan Granite (Figure 7; Bull *et al.*, 2017). All igneous units were emplaced within a vast expanse of Ordovician metasediments that cover much of the Tasmanides (Glen, 2005).

The earliest plutonic phase, and hosting the breccia mineralisation, is the Mine Granite. It is a weakly foliated, medium- to coarse-grained granite with quartz (25 vol%), K-feldspar (35 vol%), plagioclase (25 vol%), biotite (13 vol%) and muscovite (2 vol%) and accessory apatite, zircon, cordierite, ilmenite and rutile (Ren, 1989). U–Pb dating of zircon from this granite yield a crystallisation age of 428.1 ± 2.8 Ma (Bodorkos *et al.*, 2013). Aplitic microgranite dykes commonly intrude the Mine Granite, contain quartz (30 vol%), K-feldspar (45 vol%) and plagioclase (25 vol%) and accessory ilmenite, apatite and zircon (Ren, 1989).

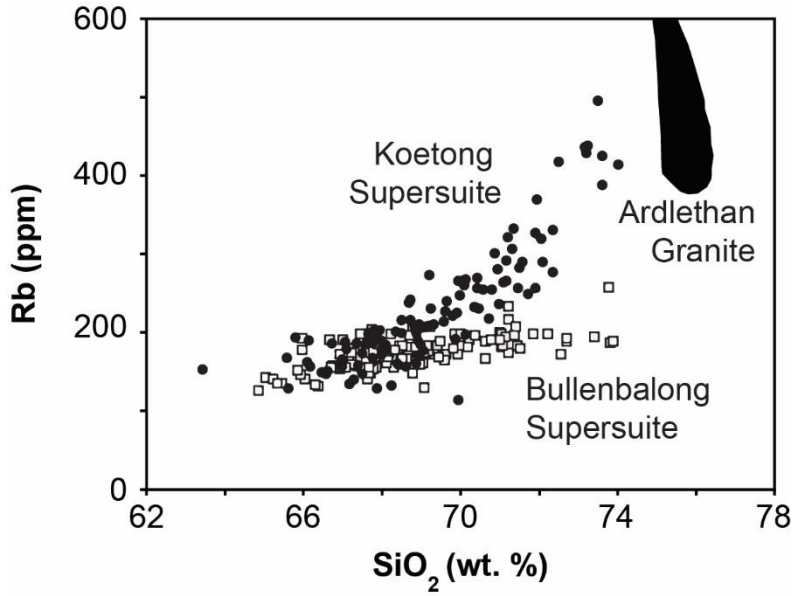

Figure 8: Increasing Rb concentration within increasing SiO_2 of granites of the Koetong Supersuite compared to the Bullenbalong Supersuite in the Lachlan Orogen. The steeper increase in the Koetong Supersuite is attributed to continued fractional crystallisation, evolving to the most fractionated end-member the Ardlethan Granite.

Late quartz–tourmaline nodules are also present in this unit. U–Pb isotopic dating of zircon from the microgranite yielded a crystallisation age of 428.3 ± 1.7 Ma (Bodorkos *et al.*, 2013). The GQFP contains up to 40 vol% K-feldspar, quartz and plagioclase euhedral to subhedral phenocrysts amongst a fine-grained matrix with accessory apatite, ilmenite, garnet and zircon (Ren *et al.*, 1995). Ren *et al.* (1995) suggest the GQFP grades into the Ardlethan Granite, and is a fractionated end-member of the same magma, however, more recent studies have reclassified the unit as a pyroclastic flow emplaced sub-aerially prior to the emplacement of the Ardlethan Granite (Bull *et al.*, 2017). Zircon U–Pb dating provided a crystallisation age of 417.8 ± 2.3 Ma, contemporaneous with and likely a southerly extension of the Gurragong Volcanics (Colquhoun *et al.*, 2005; Bodorkos *et al.*, 2013). The Ardlethan Granite has a variable texture from porphyritic to medium- and extremely coarse-grained (Ren, 1989). It is composed dominantly of quartz (35 vol%), K-feldspar (35 vol%), plagioclase (23 vol%), with minor biotite (<4 vol%) and muscovite (<2 vol%), and accessory apatite, ilmenite and zircon (Ren, 1989). The eastern margin of the Ardlethan Granite represents the upper part of the body; it is characterised by abundant quartz–tourmaline nodules up to 20 cm that make up to 3 vol% of the rock. Similarly, pyrite, chalcopyrite, fluorite and cassiterite also occur along the eastern margin within greisen granite (Ren, 1989). U–Pb dating of zircon from fresh Ardlethan Granite yielded a crystallisation age of 414.7 ± 2.3 Ma (Bodorkos *et al.*, 2013). The relatively minor Mine Porphyry includes a swarm of dykes intruding Ordovician sediments and the Mine Granite. The Mine Porphyry contains quartz and K-feldspar phenocrysts (15–30 vol%) within an aphanitic groundmass. These dykes are commonly located within the brecciated Mine Granite. In some locations the dykes cut through brecciation textures, and in others are cut by brecciation textures. These relationships constrain the brecciation event to be contemporaneous with the U–Pb zircon crystallisation age of the unit; 404.9 ± 2.3 Ma (Bodorkos *et al.*, 2013).

Ren (1989) suggested the major, minor and trace element chemistry of the Mine Granite, Ardlethan Granite, GQFP, microgranite and Mine Porphyry could result from simple fractionation processes of a single parental magma. However, recent U–Pb geochronological data (Bodorkos *et al.*, 2013, 2015) and

Sr, Nd and Hf isotopic data (Walshe *et al.*, 2011; Blevin *et al.*, 2017; this study) delineate these units into three temporally and chemically distinct events.

1) The Mine Granite and its associated microgranite dykes as part of the Koetong Suite. The Mine Granite has SiO_2 contents between 69 and 72 wt%, is peraluminous (Ren *et al.*, 1995) and has an evolved Nd isotopic composition ($\varepsilon Nd_{(i)}$ = ~–10; Walshe *et al.*, 2011), indicative of a weathered, probably sedimentary source.
2) The Ardlethan Granite and GQFP were emplaced *ca* 15 Ma after the Koetong Suite. Recent U–Pb zircon dating from granites and volcanics of the Lachlan Orogen indicates significantly more magmatism at this time than previously thought (Bodorkos *et al.*, 2013, 2015; Fraser *et al.*, 2014). The Ardlethan Granite has undergone extensive fractional crystallisation resulting in simplified petrographic features similar to a haplogranite and obscuring magmatic sources and processes. It has between 74 and 77 wt% SiO_2, is metaluminous and enriched in Li, F, Rb, Th, U, Nb, and Sn compared to the Mine Granite and the Koetong Supersuite (Ren *et al.*, 1995). The whole-rock $\varepsilon Nd_{(i)}$ composition is ~0, less radiogenic than the Mine Granite (Walshe *et al.*, 2011).
3) The Mine Porphyry was emplaced *ca* 10 Ma after the Mine Granite. Similar to the Ardlethan Granite, it is strongly felsic with SiO_2 between 76 and 77 wt%, metaluminous, and enriched in F, Rb, Th, U, Zr, Nb, Y, and Sn (Ren *et al.*, 1995). It has a juvenile $\varepsilon Nd_{(i)}$ value of 2.1 (Walshe *et al.*, 2011).

The evolution of igneous rocks at Ardlethan towards increasingly less radiogenic $\varepsilon Nd_{(i)}$ compositions is comparable to that experienced throughout the Lachlan Orogen during this period (Kemp *et al.*, 2009).

Primary cassiterite mineralisation at Ardlethan occurs within numerous breccia pipes hosted by the Mine Granite and with greisen alteration zones of the Ardlethan Granite (Figure 7). The bifurcating breccia pipes dip towards the west and are hypothesised to converge into the Ardlethan Granite at depth (Ren *et al.,* 1995). Within the Mine Breccia Pipe numerous local enrichment zones/deposits have been identified including the Wildcherry, Wildcherry South, Ardwest and Perseverance deposits. Ren *et al.* (1995) suggest that fluid over

pressurisation associated with the cooling Ardlethan Granite lead to multi-staged brecciation and mineralisation. U–Pb cassiterite dating at Ardlethan suggests mineralisation occurred between *ca* 415 and 410 Ma (Chapter 3). Ren *et al.* (1995) identified the Ardlethan Granite as the source of mineralising fluids as it was the most fractionated unit in the region, and because the breccia pipes appear to converge on its edge. Walshe *et al.* (2011) suggest the Mine Porphyry may have contributed to mineralisation, invoking mantle input into the system.

Cassiterite mineralisation within the breccia pipes is associated with intense and zoned alteration (Figure 9; Ren, 1989). Mine Granite fragments are pervasively altered with hydrothermal biotite, sericite, tourmaline, cassiterite, quartz, topaz and chlorite (Ren, 1989). Ren (1989) noted that cassiterite mineralisation was mostly strongly associated with sericitic mineralisation, a common alteration assemblage surrounding Sn deposits (Taylor, 1979; Lehmann, 1990). Sericite is seen to variably replace biotite, plagioclase and K-feldspar in the Mine Granite.

Cassiterite mineralisation within greisen zones occurs at the contact with the GQFP (Figure 7). Alteration grades from unaltered Ardlethan Granite, to propylitic and intense phyllic and siliceous alteration, and is associated with the destruction of primary biotite and feldspar and replacement with topaz and muscovite (Scott and Rampe, 1984). Intense tourmaline alteration occurs along fractures within these zones (Scott and Rampe, 1984).

2.3.3 Samples

Whole-rock samples

Whole-rock powders from the magmatic units were sampled from the collections of Bodorkos *et al.* (2013) (Ardlethan Granite, Mine Granite and Microgranite) and Ren *et al.* (1995) (Mine Porphyry) in order to determine trace element concentrations and Rb–Sr and Sm–Nd isotopic compositions. Major and trace element data for those samples are also presented in the previous publications.

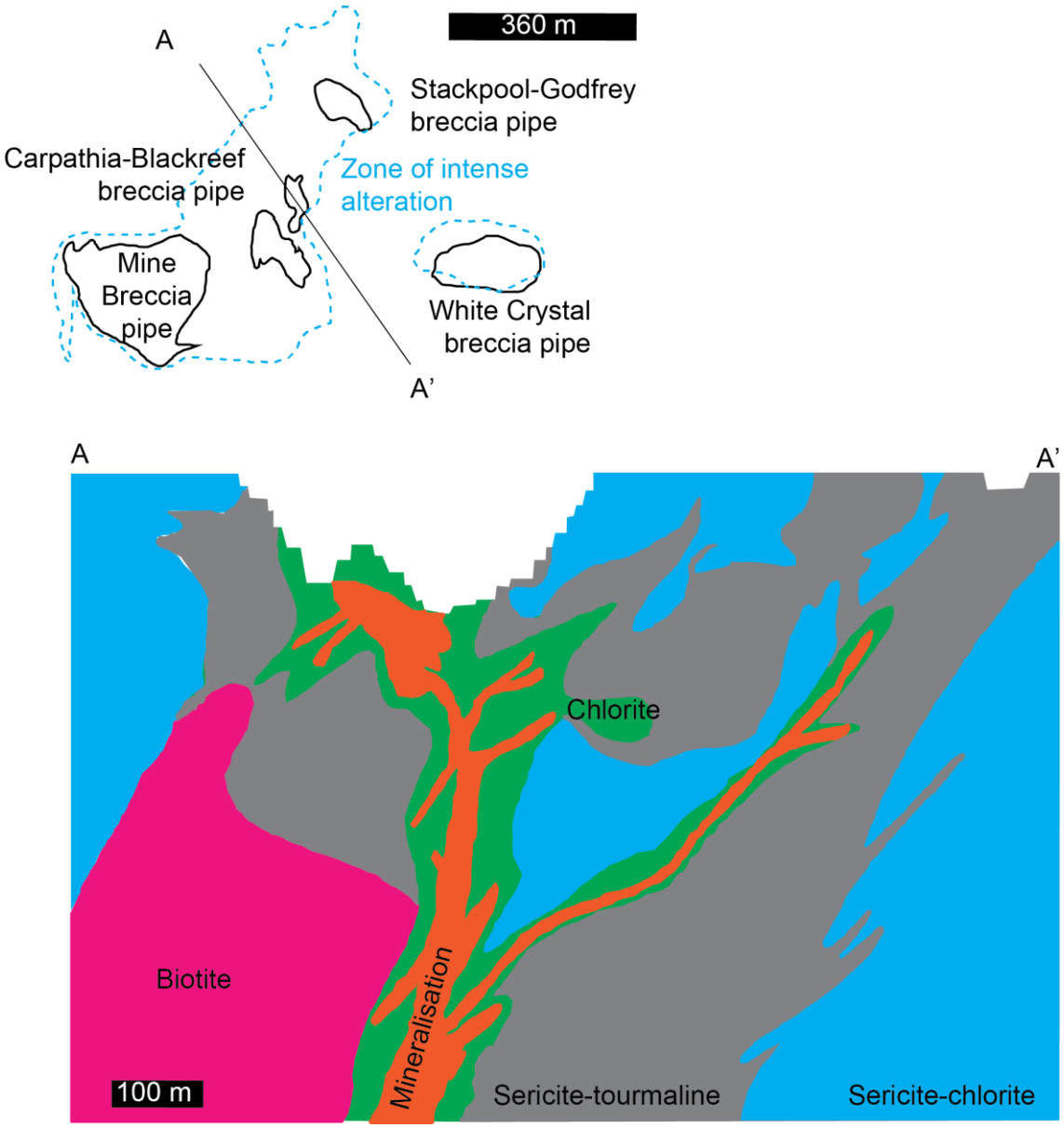

Figure 9: Alteration zones surrounding mineralisation in the Mine Breccia Pipe. The zone of alteration is shown in plan-view in the top panel. A cross-section through the breccia pipe is shown in the bottom panel. Figure modified after Ren (1989).

Tourmaline samples

Nineteen tourmaline samples were collected for major and trace element analysis from within the Ardlethan deposit and smaller satellite deposits (Table 3). These samples occur as late magmatic phases of the Ardlethan Granite and within hydrothermal deposits (breccia-, vein-, and greisen-hosted) associated with cassiterite mineralisation. Fourteen of these samples were selected for Rb–Sr and Sm–Nd isotopic analyses based on location and textural setting. Four groups of tourmalines were delineated; 1) Qtz–tourmaline nodules and interstitial tourmaline occurring within the Ardlethan Granite, 2) tourmaline ±

cassiterite ± sulfide breccia infill, 3) qtz–tourmaline veins occurring within greisen deposits and commonly associated with cassiterite, and 4) a fine, acicular tourmaline overprint. A single sample of tourmaline 'suns' (ARD19) is included in Group 3 due to its close spatial association, and is described below.

Similarly, Ren (1989) identified 4 generations of tourmaline at Ardlethan: 1) quartz–tourmaline nodules, 2) patchy tourmaline, 3) granular tourmaline, and 4) "acute" (or acicular) tourmaline. They suggest that the quartz–tourmaline nodules are associated with the patchy tourmaline and occur pre-brecciation. Granular tourmaline, commonly associated with cassiterite mineralisation, occurs post-brecciation.

Table 3: Ardlethan tourmaline sample information for this study. Host rock abbreviations: MG = Mine Granite; AG = Ardlethan Granite. Mineral abbreviations: qtz = quartz; fs = feldspar; mic = mica; cst = cassiterite; wf = wolframite; fl = fluorite; ap = apatite; gn = galena; asp = arsenopyrite; cp = chalcopyrite; sl = sphalerite; py = pyrite; rt = rutile; chl = chlorite; hem = hematite; tpz = topaz.

Sample #	Deposit	Host Rock	Minerals	Setting	Group
ARD01		MG	qtz–fs–mic	Interstitial	1
ARD02		MG	qtz	Breccia	1
ARD03		MG	qtz	Breccia	1
ARD04		AG	qtz–fs–mic	Interstitial	1
ARD05		AG	qtz	Interstitial	1
ARD06		AG	qtz	Nodules	1
ARD07	Wildcherry	MG	qtz–cst	Breccia	2
ARD08	Godfrey	MG	wf–fl–ap	Breccia	2
ARD09	Godfrey	MG	cst– gn–sl–py–cp	Breccia	2
ARD10	Godfrey	MG	wf–py–asp–cp–rt	Breccia	2
ARD11	Godfrey	MG	wf–gn–sl–py–cp–rt	Breccia	2
ARD12	Blackreef	MG	sl	Breccia	2
ARD13	Blackreef	MG	cst–rt–chl–hem	Breccia	2
ARD14	White Crystal	MG	qtz–asp–gn	Breccia	4
ARD15	Buchanan	AG	qtz–cst	Vein	3
ARD16	Titanic	AG	qtz–cst	Vein	3
ARD17	Big Bygoo	AG	qtz	Vein	3
ARD18	Little Bygoo	AG	qtz–cst	Vein	3
ARD19	Little Bygoo	AG	qtz–tpz	'Suns'	3

Here we separate the granular tourmaline of Ren (1989) into two groups (groups 2 and 3) based on their different depositional environments (breccia infill vs. greisen vein). Acicular, ("acute" of Ren 1989) tourmaline is a late overprint of the main brecciation event, comparable to Group 4 defined here.

Group 1 tourmaline occurs primarily in nodules up to 20 cm in diameter and associated with quartz (ARD05,06; Figure 10A, B). These nodules increase in abundance along the eastern margin of the Ardlethan Granite (Ren, 1989). Rare cases of interstitial tourmaline between the main granite forming minerals (feldspar, mica, quartz) (ARD04; Figure 10C, D) occur. Nodular tourmaline is black, generally coarse-grained, euhedral to subhedral. Crystal habits include granular (e.g. Figure 10D) and anhedral (Figure 10F). Crystals are zoned in both plane polarised light with blue cores and green rims (Figure 9D) and in BSE, with dark cores and light rims (Figure 10E, F). The origin of tourmaline nodules is unclear, with three prevailing hypotheses: 1) boron-rich bubbles rising through the granite (Balen and Broska, 2012), 2) immiscible hydrous borosilicate melt (Drivenes *et al.*, 2015) and 3) post-magmatic boron-rich metasomatism (Dick, 1980; Le Fort, 1991; Rozendaal and Bruwer, 1995). A lack of strong alteration or fluid pathways within the Ardlethan Granite indicates that this tourmaline did not form from an external source.

Group 2 tourmaline is texturally comparable to the granular tourmaline of Ren (1989). The quartz–tourmaline samples are commonly directly associated with cassiterite (ARD15,16,18) and other times are seemingly barren (ARD17). Tourmaline is primarily euhedral and acicular (Figure 11A–C) and associated with euhedral quartz. Group 2 tourmaline infills brecciation voids within the Mine Granite and White Crystal breccias pipes and is commonly associated with quartz, cassiterite and sulfides. Tourmaline samples were collected from the Godfrey, Blackreef, Wildcherry and White Crystal reefs. Textural habits vary across deposits and in places within samples. In the Wildcherry deposit breccia infill includes a quartz–tourmaline outer layer (Figure 11A, B), and a dominant tourmaline middle and core. Cassiterite occurs as euhedral crystals in the core of this sequence, with a close association with tourmaline (Figure 11C).

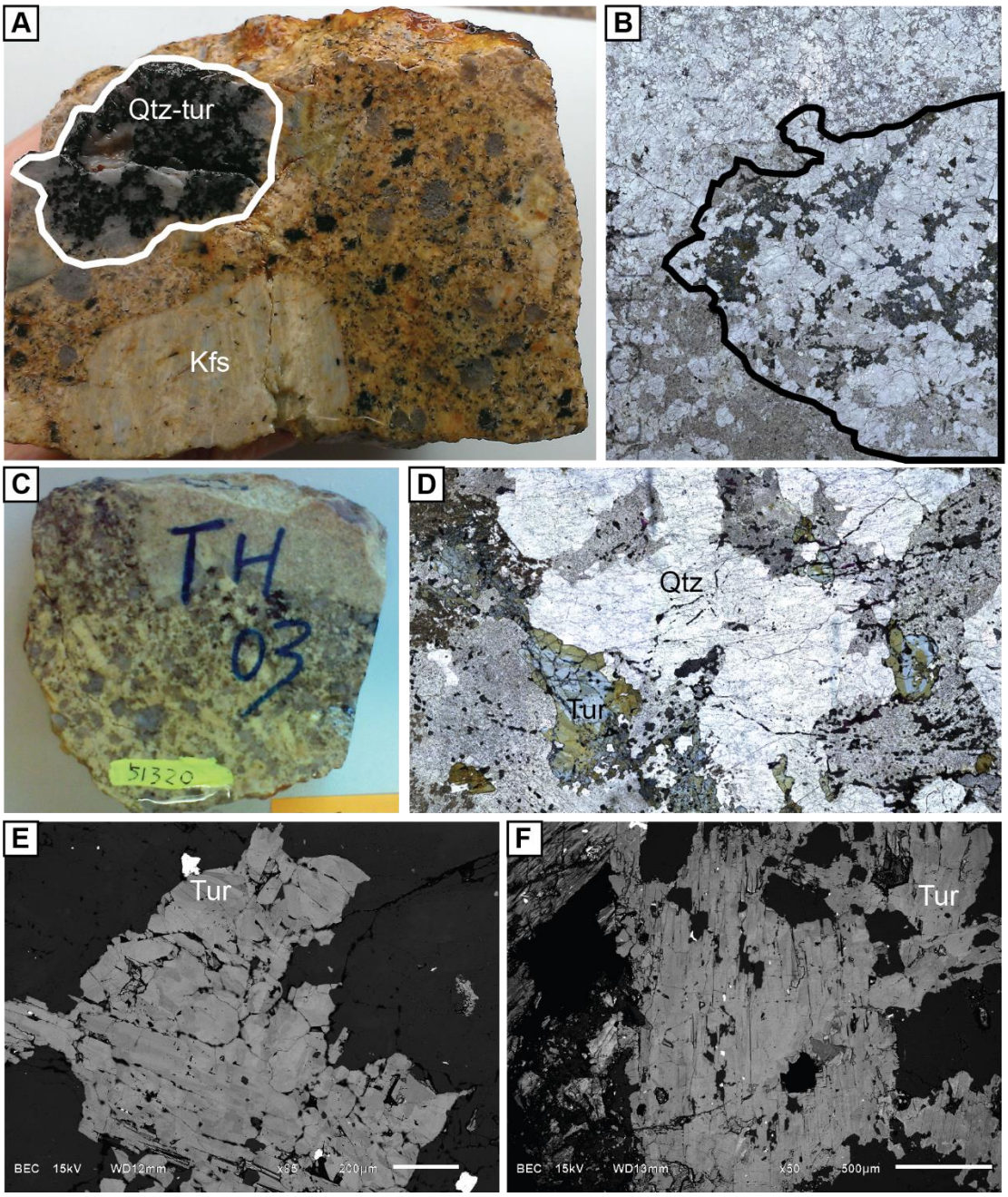

Figure 10: Setting and textural habits of Group 1 tourmaline including quartz–tourmaline nodules within porphyritic Ardlethan Granite (ARD06; A and B). ARD05 includes small (~1 cm) aggregations of tourmaline (C), and interstitial tourmaline (D). Back scattered electron (BSE) imaging (E and F) indicates compositional zoning that correlates with plane polarised light zoning (B and D) that is described in the text.

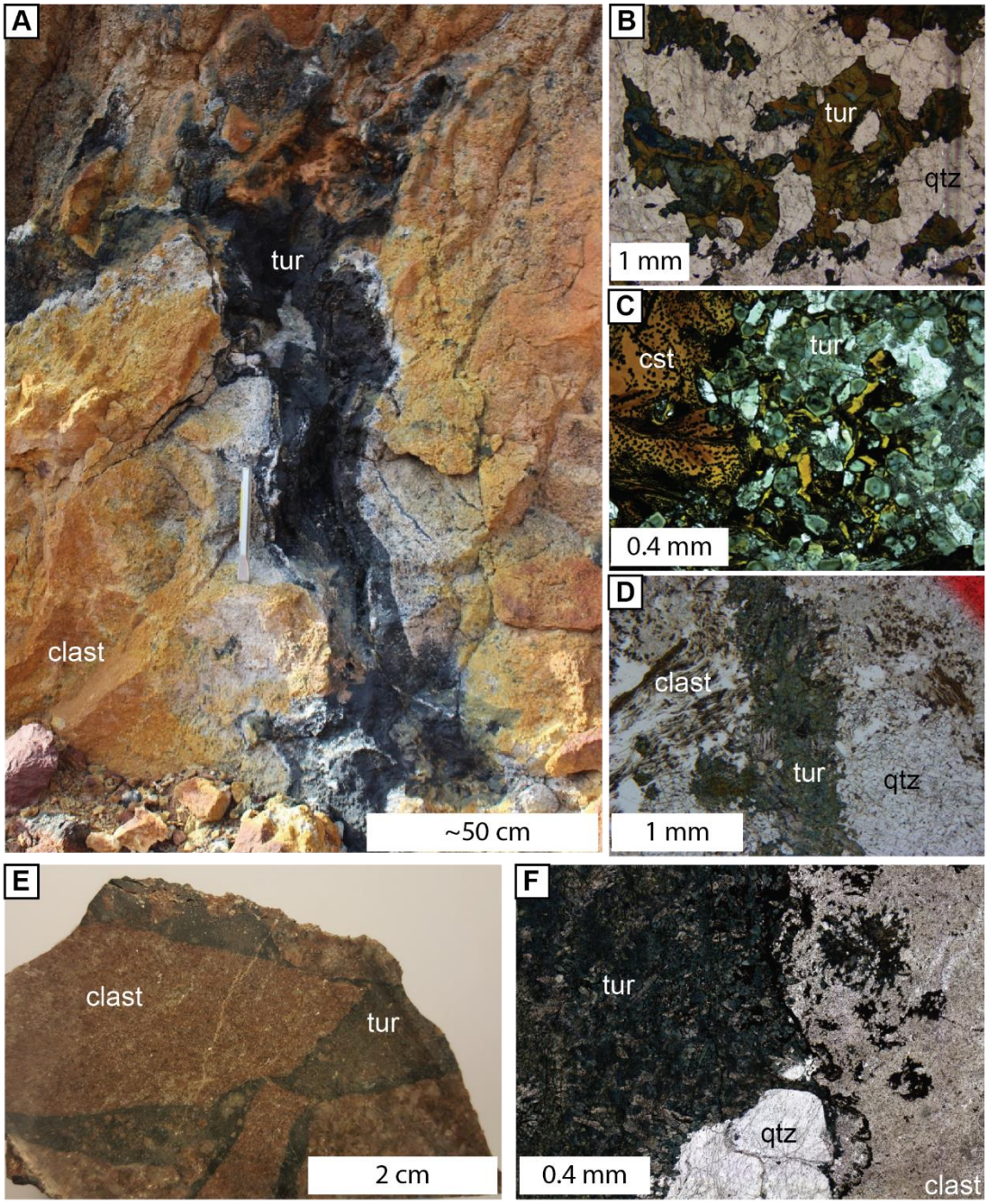

Figure 11: Setting and textural habits of Group 2 tourmaline at Ardlethan as breccia infill and alteration. Large quartz-tourmaline-cassiterite veins occur between fragments of the Mine Granite in the Mine Breccia Pipe (A; ARD07). Tourmaline is intergrown with euhedral quartz (B) and subhedral cassiterite (C). Tourmaline veinlets (D) commonly cut through breccia infill textures. Mine Granite clasts are heavily altered to sericite (E and F).

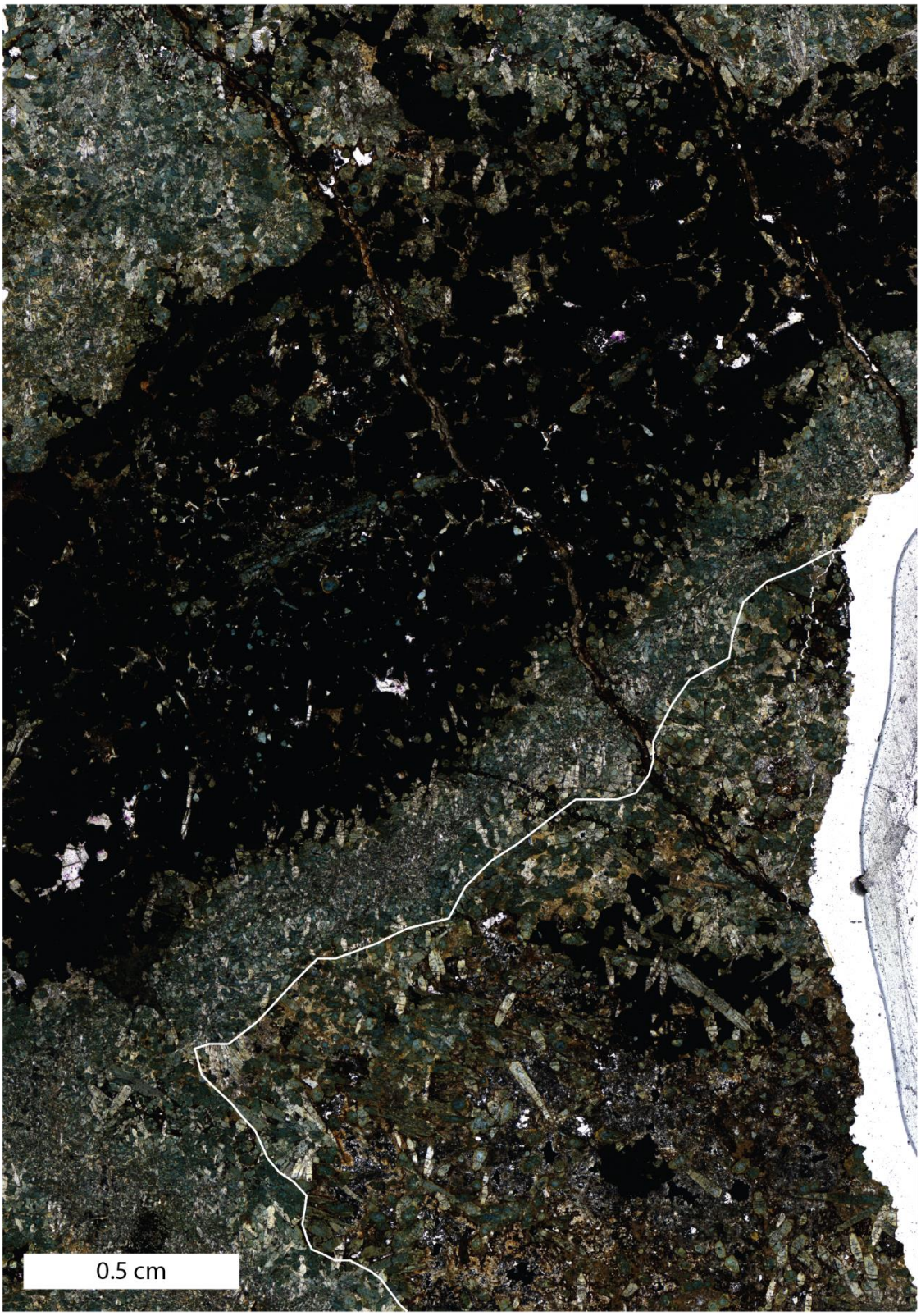

Figure 12: Thin section image in plane polarised light (PPL) of at least two generations of tourmaline from ARD10. The earlier tourmaline (wedge shape outlined in white) within the groundmass of the rock is cross cut by at least one generation of tourmaline co-precipitating with oxides (wolframite and cassiterite) and sulfides (pyrite, arsenopyrite and chalcopyrite) in veins.

When precipitating with quartz, tourmaline predominantly forms subhedral grain boundaries (Figure 11B). Conversely when precipitated with cassiterite it forms euhedral boundaries (Figure 11C). At least two generations of tourmaline are evident in the Godfrey deposit (Figure 12). Both generations are euhedral and hexagonal down the c-section, and elongate. The first generation is defined by blue cores in plane polarised light (PPL) and green rims. The second generation cross-cuts the first, is slightly finer grained, and primarily blue and unzoned in PPL. This second generation is closely associated with a sulfide mineral-bearing (predominantly pyrite) vein. A veinlet of tourmaline is also present in the Mine Breccia Pipe, that appears to postdate the breccia-infill quartz (Figure 11D). It is subhedral to euhedral with blue cores and green rims in PPL.

Group 3 tourmaline includes samples occurring in quartz-veins and greisen of the Ardlethan Granite, north of the main breccia-hosted mineralisation (Figure 7). Textural habits are predominantly quartz–tourmaline rock (Figure 13A–C) and a single sample hosting tourmaline ‘suns’ (Figure 13D). Tourmaline ‘suns’ are so defined as they are composed of numerous acicular crystals radiating from a single point. This sample originates from the Ardlethan Granite that has been pervasively altered to quartz-topaz. Samples of Group 3 coexist with cassiterite in ARD16 (Figure 13A) and ARD19 (Figure 13C). Quartz–cassiterite veins were collected adjacent to ARD17 (Figure 13B). No thin sections were made for Group 3 tourmaline.

Group 4 tourmaline is fine-grained, very acicular, and appears to post-date brecciation and cassiterite–tourmaline–quartz mineralisation. It is most prevalent in the White Crystal Breccia Pipe (Figure 14A) where it has precipitated around the grain boundaries of quartz infill (Figure 14B). It is comparable to the description of “acute” tourmaline described by Ren (1989), which is also described as common in small secondary breccia pipes, rim fragments of the Mine Granite and Mine Porphyry, and partially replace pre-existing minerals or selectively replace feldspars.

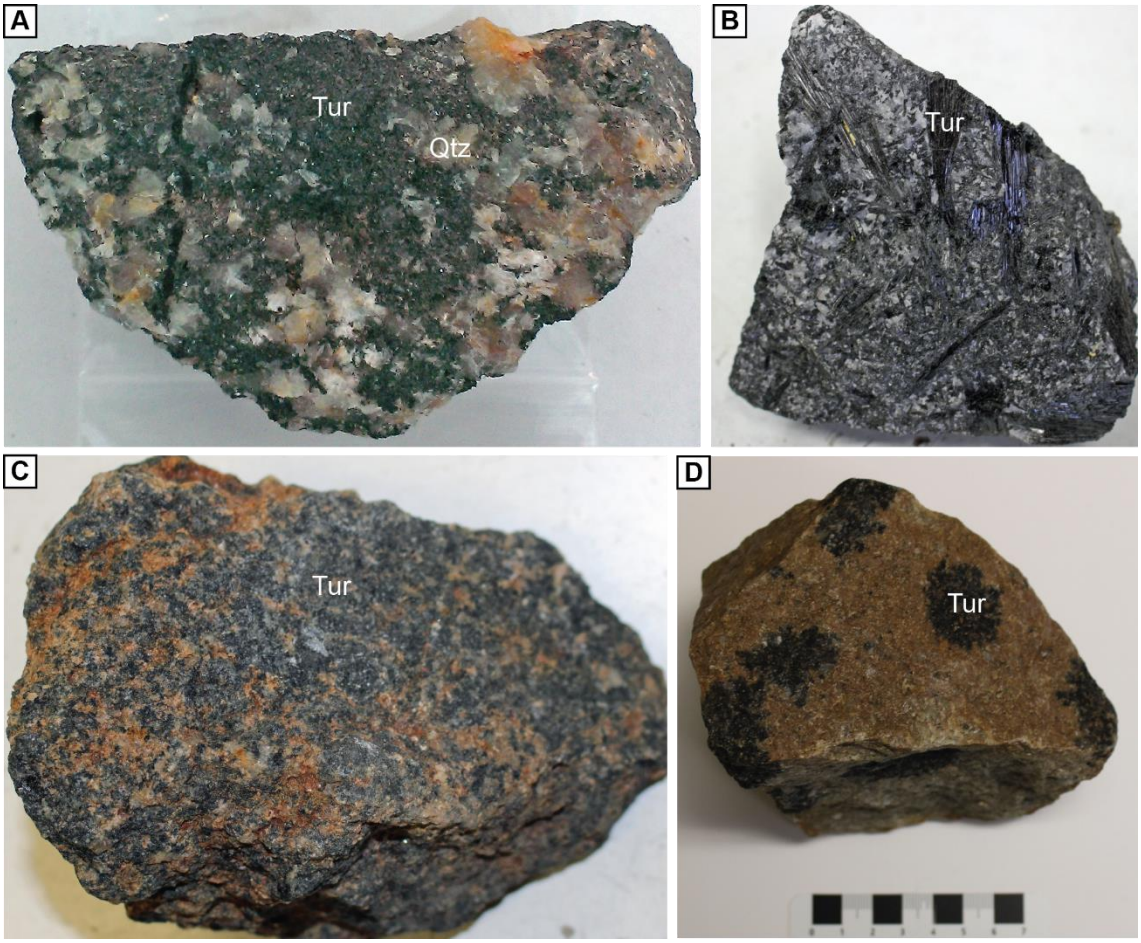

Figure 13: Group 3 tourmaline from greisen (A–C) deposits and tourmaline suns (D) from quartz–topaz rock (former granite). Quartz–tourmaline rock is associated with cassiterite in veins (A; ARD15 and C: ARD19) but elsewhere is barren (B; ARD17).

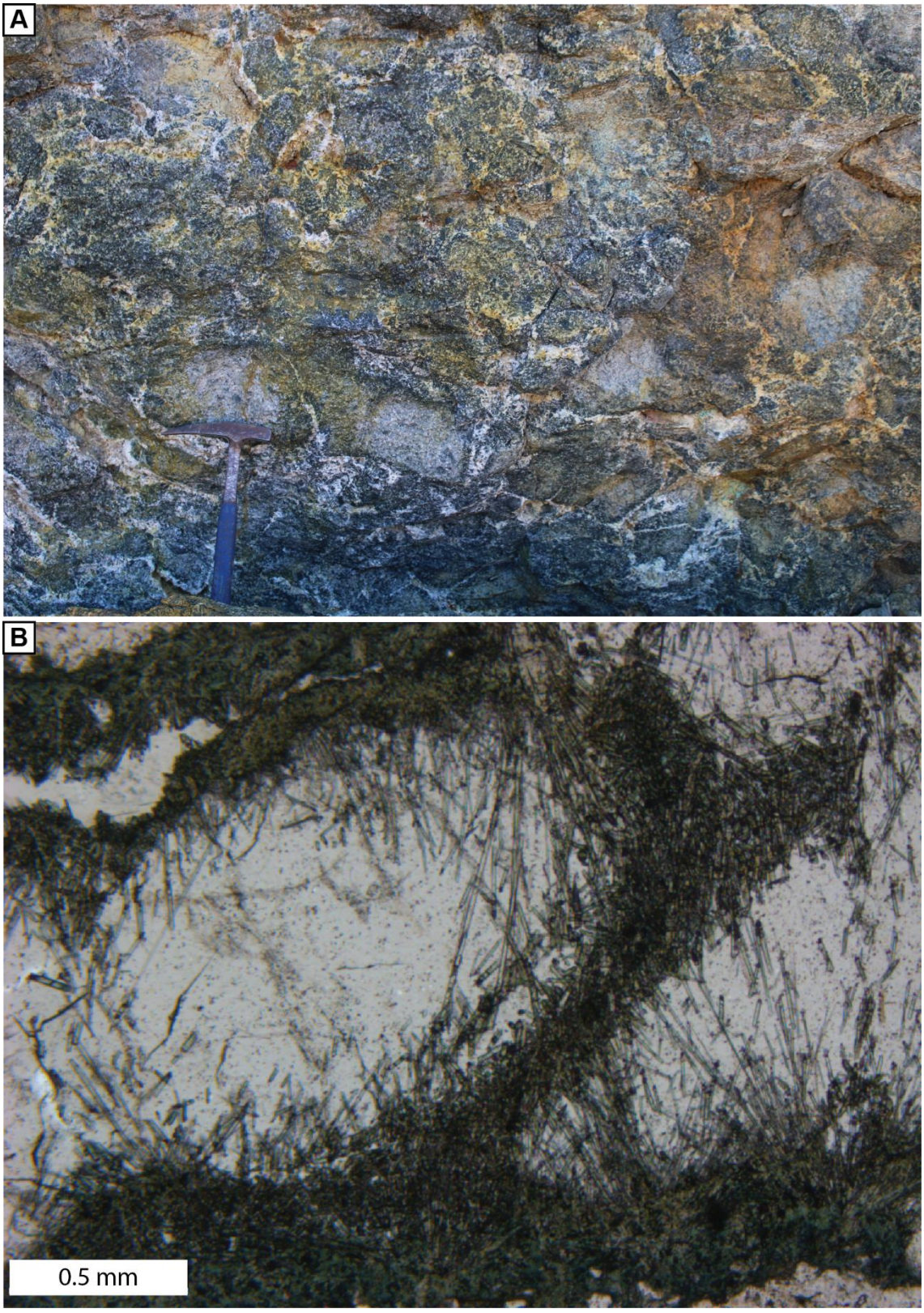

Figure 14: Tourmaline setting of the single Group 4, ARD14, where it occurs as breccia infill (A). Acicular tourmaline needles precipitated on quartz boundaries and are interpreted as post-mineralisation.

2.2.5 Results

Whole rock: major, minor and trace elements

The element abundances of the major igneous units at Ardlethan are compiled in Table 4. Ren (1989) and Ren *et al.* (1995) provide a detailed discussion on the compositional differences between these units included here. Ren *et al.* (1995) suggested that the Microgranitic dykes, GQFP, Ardlethan Granite and Mine Porphyry represent a spectrum of compositions connected through fractional crystallisation. In contrast, recent zircon U–Pb age data from all units (Bodorkos *et al.,* 2013) delineates three periods of magmatism, which precludes a simple relationship by fractional crystallisation of a common parental magma.

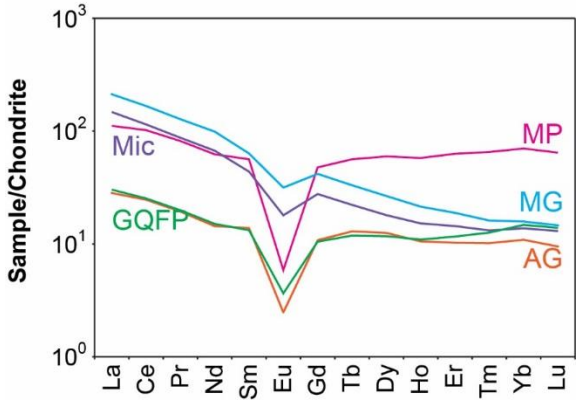

Figure 15: REE concentrations of the igneous units at Ardlethan normalised to Chondrite (Sun and McDonough, 1995). Three signatures are described in the text; 1) Mine Granite (MG) and Microgranite (Mic), 2) GQFP and Ardlethan Granite (AG) and 3) the Mine Porphyry (MP).

The Mine Granite is the least felsic unit at Ardlethan with SiO_2 69.2–71.20 wt% (Ren, 1989; this study) and relatively elevated TiO_2 (0.41–0.53 wt%), $Fe_2O_{3(T)}$ (total Fe converted to trivalent species; 2.78–3.73 wt%), MgO (1.00–1.66 wt%) and CaO (0.93–1.70 wt%) and an aluminium saturation index (ASI) of 1.33. Relative to the entire Koetong Supersuite it is moderately fractionated, also demonstrated by minor negative Eu/Eu* anomalies (Figure 15) together with slightly elevated Rb/Sr (1.5) and Sn concentrations (20 ppm). The contemporaneous Microgranitic dykes represent near minimum melt compositions with SiO_2 74.5–76.7 wt% and low TiO_2 (0.06–0.07 wt%), $Fe_2O_{3(T)}$ (0.91–1.24 wt%), MgO (0.14–0.20 wt%) and CaO (0.30–0.61 wt%). Both units are enriched in Sr, Zr, Th and depleted in U relative to the other igneous units at Ardlethan. The chondrite-normalised REE profiles of the Mine Granite and Microgranitic dykes are similar to each other in terms of overall abundance and

shape, be but have lower LREE and MREE abundances than the Ardlethan Granite (Figure 15). The Microgranitic dykes are interpreted as a fractionated end-member of the Mine Granite and are relatively enriched in the incompatible elements (e.g. Rb/Sr = 10, Sn = 29 ppm, U = 17 ppm).

The GQFP has an intermediate composition with SiO_2 (69.44–74.34 wt%); $Fe_2O_{3(T)}$ (1.99–4.34 wt%), MgO (0.23–0.78 wt%) and CaO (1.13–2.32 wt%) and ASI of 1.08. The Ardlethan Granite also represents a near minimum melt composition with SiO_2 (73.50–77.10 wt%); TiO_2 (0.04–0.27 wt%), $Fe_2O_{3(T)}$ (0.55–2.28 wt%), MgO (0.03–0.37 wt%), CaO (0.17–0.85 wt%) and an ASI of 1.14. Both units are enriched in P_2O_5 and W, and depleted in Sr, Y, Zr, LREE and Th relative to the other igneous units at Ardlethan. The chondrite-normalised REE profiles of the GQFP and Ardlethan Granite are similar to each other in terms of overall abundance and shape (Figure 15), however, the Eu/Eu* is slightly more negative in the Ardlethan Granite.

Table 4: Major and trace element compositions of the igneous units at Ardlethan. Major elements determined by XRF, trace elements by LA-ICP-MS. The major element data is from 1) Bodorkos et al. (2013), and 2) Ren et al. (1995). Trace element concentrations, determined in this study, are the average of three analyses of the $LiBO_3$ glass. $Fe_2O_{3(T)}$ is total iron concentration assuming it is all trivalent. FeO was determined by titration techniques.*

Unit	MG	Mic	GQFP	AG	MP
Reference	1 (PB-ARD-08)	2	1 (PB-ARD-06)	1 (PB-ARD-07)	2
wt%					
SiO_2	69.1	75.7	71.3	73.8	76.3
TiO_2	0.45	0.07	0.41	0.08	0.07
Al_2O_3	14.4	13.2	13.4	12.3	12.2
$Fe_2O_{3(T)}$	1.02	0.28	2.92	0.60	0.40
FeO*	2.54	0.77	1.91	0.67	1.17
MgO	1.38	0.19	0.57	0.15	0.17
CaO	1.37	0.49	1.66	0.46	0.52
MnO	0.05	0.03	0.04	0.04	0.02
Na_2O	2.28	3.40	2.64	3.08	2.24
K_2O	4.38	4.24	4.62	4.59	5.06
P_2O_5	0.212	0.19	0.198	0.178	0.06
Total	97.242	98.53	99.567	96.594	98.16

Table 4 cont.

Unit	MG	Mic	GQFP	AG	MP
Ppm (isotope)					
Sc (45)	8.0	11.9	5.8	6.5	3.3
V (51)	27.4	52.4	8.3	6.1	4.0
Cu (63)	23	22	13	11	120
Zn (66)	67	112	67	54	133
Ga (69)	41	31	17	20	39
Rb (85)	209	315	315	462	655
Sr (88)	142.0	158.7	31.6	14.9	67.1
Y (89)	32.07	23.06	17.91	17.12	92.25
Zr (90)	258.6	156.4	40.5	47.1	210.2
Nb (93)	17.7	16.1	11.2	15.1	130.6
Sn (118)	19.1	42.9	29.2	28.6	76.5
La (139)	50.2	35.0	7.2	6.7	26.4
Ce (140)	102.3	70.1	15.5	15.1	62.4
Pr (141)	11.8	8.1	1.8	1.8	7.6
Nd (146)	45.2	30.6	6.9	6.6	28.4
Sm (147)	9.4	6.5	2.0	2.0	8.3
Eu (153)	1.78	1.01	0.21	0.14	0.33
Gd (157)	8.31	5.50	2.08	2.15	9.48
Tb (159)	1.2	0.80	0.43	0.47	2.03
Dy (163)	6.54	4.43	2.89	3.08	14.66
Ho (165)	1.17	0.83	0.60	0.58	3.15
Er (166)	3.01	2.30	1.86	1.64	10.07
Tm (169)	0.40	0.33	0.31	0.25	1.61
Yb (172)	2.54	2.21	2.37	1.75	11.29
Lu (175)	0.36	0.32	0.34	0.23	1.58
Hf (178)	7.08	4.64	1.71	2.10	11.27
Ta (181)	1.38	2.07	2.52	3.74	12.78
Pb (208)	25.98	28.74	29.59	20.35	31.22
Th (232)	20.65	16.38	5.62	7.26	53.58
U (238)	4.60	7.19	16.52	14.35	23.48
Rb/Sr	1.47	1.99	9.98	31.08	9.76
Eu/Eu*	0.42	0.22	0.35	0.14	0.08

The Mine Porphyry is felsic with high SiO_2 (76.3 wt%) and K_2O (5.06 wt%), and low TiO_2 (0.07 wt%), $Fe_2O_{3(T)}$ (1.57 wt%), MgO (0.17 wt%), CaO (0.52 wt%) and P_2O_5 (0.06 wt%). It has elevated Cu, Zn, Rb, Y, Nb, Sn, REE, Ta, Th and U relative to the other units. The REE profile has a slightly positive LREE slope, strong negative Eu/Eu* anomaly and a slightly negative HREE slope (Figure 15).

Tourmaline: major, minor and trace elements

Representative major and minor element compositions of tourmaline are summarised in Table 5. The average trace element concentrations of tourmaline are in Table 6, and the total range in Table 7. The full data records are collated in Appendix 3. Reported major element totals vary between 88.51 and 91.03 wt% as B_2O_3, a major component of tourmaline was not measured.

Tourmaline has the generalised chemical formula $XY_3Z_6(T_6O_{18})(BO_3)_3V_3W$ (Hawthorne and Henry, 1999). The calculated structural formulae in Table 5 are based on 31 anions (O, OH or F) within a formula unit. The primary substitutions within the tourmaline chemical unit occur on the X (Na + K, calcic or vacancy), W (O, OH or F) and Y (Fe and Mg) sites and these variations are used for mineral classification (Henry *et al.,* 2011).

The major element variations within samples from Ardlethan occur mainly between Fe–Mg on the Y site, Na(+K)–Ca on the X site, and Al with Fe, Mg, Ti on the Z site, as displayed in Figure 16A–C. All tourmalines from Ardlethan are primarily alkalic (Figure 16A) and Fe-rich (Figure 16C), and are classified as schorl. The major element compositions of tourmaline from the Ardlethan Granite differs from tourmaline of the Mine Granite proportionally to the bulk rock compositions. The higher Mg/(Mg+Fe) of the bulk rock Ardlethan Granite is reflected in its tourmaline compared to the bulk rock of the Mine Granite and its tourmaline.

Group 1 tourmaline occurring within the Mine Granite has a relatively restricted range of major element compositions defined by relatively depleted FeO (9.87–13.55 wt%) and enriched CaO (0.12–0.76 wt%). In contrast, the tourmaline hosted by the Ardlethan Granite is enriched in FeO (14.49–18.51 wt%) and depleted CaO (<0.22 wt%). The range in Al concentrations within the Group 1 tourmalines is more restricted than that of Group 2 and Group 3 tourmalines (Figure 16B). F (0.71–0.96 wt%) and Li (96.9–335.7 ppm) contents are enriched in tourmaline within the Ardlethan Granite compared to the Mine Granite (<0.52 wt% and 15.8–150.8 ppm, respectively). Group 1 tourmaline is relatively enriched in Rb, Zn and Ta but strongly depleted in Sr, Y, Sn, the REE and Pb compared to Group 3 tourmaline.

Greisen-hosted tourmalines of Group 3 are enriched in FeO (15.22–20.25 wt%) relative to Group 1 tourmaline and depleted in CaO (<0.53 wt%). This enrichment could result from continued fractional crystallisation of the Ardlethan Granite after Group 1 crystallised. F (0.19–1.16 wt%) and Li (20.46–166.1 ppm) contents are similar to that of Group 1. The REE concentrations of Group 2 tourmaline were commonly below detection limit.

Table 5: Representative major element composition and calculated atoms per formula unit for tourmaline groups at Ardlethan. Bdl = below detection limit.

Sample No.	ARD01	ARD04	ARD06	ARD09	ARD13	ARD14	ARD17	ARD19
Host rock	MG	AG	AG	MG	MG	MG	AG	AG
Setting	Interstitial	Interstitial	Nodule	Breccia	Breccia	Breccia	Greisen	Greisen
wt%								
SiO_2	35.30	35.42	35.79	36.94	36.18	36.01	34.36	35.62
TiO_2	0.46	0.36	0.47	0.40	0.67	1.14	0.31	0.32
Al_2O_3	35.39	32.77	34.45	31.64	35.97	33.93	32.12	32.98
FeO	10.55	16.53	16.10	14.59	10.68	10.57	17.73	18.50
MgO	3.19	1.02	1.34	3.23	2.95	4.05	0.37	0.36
CaO	0.16	bdl	0.12	0.25	0.16	0.46	0.03	0.22
MnO	0.14	0.16	0.11	0.06	0.07	0.04	0.12	bdl
Na_2O	1.78	2.44	2.07	2.17	1.76	1.81	2.11	1.90
K_2O	0.04	0.08	0.04	0.03	0.03	0.04	0.04	0.07
F	0.34	bdl	0.71	0.87	0.26	0.30	1.06	0.86
Total	87.34	88.78	91.19	90.17	88.73	88.36	88.25	90.82
apfu (site)								
Si (T)	5.815	5.911	5.816	6.049	5.870	5.886	5.862	5.888
Al (T)	0.185	0.089	0.184		0.130	0.114	0.138	0.112
Al (Z)	6.00	6.00	6.00	6.00	6.00	6.00	6.00	6.00
Al (Y)	0.687	0.357	0.415	0.107	0.747	0.422	0.319	0.314
Ti (Y)	0.057	0.045	0.057	0.049	0.082	0.140	0.04	0.04
Mg (Y)	0.783	0.254	0.325	0.789	0.713	0.987	0.094	0.089
Mn (Y)	0.02	0.023	0.015	0.008	0.008	0.006	0.017	
Fe^{2+} (Y)	1.453	2.321	2.188	1.998	1.449	1.445	2.507	2.541
Ca (X)	0.028	bdl	0.021	0.044	0.028	0.081	0.005	0.039
Na (X)	0.569	0..790	0.652	0.689	0.554	0.574	0.698	0.609
K (X)	0.008	0.17	0.008	0.006	0.006	0.008	0.009	0.015
Vac	0.395	0.193	0.319	0.261	0.412	0.337	0.288	0.337
F	0.177	bdl	0.365	0.451	0.133	0.155	0.572	0.450

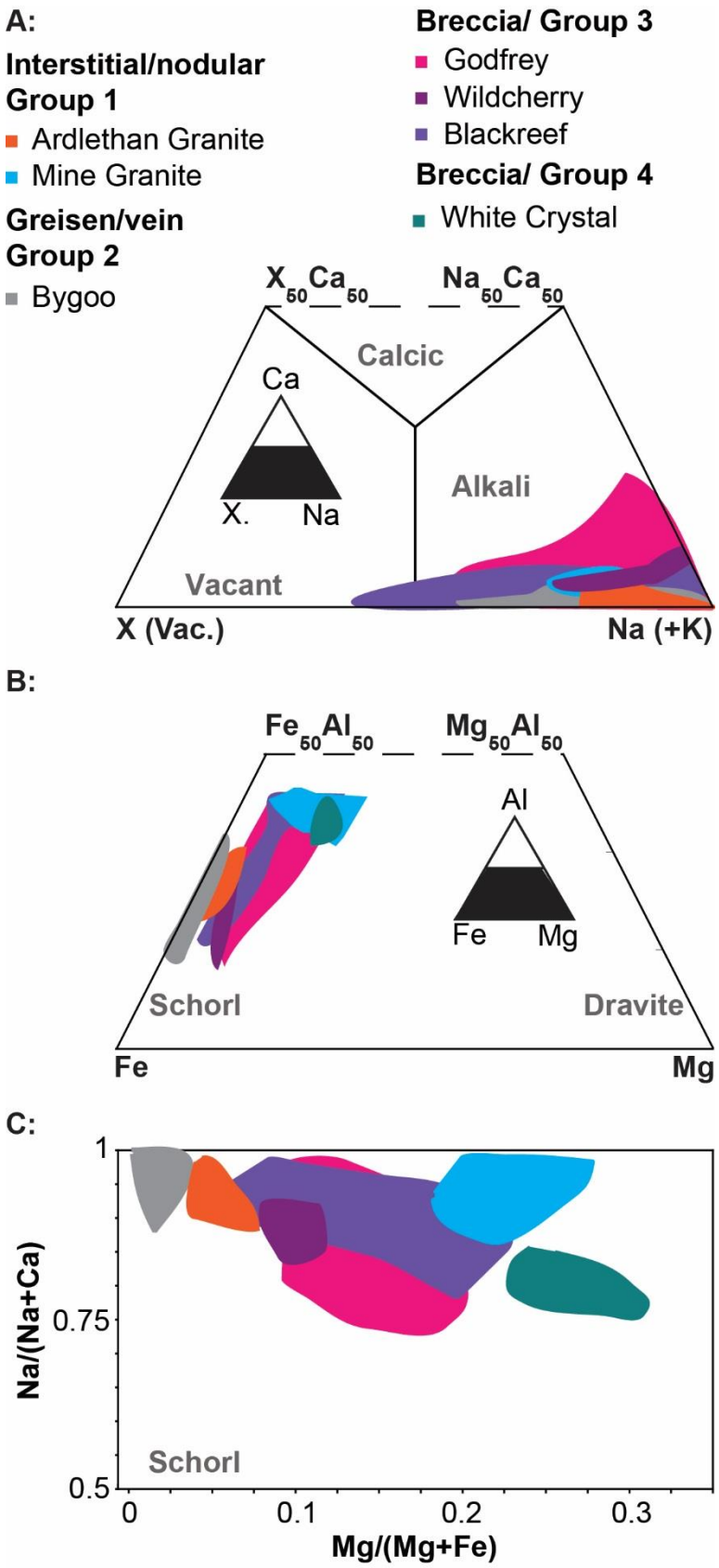

Figure 16: Major element compositions of tourmaline at Ardlethan obtained by EMP. The major chemical substitutions are shown for the X site (A) and Y site (B). These variations are combined in C.

Group 2 tourmalines have the most variable major and trace element compositions primarily in FeO (8.88–21.50 wt%), Al_2O_3 (25.86–37.55 wt%) and CaO (<0.94 wt%). F and Li contents are generally lower than groups 1 and 2 tourmaline. They are notably enriched in Sr, Y, Zr, Sn, the REE and Pb. In Figure 16 (B, C) Group 2 tourmaline has compositions intermediate between tourmaline in the Mine and Ardlethan granites, which is later inferred to be due to mixing.

REE compositions of tourmaline from Ardlethan define two types of chondrite-normalised patterns (Figure 17). Tourmaline occurring within the Ardlethan Granite (groups 1 and 3) displays lower concentrations of the REE compared to the bulk rock, however have similar pattern with a positive LREE slope and flat HREE slope, except for a pronounced positive Eu/Eu* anomalies in tourmaline, compared with negative anomalies in the whole rock. The inversed Eu/Eu* anomalies in tourmaline compared to the whole rock are discussed in Section 2.4.2 in relation to crystal-chemical effects on REE substitution into tourmaline.

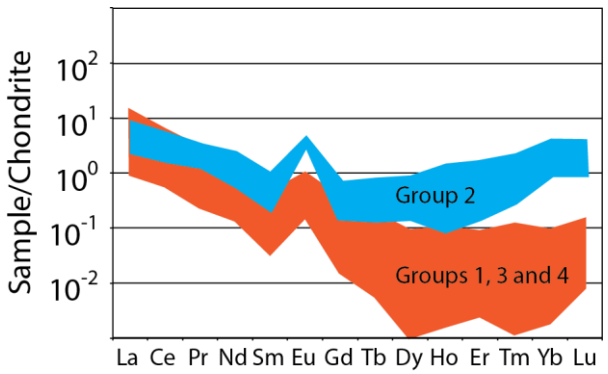

Figure 17: Chondrite-normalised REE concentrations of tourmaline at Ardlethan normalised to chondrite (Sun and McDonough, 1995). Group 2 tourmaline defines a unique pattern compared to the other groups.

Table 6: Representative trace element concentrations of tourmaline from Ardlethan determined by LA-ICP-MS. dl = detection limit; Bdl = below detection limit.

Sample No.		ARD01	ARD04	ARD06	ARD09	ARD13	ARD14	ARD17	ARD19
Host rock		MG	AG	AG	MG	MG	MG	AG	AG
Setting		Interstitial	Interstitial	Nodule	Breccia	Breccia	Breccia	Greisen	Greisen
ppm (isotope)	*dl (ppm)*								
Li (7)	0.2	61	123	134	23	31	31	156	94
Sc (45)	0.1	24.4	28.5	14.8	9.6	21.8	69.6	15.1	21.1
V (51)	0.05	31.1	39.7	25.0	69.2	74.8	472.0	2.6	11.2
Co (59)	0.05	18.2	12.6	16.6	0.3	7.9	32.3	6.3	2.0
Cu (63)	0.05	0.1	0.6	0.5	2.3	0.7	0.4	0.2	0.42
Zn (66)	0.1	420	301	576	87	381	300	434	385
Ga (69)	0.05	80.7	117.8	184.1	82.9	91.5	106.7	200.2	290.1
Rb (85)	0.05	bdl	0.29	0.05	38.43	bdl	bdl	bdl	bdl
Sr (88)	0.01	2.1	5.9	7.9	124.7	35.0	7.2	11.9	23.0
Y (89)	0.005	bdl	0.05	0.06	2.84	0.09	0.08	bdl	0.10
Zr (90)	0.005	0.13	0.06	0.28	1.87	0.71	0.43	bdl	0.06
Nb (93)	0.005	2.4	2.6	3.5	2.3	1.4	1.6	0.7	1.9
In (115)	0.01	0.9	1.7	0.9	11.0	0.9	1.0	0.5	3.1
Sn (118)	0.5	52	65	109	762	33	56	46	56
La (139)	0.005	0.76	0.36	2.96	17.22	1.06	2.62	0.03	0.421
Ce (140)	0.005	1.43	0.54	3.78	37.32	1.86	4.78	0.03	0.751
Pr (141)	0.005	0.14	0.05	0.28	3.96	0.20	0.45	bdl	0.07
Nd (146)	0.05	0.39	0.12	0.65	12.94	0.68	1.05	bdl	0.119
Sm (147)	0.05	0.07	bdl	0.07	1.90	0.11	0.12	bdl	0.03
Eu (153)	0.005	0.02	0.02	0.04	0.53	0.17	0.03	bdl	0.013
Gd (157)	0.01	0.01	bdl	0.02	0.74	bdl	0.06	bdl	0.02
Tb (159)	0.005	bdl	bdl	bdl	0.07	0.01	0.01	bdl	0.01
Dy (163)	0.01	bdl	0.01	bdl	0.33	0.01	0.02	0.01	0.02
Ho (165)	0.005	bdl	bdl	bdl	0.08	bdl	bdl	bdl	0.01
Er (166)	0.01	bdl	bdl	0.01	0.41	bdl	bdl	bdl	bdl
Tm (169)	0.005	bdl	bdl	bdl	0.10	bdl	bdl	bdl	bdl
Yb (172)	0.05	bdl	bdl	bdl	0.84	bdl	bdl	bdl	bdl
Lu (175)	0.005	bdl	bdl	bdl	0.16	bdl	bdl	bdl	bdl
Hf (178)	0.01	0.01	0.02	0.02	0.14	0.03	0.2	bdl	bdl
Ta (181)	0.005	2.97	3.02	2.21	0.50	0.82	1.93	0.44	0.97
W (182)	0.001	0.01	0.41	0.12	0.95	0.48	0.05	bdl	0.02
Pb (208)	0.05	1.82	1.12	1.01	8.14	11.79	2.39	0.70	0.25
Th (232)	0.01	bdl	0.04	0.08	1.94	0.33	0.01	bdl	0.04
U (238)	0.005	bdl	0.03	0.01	0.25	0.12	bdl	bdl	0.01

Table 7: Range of trace element concentrations of tourmaline groups at Ardlethan as determined by LA-ICP-MS. Mdn = median value of LA-ICP-MS analyses.

	Gp 1 MG		Gp 1 AG		Gp 2 AG		Gp 3 MG	
	Mdn	Range	Mdn	Range	Mdn	Range	Mdn	Range
Li	33	168–151	161	97–336	95	20–166	20	4–84
Sc	26.7	4.2–82	21.1	6.7–67	17.2	3.1–97	15.7	2.6–70
V	159.8	2.9–250	22.6	4.0–53	2.4	1.0–25	73.4	11.0–563
Co	25.0	1.1–39.4	12.8	8.1–16.9	2.6	0.2–7.7	1.5	0.2–38.5
Cu	0.5	0.1–1.4	0.6	0.4–7.5	0.4	0.1–2.2	1.0	0.1–55.4
Zn	330	165–568	532	244–631	478	66–1387	87	65–547
Ga	101.2	48.4–174	145.9	76.4–240	194.3	28.0–351	84.0	25.7–165
Rb	0.15	0.03–19.9	0.11	0.02–57.2	3.04	0.72–78.2	4.40	0.06–48.6
Sr	26.0	2.0–58.1	3.8	0.5–97	11.3	5.6–263	53.0	7.2–215
Y	0.04	<0.39	0.05	0.01–2.47	0.02	<1.06	0.68	0.02–25.3
Zr	0.85	0.04–5.07	0.28	0.01–11.5	0.15	<8.86	0.98	0.05–27.3
Nb	2.7	0.2–42.2	1.9	0.3–7.7	2.1	0.3–11.7	2.1	0.1–93
In	1.2	0.1–6.2	0.7	0.2–3.9	2.5	0.5–43.6	4.4	0.4–29.4
Sn	52	14–102	51	15–132	71	17–647	225	16–1115
La	1.32	0.02–3.32	0.44	<3.31	0.08	<6.25	2.38	0.32–27.2
Ce	1.81	0.03–6.24	0.68	<4.29	0.13	0.02–11.4	4.44	0.5–51.8
Pr	0.16	<0.619	0.07	<0.46	0.06	**<**1.1	0.40	0.046–5.57
Nd	0.43	0.05–1.78	0.20	<2.13	0.15	<2.7	1.20	0.11–19.5
Sm	0.04	<0.28	0.04	<0.79	0.05	<0.37	0.15	<3.17
Eu	0.21	0.01–0.30	0.02	<0.11	0.02	<0.30	0.19	0.03–0.77
Gd	0.02	<0.10	0.02	<0.63	0.03	<0.16	0.11	<1.84
Tb	bdl	<0.01	bdl	<0.09	0.01	<0.03	0.03	<0.46
Dy	0.01	<0.09	0.01	<0.43	0.02	<0.21	0.14	0.01–3.6
Ho	bdl	<0.03	Bdl	<0.07	bdl	<0.05	0.04	<0.85
Er	0.01	<0.081	0.01	<0.22	0.10	0.07–0.11	0.18	<2.98
Tm	bdl	<0.008	bdl	<0.04	bdl	<0.01	0.04	<0.61
Yb	0.01	<0.09	bdl	<0.23	0.02	<0.13	0.44	0.02–5.12
Lu	bdl	<0.01	bdk	<0.03	bdl	<0.02	0.09	<0.85
Hf	0.28	0.01–2.24	0.03	<0.55	0.03	<1.34	0.07	<1.21
Ta	2.52	0.19–101	1.98	0.29–4.61	1.45	0.13–25.3	1.09	0.03–14.8
W	0.12	<0.63	0.12	<2.62	0.05	<1.87	1.19	<35.18
Pb	2.38	1.31–69	1.11	0.18–106	0.94	0.25–20.03	7.08	1.04–197
Th	0.06	<0.17	0.06	<2.07	0.05	<0.73	0.55	<6.15
U	0.01	<0.38	0.03	<18.5	0.03	<1.27	0.18	<2.2

Rb–Sr and Sm–Nd isotopic compositions

The combined Rb–Sr and Sm–Nd isotopic data for tourmaline and whole-rock samples at Ardlethan are compiled in Table 8 and the calculated initial isotopic compositions are displayed in Figure 18. The Nd1 and NBS987 standard data are included in Appendix 5.

Initial $^{87}Sr/^{86}Sr_{(i)}$ was calculated to 410 Ma (discussed below) using the recently revised decay constant for ^{87}Rb ($1.3972 \times 10^{-11}\ a^{-1}$) by Villa *et al.* (2015). Additional discussion on the significance of the use of this decay constant is included in the Chapter 3. Tourmaline samples have low $^{87}Rb/^{86}Sr$ values (0.003–0.278) rendering age corrections minimal. The higher $^{87}Rb/^{86}Sr$ occurs predominantly within groups 1 and 3. All $^{87}Sr/^{86}Sr_{(i)}$ values of tourmaline range between 0.70998 and 0.71857. Tourmaline occurring within the Ardlethan Granite (groups 1 and 3) was the most variable ranging from 0.70998–0.71734 compared to the more consistently radiogenic tourmaline occurring within the Mine Granite (groups 2 and 4), which ranges from 0.71639–0.71857. In contrast, the $^{87}Rb/^{86}Sr$ values within the whole-rock samples are large and variable (4.59–31.68), such that age corrections are significant and contribute to uncertainty on the calculated $^{87}Sr/^{86}Sr_{(i)}$. Measured $^{87}Sr/^{86}Sr$ varies between 0.73753 and 0.89582, with $^{87}Sr/^{86}Sr_{(i)}$ values between 0.70827 and 0.71952. $^{87}Sr/^{86}Sr_{(i)}$ values of the whole-rock analyses of the Ardlethan Granite (0.71458) and contemporaneous GQFP (0.71149) are less radiogenic than the Mine Granite (0.71865) and its contemporaneous Microgranite (0.71952). The late Mine Porphyry is the least radiogenic with a value of 0.70827.

The $^{147}Sm/^{144}Nd$ of tourmaline is low but variable between 0.06 and +0.33. The $\varepsilon Nd_{(i)}$ of tourmaline is highly variable between –12.8 and –1.0. Groups 1 and 3 are consistently more radiogenic $\varepsilon Nd_{(i)}$ values between –5.0 and –1.0, compared to the less radiogenic Group 2 (–8.4 to –3.2). The single Group 4 analysis is the least radiogenic tourmaline at Ardlethan with a $\varepsilon Nd_{(i)}$ value of –10.0. The contemporaneous Ardlethan Granite (–3.2) and GQFP (–3.90) are more radiogenic than the Mine Granite (–9.3) and contemporaneous Microgranite (–9.3). The Mine Porphyry is the most radiogenic unit (+7.0).

Table 8: Rb–Sr and Sm–Nd data for tourmaline and whole-rocks from Ardlethan. Initial tourmaline ratios were calculated at 410 Ma (See text for explanation) using decay constants $^{87}Rb = 1.3972x10^{-11}a^{-1}$ and $^{147}Sm = 6.54x10^{-11}a^{-1}$. $\varepsilon Nd = \left(\frac{^{144}Nd/^{143}Nd_{(S)}}{^{144}Nd/^{143}Nd_{(CHUR)}} - 1\right) \times 10^4$ where $^{143}Nd/^{144}Nd_{CHUR} = 0.512638$ and $^{147}Sm/^{144}Nd_{CHUR} = 0.1967$.(0) denotes the measured isotopic value, prior to age corrections. (i) denotes initial isotopic values after age corrections. Whole-rock ratios were corrected using U-Pb zircon ages as reported in the text. T_{DM} model ages were calculated using $^{143}Nd/^{144}Nd_{DM} = 0.51315$ and $^{147}Sm/^{144}Nd_{DM} = 0.2136$.

Sample	Rb	Sr	$^{87}Rb/^{86}Sr$	$^{87}Sr/^{86}Sr_{(0)}$	2 SE	$^{87}Sr/^{86}Sr_{(i)}$	Sm	Nd	$^{147}Sm/^{144}Nd$	$^{143}Nd/^{144}Nd_{(0)}$	2 SE	$\varepsilon Nd_{(0)}$	$\varepsilon Nd_{(T)}$	T_{CHUR} (Ga)	T_{DM} (Ga)
Tur.	ppm	ppm					ppm	ppm							
ARD04	0.41	4.22	0.278	0.71662	0.00002	0.71504	0.14	0.32	0.26	0.512607	0.00002	–0.60	–3.73	–0.08	–1.95
ARD05	0.23	3.56	0.079	0.71838	0.00001	0.71734	0.77	3.75	0.12	0.512333	0.00002	–5.96	–2.11	0.63	1.38
ARD06	0.12	4.49	0.076	0.71041	0.00001	0.70998	0.42	2.00	0.13	0.512301	0.00001	–6.57	–2.84	0.72	1.47
ARD07	1.38	189.06	0.007	0.71860	0.00001	0.71857	0.78	3.67	0.13	0.512021	0.00002	–12.03	–8.42	1.36	1.99
ARD09	0.93	80.41	0.033	0.71783	0.00001	0.71764	0.75	4.68	0.10	0.511975	0.00001	–12.92	–7.71	1.01	1.53
ARD10	0.08	68.45	0.003	0.71738	0.00001	0.71736	0.32	2.77	0.07	0.511981	0.00003	–12.81	–6.11	0.78	1.23
ARD11	0.10	61.41	0.008	0.71714	0.00001	0.71709	0.37	3.74	0.06	0.512107	0.00002	–10.35	–3.20	0.59	1.03
ARD12	0.74	49.00	0.044	0.71775	0.00001	0.71750	0.67	3.05	0.13	0.512044	0.00001	–11.58	–8.26	1.42	2.09
ARD13	0.07	5.34	0.039	0.71661	0.00001	0.71639	0.38	1.81	0.13	0.512168	0.00005	–9.18	–5.44	1.00	1.69
ARD14	1.29	27.75	0.041	0.71752	0.00001	0.71729	0.83	4.11	0.12	0.511925	0.00000	–13.90	–10.00	1.45	2.03
ARD15	0.17	3.25	0.089	0.71448	0.00001	0.71398	0.11	0.20	0.33	0.512955	0.00002	6.18	–1.04	0.35	–0.25
ARD16	0.21	19.30	0.031	0.71141	0.00001	0.71124	2.49	0.17	0.29	0.512227	0.00005	–8.01	–4.97	–0.70	–1.94
ARD19	0.37	22.68	0.048	0.71091	0.00001	0.71065	0.35	1.55	0.14	0.512301	0.00001	–6.58	–3.38	0.84	1.65
Whole-rock glass															
AG	831.8	203.03	11.85	0.78181	0.00001	0.71458	7.49	30.12	0.15	0.512350	0.00001	–5.62	–3.19	0.94	1.92
GQFP	229.3	144.51	4.59	0.73753	0.00001	0.71149	10.39	51.57	0.12	0.512237	0.00001	–7.82	–3.90	0.81	1.51
Mic G	346.0	32.20	31.09	0.89582	0.00001	0.71952	2.24	8.14	0.17	0.512078	0.00001	–10.92	–9.34	2.79	3.42
MG	322.0	149.81	6.07	0.75305	0.00001	0.71865	6.30	30.45	0.12	0.511967	0.00006	–13.09	–9.34	1.42	2.03
MP	677.6	61.88	31.68	0.88882	0.00001	0.70827	7.62	94.06	0.05	0.512595	0.00001	–0.83	6.95	0.04	0.51

In Figure 18, Group 2 tourmaline defines a curvilinear array between the Ardlethan Granite and Mine Granite. No tourmaline compositions extend into the radiogenic $\varepsilon Nd_{(i)}$ compositions of the Mine Porphyry (Figure 18).

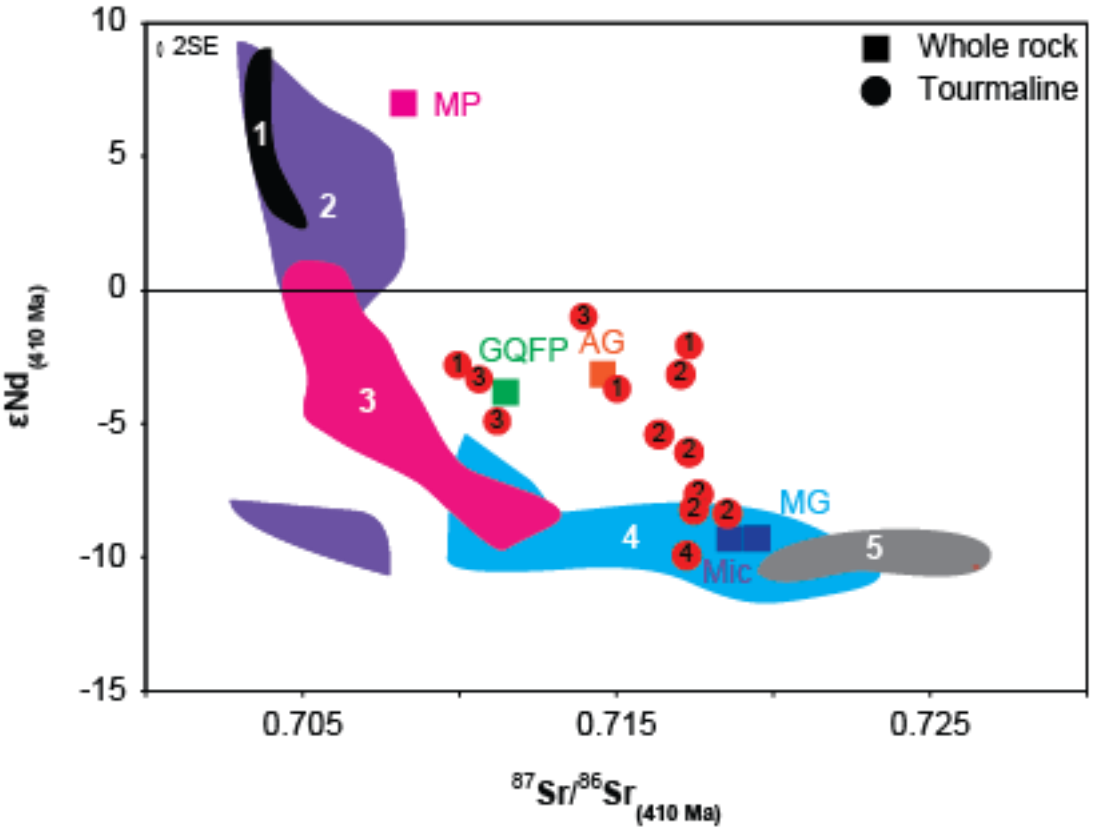

Figure 18: Sr–Nd isotopic compositions of tourmaline and whole-rock samples of Ardlethan measured in this study compared to the major rock units of the Lachlan Orogen. Groups are labelled for each tourmaline sample. Isotopic fields include 1) Mantle xenoliths of Bingie, 2) Cambrian Greenstone, 3) I-type igneous units, 4) S-type igneous units, and 5) Ordovician metasediments. Data sources include Nelson et al., 1984; McCulloch and Woodhead, 1993; McDonough and McCulloch, 1993; Keay et al., 1997. Whole-rock analyses reported here include MP: Mine Porphyry, GQFP: Garnet quartz feldspar porphyry, AG: Ardlethan Granite, Mic: Microgranite and MG: Mine Granite.

Quartz $\delta^{18}O$

Ren (1989) reported $\delta^{18}O$ values of whole rock and numerous mineral separates including quartz and cassiterite determined using the bulk fluorination technique. However, Fekete *et al.* (2016) show that $\delta^{18}O$ values within a single quartz grain can vary significantly in magmatic-hydrothermal deposits (e.g. –4.6 to 12.8 ‰), demonstrating the importance of *in-situ* analyses.

Average compositions and the total range of $\delta^{18}O_{SMOW}$ measured for this study for quartz in the igneous units and within deposits surrounding Ardlethan are presented in Table 9. The complete data set is compiled in Appendix 4.

$\delta^{18}O_{SMOW}$ compositions of a co-existing fluid with the quartz were calculated according Equation 4 (Pollington *et al.,* 2016):

$$10^3 * ln\alpha_{Qtz-fluid} = 2.91\ (\pm\ 0.04) *\ 10^6/T^2 \qquad \text{Equation 4}$$

where α is the experimentally derived fractionation factor. Temperature (T), reported in ºC, was determined through microthermometry techniques of fluid inclusions (Ren, 1989). Temperature estimates are of this study constrained by the inclusion data of Ren (1989).

Ren *et al.* (1995) reported highly variable fluid inclusion microthermometry data, which indicate quartz precipitation occurring at 180–380ºC. In this study hydrothermal temperatures were assumed to be 350ºC for the breccia- and vein-hosted quartz, coincident with cassiterite precipitation (Ren *et al.,* 1995). Magmatic quartz was estimated to have formed at 550ºC (Ren *et al.,* 1995). Quartz from White Crystal precipitated after cassiterite mineralisation at ~250ºC (Ren, 1989).

Ren *et al.* (1995) reported whole-rock $\delta^{18}O_{SMOW}$ values for the Ardlethan Granite (+10.0–+10.5 ‰), Mine Porphyry (+9.9 ‰) and the Mine Granite (+8.7 ‰). An estimate of the sedimentary country rock is provided by Cox (2007) from limestone of the Taemas area, Lachlan Orogen, of 23–25 ‰.

Table 9: Quartz $\delta^{18}O$ compositions from Ardlethan measured by SHRIMP II. Water compositions calculated using equation of Pollington et al., 2016 and temperatures of Ren (1989) as discussed in the text.

Unit/Deposit	Setting	Group	Av. $\delta^{18}O$ ‰ (n)	2 SE	Range	Av. $\delta^{18}O$ (‰) water
Mic G	Magmatic	1	9.40 (15)	0.30	8.29–10.14	5.1
AG	Magmatic/ nodules	1	11.38 (38)	0.14	9.46–12.56	5.9
MP	Magmatic	1	9.45 (8)	0.27	8.97–10.17	5.2
Wildcherry	Breccia	2	13.28 (9)	0.23	12.71–13.76	5.8
Blackreef	Breccia	2	13.46 (19)	0.48	11.34–15.06	6.0
Godfrey	Breccia	2	12.33 (18)	0.56	9.79–14.42	4.8
White Crystal	Breccia	4	13.07 (27)	0.51	10.43–15.29	2.5
Buchanan	Vein	3	11.94 (11)	0.40	10.67–13.16	4.5
Titanic	Vein	3	11.88 (10)	0.12	11.44–12.14	4.4
Little Bygoo	Vein	3	11.84 (22)	0.12	11.23–12.46	4.4

Measured $\delta^{18}O$ values of quartz presented here range between +8.29 and +15.29 ‰. Ren (1989) report a similar range in $\delta^{18}O$ bulk quartz separates between 8.2–13.8 ‰. However, using *in-situ* techniques, we show significant $\delta^{18}O$ variability within samples and grains (e.g. 9.79–14.42 ‰ in the Godfrey Deposit). The most ^{18}O-depleted values are within the igneous units and oxygen becomes increasingly enriched in ^{18}O into the breccia and vein deposits. The average calculated water composition inverts this relationship, with magmatic quartz containing the most ^{18}O enriched values (+5.10–+5.86 ‰) with progressively ^{18}O depleted values into hydrothermal environments (+2.54–+5.97 ‰; Figure 19). Quartz from the Ardlethan Granite displays a small range in $\delta^{18}O$ values (Table 9); these values are also comparable with magmatic quartz separate data of Ren (1989) (+11.9) and slightly enriched in ^{18}O relative to whole-rock fluorination values of Ren (1989) (+10–+10.5 ‰). There is no change in isotopic values from interstitial to nodular quartz indicating similar crystallisation temperatures.

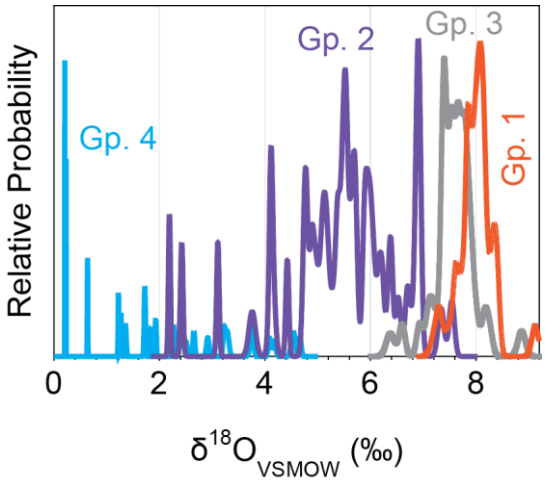

Figure 19: Relative probability distribution of SHRIMP $\delta^{18}O$ quartz analysis at Ardlethan coloured by tourmaline groups outlined in Table 3.

2.2.6 Discussion

The origin and evolution of the Ardlethan Granite

The intimate spatial and temporal association of the Ardlethan Granite with cassiterite mineralisation, indicates it is the probable source of mineralising fluids as initially suggested by Ren *et al.* (1995). Walshe *et al.* (1995; 2011) suggest that the intrusion of the Mine Porphyry contributed to the Sn forming event.

As Sn and the REE (specifically Sm and Nd) are expected to complex favourably with the low pH, high-Cl hydrothermal fluids (e.g. Duc-Tin *et al.* 2007; Migdisov and Williams-Jones, 2014) associated with the Ardlethan Sn deposits, the $\varepsilon Nd_{(i)}$ of tourmaline associated cassiterite characterise the provenance of mineralising fluids. The variable $\varepsilon Nd_{(i)}$ compositions (–12.8 to –1.04) of tourmaline associated with cassiterite (Table 8; Figure 18) are significantly less evolved than the radiogenic Mine Porphyry (+6.95). Instead, tourmaline associated with cassiterite displays an array of Rb–Sr and Sm–Nd isotopic compositions between the Ardlethan Granite and Mine Granite (Figure 18). In this context it is important to understand the processes that lead up to the emplacement of the Ardlethan Granite and have led to economic mineralisation of Sn, and the subsequent role of the Mine Granite.

The Ardlethan Granite was initially considered to be part of the Silurian Koetong Supersuite (Blevin and Chappell, 1995; Ren *et al.,* 1995; Walshe *et al.,* 1995, 2011; White *et al.,* 2001) because of its: 1) location within the well-defined linear belt and intrusion into the Mine Granite (also part of the Koetong Supersuite); 2) previously assumed crystallisation age of *ca* 430 Ma; and 3) geochemistry commonly lies along linear and curvilinear trends defined by the Koetong Suite in bivariate plots (most notably SiO_2 vs Rb; Figure 8; and SiO_2 vs Sr; White *et al.,* 2001).

In contrast, isotopic provenance and geochronological evidence indicates that the Ardlethan Granite was emplaced *ca* 15 Ma after the Koetong Supersuite (Bodorkos *et al.,* 2013) and with a significantly more radiogenic isotopic source (Walshe *et al.,* 1995, 2011; Blevin *et al.,* 2017; this study). Granitic magmatism occurring at *ca* 430 Ma in the Lachlan Orogen (including the Mine Granite)

generally have whole-rock $\varepsilon Nd_{(i)}$ (~–10) and zircon $\varepsilon Hf_{(i)}$ (~–15) (McCulloch and Chappell, 1982; Kemp *et al.,* 2009; Walshe *et al.,* 2011; Blevin *et al.,* 2017). Granitic magmatism then transitions towards whole-rock $\varepsilon Nd_{(i)}$ of –6.5 to –0.70 and zircon $\varepsilon Hf_{(i)}$ compositions of –8 to –1 between 420 and 410 Ma (McCulloch and Chappell, 1982; McCulloch and Woodhead, 1993; Kemp *et al.,* 2007, 2009; Walshe *et al.,* 2011, Blevin *et al.,* 2017; this study). Blevin *et al.* (2017) showed that the Ardlethan Granite contains comparable $\varepsilon Hf_{(i)}$ (–5 to 0) and $\delta^{18}O$ (7.6–9.3) zircon to the proximal and contemporaneous Burrandana Granite (417.7 ± 2.8) and Gurragong (416.5 ± 2.4 Ma) and Wallaroobie Volcanics (418.7 ± 1.8 Ma) (Bodorkos *et al.,* 2013).

Kemp *et al.* (2009) proposed that this temporal isotopic trend throughout the Lachlan Orogen was caused by tectonic shift from convergence at *ca* 430 Ma followed by extension induced by slab retreat that terminated by *ca* 390 Ma (Figure 20); and the Ardlethan Granite intruded in an intermediary stage. Walshe *et al.* (2011) propose that the increasingly radiogenic $\varepsilon Nd_{(i)}$ from the Mine Granite to the Mine Porphyry (–10 to +7 ‰) represents an increasing mantle component in the magmas derived either by mixing or mingling of mantle and crustal-derived magmas in the middle to upper crust, or mantle-derived fluids metasomatising melts in the middle to upper crust.

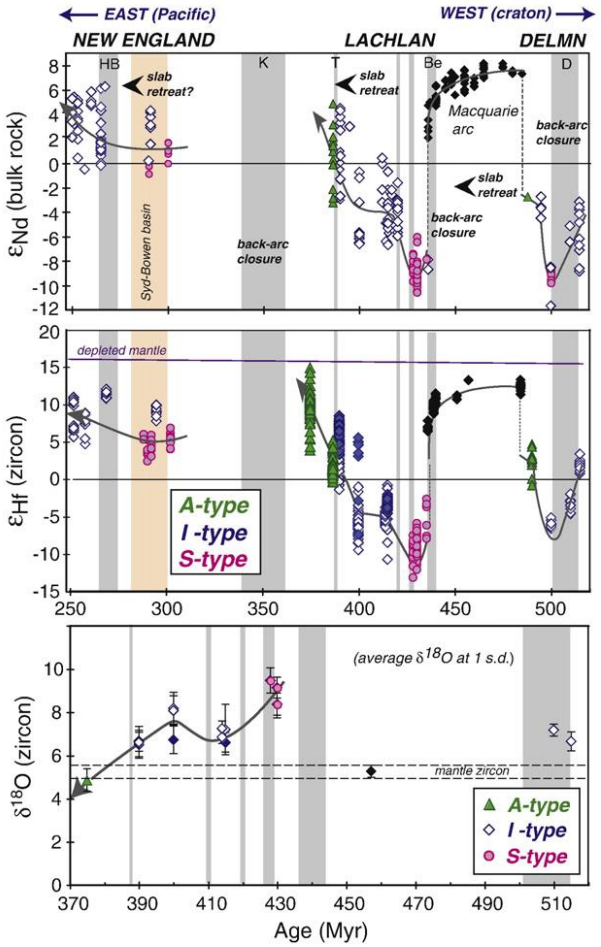

Figure 20: Kemp et al. (2009, figure 4) showing the secular isotopic evolution of granites in the Tasmanides. Whole rock εNd (top) trends are the same as zircon εHf (middle values). Zircon $\delta^{18}O$ data (bottom) is more limited but is generally the inverse of the other isotopic systems.

Ren *et al.* (1995) classify the Ardlethan Granite as S-type based on low Na_2O (3.1 wt%), and high K_2O (4.8 wt%) and ASI (1.14). However, as granites become increasingly fractionated their compositions converge towards the minimum temperature compositions (Tuttle and Bowen, 1985), precluding identification of source rocks based on major elements and mineral abundances (e.g. Chappell, 1996). Extreme crystal fractionation in the Ardlethan Granite is evidenced by the low K/Rb (~80; K-feldspar), a pronounced negative Eu/Eu* anomaly (plagioclase; Figure 15), and high Rb/Sr (>31; incompatible–compatible pair) of the bulk-rock analyses (Blevin, 2004; this study). Similarly, the strong enrichment in Sn (~30 ppm) relative to bulk continental crust (2.5 ppm; Taylor and McClennan, 1995) and the depleted mantle (0.1 ppm; Salters and Stracke, 2004) indicates extensive fractional crystallisation.

Estimation of the initial $^{87}Sr/^{86}Sr$ composition of the Ardlethan Granite based on whole rock data is difficult due to the uncertainty introduced by large age corrections associated with the relatively elevated $^{87}Rb/^{86}Sr$ (11.85). Bodorkos *et al.* (2013) reported a U–Pb zircon age for the Ardlethan Granite of 414.7 ± 2.3 Ma and Richards *et al.* (1982) reported a K–Ar date of 410 ± 2.5 Ma. Assuming an $^{87}Rb/^{86}Sr$ of 11.85 for the entire unit, the calculated $^{87}Sr/^{86}Sr_{(i)}$ composition of whole-rock data range from 0.71343–0.71419 based on the uncertainty in the U–Pb zircon age, and between 0.71417 and 0.71499 based on the uncertainty in the K–Ar age. A two-point isochron using the whole-rock and tourmaline analyses from ARD04 yields an age of 407.1 ± 3.2 Ma and an initial $^{87}Sr/^{86}Sr$ of 0.715053 ± 0.00004, however equilibrium is not certain. More work is required to properly constrain the $^{87}Sr/^{86}Sr_{(i)}$ of the Ardlethan Granite.

The variability in $^{87}Sr/^{86}Sr_{(i)}$ compositions of Group 1 tourmaline is difficult to interpret. $^{87}Sr/^{86}Sr_{(i)}$ heterogeneity within tourmaline samples is undetermined and could account for the spread in measured values. Partial replacement textures are common, but do not correlate with major changes in major or trace element chemistry. The least radiogenic composition occurs within nodular tourmaline (ARD06), which has an $^{87}Sr/^{86}Sr_{(i)}$ and $\varepsilon Nd_{(i)}$ composition comparable to the GQFP (Figure 18). The $^{87}Sr/^{86}Sr_{(i)}$ composition of magmas evolved from 0.71149 in the GQFP at 417.8 ± 2.2 Ma (Bodorkos *et al.,* 2013) to 0.71458 in the Ardlethan Granite at 414.7 ± 2.3 Ma (Bodorkos *et al.,* 2013). From a single Sr reservoir and over a period of *ca* 3 Ma, the $^{87}Sr/^{86}Sr$ of a melt could evolve this range if the $^{87}Rb/^{86}Sr$ ratio of the magma was ~40. Therefore, the less radiogenic $^{87}Sr/^{86}Sr_{(i)}$ tourmaline could be related to an earlier phase of the Ardlethan Granite at *ca* 417 Ma. Similarly, the greisen deposits (ARD16 and ARD19) with similar $^{87}Sr/^{86}Sr$ (Figure 18) would have formed during this earlier pulse. This is supported by cassiterite ages, which indicate greisen mineralisation occurred first at *ca* 415 Ma (See Chapter 3).

Although variable, the $^{87}Sr/^{86}Sr_{(i)}$ composition of the Ardlethan Granite and Group 1 tourmaline is within the range of S-type magmatism in the Lachlan Orogen (Chappell and White, 2001) whilst the $\varepsilon Nd_{(i)}$ compositions of the whole-rock Ardlethan Granite and Group 1 tourmalines (–3.73 to –2.11) are more

consistent with the I-type granitic magmatism of the Berridale and Kosciusko batholiths (McCulloch and Chappell, 1982; Figure 18).

Source modelling

The $^{87}Sr/^{86}Sr_{(i)}$ and εNd_i of the Ardlethan Granite is unique to the Lachlan Orogen, in that it has a Sr isotopic composition like S-type granites, but εNd is more like I-type granites (Figure 18). The proximal and *ca* 417 Ma Burrandana and Kyeamba granites that intruded contemporaneously with the GQFP and before the *ca* 415 Ma Ardlethan Granite, have similar $\varepsilon Nd_{(i)}$ (–3.01 and –3.79, respectively), but less evolved $^{87}Sr/^{86}Sr_{(i)}$ (0.70731 and 0.70980, respectively; Figure 18) and SiO_2 (71.46–71.70 wt%). Similarly, the Burrandana Granite, Glenbog Granodiorite, Kadoona Dacite (Kemp *et al.,* 2009) and Walleroobie and Gurragong volcanics have zircon $\varepsilon Hf_{(i)}$ (–5–0 ‰) and $\delta^{18}O$ (6–9 ‰) compositions within the range of the Ardlethan Granite and GQFP (Blevin *et al.,* 2017). These isotopic data indicate more widespread magmatism at *ca* 415 Ma than previously thought (e.g. Chappell and White 1992), derived from a weathered, moderately juvenile isotopic source.

The haplogranite composition of ‘tin’ granites like the Ardlethan Granite can be attributed to two processes; small degree partial melting or extreme fractional crystallisation. Although partial melting can fractionate $^{87}Sr/^{86}Sr_{(i)}$ and $\varepsilon Nd_{(i)}$ of a melt from its source (Zeng *et al.,* 2005), it is not considered a dominant process at Ardlethan for the following reasons:

1. Partial melting of an S-type source would generate a high ASI (e.g. 1.33 from experiments Castro *et al.,* 2010), similar to the Mine Granite (1.3), and higher than that of the Ardlethan Granite (1.1).
2. Partial melting of an I-type source would require miniscule degrees of <1% melt separation to generate the haplogranite compositions of the Ardlethan Granite (Abbot, 1981; Beard and Lofgren. 1991; Rushmer, 1991; Beard *et al.,* 2005; Sisson *et al.,* 2005), and such miniscule amounts of melt do not easily separate from their source (Arzi, 1978; Clemens and Vielzeuf, 1987; Sawyer, 1994; Vigneresse *et al.,* 1996).
3. In addition to 2, geochronological data indicates that the Ardlethan Granite was emplaced contemporaneously with widespread magmatism occurring over a 150 km strike within the Lachlan Orogen (Bodorkos *et*

al., 2013). To generate these haplogranite compositions from small degrees of partial melt would require melting an area significantly larger than the entire Lachlan Orogen.

The haplogranitic composition of the Ardlethan Granite is therefore attributed to extensive fractional crystallisation.

Assimilation and fractional crystallisation

Ren *et al.,* (1995) inferred fractional crystallisation created the haplogranitic composition of the Ardlethan Granite that is characterised by strong negative Eu/Eu* anomalies and flat REE chondrite-normalised concentrations (Figure 15), high Rb/Sr and Sn concentrations and low K/Rb and Sr, Y and LREE concentrations. These features are particularly apparent in the compositional contrast between the GQFP and the Ardlethan Granite, indicating much of the chemical evolution occurred following emplacement of the volcanics. The major and trace element compositions of these granites, and others that have intruded contemporaneously with the Ardlethan Granite are shown in Figure 21. Granites show linear trends with increasing SiO_2 for MgO, FeO, CaO and K_2O. However, the Kyeamba, Burrandana and Ardlethan granites show increasing Sn with SiO_2 compared to the stable concentrations within the other *ca* 415 Ma granites.

Fractional crystallisation alone, however, cannot explain the increasing $^{87}Sr/^{86}Sr_{(i)}$ but stable $\varepsilon Nd_{(i)}$ from the GQFP to the Ardlethan Granite (Figure 18). This trend of increasing $^{87}Sr/^{86}Sr_{(i)}$ is also evident with the inclusion of the Burrandana (0.70771) and Kyeamba (0.71036) granites.

Assimilation of Ordovician sediments during fractional crystallisation can cause these effects because the significantly different partition coefficients of Sr ($^{Sr}D_{Mineral/melt}$ = ~2) and Nd ($^{Nd}D_{Mineral/melt}$ = 0.1) in felsic melts. With continued fractional crystallisation and removal of the Sr from the residual melt primarily through the crystallisation of plagioclase (Bea *et al.,* 1994), the Sr isotopic composition of the assimilant will be adopted more readily than Nd (DePaolo, 1981).

The evolution of $^{87}Sr/^{86}Sr_{(i)}$ and $\varepsilon Nd_{(i)}$ through assimilation and fractional crystallisation (AFC) processes in felsic melts can be modelled for each isotopic system using the equations of DePaolo (1981):

$$\varepsilon_m = \frac{\frac{r\ C_a}{r-1\ z}(1-F^{-z})\varepsilon_a + C_m^0 F^{-z}\varepsilon_m^0}{\frac{r\ C_a}{r-1\ z}(1-F^{-z}) + C_m^0 F^{-z}} \qquad \text{Equation 5}$$

where: $z = \frac{r+D-1}{r-1}$; and the following terms are defined as: ε_m = isotopic composition of the magma; ε_a = assimilant, ε^0_m = initial magma. C_a = concentration in the assimilant; C_m concentration in the initial magma. D = partition coeffecient; r = $\frac{rate\ of\ assimilation}{rate\ of\ frac.\ crystal.}$; F = fraction of melt remaining. F and r are the only unknown parameters in the equation and have important geological meaning.

ε^0_m, ε_a, C_a and C_m are derived from published analyses of source rocks in the Lachlan Orogen and show significant heterogeneity. The partition coefficient, D (D = $\frac{concentration\ in\ minerals}{concentration\ in\ melt}$) for Nd and Sr in silicate melts is estimated at 0.01 ± 0.0005 and 2 ± 0.1, respectively. Sr is more compatible in peraluminous granitic melts than Nd, as it is sequestered primarily into plagioclase (e.g. Bea *et al.,* 1994). The strong negative Eu/Eu^* anomalies indicate significant removal of plagioclase from the Ardlethan Granite. Alternatively, Nd shows strong affinities for apatite (e.g. Bea *et al.,* 1994). The increasing P_2O_5 (Figure 21) and the presence of accessory apatite within the Ardlethan Granite indicate that Nd was not significantly removed from the system during fractional crystallisation. To simultaneously solve the Equation 5 for F and r, whilst also accounting for the variability in the above parameters, Monte-Carlo simulations were performed with 10 000 iterations assuming uniform a distribution of isotopic concentrations and compositions within the defined uncertainty.

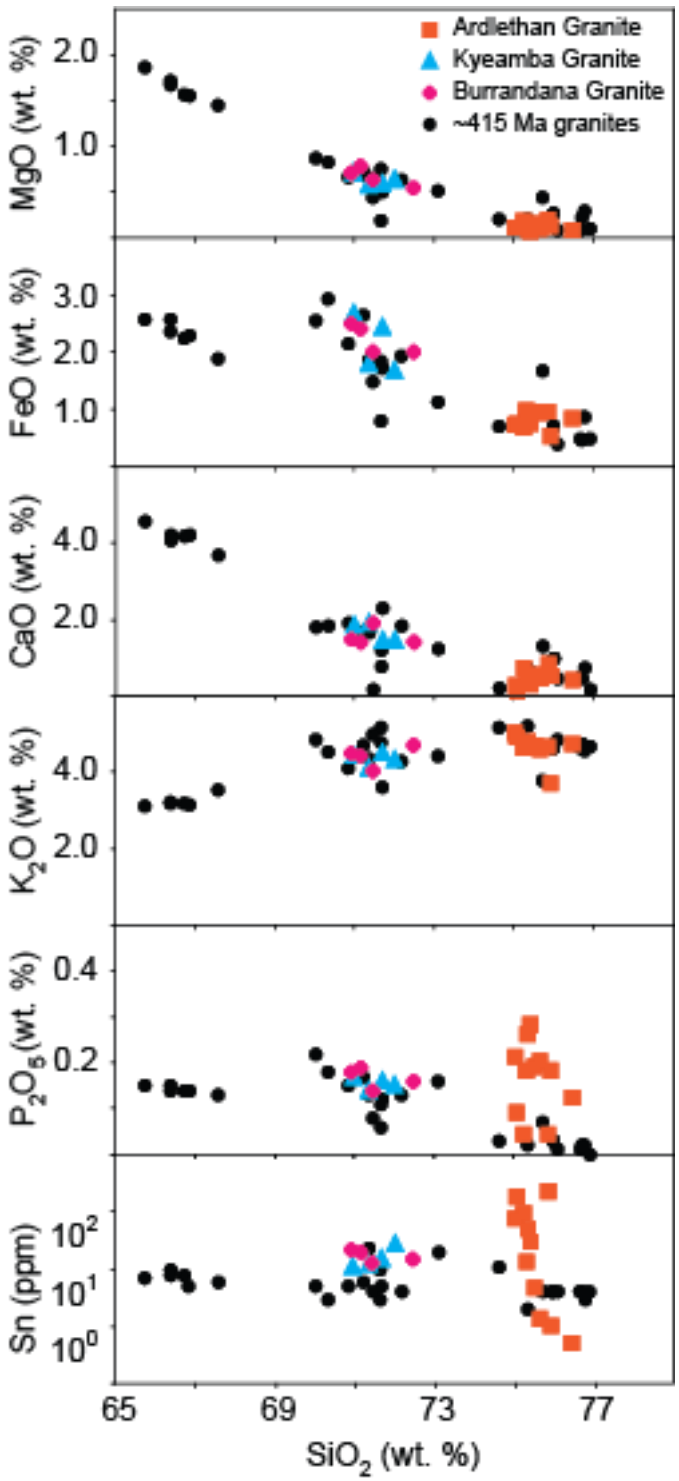

Figure 21: Major and trace element bivariate plots for granites intruding the Lachlan Orogen ca 415 Ma and interpreted to be genetically related to the Ardlethan Granite. Data from Blevin, 2002.

These simulations were performed by using the isotopic composition of the two I-type source components identified in the Lachlan Orogen undergoing fractional crystallisation and assimilation of Ordovician sediments. The I-type components include: 1) mantle represented by harzburgite and lherzolite xenoliths in southeastern Australia (McDonough and McCulloch, 1987), and 2)

oceanic crust represented by outcropping greenstone belts (Nelson *et al.,* 1984; McDonough and McCulloch, 1987).

The isotopic composition of the mantle is estimated from xenoliths occurring at Bingie Bingie, eastern Lachlan Orogen, and is relatively restricted with $^{87}Sr/^{86}Sr_{(410\ Ma)}$ of 0.7039 ± 0.002 and $\varepsilon Nd_{(410\ Ma)}$ of 5.2 ± 1.6 (Figure 18; Keay *et al.,* 1997). The Sr (570 ± 84 ppm) and Nd (30 ± 4.5 ppm) concentration within these enclaves does not indicate large compositional heterogeneities. Although two groupings of Cambrian greenstones have been identified isotopically (Figure 18; Nelson *et al.,* 1984; McDonough and McCulloch, 1987), only the most primitive is used in modelling. These rocks have variable $^{87}Sr/^{86}Sr_{(410\ Ma)}$ of 0.706 ± 0.001, Sr concentration of 150 ± 75 ppm and $\varepsilon Nd_{(410\ Ma)}$ of 3.2 ± 1.5 and Nd concentration of 5 ± 2.6 ppm. The Ordovician sediments display minimal $\varepsilon Nd_{(410\ Ma)}$ variation (~ 10 ± 0.37), but variable $^{87}Sr/^{86}Sr_{(410\ Ma)}$ (0.72407 ± 0.002), Sr (Sr = 191 ± 50 ppm) and Nd (57 ± 16 ppm) concentrations.

Figure 22A shows model of AFC between a melt derived from a mantle source and assimilated with Ordovician sediments, and can reproduce the $^{87}Sr/^{86}Sr_{(i)}$ and $\varepsilon Nd_{(i)}$ composition of the Ardlethan Granite with highly variable F (0.48 -0.33/+0.44) and r (0.54 -0.27/+0.38). Conversely, Figure 22B shows that AFC from a melt derived from oceanic crust source and assimilated with Ordovician sediments requires restricted and low values of F (0.14 -0.12/+0.56) and r (-0.07/+0.30). This second scenario explains better the haplogranite composition, and moderate ASI of the Ardlethan Granite as a low F (0.14) indicates prolonged fractionation crystallisation, and low r (0.09) indicates a relatively minor sedimentary component in the final melt.

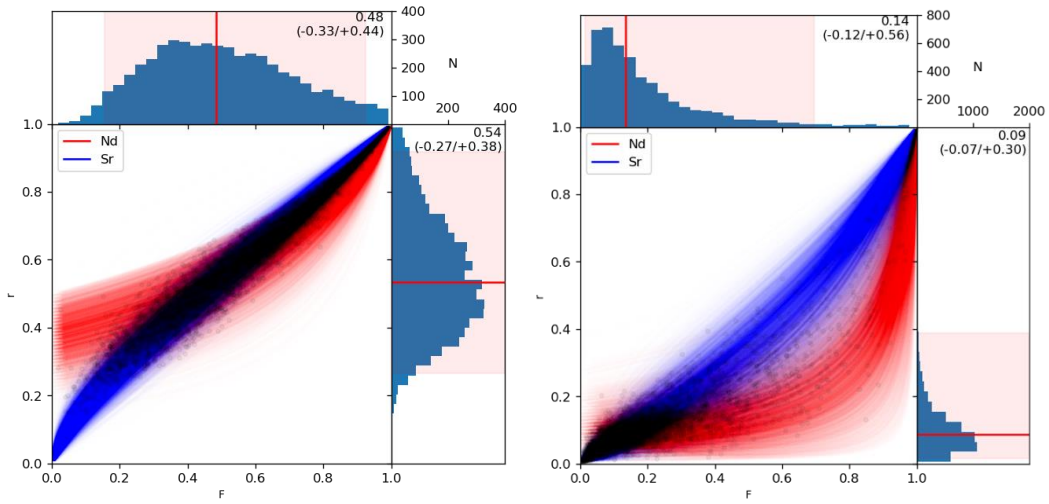

Figure 22: Monte-Carlo simulations of F and r values of the Assimilation and Fractional Crystallisation (AFC) modelling equation of DePaolo (1981) as applied to the Ardlethan Granite. The left panel represents AFC of a mantle source with Ordovician sedimentary assimilant, and the right panel represents an oceanic crust source and Ordovician sedimentary assimilant. Red traces represent the F and r combination that can will produce the $\varepsilon Nd_{(i)}$ composition of the Ardlethan Granite. Blue traces represent F and r values for Sr. The multiple traces were produced by varying the composition parameters (concentration and isotopic ratio) of the end-members. Where the blue and red traces intersect, marked by a black dot, represents a F and r value that produces both the $^{87}Sr/^{86}Sr_{(i)}$ and $\varepsilon Nd_{(i)}$ of the Ardlethan Granite. A probability histogram of these intersections is show on the borders for the graphs.

Sn enrichment

Ren *et al.* (1995) reported tin concentrations within the Ardlethan Granite increasing from 15 ppm in the main part of the body to 300 ppm towards the eastern margin where most mineralisation occurs. Sn concentrations of the Ardlethan Granite reported here are within this range (~50 ppm). This is approximately five times more abundant than the average crustal value (Taylor and McClennan, 1995).

In the previous section, isotopic modelling of AFC processes indicates that the Ardlethan Granite originated from melting of a isotopically juvenile (oceanic crust) source. Melts underwent extreme fractional crystallisation and minimal assimilation of weathered sedimentary rocks. The concentration of Sn during AFC processes can be modelled with an assumed mineral–melt partitioning coefficient of Sn near 0. Sn is shown to increase with SiO_2 relative to the *ca* 415 Ma Granites (Figure 21) indicating is incompatibility. Williamson *et al.,* (2016) assumed a $^{Sn}D_{Mineral/melt} \approx 0$ in the parental melts of the Cornubian Batholith because of the high solubility of Sn over a range of oxygen fugacity in reduced felsic melts (> 1000 ppm SnO_2; Stemprok, 1990; Taylor and Wall, 1992) that prevents cassiterite precipitation, and the large ionic radius (0.93 Å) and low

charge of Sn^{2+} that prevents its incorporation into the major mineral phases. The reduced composition of the Ardlethan Granite (Blevin 2004) indicates that Sn^{4+} was minor, preventing its substitution into Ti^{4+} bearing minerals such as titanite ($^{Sn}D_{Mineral/melt}$ = ~100; Antipin *et al.,* 1981).

Sn concentrations have not been reported for the Cambrian greenstones of the Lachlan Orogen, however modern MORB are below 1.7 ppm (e.g. Yi *et al.,* 2000) and commonly <1.3 ppm. Partial melting of these source rocks will enrich Sn in the melts if no Ti-bearing restite phases such as biotite, ilmenite and rutile are present. Approximately 20 volume % melt generation is thought to be a critical minimum before which granite melts are trapped in their source region forming migmatites (Arzi, 1978; Clemens and Vielzeuf, 1987; Sawyer, 1994; Vigneresse *et al.,* 1996). Assuming 20 vol % partial melting of an oceanic crust, and incompatibility of Sn in restite phases, Sn concentrations in parental melts will be enriched 5 times more than the source rocks. Larger partial melt volumes will reduce the concentration of Sn in the melt. Wolf *et al.,* (2018) suggest that source rocks can also enriched in Sn by multiple, low-temperature melt extractions in which Sn is sequested into the restite phases.

Figure 23 shows the enrichment of Sn during AFC with the r values determined in Figure 22, and by Rayleigh fractionation for comparison. The initial 20 vol. % melt begins with a Sn concentration of 7.5 ppm (a 5 times enrichment of average MORB value 1.5 ppm). Sn concentration of the assimilant is set to 4 ppm (Blevin 2002). Fractionation crystallisation alone would require near complete crystallisation (97%) achieve the Sn concentrations in the residual melt that formed the Ardlethan Granite. Conversely incorporation of the slightly enriched Ordovician sediments through AFC processes requires 30–70% crystallisation, dependent on the r value, to produce 50–300 ppm Sn in the residual melts. In Figure 22 the r value was more precisely constrained than the F value due to the path of the $\varepsilon Nd_{(i)}$ traces. By fixing the r value to 0.09 in AFC modelling of Sn indicates that a minimum of 60% crystallisation is required to produce 50 ppm in the residual melts of the Ardlethan Granite. Larger volumes of partial melting of protolith, the presence of Sn-bearing restite or $^{Sn}D_{Mineral/melt} > 0$ will require further crystallisation (lower F) to produce the elevated Sn concentrations of the Ardlethan Granite.

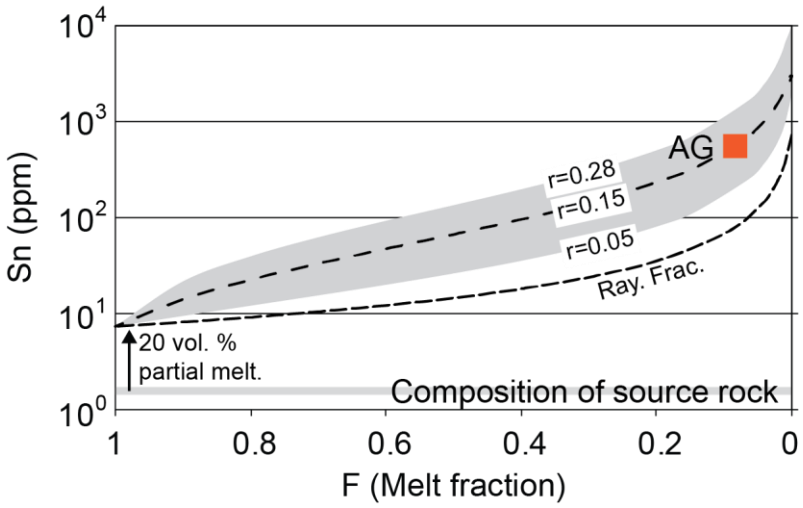

Figure 23: Modelled enrichment of Sn during Rayleigh Fractional and AFC processes after 20 vol. % partial melting of a greenstone protolith. The grey fields represent the curves between the maximum and minimum r (rate of assimilation/rate of frac. Cryst) values determined in Figure 22. The Ardlethan Granite (AG) is placed at the r and F values determined in Figure 22.

Summary

Isotopic data presented and discussed here indicates that the Ardlethan Granite, and potentially other felsic magmatism at *ca* 415 Ma (Burrandana Granite, Glenbog Granodiorite, Kadoona Dacite and Walleroobie and Gurragong volcanics), are chemically and temporally distinct from the Koetong Supersuite. The *ca* 415 Ma igneous units were emplaced during slab retreat following convergence (Kemp *et al.,* 2009) and are marked by regionally intermediate $^{87}Sr/^{86}Sr_{(i)}$ and $\varepsilon Nd_{(i)}$ whole rock compositions, and $\varepsilon Hf_{(i)}$ and $\delta^{18}O$ zircon compositions. The Ardlethan Granite was derived from melting of juvenile source rocks with a minor weathered component. The haplogranite chemistry of the Ardlethan Granite is hypothesised to the result of prolonged AFC incorporating sedimentary (weathered) rocks. Monte-Carlo modelling of the $^{87}Sr/^{86}Sr_{(i)}$ and $\varepsilon Nd_{(i)}$ composition of parental melts of the Ardlethan Granite during AFC indicates ~85% crystallisation is required, with relatively minor assimilation of sedimentary rock (r = 0.09). The effect of AFC on the concentration of Sn in the residual melts is modelled, despite numerous assumptions, renders imprecise, but overlapping F and r values.

Magmatic to hydrothermal processes

Fluid formation and greisen mineralisation

AFC modelling in the previous section indicates magmatic enrichment of Sn 30 times greater than in the inferred source rocks. Magmatic crystallisation of cassiterite requires an order of magnitude greater enrichment to occur (~1000 ppm; Stemprok, 1990; Taylor and Wall, 1992; Naumov and Kamenetsky, 2006). At Ardlethan, cassiterite mineralisation is hydrothermal, occurring in veins and breccia infill. Therefore, a secondary enrichment process, within the magmatic to hydrothermal transition is required to create the economic mineralisation.

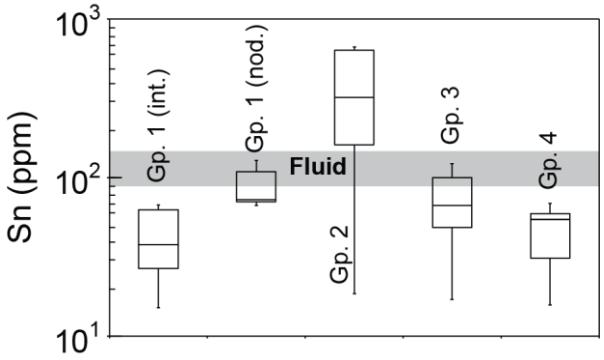

Figure 24: Box and whisker plot of tourmaline LA-ICP-MS Sn concentrations from Ardlethan in tourmaline groups of Table 1. The Sn concentration modelled in a fluid emanating from the Ardlethan Granite is shown in the grey bar.

Sn concentrations in tourmaline record the enrichment from within the magmatic environment and through to the hydrothermal environment (Figure 24). Interstitial tourmaline of Group 1 occurring within the Ardlethan Granite has a median Sn concentration of 37 ppm that increases to 73 ppm in nodular tourmaline of Group 1. The increase across this textural transition indicates that fluid separation and sequestration of Sn has not occurred prior to the formation of quartz–tourmaline nodules.

The Sn concentration of a fluid separating from the Ardlethan Granite is estimated using the equation for 'first boiling' by Candela (1989):

$$C_{fluid}^{i} = D_{\frac{fluid}{melt}}^{i} * C_{O}^{i}(1 - [(1 - F)C_{O}^{water}])^{D\frac{fluid}{melt}-1} \quad \text{Equation 6}$$

where C^{i}_{fluid} is the concentration of Sn in a fluid exsolved from the initial silicate melt (C^{i}_{O}), $D^{i}_{\frac{fluid}{melt}}$ is an estimate of the fluid/melt partition of Sn (discussed below), C^{water}_{O} is the initial concentration of water in the silicate melt immediately prior to boiling and $F_{(water)}$ is the mass of water in the melt following boiling relative to the initial mass in the melt. A $F_{(water)}$ of 0.14 is used for the calculation because the maximum measured H_2O the Ardlethan Granite is 1.0 wt% (Blevin, 2002) and 7 wt% represents the water saturation point in the Qz–Ab–Or experimental system at 650°C and 0.3 GPa (Holtz and Johannes, 1994). There are numerous variables within Equation 6 that rely on assumptions and so calculations are intended to provide broad estimates of the Sn concentration of fluids exsolved from the Ardlethan Granite melts.

Estimates of melt/fluid partition coefficients for Sn ($D^{fluid/melt}_{Sn}$) vary between 0.002 and 12 (Nekrasov *et al.,* 1980; Keppler and Wyllie, 1991; Duc-Tin *et al.,* 2007; Zajacz *et al.,* 2008). The availability of HCl is the most sensitive factor to Sn solubility in a fluid (Duc-Tin *et al.,* 2007; Zajacz *et al.,* 2008). Duc-Tin *et al.* (2007) show that HCl increases Sn solubility more than NaCl by 2 orders of magnitude. Ren (1995) measured NaCl in fluid inclusions between 30 and 65 wt% equivalent in the Ardlethan Granite. Experimental data indicate that in peraluminous melts at 800°C/100 MPa, HCl will account for about 25–40% of total chlorine (Manning 1989). HCl is estimated in the Ardlethan Granite to be 2.5 M. Duc-Tin *et al.* (2007) estimated $D^{fluid/melt}_{Sn}$ between 2 and 4 for peraluminous melts at 700°C, 100–200 MPa, log f_{O2} ~ NNO, and HCl between 0.5 and 4.4 M. For $D^{fluid/melt}_{Sn}$ = 2–4, the calculated Sn concentration of a fluid generated from first boiling in the Ardlethan Granite is 95–166 ppm (Figure 24). Halving the assumed C^{water}_{O} (F = 0.29) marginally increases these values of 97–185 ppm.

Predicted Sn concentrations of fluids at Ardlethan are consistent with Sn concentrations reported in Group 3 tourmaline indicating fluid separation from the Ardlethan Granite led to greisen-style mineralisation. The identical REE pattern of the Group 1 and Group 3 tourmalines (Figure 17) further indicates that fluids emanating from the Ardlethan Granite led to greisen mineralisation.

The calculated fluid $\delta^{18}O$ values of the Ardlethan Granite (+5.86) are most similar with compositions in quartz associated with greisen mineralisation (+4.35; Table 9; Figure 25). The slight offset in $\delta^{18}O$ is attributed to the lower formation temperatures associated with quartz precipitation between the Ardlethan Granite (~450ºC) and qtz–tur–cst veining (350ºC). Sr, Y, Sn, LREE and Pb increase in concentration from Group 1 to Group 3 tourmaline also indicating hydrothermal mobilisation of these elements.

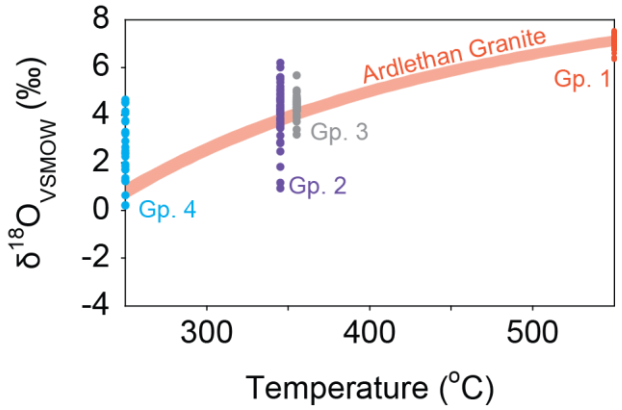

Figure 25: Variations in $\delta^{18}O$ quartz values as a function of temperature from Ren (1989). The evolving temperature dependent composition of the Ardlethan Granite is modelled using the equation of Pollington et al. (2016).

Fluid–rock mixing

Sn within Group 2 tourmaline associated with cassiterite shows significantly greater enrichment than predicted purely from the separation of a fluid from a peraluminous melt (Figure 24). Elevated Sn concentrations indicate that tourmaline precipitated before cassiterite and that another enrichment process occurred. Breccia infill textures in the Wild Cherry deposit confirm the early precipitation of tourmaline relative to cassiterite (Figure 11A). Cassiterite occurs as euhedral crystals growing into voids surrounded by thick (~1 m) tourmaline selvage.

All tourmaline samples within Group 2 tourmaline has comparable LREE concentrations. Group 1 tourmaline, however, differs with enriched HREE (Figure 17). Fractionation of the LREE and HREE elements is commonly reported in hydrothermal environments associated with highly fractionated granites (e.g. Maruéjol *et al.,* 1990; Salvi and William-Jones, 1996; Jiang *et al.,* 1999, 2004; Yavuz *et al.,* 2011). Wood (1990) showed that at 300ºC Lu (and

HREE) is almost twice as stable as La (and LREE) in fluoride complexes. REE fractionation due to the formation of fluoride complexes, however, is unlikely as Migdisov and Williams-Jones (2014) show that the REE are more soluble in Cl-complexes. Although topaz is a common gangue mineral associated within the breccia pipes (Ren *et al.,* 1989), fluorine concentrations in tourmaline are highest in Group 1 and Group 3 where there is no HREE enrichment. Additionally, there is no correlation between F and the HREE observed in tourmaline of the breccia deposits. Marks *et al.* (2013) suggested plagioclase dissolution led to HREE enrichment over LREE after the experimental data of Shibata *et al.* (2006). Salvi and Jones (1996) also correlate the enrichment of HREE relative to LREE with low temperature (≤ 200ºC) Ca-bearing fluids derived from the country rocks. Plagioclase dissolution is evident in the Mine Granite and the major elements of tourmaline become more Ca rich in the breccia pipes (Figure 16A, C), but there is no correlation between the HREE and Na_2O or CaO in tourmaline. Furthermore, plagioclase dissolution would also be expected in the greisen deposits (Group 3) as the Ardlethan Granite contains ~23 vol% plagioclase (Ren, 1989), however, Group 3 tourmalines have no HREE enrichment (Figure 17). Jiang *et al.* (1999) attribute HREE enrichment in hydrothermal fluids to a new magmatic pulse from a different source. The Mine Porphyry is slightly enriched in the HREE, but tourmaline Sr and Nd isotopic data indicate no contribution of this unit to hydrothermal fluids at Ardlethan. The lack of HREE enrichment in Group 4 tourmaline indicates that the mechanism leading to HREE enrichment ceased after cassiterite mineralisation.

The $^{87}Sr/^{86}Sr_{(i)}$ and $\varepsilon Nd_{(i)}$ of Group 2 tourmaline at Ardlethan define an array that indicate hydrothermal fluids interacting with the Mine Granite host rock. To evaluate this process the isotopic mixing equation of DePaolo and Wasserburg (1979) was used;

$$(\varepsilon_x)_m = \frac{X_1[x']_1\varepsilon_x+(1-X_1)[x']_2(\varepsilon_x)_2}{X_1[x']_1+(1-X_1)[x']_2} \qquad \text{Equation 7}$$

where $(\varepsilon_x)_m$ = the isotopic composition of a two-component mixture, X_1 = weight fraction of component 1 (between 0 and 1), $[x']_1$ = element concentration of

component 1 (e.g. ppm) and ε_x = isotopic ratio of component 1 (e.g. $^{87}Sr/^{86}Sr$). Component 1 is the fluid emanating from the Ardlethan Granite with an isotopic composition defined by Group 1 tourmaline: $^{87}Sr/^{86}Sr$ = 0.7146, Sr = 203 ppm, εNd = –3.19, and Nd = 45 ppm. Component 2 is the Mine Granite defined by whole-rock data reported here: $^{87}Sr/^{86}Sr$ = 0.7187, Sr = 149 ppm, εNd = –9.34, and Nd = 6.56 ppm. The modelled curve of this fluid leaching between X_1 = 0–1, is displayed in Figure 26.

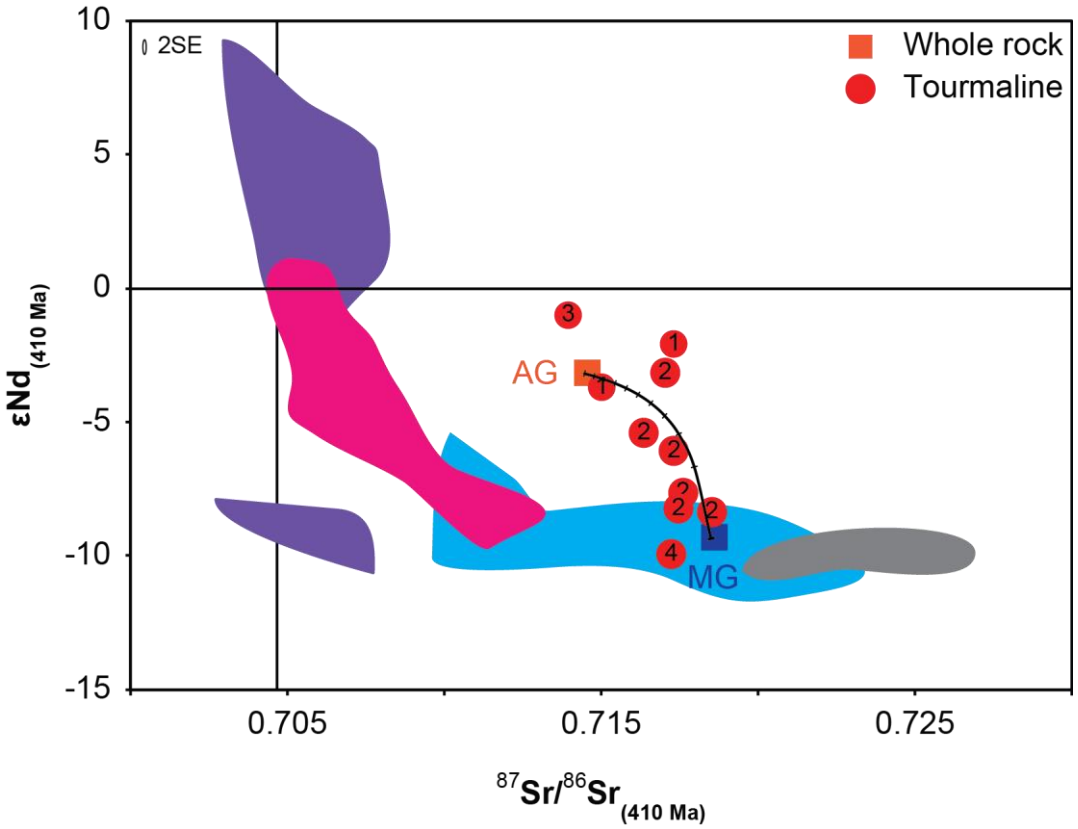

Figure 26:Isotopic mixing modelling with equations of DePaolo (1979) for tourmaline between the Ardlethan Granite (AG) and Mine Granite (MG) end members. Compositional fields of other units in the Lachlan Orogen are described in Figure 18. The numbers on tourmaline points indicates its group.

The array of Group 2 $^{87}Sr/^{86}Sr_{(i)}$ and $\varepsilon Nd_{(i)}$ can be reproduced by ~50–96% isotopic mixing between the fluid and the Mine Granite. Fluid leaching is also evident in the major element compositions of Group 2 tourmalines, which are intermediate between the Mine Granite and Ardlethan Granite in their Fe–Mg and Na(+K)–Ca substitutions (Figure 16). Ren *et al.* (1995) reported similar Fe enrichments in secondary biotite and chlorite hosted in the Mine Granite but associated with the intrusion of the Ardlethan Granite. Fresh samples of the Mine Granite are defined by a $\delta^{18}O$ value of +8.7 ‰ (Ren, 1995). Increasing

alteration within the Mine Granite coincides with increasing $\delta^{18}O$ values up to +11.7 ‰, comparable with the fresh Ardlethan Granite $\delta^{18}O$ of +11.38 ‰. The calculated $\delta^{18}O$ fluid values reported here for Group 2 quartz vary significantly between the calculated Ardlethan Granite fluid at ~350^{o}C and heavier compositions. The poor temperature constraints on quartz precipitation likely add to the excess scatter. Using better temperature constraints, Ren *et al.,* (1995) reported a systematic decrease in fluid $\delta^{18}O$ values with temperature, which they attributed to cooling magmatic fluids from the Ardlethan Granite in rock buffered conditions.

Fluid leaching of the Mine Granite is associated with a general increase in Sn concentrations within tourmaline (Figure 27). The unaltered Mine Granite contains up to 56 ppm Sn, whilst altered samples as little as 8 ppm (Ren, 1989). Scavenging of Sn from host rocks has been suggested for the Tanjungpanda deposit (Lehmann and Harmanto, 1990). Lehmann and Harmanto (1990) suggest that Sn was remobilised from the host granite by reduced fluids. Eugster (1986) show that Sn solubility in a fluid at 500^{o}C will increase from 0.1 ppm at the hematite–magnetite (HM) buffer to 100 ppm at the quartz–fayalite–magnetite (QFM) buffer. Ren (1989) calculated the log fO2 of the mineralisation fluids to be 4–5 units below the HM buffer, or 1–2 units above the QFM between 385 and 440^{o}C. The log fO2 of the Mine Granite is unknown, but likely reduced due to the presence of ilmenite and no magnetite (Ren, 1989). Although this low fugacity is thought to be encourage Sn mobility, as Sn^{2+} binds with Cl-rich fluids, however recently Schmidt (2017) showed that Sn^{4+} can be mobile in chloride complexes, including $[SnCl_4(H_2O)_2]_0$ and $[SnCl_3(H_2O)_3]$.

Leaching was most effective in brecciated zones where there was a greater exposure of Mine Granite fragments to the fluids emanating from the Ardlethan Granite. In many locations brecciation has created low permeability rock-flour breccia, elsewhere fragment-supported breccias have channellised fluid flow (Ren, 1989). Fluid flow through these zones has caused pervasive alteration of the primary mineralogy of the Mine Granite (Figure 9). Ren *et al.,* (1995) defined three alteration assemblages defined on the dominant alteration mineral; biotite, sericite and chlorite. Alteration involves replacement of magmatic K-feldspar,

plagioclase and biotite with these minerals (Ren *et al.,* 1995). Although the Sn concentration of magmatic K-feldspar, plagioclase and biotite in the Mine Granite is unknown, the minerals are present in large volumes: K-feldspar = 35 vol. %, plagioclase = 25 vol. % and biotite = 10–15 vol. % (Ren 1989) .

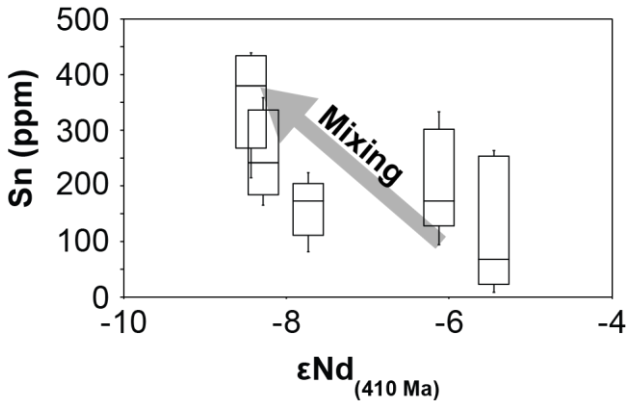

Figure 27: Box and whisker plot of Sn concentration of Group 2 tourmaline increasing with lower εNd. Increasing $\varepsilon Nd_{(i)}$ in Group 2 tourmaline is associated with increased fluid leaching of the Mine Granite, as discussed in the text.

Within the Cornubian Batholith, muscovite (50–70 ppm), plagioclase (10–20 ppm), orthoclase (10–15 ppm) and tourmaline (5–20 ppm) are the major reservoirs of Sn in the magmatic mineralogy (Simons *et al.,* 2017), however biotite is not present. Partitioning coefficients of Hu *et al.* (2016) for metaluminous acidic melts indicate biotite ($D^{Sn}_{biotite-melt} = 3.19$) and magnetite ($D^{Sn}_{magnetite-melt} = 7.4$), when present, are the primary hosts of Sn. Sn within magmatic minerals of the Mine Granite likely reside primarily in biotite, substituting for Ti^{4+}, which makes up 10–15% of the rock. Further Sn will be hosted in the accessory phases ilmenite and rutile, however leaching of these phases is more difficult. The Sn concentration of biotite of the Mine Granite has not been analysed so mass balance equations are difficult.

Ren *et al.* (1995) attributed cassiterite precipitation to cooling hydrothermal fluids and increasing pH and f_{O2} during fluid–rock interaction with the Mine Granite. As previously discussed, the solubility of Sn is two orders of magnitude more sensitive to HCl concentration over NaCl concentration (Kovalenko *et al.,* 1986). The precipitation of Sn at Ardlethan is therefore more likely the result of decreasing HCl molarity during wall rock mixing and resulting in widespread chlorite alteration (Figure 9). Precipitation temperature estimates for chlorite

alteration range from 290 to 105^{o}C, and cassiterite precipitation likely occurred in the upper temperature range (Ren, 1989).

Group 4 tourmaline, interpreted as precipitating post-mineralisation, has equilibrated with the Mine Granite in major element concentrations and isotopic compositions.

2.2.7 Conclusions

Magmatic to hydrothermal processes leading to economic Sn mineralisation are difficult to decipher due to extended fractional crystallisation of the parental magma that disguise the magmatic source rocks, and pervasive hydrothermal alteration, which overprints magmatic-hydrothermal processes. Tourmaline major, trace concentrations and Rb–Sr and Sm–Nd isotopic compositions show large compositional trends through the magmatic to hydrothermal stages at Ardlethan. In conjunction with whole-rock chemistry and quartz $\delta^{18}O$ values, 4 texturally distinct and chemically distinct groups of tourmalines were identified and attributed to specific processes occurring across the magmatic to hydrothermal transition.

Tourmaline occurs within the Ardlethan Granite as a late magmatic phase and primarily mimics the bulk rock composition. The unique isotopic composition of the Ardlethan Granite, compared with other granites of the Lachlan Orogen, is modelled by AFC processes involving minor incorporation of Ordovician sediments, and leading to the enrichment of Sn in the residual melt. Enrichment of Sn in tourmaline from interstitial (~37 ppm) to nodular (~73 ppm) settings and indicates Sn enrichment during late fractional crystallisation. Sn in tourmaline of greisen deposits (~70 ppm) is equal to a model composition of a fluid exsolving from the Ardlethan Granite. The major element and REE composition of greisen-hosted tourmaline (Group 3), and the $\delta^{18}O$ of quartz that has coprecipitated with this tourmaline, indicate that fluid fractionation lead to cassiterite mineralisation in greisen deposits. .

Tourmaline associated with breccia-pipe cassiterite mineralisation provides geochemical evidence for fluid leaching of the host rock, the Mine Granite. This evidence is most clear in the major element and isotopic composition of tourmaline within the Mine Granite compared with tourmaline of the Ardlethan Granite. Fluid leaching of the Mine Granite, which is best quantified by $\varepsilon Nd_{(i)}$ and $Fe/(Fe+Mg)_{apfu}$ in tourmaline, is accompanied by increasing Sn concentrations in tourmaline, and by inference the fluid. The increased Sn is inferred to be scavenged from the fertile host rock, the Mine Granite. Cassiterite precipitation was triggered by decreasing HCl within the fluid attributed to widespread chlorite mineralisation associated with breccia formation. Following

cassiterite precipitation, low temperature fluids associated with sulfide mineralisation in the breccia pipes were chemically equilibrated with the host rocks.

2.3 Melt compositions and the transition to hydrothermal fluids in the Mole Granite polymetallic system

2.3.1 Introduction

The Mole Granite of eastern Australia is an intensively studied magmatic to hydrothermal mineral system due to its association with a world class polymetallic mineral district. Previous research has focused on the processes leading to the formation of a fluid emanating from the crystallising Mole Granite, and its chemical evolution resulting from the interaction with meteoric fluids (Mulholland, 1943; Lonergan, 1971; Eadington, 1977, 1983; Kleeman, 1982; Plimer and Kleeman, 1985; Sun and Eadington, 1987; Rankin *et al.,* 1992; Heinrich *et al.,* 1992, 1999; Kleeman *et al.,* 1997; Audétat *et al.,* 1998, 1999; Audétat *et al.* 2000a, 2000b, 2008; Henley *et al.,* 1999; Mavrogenes *et al.,* 2002; Pettke *et al.,* 2005; Schaltegger *et al.,* 2005; Fekete *et al.,* 2016). Whole-rock and quartz oxygen isotope compositions of the magmatic units indicate widespread mixing between magmatic fluids of the Mole Granite and meteoric fluids (Sun and Eadington, 1987; Fekete *et al.,* 2016). Laser ablation ICP-MS studies of melt and fluid inclusions (Audétat *et al.,* 1998, 2000a, 2000b, 2008) have provided direct estimates of their major and trace element compositions but with large uncertainties. Those studies show dilution of magmatic fluids with meteoric fluids.

Tourmaline is a common mineral in these systems and is found in both magmatic and hydrothermal settings. The difference in chemical composition of tourmaline of both these settings can provide new perspectives on the compositional changes (both elemental abundance and isotopic composition) occurring at the magmatic–hydrothermal transition.

In this Chapter, the nature of the source rocks and subsequent magmatic processes leading up to the emplacement of the Mole Granite, and by inference the Mole Supersuite (Mole SS), are discussed in the context of new tourmaline and whole-rock geochemistry presented here and within a parallel study (Laker, 2017). Tourmaline from hydrothermal settings surrounding the Mole Granite is also presented to quantify compositional changes across the magmatic-

hydrothermal transition.

2.3.2 Geology

The New England Orogen (NEO) is the youngest tectonic component of the Tasmanides of eastern Australia (Glen, 2005). The NEO is subdivided into a southern (sNEO) and northern (nNEO) terrain, separated by Mesozoic cover. Only the sNEO is described here. The substrate of the sNEO is oceanic crust east of the Peel-Manning Fault system, and mixed oceanic and continental to the west (Figure 28; Glen et al., 2005). Remnant oceanic floor sequences occur in accretionary trench sequences (Cawood, 1982). Buried Neoproterozoic sedimentary deposits, associated with the development of the Delamerian and Lachlan orogens, are inferred to extend partially into the NEO (Bruce *et al.,* 2000; Powell and O'Reilly, 2001; Bennett *et al.,* 2002).

The sNEO consists of forearc sedimentary sequences of the Tamworth Belt in the west and accretionary trench sequences of the Tablelands Complex in the east (Figure 28; Glen 2005). The lower Tamworth Belt includes two units; lower Middle Devonian low-K, juvenile, intra-oceanic island arc volcaniclastics, and an upper sequence of Carboniferous convergent continental plate margin sediments (Leitch, 1974). Sediments of the Tablelands Complex are predominantly deep marine turbidites that accumulated in a continental magmatic arc trench (Leitch, 1974). Convergent magmatism in the Tamworth Complex was terminated by compression of the Tablelands Complex at *ca* 300 Ma (Glen, 2005). Compression was followed by extension resulting in rift basin formation and S-type granite (Hillgrove and Bundarra supersuites) emplacement between 300 and 284 Ma. After compression and crustal thickening associated with the Hunter Bowen Event (265–255 Ma), voluminous I-type granites were emplaced, predominantly in the Tablelands Complex (Figure 28) between 255 and 233 Ma (Landenberger *et al.,* 1995; Phillips *et al.,* 2011).

New England Batholith (NEB)

The New England Batholith includes Permian to Triassic granites emplaced predominantly within the Tablelands Complex (Figure 28). The batholith outcrops over 15 000 km^2 (Shaw and Flood, 1981) and includes six Supersuites with distinctive mineralogy, geochemistry and isotopic composition (Shaw and Flood, 1981; Hensel *et al.,* 1985; Bryant *et al.,* 1997; Landenberger *et al.,* 2000) including; 1) Hillgrove Supersuite (HSS); 2) Bundarra Supersuite (BSS); 3) Clarence River Supersuite (CRSS); 4) Moonbi Supersuite (MSS); 5) Uralla Supersuite (USS) and 6) leucomonzogranites. The isotopic composition of these supersuites has been determined on whole-rock samples for Rb–Sr and Sm–Nd (Hensel *et al.,* 1985; Landenberger *et al.,* 2000), $\delta^{18}O$ (O'Neil *et al.,* 1977) and ^{7}Li (Bryant *et al.,* 2004), and in zircon for $\varepsilon Hf_{(i)}$ (Phillips *et al.,* 2011; Jeon *et al.,* 2012, 2014; Laker, 2017) and $\delta^{18}O$ (Jeon *et al.,* 2012, 2014; Laker, 2017) and are summarised in Table 10. The $^{87}Sr/^{86}Sr_{(i)}$ and $\varepsilon Nd_{(i)}$ compositions of the NEB Supersuites and sedimentary units are shown in Figure 29.

S-type magmatism of the HSS and BSS is characterised by early Permian granites (303–289 Ma) with peraluminous, reduced, and relatively evolved isotopic compositions (Collins *et al.*, 1993; Kent, 1994; Craven, 2010; Cawood *et al.*, 2011; Craven *et al.*, 2012; Table 10). The HSS includes foliated granodiorites and monzogranites (Dirks *et al.,* 1993) emplaced between 303 and 289 Ma (Collins *et al.*, 1993; Kent, 1994; Craven, 2010; Cawood *et al.*, 2011; Craven *et al.*, 2012). The mafic units contain biotite, actinolite, cummintonite, almandine garnet and ilmenite (Flood and Shaw, 1977). SiO_2 contents (65–71 wt%) vary with strongly enriched LREE and small negative Eu/Eu* anomalies (Dirks *et al.*, 1993; Flood and Shaw, 1977; Shaw and Flood, 1981).

Table 10: Isotopic compositions of the granite supersuites of the New England Batholith. Sr and Nd data compiled from Hensel et al. (1985), Bryant et al. (1997), Landenberger et al. (2000). $\delta^{18}O$ data from O'Neil et al. (1977). $\delta^{7}Li$ from Bryant et al. (2004) and εHf zircon data from Kemp et al. (2009) and Philips et al. (2011).

Suite/Supersuite	Age (Ma)	$^{87}Sr/^{86}Sr_{(i)}$	$\varepsilon Nd_{(i)}$	$\delta^{18}O$	$\delta'Li$	$\varepsilon Hf_{(i)}$ (zrc)	$\delta^{18}O$ (zrc)
HSS	303–289	0.705–0.706	–1–+2	10–12	0.4–1.7	1–7	9–11
BSS	289–287 ±	0.706	–1–0	12–13	–0.1–2.1	4–18	10–13
CRSS	265–250	0.704–0.705	2–6		2.2–8.0	11–16	
MSS	258–249	0.704–0.706	1–2	8–9	1.9–4.2	3–8	6–9
USS	250	0.705–0.707	0–1	8–10–	–1.3–3.9	–3–16	
'Leuco'	250–233				0.2–3.9	–5–16	

The HSS is the most isotopically evolved Supersuite in the NEB with $^{87}Sr/^{86}Sr_{(i)}$ between 0.705 and 0.710, $\varepsilon Nd_{(i)}$ = ~0, with T_{DM} model ages between 1256 and 938 Ma, homogenous $\varepsilon Hf_{(i)}$ zircon between 1 and 7, and $\delta^{18}O$ between 10 and 12 (Table 10). The BSS includes undeformed monzogranites emplaced between 290 and 285 Ma (Jeon *et al.,* 2012). It is dominated by felsic compositions (72–75 wt% SiO_2) and contains cordierite, biotite, almandine garnet and ilmenite (Shaw and Flood, 1981). Isotopically, the USS is comparable to the HSS, although the USS is slightly less evolved than the HSS, with $^{87}Sr/^{86}Sr_{(i)}$ = ~0.706, $\varepsilon Nd_{(i)}$ = ~0, variable $\varepsilon Hf_{(i)}$ between 4 and 18 and $\delta^{18}O$ between 12 and 13 (Table 10). S-type magmatism in the NEB is defined by $^{87}Sr/^{86}Sr_{(i)} > 0.705$ and $\delta^{18}O > 10$ (O'Neill *et al.,* 1977; Shaw and Flood, 1981; Hensel *et al.,* 1985). These granites are inferred to have formed predominantly from partial melting of weathered Carboniferous volcaniclastic sediments soon after their deposition, and emplaced rapidly in upper crustal levels (Flood and Shaw, 1977; Shaw and Flood, 1981; Hensel *et al.*, 1985; Jeon *et al.*, 2012, 2014; Phillips *et al.* 2011).

I-type magmatism was initiated following almost 30 Ma of extension in the NEO (Bryant *et al.,* 2004; Kemp *et. al.,* 2009; Phillips et al., 2011). The CRSS is characterised by fine-grained granodiorite to tonalities (60–73 wt% SiO_2) that cooled rapidly between 250 and 265 Ma (Hensel *et al.,* 1985; Bryant *et al.,* 1997). The CRSS is distinctly K_2O poor and CaO rich relative to the other supersuites of the NEB (Shaw and Flood, 1981) and has the most depleted mantle-like $^{87}Sr/^{86}Sr_{(i)}$ (0.704–0.705), $\varepsilon Nd_{(i)}$ (2–6) and $\varepsilon Hf_{(i)}$ zircon (11–16) compositions (Table 10). The tectonic setting and primitive isotopic geochemistry indicate partial melting of an amphibolite source and the addition of upper mantle components and rapid emplacement in the upper crust (Hensel *et al.,* 1985; Bryant *et al.,* 1997; Phillips *et al.,* 2011).

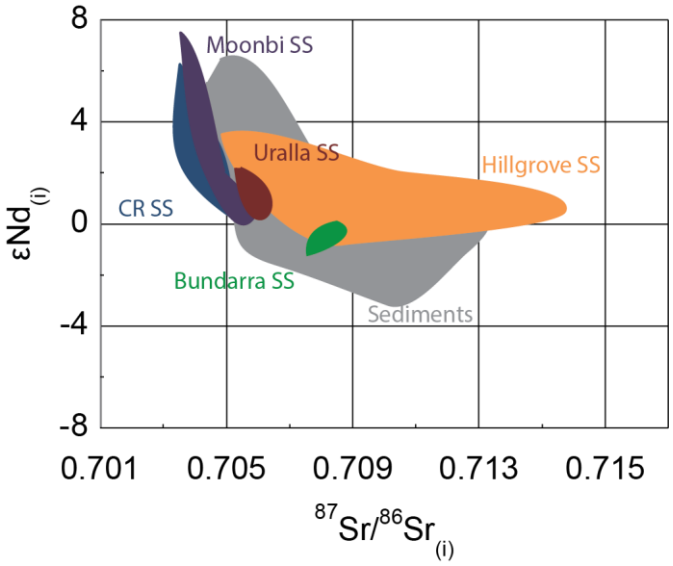

Figure 28: Published $^{87}Sr/^{86}Sr_{(i)}$ and $\varepsilon Nd_{(i)}$ data from granites of the NEB. Initial compositions are calculated from U-Pb ages of the supersuites (see Table 1). The sediments were calculated to 350 Ma. Data sources are in Table 1.

The unfoliated high K-monzonites to leucomonzogranites of the Moonbi Supersuite (MSS) (54–76 wt% SiO_2) were emplaced between 258 and 249 Ma (Belouscova *et al.,* 2006; Shaw and Flood, 2009). The MSS includes a more mafic southern group with higher K, Rb, Th, Ba, Sr and low Y and HREE relative to the northern section. Overall the suite is characterised by high K_2O, Sr, and BaO relative to the other supersuites of the NEB (Shaw and Flood, 1981). Magnetite and high Fe^{3+}/Fe^{2+} indicate an oxidised magma. The homogenous isotopic composition of the MSS ($^{87}Sr/^{86}Sr_{(i)}$ = 0.704–0.706, $\varepsilon Nd_{(i)}$ = 1–2, $\delta^{18}O$ = 6–9, and $\varepsilon Hf_{(i)}$ zircon = 3–8), low ASI, oxidised mineralogy and high K_2O are widely accepted to be characteristics indicating island arc shoshonite or calc-alkaline source rock, potentially a basaltic underplate emplaced during subduction (Shaw and Flood, 1981; Bryant *et al.,* 2004; Phillips *et al.,* 2011).

The Uralla Supersuite (USS) is contemporaneous with the MSS, but it displays significantly more chemical variation (O'Neil *et al.,* 1977; Shaw and Flood, 1981; Bryant *et al.,* 2004). The USS includes monzogranites, granodiorites and tonalities (54–68 wt% SiO_2; Shaw and Flood, 1981). The mafic variants include hornblende–biotite ± clinopyroxene ± orthopyroxene (Shaw and Flood, 1981). Compared to the MSS it contains lower K_2O, P_2O5, Ba, Sr and Nb and for a given SiO_2. The predominance of ilmenite, with occasional magnetite, and transitional to low Fe^{3+}/Fe^{2+} indicates the USS is moderately reduced compared to the HSS and BSS. The $^{87}Sr/^{86}Sr_{(i)}$ varies between 0.705 and 0.707, $\delta^{18}O$ between +7–+10 ‰, and $\delta^{7}Li$ between –1.3 and +3.9 ‰), and more significantly the $\varepsilon Hf_{(i)}$ in zircon between–3 and 16 (Table 10). These data indicate mixing

between a MSS like source and an S-type like source (O'Neill *et al.,* 1977; Shaw and Flood, 1981; Bryant *et al.,* 1997; Landenberger *et al.,* 2000; Shaw and Flood, 2009; Phillips *et al.,* 2011; Jeon *et al.,* 2014).

Emplacement of the MSS and USS occurred in the final stages of the Hunter Bowen crustal thickening event, and continued during widespread extension (Landenberger *et al.,* 1995). The thickened crust negated passage of mantle melts into the upper crust (Phillips *et al.,* 2011). Instead, granite genesis for much of the MSS involved melting of a lower crustal shoshonitic source (O'Neil *et al.,* 1977; Shaw and Flood, 1981; Hensel *et al.,* 1985; Bryant *et al.,* 2007; Phillips *et al.,* 2011; Jeon *et al.,* 2014). With continued extension and activation of asthenosphere piercing faults (Kemp *et al.,* 2005), depleted-mantle melts became an increasing component in granites as evidenced by $\varepsilon Hf_{(i)}$ in zircon of the USS (Shaw and Flood, 2009; Phillips *et al.,* 2011).

The leucomonozogranites of the NEO represent a group of enigmatic plutons characterised by shallow emplacement and predominantly minimum melt compositions. Granites assigned to this group of rocks intruded over a long period (250–230 Ma) and display variable whole-rock $^{87}Sr/^{86}Sr_{(i)}$ and $\delta^{18}O$ and $\varepsilon Hf_{(i)}$ in zircon isotopic compositions (Hensel *et al.,* 1987; Bryant *et al.,* 1997; Phillips *et al.,* 2011). The group includes Early Triassic I-type magmatism,

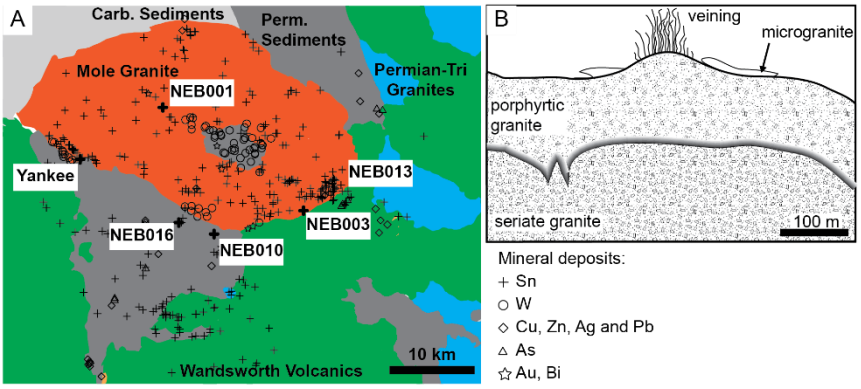

Figure 29: A) Geological map of the Mole Granite and its host rocks. Over 1200 mineral deposits are associated with the granite and show a strong zonation from W dominated within and surrounding the Torrington Pendant, Sn dominant within and proximal to the granite, and base metal dominant in distal deposits. Tourmaline sampled in this study is from a variety of textural settings (see text) from within the Mole Granite and in the surrounding host rocks. B) Cross-section of the Mole Granite showing the relationship between the main textural phases. Figure modified from Audétat et. al., (2000b).

followed by Late Triassic A-type magmatism. Waltenburg *et al.* (2015) introduced the Mole Supersuite (MLSS) to include the I-type granites and suggested chemical affinity with the USS. Granites assigned to the 'leucomonzogranites' group include the Gilgai (251.8 ± 1.7 Ma), Elsemore (250.3 ± 1.8 Ma), Dumboy-Gragir en (252 ± 1.3 Ma) and Mole (249.2 ± 1.5 Ma). The leucomonzogranites are characterised by consistently high SiO_2 (74–77 wt%), high Li, Rb, U, Th and F, large negative Eu/Eu* anomalies and relatively flat REE slopes (Shaw and Flood, 1981; Hensel *et al.*, 1985; Vickery *et al.,* 1997). These leucogranites are notably associated with Sn, Mo, W, Bi, Ag, Au, U and base metal mineralisation (Weber, 1974; Barnes *et al.,* 1988; Blevin and Chappell, 1993; Plimer *et al.,* 1991; Brown and Shroud, 1993). The more mafic granites are I-type and the more felsic units are A-type and have higher Ga/Al, Nd, Y, HREE and F contents compared to the I-type granites. (Landenberger and Collins, 1996). Very few published isotopic data for the leucomonzogranites exists, of which a large range of compositions is evident (Bryant *et al.,* 1997, 2004; Phillips *et al.,* 2011). $^{87}Sr/^{86}Sr_{(i)}$ compositions of this group are particularly problematic to determine due to the extremely elevated Rb/Sr values associated with these granites.

Jeon *et al.* (2012) inferred rapid accretion processes within the New England Orogen. They conclude that as little as 15 Ma was required to progress from sedimentary deposition, burial, and remelting to emplacement of the Bundarra Supersuite. This rapid accretion, and low $^{176}Lu/^{177}Hf$ and $^{147}Sm/^{144}Nd$, has not significantly modified the $\varepsilon Hf_{(i)}$ and $\varepsilon Nd_{(i)}$ composition of the original sediments from the Bundarra Supersuite (Hensel *et al.,* 1985; Bryant *et al.,* 1997; Landenberger, 2000; Phillips *et al.,* 2011; Jeon *et al.,* 2012, 2014; Laker, 2017; this study). Conversely, due to the fractionation of Rb and Sr through melting

and magmatic processes and the shorter half-life of ^{87}Rb as compared with ^{147}Sm and ^{176}Lu, distinguishable variations of $^{87}Sr/^{86}Sr_{(i)}$ are manifested amongst the igneous Supersuites. However, the calculated $^{87}Sr/^{86}Sr_{(i)}$ have large errors owing to age uncertainties propagating into the corrections for *in-situ* Rb decay. Jeon *et al.,* (2012) also showed $\delta^{18}O$ zircon compositions easily distinguish the Carboniferous sediments from the subsequent Bundarra Supersuite.

Mole Granite

The Mole Granite outcrops over an area of 650 km^2. It is, however, estimated to continue to 1 km depth and have a volume of 2000 km^3 (Kleeman, 1982). It has sill like geometry and intrudes Triassic volcanics (Emmaville Volcanics) in the

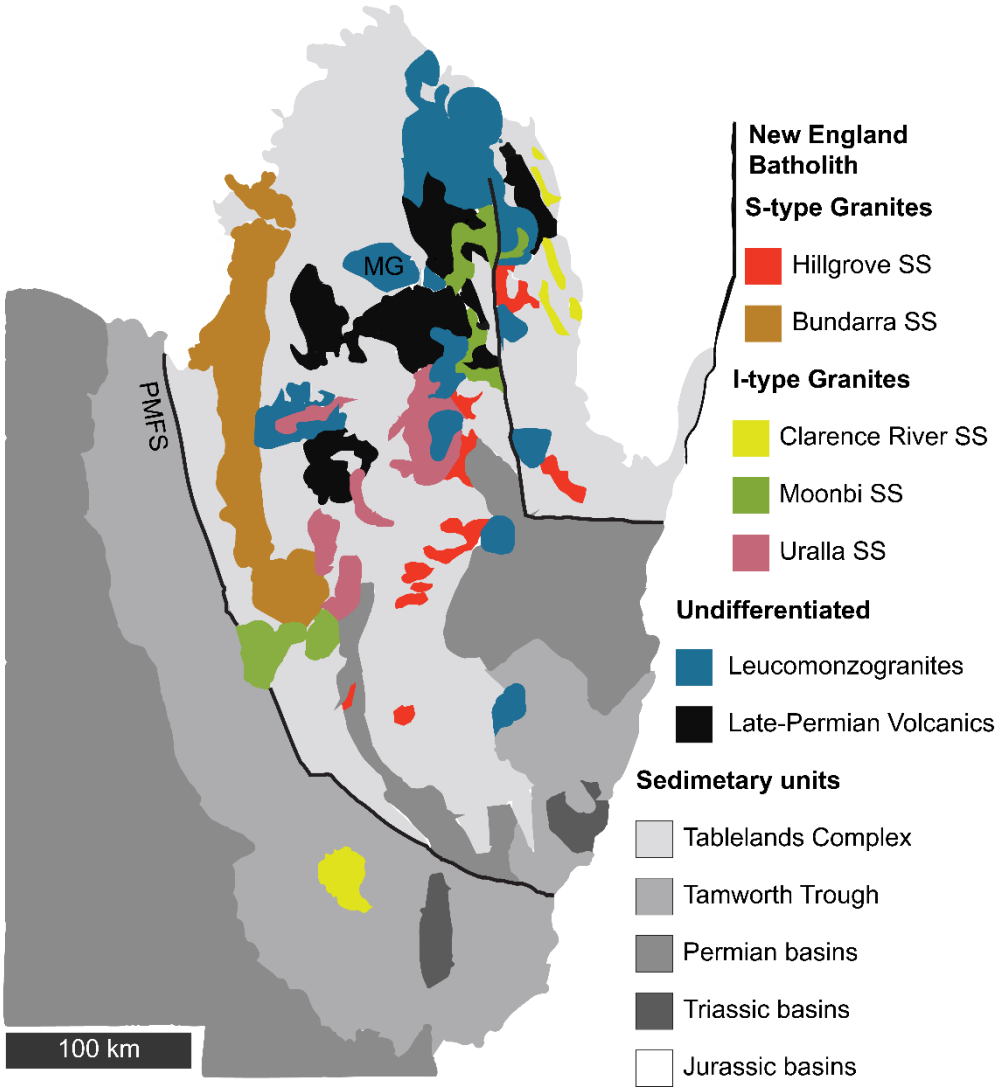

Figure 30: Geological map of the southern New England Orogen of eastern Australia. The Peel-Manning Fault system (PMFS) marks the structural boundary between the west and east sections. The six Supersuites of the New England Batholith are predominantly east of this boundary. The Mole Granite (MG) is a pluton of the leucomonzogranites.

southeast, and Permian sediments (southwest and north) (Figure 29). Drill-hole intersections have identified numerous buried ridges of the Mole Granite along the southern boundary, which are commonly zones of rich mineralisation (Kleeman, 1982; Plimer and Kleeman, 1985). The roof of the granite undulates with the deformed structure of the host rocks (Stegman, 1982). Numerous roof pendants occur within the pluton, although only the metapelitic Torrington roof pendant is large enough to be mapped (Figure 29; Kleeman, 1982; Brown, 2006). Unmapped pendants include I-type granite on the eastern margin and granodiorite enclaves with K-feldspar, euhedral quartz megacrysts and biotite near Butlers Mine (Kleeman *et al.,* 1997).

The Mole Granite is mapped as a single pluton although Brown (2016) noted three variants in airborne radiometric and magnetic data. Similarly, Kleeman (1982) and Kleeman *et al.* (1997) describe three textural variants; 1) porphyritic granite, 2) seriate granite and 3) microgranite (Figure 29). The porphyritic granite is predominant in the upper parts of the pluton and along the contacts. It consists of large poikilitic K-feldspar phenocrysts, plagioclase, quartz and biotite in a groundmass of comparable composition. In places the K-feldspar phenocrysts show albitic overgrowths (Kleeman *et al.,* 1997). Accessory ilmenite, monazite and apatite occur (Kleeman, 1985). Magmatic topaz is absent from the seriate granite, accessory in the porphyritic granite and abundant (several weight %) in the microgranite (Audétat *et al.,* 2000a). The porphyritic granite grades into the seriate texture that constitutes the bulk of the pluton (Figure 29). The microgranite occurs commonly as dykes cutting through the porphyritic granite. In places the dykes are aligned at 060^{o}, following structural joints. Their occurrence is spatially associated with mineralisation within the pluton. The major element composition of the Mole Granite represents the eutectic in the Qz–Ab–Or system at 0.1–0.2 GPa (Laker, 2017). Trace element compositions of the seriate and porphyritic phases are enriched in Rb, Sn, Y, Th and U, and depleted in Sr and Ba (Laker, 2017) relative to the average upper crust (Rudnick and Gao, 2014). The microgranite phase is further enriched in Cu, Rb and U compared to the other textural phases (Laker, 2017).

Mineralisation

Over 1200 mineral deposits are associated with the Mole Granite and occur near ridges within the granite associated with the structural emplacement (Plimer and Kleeman, 1985). Jointing, hydrothermal veins, pegmatites and microgranitic dykes are commonly aligned along 060º (Plimer and Kleeman, 1985). Mineralisation occurs within sheeted veins, pegmatites, silexite (quartz–topaz rock) and large veins.

Figure 31: Pegmatite intruding and brecciating the Torrington Pendant.

The sheeted veins occur only within the metamorphic host rocks on the southern margin of the Mole Granite. The veins are steeply dipping and predominantly strike NE. Veins host quartz with variable cassiterite, arsenopyrite, pyrite, galena, sphalerite, argentian tetrahedrite ($Cu_6[Cu_4(Fe,Zn)_2]Sb_4S_{13}$), silver sulfosalts, tourmaline, topaz, muscovite, calcite and stibnite (Plimer and Kleeman, 1985). Pegmatites intrude the Torrington roof pendant along 060–075º strike and brecciate the metapelite (Figure 31). They are composed primarily of perthite, quartz, muscovite, albite and beryl that have been partially replaced by Li-biotite, topaz, tourmaline, fluorite, muscovite, arsenopyrite, cassiterite and kaolinite (Kleeman, 1985). At the former township site of Bismuth, native bismuth, bismuthinite and Bi-sulfosalts are also present with wolframite, base metal sulfides, Co, Fe, Ni–As, Sb sulfides, uraninite and monazite (Lawrence and Markham, 1963).

Silexite is restricted to the contact zones of the pluton. It forms from alteration of Mole Granite to quartz–topaz and variable wolframite, Li-siderophyllite, F-schorl, F-muscovite, beryl, molybdenite, chalcopyrite, bismuth, bismuthinite and dickite (Plimer *et al.,* 1995). Topaz makes up 20–30 vol. % of the rock (McClatchie, 1981; Creech, 1992). Textures and structures of the microgranite, seriate granite and porphyritic granite are occasionally preserved.

Large veins, several metres wide, occur in the upper zones of the seriate granite, their emplacement controlled by joints, faults, shears and microgranite dykes. These veins contain the richest mineralisation in the Mole Granite system. Quartz, K-feldpsar, sphalerite, chalcopyrite, galena, chlorite, monazite, cassiterite, wolframite and tourmaline occur.

The Wandsworth Volcanics

Late Permian to Early Triassic volcanics outcrop over a large area in the central and eastern blocks of the sNEO (Figure 28). Collectively, the volcanics form the Wandsworth Volcanic Group which includes mafic to felsic units of ignimbrite, rhyolite, andesite, basalt and tuffs (Barnes *et al.,* 1991). These units are predominantly flat lying. Steep dipping units are associated with caldera structures. Barnes *et al.* (1991) defined a broad stratigraphy including 1) basal terrestrial and shallow marine conglomerates, sandstones and mudstone, 2) andesitic to rhyolitic pyroclastic and lava flows with hyperbassal intrusions, 3) dacitic to rhyolitic volcaniclastics, predominantly ignimbrite (including the Emmaville Volcanics and Tent Hill Volcanics), and 4) the crystal rich ignimbrite Dundee Rhyodacite. Surrounding the Mole Granite are the Emmaville Volcanics and Dundee Rhyodacite, estimated to be 3–4 km thick. U–Pb zircon ages imply emplacement of the entire volcanic pile between 265 and 251 Ma (Li *et al.,* 2012; Rosenbaum *et al.,* 2015). Barnes *et al.,* (1991) infer that the Wandsworth Volcanics are the extrusive equivalents of the MSS.

2.3.3 Samples

Whole-rock granite, sediment and tourmaline samples were collected for the measurement of major and trace element concentrations and Rb–Sr and Sm–

Nd isotopic compositions. Quartz concentrates were isolated from these samples for $\delta^{18}O$ determination by SIMS.

Table 11: Whole-rock sample information of units analysed for Rb–Sr and Sm–Nd isotope compositions in this study and major and trace element and zircon U–Pb, $\varepsilon Hf_{(i)}$ $\delta^{18}O$ in Laker (2017).

Sample	Lat;Long	Unit	Granite phase	Deposit
NEB142	–29.234: 151.699	Mole Granite	Seriate	
NEB143	–29.247: 151.691	Mole Granite	Seriate	
NEB171	–29.326: 151.788	Mole Granite	porphyritic	Curnow
NEB173	–29.326: 151.634	Mole Granite	porphyritic	Butlers
NEB174	–29.326: 151.634	Mole Granite	Microgranite	Butlers
NEB175	–29.340: 151.692	Mole Granite	porphyritic	Wallaroo
NEB176	–29.340: 151.692	Mole Granite	Microgranite	Wallaroo
NEB177	–29.226: 151.570	Mole Granite	porphyritic	Burtons
NEB178	–29.469: 151.625	Dundee Rhyodacite		
NEB179	–29.316: 148.236	Emmaville Volcanics		
NEB1711	–29.469: 151.625	Bondonga Beds		

Eight samples of the Mole Granite were collected, representing a range of textures and locations (Figure 32; Table 11). In a parallel study, Laker (2017) analysed the U–Pb, εHf and $\delta^{18}O$ compositions of zircon from these textural phases. Two samples were collected from the volcanic pile emplaced immediately prior and adjacent to the Mole Granite (Emmaville Volcanics and the Dundee Rhyodacite). A single sample of the fine grained, massive meta-mudstone host rock (Bondonga Beds), was also sampled adjacent to the Mole Granite.

Eleven tourmaline samples were collected and grouped based on their texture and host rock (Figure 29; Table 12). Groups are defined as follows; 1) magmatic and magmatic-hydrothermal tourmaline precipitated in quartz-tourmaline nodules during cooling of the Mole Granite; 2) magmatic-hydrothermal tourmaline in pegmatitic quartz vein; 3) hydrothermal tourmaline associated with mineralisation hosted by the Mole Granite;4) hydrothermal tourmaline associated with mineralisation hosted by volcanic country rocks; and 5) hydrothermal tourmaline associated with mineralisation hosted by

*Table 12: Tourmaline samples for major and trace element concentration and Rb-Sr and Sm-Nd isotopic analysis. *Tourmaline is classified into five groups defined by its texture and geological setting. Mineral abbrevations: qtz = quartz; tur = tourmaline; kfs = K-feldspar; bt = biotite; cst = cassiterite; Asp = arsenopyrite.*

Sample	Deposit name	Host rock	Setting	Group*	Metal association
NEB142t		Mole Granite	Qtz–Tur orbicules	1	None
NEB143bt		Mole Granite	Qtz–Tur pegmatitc vein	2	None
NEB170t		Mole Granite	Qtz–Tur orbicules	1	None
NEB006t	Curnow	Mole Granite	Tur–Kfs veins (?)	3	Sn
NEB007t	Gadens Lode	Mole Granite	Qtz–Kfs–Tur–bt veins	**3**	**Sn, W, Cu,** U, As, Mo, REE
NEB008t	Gadens Lode	Mole Granite	Qtz–Kfs–Tur–bt veins	**3**	**Sn, W, Cu,** U, As, Mo, REE
NEB012t	Heisers Lode	Mole Granite	Tur–cst veins	**3**	**U**, Sn, W
NEB014t	McDowells Contact Lode	Mole Granite	Tur–Kfs veins (?)	**3**	**Sn**, Pb, Zn, Ag, Bi, Mo
NEB015t	East Britain Stockworks	Emmaville Volcanics	Qtz–tur veins	**4**	**Sn**, As, Cu, Pb, Zn
NEB016t	McDonalds Lode	Bondonga Beds	Qtz–tur veining	**5**	**Sn**
NEB017t	Taronga	Bondonga Beds	Cst–Asp–tur veining	**5**	**Sn**, Cu, As, Ag, Zn, W, Pb, Mo, Bi

sedimentary country rocks. Tourmaline geochemistry within groups can be highly variable, and groupings are used to compare datasets more generally.

Group 1 tourmaline includes magmatic and magmatic-hydrothermal tourmaline within the porphyritic Mole Granite. Tourmaline occurs with quartz in orbicules approximately 2 cm in diameter (Figure 33A–C). On occasion tourmaline orbicules are surrounded by a biotite depletion halo, indicating competition for Fe in a magmatic environment. Elsewhere orbicules are restricted to fracture surfaces and represent escaping fluids from the crystallising granite. The single sample of Group 2 tourmaline occurs in a pegmatitic vein within the granite with quartz (Figure 33D). Tourmaline aggregates of groups 1 and 2 are euhedral and prismatic. Compositional zoning is faint in BSE and defined by irregular light and dark bands approximately 20 µm thick.

Group 3 tourmaline is hydrothermal, in veins hosted by the Mole Granite and associated with mineralisation (Table 12). Tourmaline does not co-precipitate

with quartz–cassiterite veins, but appears to pre-date mineralisation. Two assemblages are present; 1) high temperature quartz–K-feldspar–tourmaline ± biotite (Figure 34A, B) and 2) lower temperature quartz–tourmaline (Figure 34C). Groups 4 and 5 tourmaline occurs in quartz–tourmaline veins hosted by the Emmaville Volcanics and Bondonga Beds, respectively (Figure 34E, D).

Group 4 tourmaline is associated with a sheeted-vein system (East Britain) above a buried ridge of the Mole Granite. Group 5 tourmaline is associated with multi-staged, tourmalinisation of the Bondonga Beds. Texturally, tourmalinisation occurred prior to and synchronous with quartz–cassiterite veining.

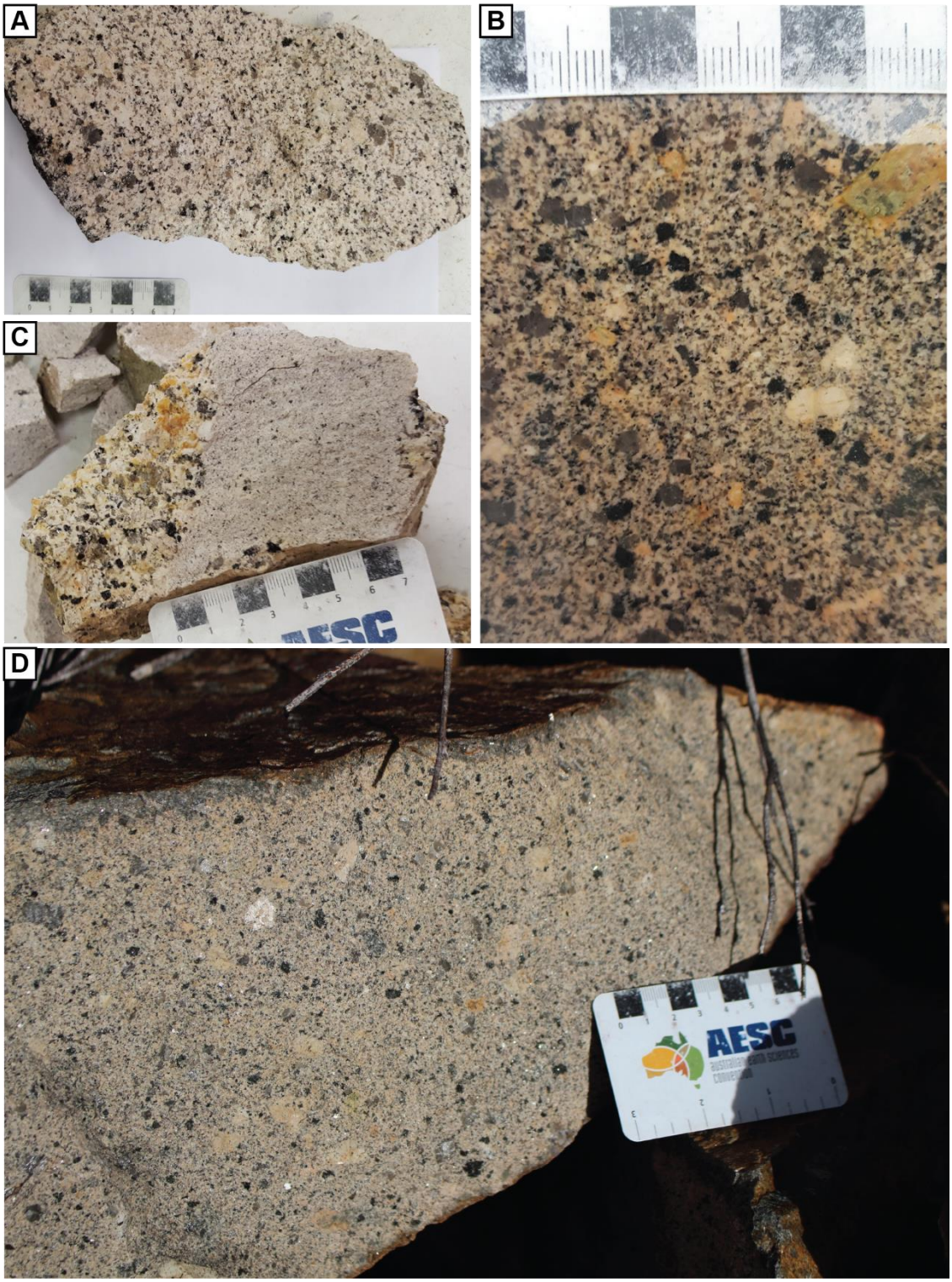

Figure 32: Textural phases of the Mole Granite including the Seriate granite (A–C), porphyritic granite (D) and microgranite (C).

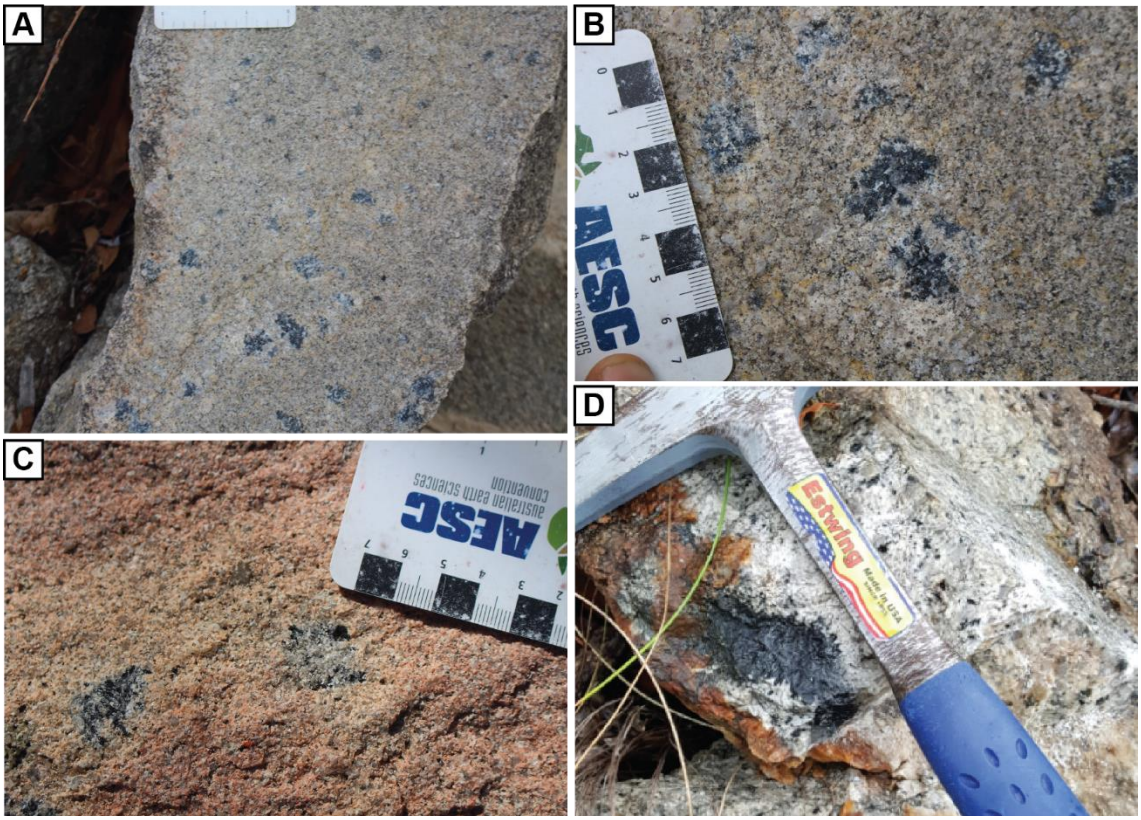

Figure 33: Tourmaline of Group 1 occurs with quartz in nodules approximately ~2 cm in diameter (A–C). Nodules commonly form on flat fracture surfaces and have lighter haloes associated with biotite depletion. In C the grain size increases towards the nodules. Group 2 tourmaline is from a single pegmatitic sample of predominantly quartz (D).

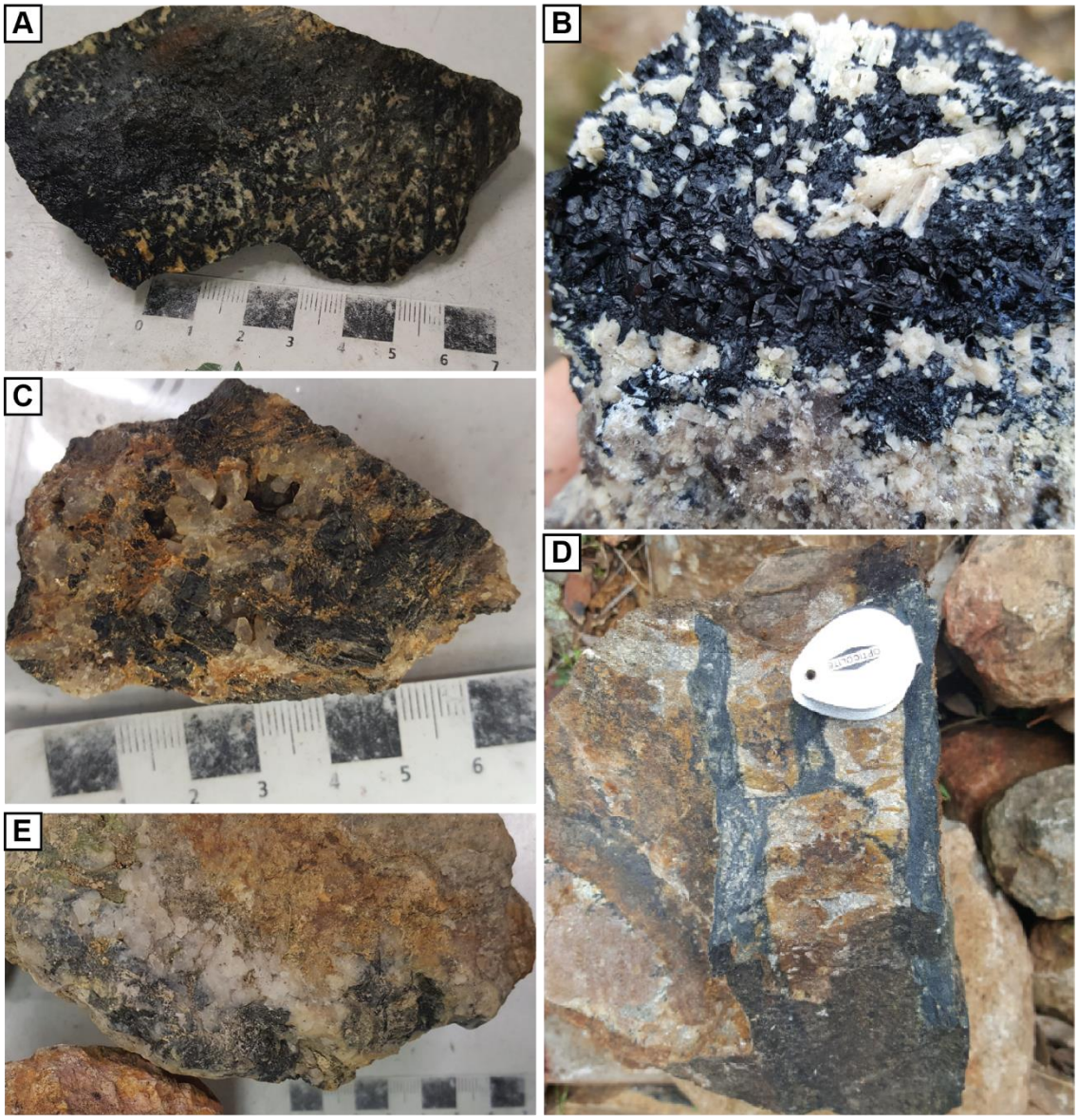

Figure 34: Tourmaline of Group 3 includes two assemblages; 1) quartz–K-feldspar ± biotite (A and B) and quartz–cassiterite (C). Group 4 tourmaline occurs with quartz in a coarse-grained vein hosted within the Emmaville Volcanics (E). Group 5 tourmaline is derived from brittle tourmalinisation of the Bondonga Beds, with associated, but coeval quartz–cassiterite veining.

2.3.4 Results

Whole rock major, minor and trace elements

Elemental concentrations of the Mole Granite, Dundee Rhyodacite, Emmaville Volcanics and the Bondonga Beds were reported in Laker (2017) and summarised here, and representative analyses are presented in Table 13.

The major element composition of the Mole Granite lies on the eutectic in the quartz–orthoclase–albite system water saturated haplogranite melts at 710^{o}C at 0.1 GPa (Figure 35; Tuttle and Bowen, 1954; Johannes *et al.,* 1984). The granite contains between 75.1 and 78 wt% SiO_2; 11.65–15.32 wt% Al_2O_3, 3.42–4.92 wt% Na_2O, and 4.63–5.10 wt% K_2O. The Mole Granite is distinctly A-type according to the classification system of Whalen *et al.*, (1987), including elevated Rb (650 ppm), Zr (167 ppm), Nb (19.5 ppm), Ga (20.1 ppm), Y (151 ppm) and Ce (139 ppm) and low Sr (8.21 ppm) compared to I- and S-type granites. The Mole Granite is also depleted in Ba, Sr, Eu, Ti and P and has flat chondrite-normalised REE compositions interrupted by a distinct negative Eu/Eu* anomalies, relative to the average Phanerozoic Granite (Condie, 1993). The ASI is predominantly peraluminous varying between 1.05 and 1.15. When the porphyritic and microgranite are in contact (Figure 32C), the microgranite phase of the Mole Granite has lower SiO_2, Fe_2O_{3t} (total iron assuming Fe^{3+}), MgO, K_2O, P_2O_5, Sc, Sr, Zr, Ba, and higher Al_2O_3, CaO, Na_2O, Ga, Nb than the porphyritic texture.

The Dundee Rhyodacite and Wandsworth Volcanics are less felsic, with 64.2 and 63.0 wt% SiO_2, 15.8 and 16.1 wt% Al_2O_3, 1.97 and 2.68 wt% MgO, 4.19 and 3.92 wt% CaO, 3.64 and 3.32 wt% Na_2O and 3.43 and 4.00 wt% K_2O, respectively. The volcanics are metaluminous (ASI =~0.93). The trace element budget of the extrusive units is enriched in Sc, V, Sr, Ba and Zr, and depleted in Rb, Nb, Y, Pb, Th, and U relative to the Mole Granite. Both the Dundee Rhyodacite and Wandsworth Volcanics have similar chondrite normalised REE patterns with a negative LREE slope and flat MREE to HREE (Figure 36).

The Bondonga Beds contain 68.1 wt% SiO_2, are strongly peraluminous (ASI = 1.29) and have elevated MgO (1.46 wt%), Fe_2O_{3t} (4.78 wt%), CaO (1.2 wt%), Sr, Ba, and depleted in Rb, Nb, Y, Pb, Th, U relative to the Mole Granite. The

chondrite-normalised REE concentrations are comparable in total abundance and shape to the adjacent volcanic units (Figure 36).

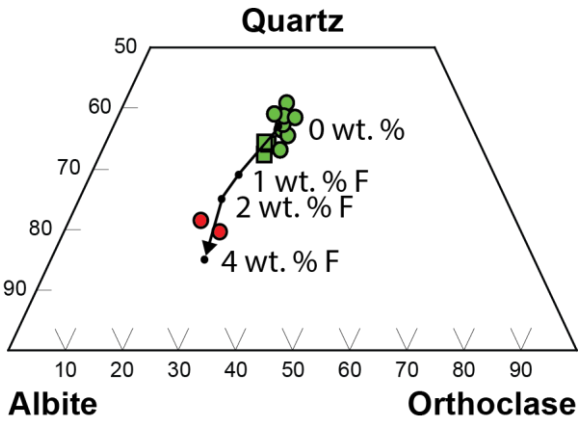

Figure 35: The major element chemistry of the Mole Granite (green) coincides with the eutectic in the quartz–albite–orthoclase system in water saturated melts at 0.1 GPa and 710°C (Tuttle and Bowen, 1954; Johannes et al., 1984). Circles represent the seriate and porphyritic phases and squares the microgranite phase of the Mole Granite. The Dundee Rhydodacite and Wandsworth Volcanics are shown in red for comparison, they are not considered eutectic melts. Incorporation of F into the melt drives the eutectic away from quartz (Manning, 1981).

Table 13: Whole-rock (XRF) and trace element (LA-ICP-MS) concentrations of the representative samples of the Mole Granite, and the host rocks of the Emmaville Volcanics (NEB179) and Bondonga Beds (NEB1711). LOI is the total loss on ignition during glass fusion. ASI is the aluminium saturation index as described in the text. Fe_2O_{3t} represents the total iron assuming 3+ species. Data from Laker (2017).

	NEB 142 Seriate	NEB171 Porphyrtic	NEB172 Microgranite	NEB179 Volcanics	NEB1711 Sediments
Wt%					
SiO_2	77.3	78.0	75.9	63.0	68.1
TiO_2	0.01	0.09	0.02	0.87	0.63
Al_2O_3	12.2	11.8	13.2	16.1	15.0
Fe_2O_{3t}	1.20	1.10	0.45	5.04	4.78
MnO	0.03	0.02	<0.01	0.11	0.07
MgO	0.09	0.10	0.06	2.68	1.46
CaO	0.43	0.16	0.18	3.92	1.20
Na_2O	3.49	3.43	4.39	3.32	3.43
K_2O	4.81	4.68	4.77	4.00	3.51
P_2O_5	0.02	0.01	0.01	0.40	0.14
LOI	0.68	0.70	0.58	0.80	1.26
S%	<0.01	<0.01	<0.01	<0.01	0.05
ASI	1.04	1.08	1.04	0.95	1.29
Total	100.4	100.2	99.5	100.2	99.6

Table 12 continued

ppm	NEB 142	NEB171	NEB172	NEB179	NEB1711
Sc	7.40	9.75	6.71	31.1	22.3
V	<3	<3	<3	124	97.5
Cr	31.5	<1	1.55	102	38.1
Ni	5.63	21.5	9.26	62.9	15.8
Cu	2.5	3.1	4.3	5.3	10.3
Zn	21.9	34.3	20.6	112	92.3
Ga	20.1	19.2	30.5	29.3	22.0
As	BLD	15.7	14.8	4.3	5.9
Rb	659	649	786	229	124
Sr	8.21	7.67	4.14	492	191
Y	151	91.9	76.9	37.5	33.8
Zr	167	122	99.8	281	216
Nb	19.5	19.6	36.1	13.8	9.52
Mo	1.53	<1	<1	<1	<1
Sn	7.0	7.2	5.8	9.3	3.4
Sb	<3	<3	<3	<3	<3
Ba	17.9	29.4	11.5	837	431
La	52.5	76.1	48.7	47.6	32.4
Ce	139	129	126	72.9	57.5
Pr	15.0	18.7	8.64	11.7	7.65
Nd	68.1	73.2	48.8	38.8	29.0
Sm	18.6	16.3	11.5	7.58	6.02
Eu	0.08	0.18	0.14	1.76	1.18
Gd	19.4	12.8	8.9	5.97	5.30
Tb	3.67	2.27	1.73	0.81	0.78
Dy	27.9	16.8	13.5	5.38	5.55
Ho	5.39	3.17	2.71	0.99	1.06
Er	17.1	10.6	9.6	4.29	4.05
Tm	2.65	1.66	1.68	0.597	0.581
Yb	20.5	12.3	13.0	3.61	3.82
Lu	2.91	1.68	1.86	0.42	0.50
Hf	6.46	5.46	7.33	10.1	7.11
Pb	–	30	40	15.1	16.5
Th	43.2	44.5	24.4	27.1	12.8
U	17.2	10.5	57.4	5.73	2.39

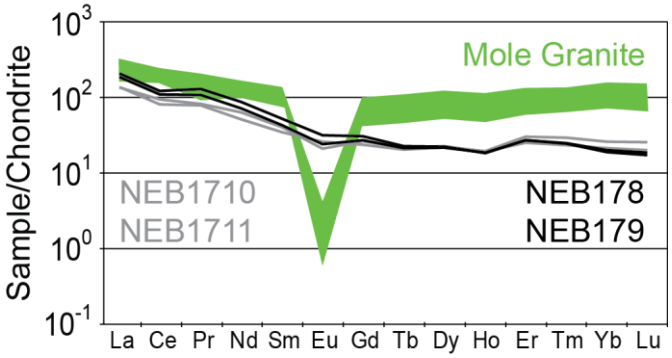

Figure 36: Chondrite-normalised REE of the Mole Granite (green) and its host rocks including the Bondonga Beds (grey; NEB1710, NEB1711) and Emmaville Volcanics (black; NEB178, NEB179). Chondrite values of Sun and McDonough (1995).

Tourmaline major, minor and trace elements

Representative major and minor element compositions of tourmaline are summarised in Table 14 and trace elements in Table 15. Marks *et al.* (2013) reported element fractionation of Ca, Ti, K, REE, Sr and Pb and the REE between the major crystallographic growth sectors (a and c) of tourmaline. By analysing numerous randomly oriented grains, the median values are taken as representative for the sample. The full data records are collated in Appendix 3. Reported totals vary from 87.16 to 90.8 wt% as B_2O_3 was not measured.

Table 14: Representative major element concentrations of tourmaline by EMP. .

Sample No.	NEB142t	NEB143bt	NEB007t	NEB015t	NEB016t
Host Rock	MG	MG	MG	BB	EV
Group	1	2	3	4	5
Wt%					
SiO_2	36.22	36.39	36.58	36.20	36.73
TiO_2	0.64	0.44	0.22	0.54	0.21
Al_2O_3	33.18	31.43	30.82	33.08	33.55
FeO	16.68	17.01	17.31	13.66	11.08
MgO	0.50	1.00	1.19	2.21	4.15
CaO	0.05	0.01	0.02	0.09	0.36
MnO	0.09	0.07	0.07	0.08	0.17
Na_2O	2.32	2.56	2.78	2.30	2.39
K_2O	0.04	0.05	0.05	0.03	0.04
F	0.99	0.82	0.87	0.68	0.95
Total	90.71	89.79	89.91	88.87	89.62

Tourmaline has the generalised chemical formula $XY_3Z_6(T_6O_{18})(BO_3)_3V_3W$ (Hawthorne and Henry, 1999). The primary major element variations within samples from Mole Granite system occur between Fe–Mg on the Y site, Na(+K)–Ca on the X site, and Al with Fe, Mg, Ti on the Z site, are displayed in Figures 37A–C.

Tourmaline from the Mole Granite system is dominantly alkali (Figure 37A), however tourmaline from the Taronga deposit (NEB017t) extends slightly into X vacancy field. Tourmaline is rich in Na relative to Ca and Fe relative to Mg, being of schorl composition (Figure 37B, C).

Groups 1 and 2 tourmalines have moderately high Fe/Mg and Na/Ca compared to the other tourmaline groups (Figure 37). Fluorine (0.05–1.26 wt%) and Li (10.22–527 ppm) are most concentrated in group 1 and 2 tourmaline, whilst relatively depleted in Sn (17.4–398), and Sr (0.3–58.4 ppm). The REE pattern of NEB142t (qtz-tur nodule) and NEB143bt (qtz-tur pegmatite) have positive LREE slopes, strong negative Eu/Eu* anomalies, and flat HREE slopes, that overlap with the Mole Granite whole rock composition. NEB142t shows slight increased LREE enrichment that is more similar to the whole-rock REE concentrations than NEB143bt (Figure 38). The REE concentration of NEB170t is distinct in groups 1 and 2 tourmalines and contains lower REE concentrations overall and lacks a strong negative Eu/Eu* anomaly (Figure 38A).

Group 3 tourmaline is chemically varied and predominantly contains lower Fe/Mg, Na/Ca (Figure 37) and Li (21.71–248 ppm). Kfs-tur veining at Curnow (NEB006t) overlaps with Group 1 tourmaline in all major element diagrams of Figure 37. However, its chondrite-normalised REE pattern is depleted in overall abundances, and has a slight negative HREE slope (Figure 38C). NEB006t is also depleted in all trace elements with the exception of Li. Sn concentrations are variable, though enriched in Group 3, between 20.4 and 1280 ppm. The highest concentrations of Sn occur in high-temperature qtz-kfs-tur ± bt assemblages of NEB008t (Gadens Lode) and NEB014t (McDowells Lode), along with increased Fe/Mg, Ca/Na (+K), LREE, Th, Sr, Nb, As, and V. However, the other high-temperature assemblage sample of Gadens Lode (NEB007t) and low temperature tur-cst veining of Heisers Lode (NEB012t), are

relatively depleted in Sc, Zn, Nb, LREE, Ta, Pb and Th to other Group 3 tourmalines. The chondrite-normalised REE patterns of Group 3 tourmalines are characterised by negative LREE slopes, negative to flat Eu/Eu* anomalies, and positive HREE slopes (Figure 38B, C).

The single tourmaline sample of Group 4, occurring in qtz-tur veins within the Emmaville Volcanics, has high Na/Ca like Group 1 tourmalines, but lower Fe/Mg (Figure 37B and C). It is depleted in F, Li and Cu relative to the other tourmaline groups of the Mole Granite system. The chondrite-normalised REE patterns are similar to those of Group 3, in terms of the overall abundances, slight positive LREE slope and negative HREE slope (Figure 38C). Group 4 tourmaline does not have a distinct Eu/Eu* anomaly.

Group 5 tourmalines, which occurs in two vein samples in the Bondonga Beds, contains the lowest Fe/Mg values from the Mole Granite system (Figure 37B and C). Group 5 tourmalines are depleted in Li, Sc, REE, though elevated in Cu, Zn and Sr relative to the other tourmaline groups of the Mole Granite system. The chondrite-normalised REE patterns are similar in abundance and shape to those of Group 3, however NEB016t of the McDonalds Lode is defined by a conspicuous positive Eu/Eu* anomaly (Figure 38).

Rb–Sr and Sm–Nd isotopic compositions

The Rb–Sr and Sm–Nd isotopic data for tourmaline and whole-rock samples from the Mole System are presented in Table 16. $^{87}Sr/^{86}Sr_{(i)}$ and $\varepsilon Nd_{(i)}$ of tourmaline is calculated to 247 Ma. This represents the closure of the Rb–Sr isotopic system in the Mole Granite (discussed below). Although, the low $^{87}Rb/^{86}Sr$ and $^{147}Sm/^{144}Nd$ of tourmaline means these corrections are minor. Initial isotopic compositions of the whole-rock samples and tourmaline are presented in Figures 39 and 40, respectively.

Table 15: Representative trace element analyses of tourmaline by LA-ICP-MS. dl = detection limit, bdl = below detection limit.

Sample No.		NEB142	NEB143b	NEB007	NEB015	NEB016
Host Rock		MG	MG	MG	BB	EV
Group		1	2	3	4	5
ppm (isotope)	*dl (ppm)*					
Li (7)	0.35	100	169	53	12	19
Sc (45)	0.07	66	233	24	125	14
V (51)	0.03	4.5	43.2	24.5	44.2	63.8
Mn (55)	0.46	650	570	570	775	90
Co (59)	0.01	7.3	6.3	0.9	0.5	0.6
Cu (63)	0.07	0.5	3.2	8.8	3.2	2.5
Zn (66)	0.26	186	162	90	128	225
Ga (69)	0.05	9	147	17	54	70
As (75)	1.29	3.3	2.4	2.2	3.3	5.3
Rb (85)	0.04	0.8	1.2	0.7	0.1	0.2
Sr (88)	0.004	2.2	24.6	15.2	12.2	385.7
Y (89)	0.003	0.4	0.3	0.4	0.4	0.4
Zr (90)	0.008	0.3	1.4	1.0	0.77	0.3
Nb (93)	0.001	1.6	6.5	1.1	5.2	0.1
Mo (95)	0.05	bdl	0.3	0.2	bdl	0.1
In (115)	0.01	0.6	3.7	2.6	3.8	3.7
Sn (119)	0.17	52	154	145	367	146
La (139)	0.002	0.7	0.9	0.7	8.3	2.2
Ce (140)	0.003	4.7	0.2	1.3	17.4	3.8
Pr (141)	0.002	0.4	0.2	0.1	1.6	0.4
Nd (146)	0.009	1.3	0.8	0.4	4.1	1.0
Sm (147)	0.01	0.2	0.2	0.7	0.6	0.7
Eu (153)	0.003	0.4	0.5	0.2	0.3	0.6
Gd (157)	0.01	0.2	0.3	0.3	0.3	0.3
Tb (159)	0.002	0.2	0.6	1.0	0.3	0.2
Dy (163)	0.006	0.2	0.4	0.7	1.0	0.9
Ho (165)	0.001	0.3	0.8	0.1	0.3	0.3
Er (166)	0.004	0.6	0.4	0.3	0.5	0.4
Tm (169)	0.001	0.9	0.7	0.5	0.7	0.9
Yb (172)	0.006	0.3	0.6	0.6	0.8	0.2
Lu (175)	0.001	0.5	0.1	0.2	0.3	0.9
Hf (178)	0.008	0.1	0.2	0.9	0.4	0.3
Ta (181)	0.002	1.1	3.2	0.3	17.4	bdl
W (182)	0.004	0.5	1.6	0.8	1.2	0.3
Pb (208)	0.01	1.3	16.4	3.1	19.8	11.2
Bi (209)	0.01	0.2	0.5	0.2	2.9	0.7
Th (232)	0.004	0.3	0.9	0.3	0.1	0.3
U (238)	0.003	0.5	0.7	0.8	0.3	0.8

$^{147}Sm/^{144}Nd$ of all tourmaline is low (0.07–0.13). The measured $^{143}Nd/^{144}Nd$ rages between 0.51225 and 0.512617, or $\varepsilon Nd_{(0)}$ between –7.51 and –0.40. Calculated $\varepsilon Nd_{(i)}$ of all tourmalines varies between –5.27 and +2.32. All tourmaline samples, except NEB017t, have $\varepsilon Nd_{(i)}$ between 1.12 and 2.32, that is within the range of the Mole Granite whole-rock samples (1.25–5.27). No Nd isotopic data were obtained from NEB143bt (Group 2) due to its very low Nd concentration. NEB017t, hosted within the Bondonga Beds, has the least radiogenic $\varepsilon Nd_{(i)}$ composition of –5.27.

All tourmaline samples, with the exception of NEB017t, define a $^{147}Sm/^{144}Nd$ and measured $^{143}Nd/^{144}Nd$ isochron with an apparent age of 237 ± 110 Ma and projected initial composition of $^{143}Nd/^{144}Nd_{(i)} = 0.512417$ or $\varepsilon Nd_{(i)} = -4.31$ (Figure 41A). The large error associated with this age estimation is attributed primarily to the low and small spread in $^{147}Sm/^{144}Nd$. Including the whole-rock data from the Mole Granite increases the spread in $^{147}Sm/^{144}Nd$ and the isochron age is improved to 243 ± 59 Ma with an initial composition of 0.512421 or εNd of –4.23 (Figure 41B). These isochron data indicate that tourmaline (except NEB017t) originate from a isotopically similar $^{143}Nd/^{144}Nd_{(i)}$ source as the Mole Granite, and only differ by their $^{147}Sm/^{144}Nd$.

$^{87}Rb/^{86}Sr$ of the tourmalines are also low overall (<0.69) compared to the Mole Granite whole-rock analyses (90–300). Groups 1 and 2 tourmalines contain the highest values relative to the other groups. The measured $^{87}Sr/^{86}Sr$ compositions of tourmaline are variable between 0.70547–0.71298. The low $^{87}Rb/^{86}Sr$ means that most age corrections are minor and calculated $^{87}Sr/^{86}Sr_{(i)}$ varies between 0.70547 – 0.71064. The largest age correction was applied to sample NEB142t with an $^{87}Rb/^{86}Sr$ of 0.691 that changed the $^{87}Sr/^{86}Sr_{(m)}$ of 0.71298 to a $^{87}Sr/^{86}Sr_{(i)}$ of 0.71064. The most radiogenic $^{87}Sr/^{86}Sr_{(i)}$ compositions occur in Group 1 (0.71064 and 0.70997), whilst Group 2 (0.70786) is similar with Group 3 (0.70632–0.70843), Group 4 (0.70703) and Group 5 (0.70547–0.70869). Isochron relationships between tourmaline samples are not present due to the low and relatively invariant $^{87}Rb/^{86}Sr$.

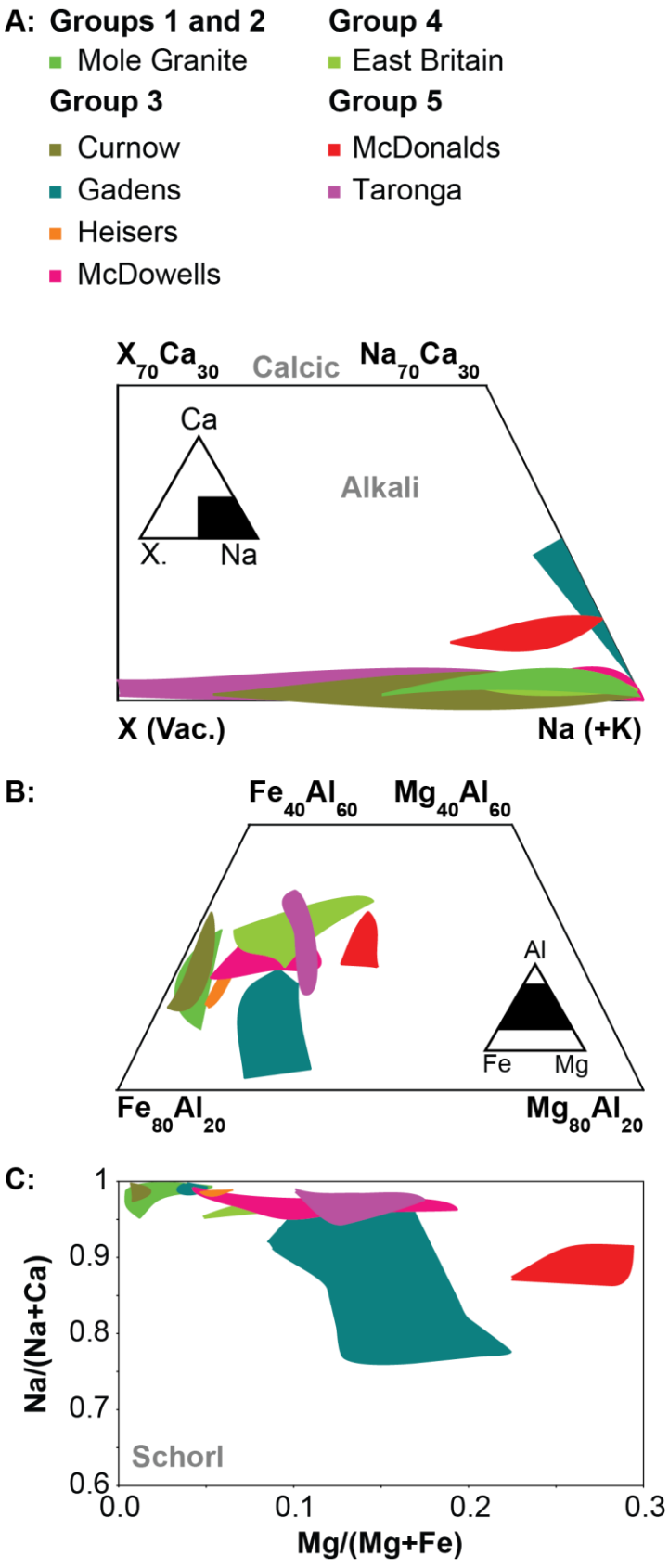

Figure 37: Major element compositions of tourmaline by EMP. The major chemical substitutions are shown for the X site (A) and Y site (B). These variations are combined in C.

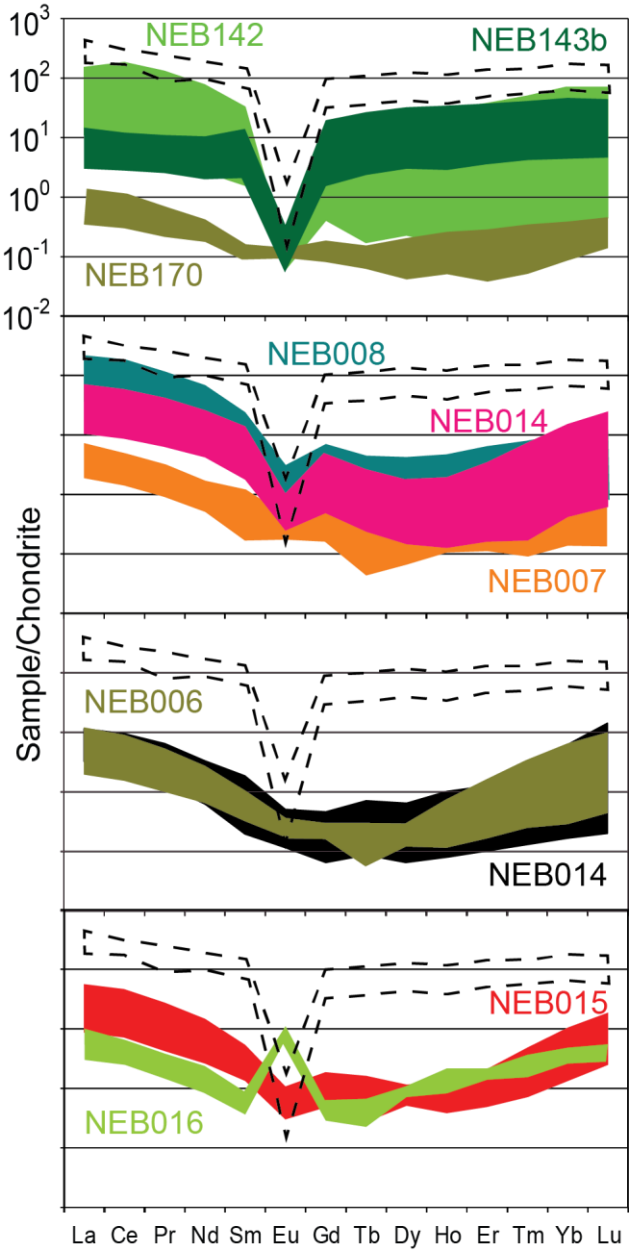

Figure 38: Chondrite-normalised REE of tourmaline. The dashed line represents the whole-rock variation in the Mole Granite.

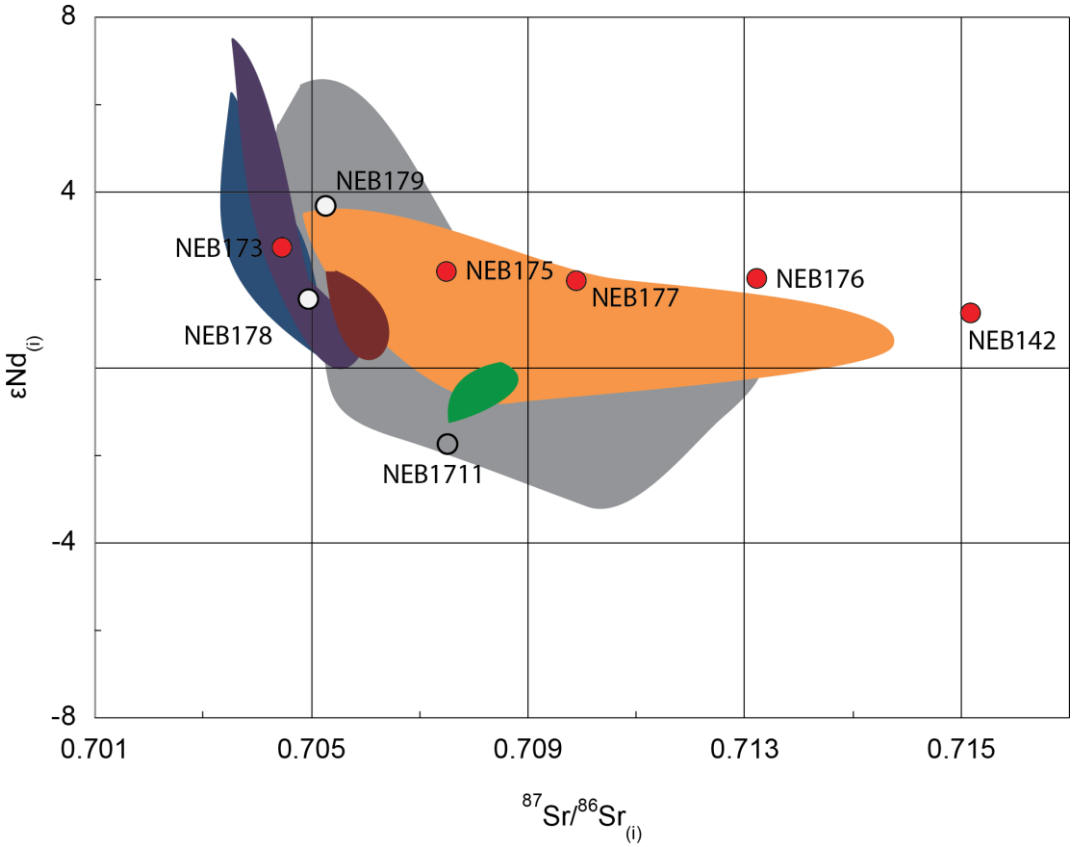

Figure 39: $^{87}Sr/^{86}Sr_{(i)}$ and $\varepsilon Nd_{(i)}$ of whole-rock analyses in this study. Granite samples are in red, volcanics in white and sediments in grey. The shaded fields for the NEB and sediments (defined in Figure 29) are calculated to 250 Ma.

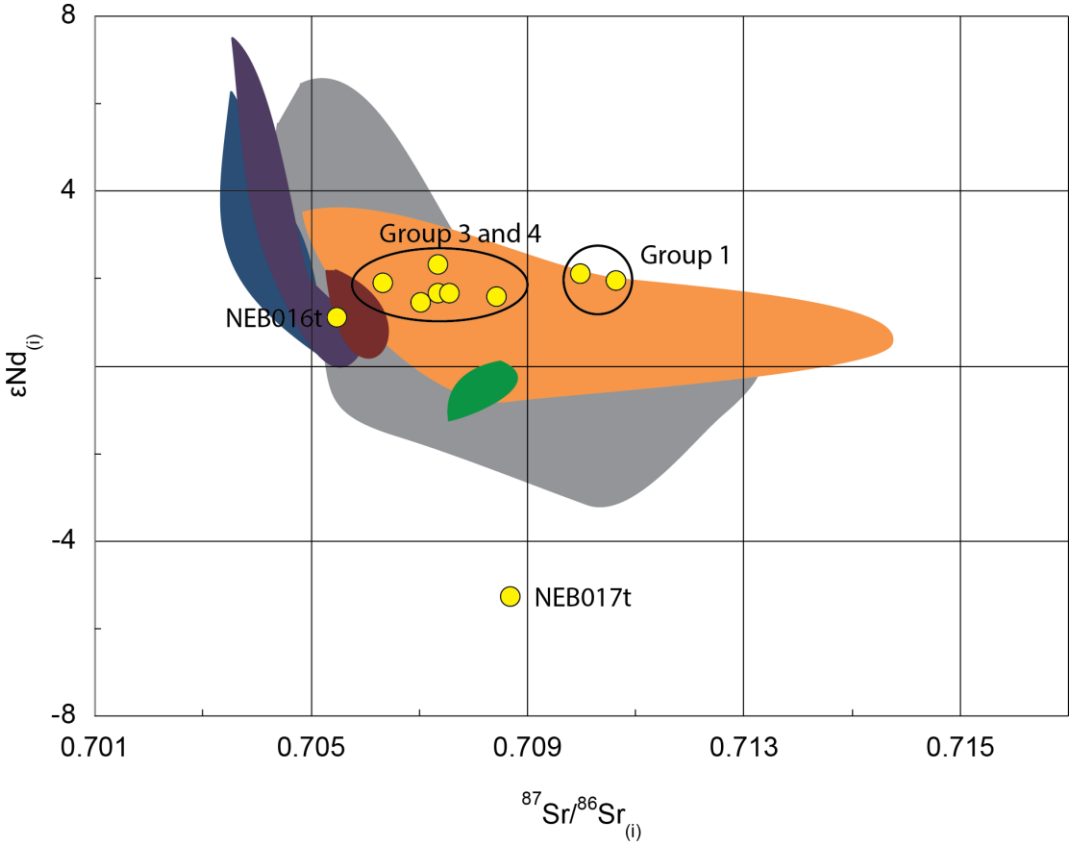

Figure 40: $^{87}Sr/^{86}Sr_{(i)}$ and $\varepsilon Nd_{(i)}$ of tourmaline (yellow circles) in this study. The shaded fields represent regional geological units of the NEO as shown in Figure 29.

The whole-rock Mole Granite composition shows highly variable and elevated $^{87}Rb/^{86}Sr$ (90–299), requiring large age corrections to calculate the initial $^{87}Sr/^{86}Sr$ composition. A whole-rock Rb–Sr isochron of the granitic textural phases in this study indicates an $^{87}Sr/^{86}Sr_{(i)}$ composition of 0.711 ± 0.013 with an MSWD of 1.8 (Figure 42). Incorporation of whole-rock data from the Mole Granite of Kleeman *et al.* (1997), however, yields a more precise estimation of $^{87}Sr/^{86}Sr_{(i)}$ to 0.7085 ± 0.0059 with an MSWD of 0.80 (Figure 42B). Including fluorite data of Kleeman *et al.* (1997) from within the Mole Granite, with Rb/Sr <1, this estimate is improved to 0.70650 ± 0.00024 with an MSWD of 0.73 (Figure 42). The $^{87}Sr/^{86}Sr_{(i)}$ isochron intercept from only whole-rock data of this study is within error of Group 1 tourmaline. The $^{87}Sr/^{86}Sr_{(i)}$ derived from the whole-rock isochron that includes the whole-rock and fluorite data of Kleeman *et al.,* (1997) is significantly less radiogenic than Group 1 tourmaline (0.71064 and 0.70997). If the latter isochron intercept ($^{87}Sr/^{86}Sr_{(i)}$ = 0.70650 ± 0.00024) is used, it indicates that Group 1 tourmaline, occurring as qtz-tur nodules within the Mole Granite, are not in equilibrium with the whole-rock Mole Granite composition. The implications of this are considered in the discussion.

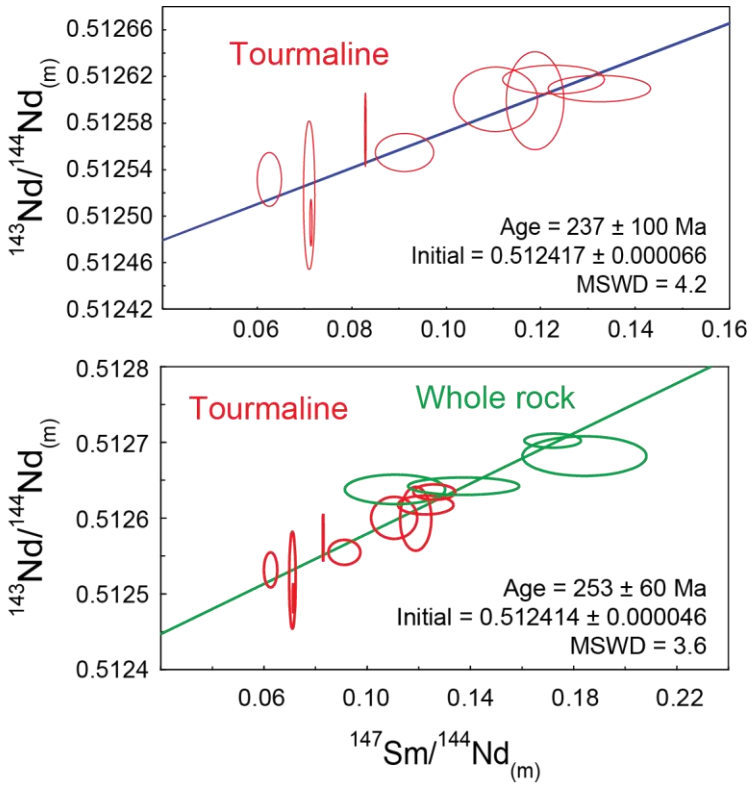

Figure 41: Sm–Nd isochron data for tourmaline (A) and tourmaline and the Mole Granite whole rock.

The Dundee Rhyodacite and Wandsworth Volcanics (NEB178, 179) have $^{87}Rb/^{86}Sr$ between 1 and 2. $^{87}Sr/^{86}Sr_{(i)}$ compositions were calculated using the U–Pb zircon ages of 254 Ma for the Dundee Rhyodacite (U–Pb TIMS; Brownlow and Cross, 2010) and although are not within error (0.70501 ± 0.00001 and 0.70519 ± 0.00001, respectively), are both less radiogenic than the Mole Granite. The Bondonga Beds have low $^{87}Rb/^{86}Sr$ (2), moderate $^{87}Sr/^{86}Sr_{(i)}$ (0.70751; calculated to 250 Ma) and evolved $\varepsilon Nd_{(i)}$ (–1.75). These data are within the previously reported range (Hensel *et al.,* 1985).

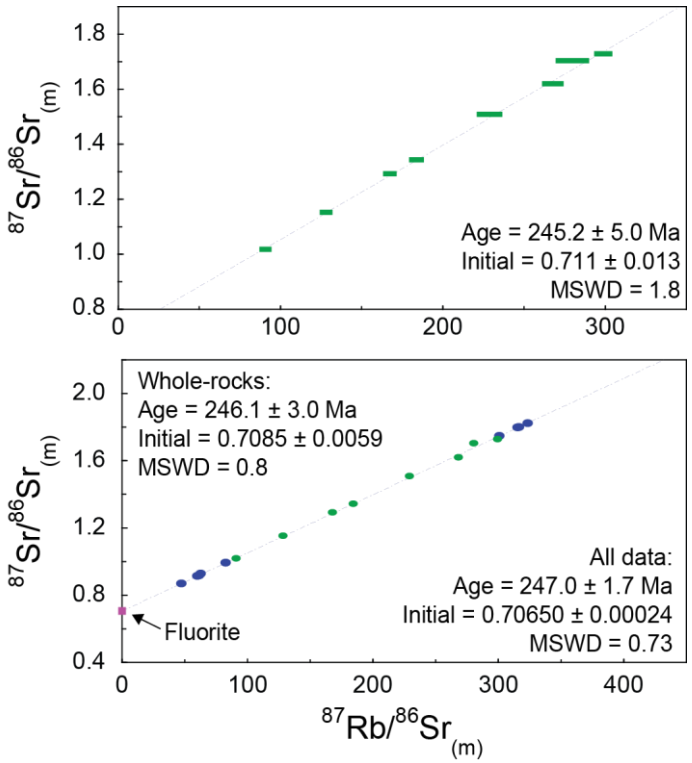

Figure 42: Rb–Sr isochron data for the Mole Granite whole-rock data of this study (top), including the whole-rock (blue) and fluorite (purple) data of Kleeman et al. (1995)(bottom).

Table 16: Rb–Sr and Sm–Nd isotope data for tourmaline and whole-rock analyses from the Mole Granite. Initial tourmaline ratios were calculated to 245 Ma (See text for explanation) using decay constants $^{87}Rb = 1.3972x10^{-11}a^{-1}$ and $^{147}Sm = 6.54x10^{-11}a^{-1}$. $\varepsilon Nd = \left(\frac{^{144}Nd/^{143}Nd_{(S)}}{^{144}Nd/^{143}Nd_{(CHUR)}} - 1\right) \times 10^4$ where $^{143}Nd/^{144}Nd_{CHUR} = 0.512638$ and $^{147}Sm/^{144}Nd_{CHUR} = 0.1967$.

Sample	Rb	Sr	$^{87}Rb/^{86}Sr$	$^{87}Sr/^{86}Sr_{(0)}$	2SE	$^{87}Sr/^{86}Sr_{(T)}$	Nd	Sm	$^{147}Sm/^{144}Nd$	$^{143}Nd/^{144}Nd_{(0)}$	2 SE	$\varepsilon Nd_{(0)}$	$\varepsilon Nd_{(T)}$	T_{CHUR}	T_{DM}
Tourmaline	(ppm)	(ppm)	(moles)				(ppm)	(ppm)	(moles)					(Ga)	(Ga)
NEB006t	0.094	9.13	0.030	0.70853	0.00001	0.70843	0.74	0.09	0.07	0.51252	0.000026	–2.34	1.59	0.146	0.676
NEB007t	0.006	31.84	0.001	0.70735	0.00001	0.70735	2.00	0.39	0.12	0.51260	0.000017	–0.76	1.68	0.076	0.886
NEB008t	0.020	53.44	0.001	0.70755	0.00002	0.70755	17.11		0.09	0.51255	0.000007	–1.62	1.68	0.121	0.742
NEB012t	0.045	15.78	0.008	0.70736	0.00001	0.70733	0.49	0.07	0.08	0.51257	0.000013	–1.24	2.32	0.086	0.672
NEB014t	0.093	14.66	0.018	0.70638	0.00001	0.70632	26.66	5.42	0.12	0.51262	0.000005	–0.40	1.91	0.043	0.893
NEB015t	0.154	30.95	0.001	0.70703	0.00001	0.70703	127.78	28.04	0.13	0.51261	0.000005	–0.56	1.45	0.068	1.015
NEB016tt	0.002	151.46	0.000	0.70547	0.00001	0.70547	0.41	0.05	0.07	0.51249	0.000008	–2.80	1.12	0.175	0.704
NEB017t	0.020	66.06	0.001	0.70869	0.00001	0.70869	6.05	1.25	0.12	0.51225	0.000010	–7.51	–5.27	0.818	1.538
NEB142t	3.889	16.28	0.691	0.71298	0.00001	0.71064	4.35	0.80	0.11	0.51260	0.000011	–0.73	1.97	0.067	0.813
NEB143bt	0.452	50.32	0.026	0.70795	0.00001	0.70786	0.14	0.01	0.00						
NEB170t	0.529	3.99	0.384	0.71127	0.00001	0.70997	6.19	0.64	0.06	0.51253	0.000009	–2.08	2.12	0.121	0.625
Whole Rock															
NEB142	672.2	8.49	229.187	1.50877	0.00002	0.72986	55.14	16.82	0.18	0.51268	0.000011	0.86	1.25	–0.537	2.414
NEB143	752.1	7.76	280.480	1.70423	0.00002	0.75487									
NEB171	732.0	7.89	268.263	1.62000	0.00002	0.69492	74.58	16.26	0.13	0.51265	0.000006	0.20	2.27	–0.024	0.933
NEB173	538.6	17.13	90.976	1.01869	0.00003	0.71088	61.57	11.30	0.11	0.51264	0.000008	0.00	2.69	0.000	0.760
NEB174	573.8	5.54	299.438	1.72825	0.00002	0.70436	104.85	10.30	0.06	0.51269	0.000005	0.93	5.27	–0.053	0.460
NEB175	560.9	8.81	184.306	1.34407	0.00002	0.73096	64.79	13.53	0.13	0.51263	0.000004	–0.07	2.10	0.008	0.898
NEB176	536.2	9.25	167.748	1.29262	0.00002	0.72020	52.42	14.93	0.17	0.51270	0.000004	1.25	2.04	–0.397	1.633
NEB177	534.5	12.05	128.370	1.15328	0.00001	0.71878	97.80	22.27	0.14	0.51264	0.000005	0.08	1.94	–0.011	1.016
NEB178	107.2	246.66	1.258	0.70943	0.00001	0.70501	27.55	5.65	0.12	0.51260	0.000007	–0.83	1.53	0.089	0.941
NEB179	124.4	184.18	1.955	0.71205	0.00001	0.70519	48.41	6.89	0.09	0.51264	0.000006	0.13	3.72	–0.009	0.604
NEB1711	68.8	95.50	2.085	0.71471	0.00001	0.70751	27.50	7.32	0.16	0.51249	0.000004	–2.90	–1.75	0.628	1.894

Quartz $\delta^{18}O$

Average compositions and the total range of $\delta^{18}O$ values for quartz in the igneous units and within deposits surrounding the Mole Granite are presented in Table 17. Table 17 includes the range of quartz $\delta^{18}O$. The complete dataset are compiled in Appendix 4. $\delta^{18}O$ compositions of a co-existing fluid with the quartz were calculated using Equation 4. Feteke *et al.* (2016) show fluid inclusion temperatures within a single quartz grain of the Yankee Lode vary from 500–220^{o}C, which has dramatic effects on the calculated fluid composition (Equation 4). They described six generations of fluids based on CL imaging, fluid inclusion temperature estimates and the $\delta^{18}O$ composition of quartz. The first three generations record the slow cooling of a magmatic fluid from 500–413^{o}C with a corresponding decrease of $\delta^{18}O_{fluid}$ from +10.1 to +6.1. Quartz generations 4 and 5 (Q3b and Q4 in Feteke *et al.,* 2016) mark the incursion of lighter meteoric waters associated cooling and a dramatic decrease in $\delta^{18}O_{fluid}$ from +5.8 to –15.4. Our study does not have the same constraints on temperature of quartz precipitation as Feteke *et al.* (2016). Therefore, calculated $\delta^{18}O_{fluid}$ are more poorly constrained. Regardless, the $\delta^{18}O$ composition of quartz presented here will be discussed later within the framework of Sun and Eadington (1987) and Feteke *et al.* (2016).

Magmatic quartz from within the Mole Granite displayed little heterogeneity in $\delta^{18}O$ and a weighted average of +11.00 ± 0.07‰ (1SD). This value agrees with magmatic quartz data of Sun and Eadington (1987) and Feteke *et al.* (2016). The $\delta^{18}O$ compositions of zircon within the Mole Granite are between +7.8 and +8.3 (Laker 2017) that is comparable with the bulk rock value of ~+10.5 ‰ after correcting for high SiO_2 (Lackey *et al.,* 2008). Bulk magmatic quartz concentrates based on fluorination data of Sun and Eadington (1987) from Wallaroo (+9.8 ‰), Dutchman's (+10.3 ‰) and Elliot's (+10.4 ‰) are also similar in composition to magmatic quartz measured here.

Quartz pegmatite veins of the Torrington Pendant (NEB002), and hydrothermal quartz veins from Gadens Lode (NEB008,009), McDowells Contact Lode (NEB014), East Britain Stockworks (NEB015) and McDonalds Lode (NEB016) contain have restricted quartz $\delta^{18}O$ compositions (Table 17) with a combined

weighted mean average of 11.73 ± 0.19 (1SD). Fluid compositions for the samples were calculated using a single temperature of 400°C (Sun and Eadington 1987) and vary between 7.77 and 9.15 ‰. These elevated compositions are similar to predicted magmatic and early, fluid compositions (Sun and Eadington, 1987; Feteke *et al.,* 2016; this study) and indicate precipitation of these quartz samples prior to incursion of meteoric water and significant temperature loss.

Table 17: Combined SIMS quartz $\delta^{18}O$ compositions from the Mole Granite. For samples with homogenous $\delta^{18}O$ compositions the average of all in-situ analyses is presented. The composition of a fluid coexisting with quartz were calculated using the fractionation factor of Pollington et al. (2016). As discussed in text, the temperature constraints on quartz precipitation are poor, but are considered 400°C. For quartz with large heterogeneity in $\delta^{18}O$, only the range of in-situ analyses are shown.

Sample	Group	Av. $\delta^{18}O$ (‰)	2 SE	Av. $\delta^{18}O$ (‰) water
NEB142	1	10.27	0.78	7.77
NEB143b	2	11.31	0.25	8.33
NEB170	1	11.25	0.12	8.48
NEB008	3	11.62	0.14	8.83
NEB014	3	11.8	0.35	9.07
NEB015	4	11.94	0.18	9.15
NEB016	5	11.41	0.55	8.63
		Range (‰)		
NEB001	3	–7.08–+10.92		
NEB003	3	–2.14–+11.20		
NEB007	3	–11.40–2.06		
NEB011	3	–5.71– –0.32		
NEB013	3	–7.84–+4.34		

Quartz–cassiterite veining at Burtons Prospect (NEB001), Wallaroo (NEB003), Gadens Lode (NEB007), Smiths Lode (NEB011) and Curnow (NEB013) has measured quartz $\delta^{18}O$ values between –11.40 and +11.20. Similarly, Feteke *et al.,* (2016) reported $\delta^{18}O$ variations in a single quartz crystal of the Yankee deposit between –4.6 and +12.90. Quartz-cassiterite vein precipitation occurred in the Yankee deposit with the incursion of light meteoric waters and temperature drop from 478 to 390°C (Feteke *et al.,* 2016). $\delta^{18}O_{fluid}$ compositions cannot be derived from these quartz samples of this study because the temperature constraints are poor.

Table 18: Whole-rock laser fluorination $\delta^{18}O$ compositions of major units determined by GNS.

Geological Unit	**Sample #**	**$\delta^{18}O$ (‰)**
Dundee Rhyodacite	NEB178	7.2
Emmaville Volcanics	NEB179	1.0
Bondonga Beds (pendant)	NEB1710	9.7
Bondonga Beds	NEB1711	10.2
Mole Granite	NEB146	6.5

2.3.5 Discussion

The origin and evolution of the Mole Granite

Source characterisation

Within the NEB, the Mole Granite is transitional between an I-type and an S-type granite in respect to whole-rock $\varepsilon Nd_{(i)}$, $\delta^{18}O$ and $^{87}Sr/^{86}Sr_{(i)}$ (this study) and $\varepsilon Hf_{(i)}$ zircon compositions (Laker, 2017). Similarly, the Gilgai Granite, part of the Mole SS, has variable $\delta^{7}Li$ that falls between compositions of the MSS, and S-type granites of the NEB (Bryant *et al.,* 2004). Although emplacement of the Mole Granite was contemporaneous with the MSS and USS, the elevated $^{87}Sr/^{86}Sr_{(i)}$ (0.70650) and $\delta^{18}O$ (10.5‰) are only comparable with the USS ($^{87}Sr/^{86}Sr_{(i)}$ between 0.705 and 0.707, and $\delta^{18}O$ between +8–+10).

The major and trace element compositions of the USS and Mole SS from the CHAPGRAN database (Bryant and Blevin, 2017) are compared in Figures 43–46. The MSS and the Wandsworth Volcanics are included for comparison. Major element variation diagrams for the USS, MSS and Wandsworth Volcanics display linear relations for all major elements towards the Mole SS at high SiO_2 (Figure 43). In the mafic endmembers, the USS is distinguished from the MSS by lower K_2O (Figure 43C), P_2O_5 (Figure 43D), Sr and Ba (Figure 44A and C), and Th (Figure 44D) but higher Y (Figure 44B) and more distinct negative Eu/Eu* anomalies (Figure 45; Shaw and Flood, 1981). Figure 46A and B show the geochemical evolution of these supersuites through incompatible/compatible element ratios. The MSS, USS and the Wandsworth Volcanics show parallel Rb/Sr trends with increasing SiO_2, and the Mole SS is significantly higher (Figure 46A). The MSS has slightly lower K/Rb than the USS and Wandsworth Volcanics for the range in SiO_2, due to its K-rich source (Shaw and Flood, 1981; Bryant *et al.,* 2004; Phillips *et al.,* 2011), however, the K/Rb is lower again for the Mole Supersuite (Figure 46B). The chondrite-normalised REE patterns of the MSS, USS and Wandsworth Volcanics and the Bondonga Beds are also largely remarkably similar in overall abundance and shape, yet distinct from the REE concentrations of the Mole Granite (Figure 36). The geochemical trends in Figures 43, 44 and 46 indicate the Wandsworth Volcanics, like the Mole SS, have a closer geochemically affinity with the USS than the MSS as suggested by Barnes *et al.* (1991). The Mole SS, however, is significantly more evolved than both the USS and MSS.

The intermediate $^{87}Sr/^{86}Sr_{(i)}$ and εNd(i) isotopic composition of the Mole Granite and USS, and the Wandsworth Volcanics by inference, between I- and S-type rocks of the NEB could result from either:

1) Partial melting of young volcaniclastic metasediments.
2) Melting of an I-type source rock and magma assimilation of pelitic materials during ascent and emplacement.
3) Partial melting of an interface region that includes both I-type and S-type components.

Partial melting of young volcaniclastic metasediments would yield higher $\delta^{18}O$ values than demonstrated in the USS (+8–+10 ‰) and Mole Granite (+10.5 ‰) as Jeon *et al.,* (2012) show that the BSS originates from partially melted volcaniclastic sediments and generated magmas with a $\delta^{18}O$ of +11.5 ‰.

It is unclear whether the parental magmas of the USS and Mole SS were produced by sedimentary assimilation or melting of a mixed I-type and S-type region. Shaw and Flood (1981) favoured the latter as it would be unusual if only the USS (and Mole SS) incorporated sedimentary components, whilst the adjacent and contemporaneous MSS and CRSS did not.

The chemical variability within the USS (Figure 43, 44 and 46) is attributed to physical mixtures of source rocks (Shaw and Flood, 1981) where felsic granites contain a larger component of the felsic S-type source. Evidence for fractional crystallisation from inflections on bivariate diagrams, or the presence of cumulate rocks within the USS is lacking (e.g. Shaw and Flood, 1981). Slight negative Eu/Eu* anomalies suggest partial removal of feldspar from the parental magmas (Figure 45). Assimilation or melting of an interface region (with I- and S-type components) explains the lack of Sn enrichment with increasing SiO_2 in the USS, as mixing will not enrich Sn in melts (Figure 44E).

Partial melting alone, however, cannot account for the haplogranitic composition of the Mole Granite, without unrealistically small degrees melt generation.

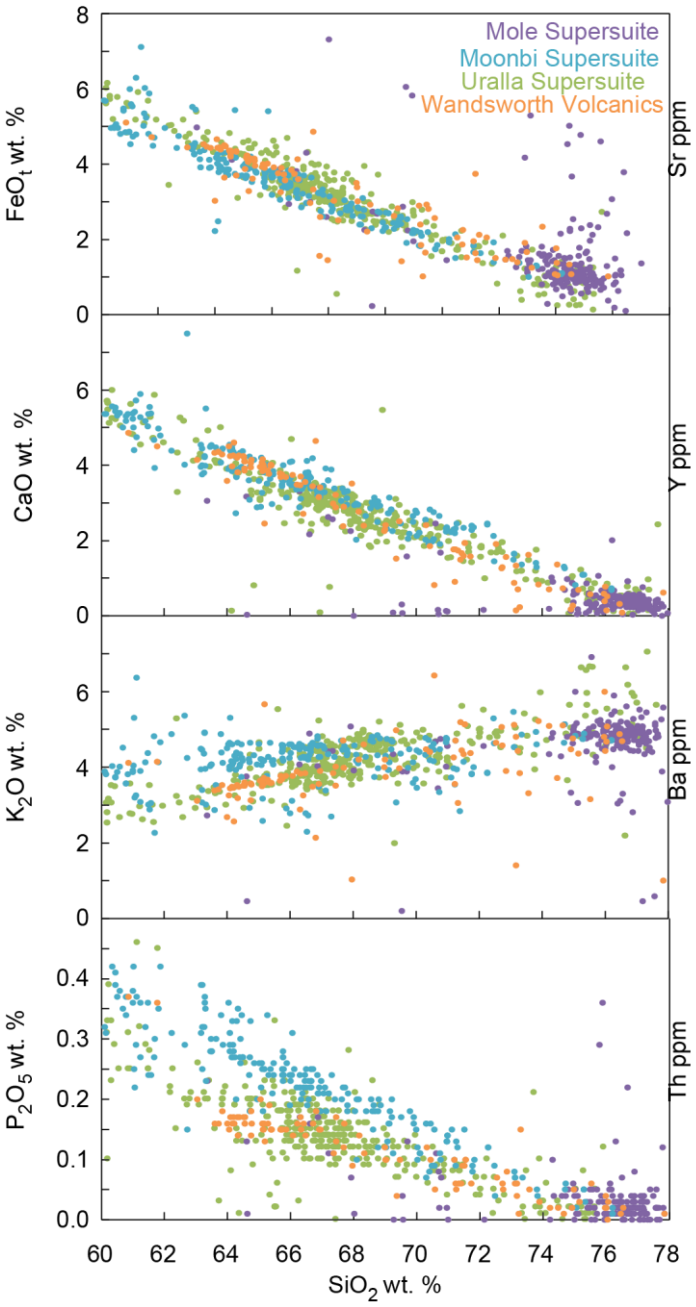

Figure 43: Major element variation within the I-type supersuites of the NEB from the CHAPGRAN database (Bryant and Blevin 2017). Isotopic compositions suggest an affinity between the Mole Supersuite and the Uralla Supersuite. The Moonbi Supersuite and Wandsworth Volcanics are included for comparison.

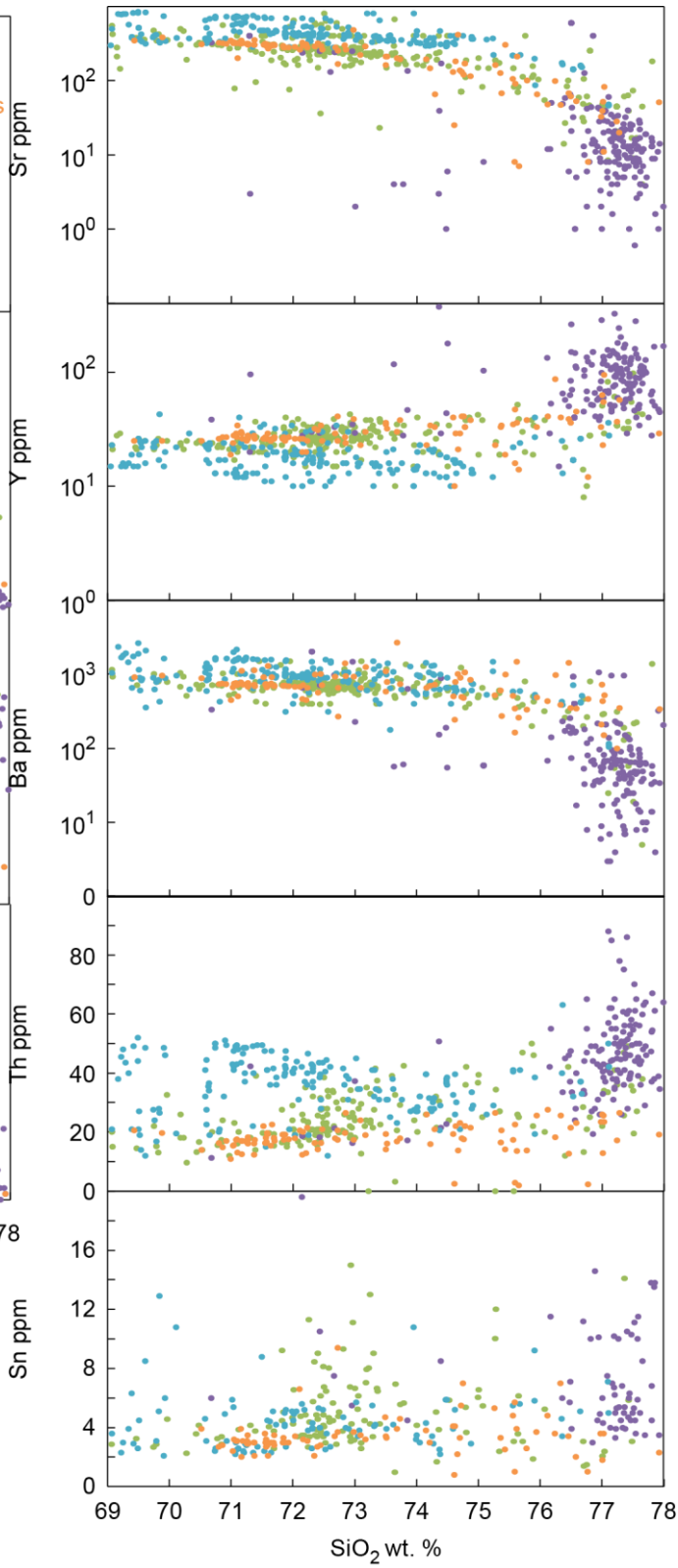

Figure 44 Trace element variation of the I-type supersuites of the NEB from the CHAPGRAN database (Bryant and Blevin 2017). Colour scheme as in Figure 43.

Experimental studies indicate that dehydration melting of amphibole and biotite at <1 GPa can generate between 12–48 % melt over a narrow temperature range (Rushmer, 1991; Sen *et al.,* 1994; Sisson *et al.,* 2005). An alkali basalt source at 0.8 GPa and 875ºC will contain <0.1 % melt, that increases to 2–5 % at 925ºC and 20% at 935ºC (Rushmer, 1991). Also, at 0.8 GPa, melting of an island arc tholeiite source increased from 2 % melt volume at 800ºC to 10% at 825ºC. The addition of unbound water greatly increases this melt generation (Rushmer, 1991). The initial 2 volume % of melts generated by dehydration of a basaltic amphibolite at 925ºC and 1.5 GPa produced a melt with 69.49 wt.% SiO_2 and a ASI of 1.03 (Rushmer, 1991). Therefore, partial melting alone is unlikely to generate the haplogranitic and weakly peraluminous melts of the Mole SS as it would require generation and removal <2 volume % melt, within very a narrow temperature range (50ºC). Also, small degree partial melts are unlikely to have been generated at the same time as voluminous granite emplacement of the USS which began at *ca* 255 Ma and continued following the emplacement of the Mole Granite into the Late Triassic.

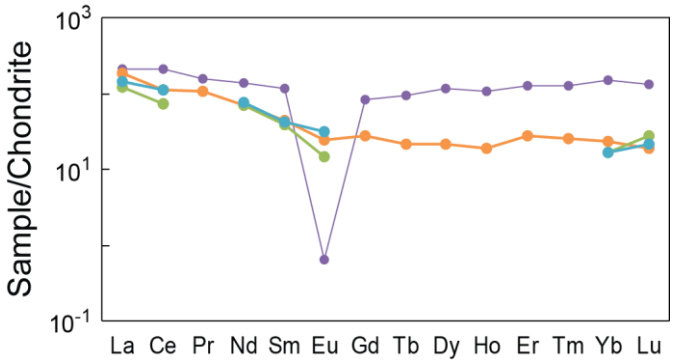

Figure 45: Chondrite-normalised REE for the I-type supersuites of the NEB. Colour scheme as in Figure 43.

Magmatic evolution

The haplogranitic composition of the Mole Granite is attributed to fractional crystallisation from the parental magmas of the USS. Within the Mole Granite, and over a small range of SiO_2 (75.1–77.3 wt.%), geochemical evidence for removal of plagioclase and K-felspar from residual melts by fractional crystallisation incudes strong negative Eu/Eu* anomalies, and collinearity of Eu/Eu* anomalies with Ba, Rb and Sr (Laker, 2017). Fractional crystallisation of feldspars from the parental magma of the Mole Granite will also impart the

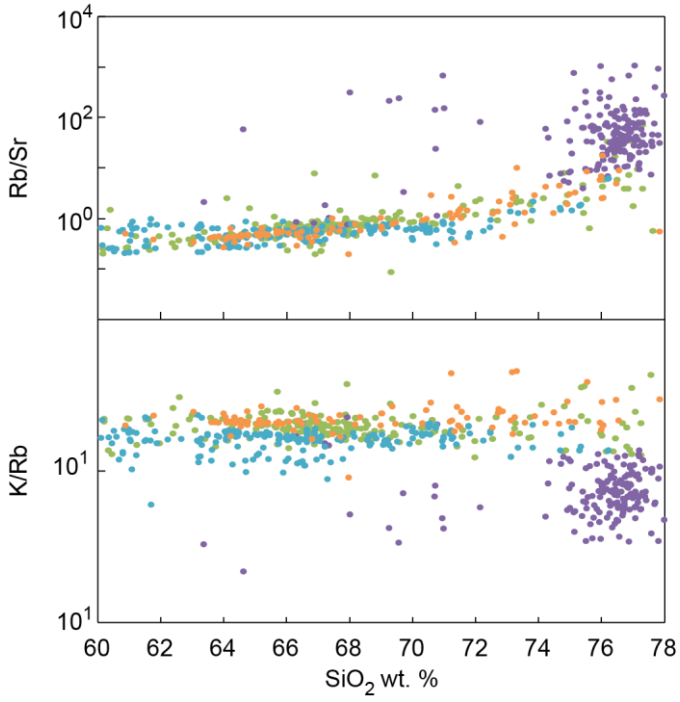

Figure 46: Element ratios for the I-type supersuites of the NEB. Colour scheme as in Figure 43.

sharp decrease in Sr and Ba concentrations (Figure 44A and 18C) and Rb/Sr and K/Rb (Figure 4A and B) from the USS to the Mole SS. The distinct increase in Y (Figure 44B), HREE (Figure 45) and Th (Figure 44D) from granites of the USS to the Mole SS, and variability in other trace elements is more difficult to decipher as with increased fractional crystallisation accessory phases control much of the trace element budget. Landenberger and Collins (1996) modelled Rayleigh fractionation of major and trace element composition of A-type granites from the Chaelundi Complex within the NEB. Modelling of the Chaelundi Complex as an analogue for the Mole SS is ideal because unlike most A-type granites of the NEB, the Chaelundi Complex shows a wide compositional range from quartz monzonite to leucogranite and SiO_2 between 66–76 wt.%. The quartz-monzonite, with 66.75 wt.% SiO_2 has comparable REE concentrations to the Dundee Rhyodacite, and granites of the USS (Landenberger and Collins, 1996). Landenberger and Collins (1996) showed consistency between major and trace element models, and that the most felsic A-type rocks represent the final 30% volume fraction of the initial melt volume after Rayleigh fractional crystallisation and removal of plagioclase and orthoclase, quartz, biotite and hornblende, and minor ilmenite and ferrohypersthene. Y and Th are also enriched in the Landenberger and Collins (1996) model to concentrations similar to those observed in the Mole SS. The

chondrite-normalised REE concentrations of the A-type Chaelundi Complex are shown in Figure 47. With increasing SiO_2 the REE concentrations change from slightly inclined patterns with a weak Eu/Eu* anomaly, to patterns similar to the Mole Granite at 75.69 wt.% SiO_2. To produce the relatively flat REE chondrite normalised shape Landenberger and Collins (1996) indicate minor (0.2%) allanite is required to reduce LREE concentrations. The Mole Granite has a steeper LREE shape, and overall higher abundance than the leucogranite of the Chaelundi Complex, and would suggest allanite crystallisation did not occur in the parental magmas of the Mole Granite (Figure 47).

The definition of a mixed I- and S-type isotopic composition in the A-type Mole SS is significant for the understanding of A-type granites more generally. Many genetic models for A-type granites attempt to reconcile the fluorine-rich and H_2O-poor composition of a refractory source that has previously undergone dehydration melting (Collins *et al.,* 1982; Creaser *et al.,* 1991; Landenberger and Collins, 1996; King *et al.,* 1997). This model is not appropriate for the Mole SS because it is emplaced simultaneously with and adjacent to other plutons of the USS that do not have the characteristic A-type compositions. Instead, we propose that the A-type characteristics of the Mole Granite are developed during fractional crystallisation processes at shallow depths, as demonstrated by Landenberger and Collins (1996).

Shallow emplacement of the Mole Granite

A-type granites have, by definition, low H_2O (Whalen *et al.,* 1987). Fluid exsolution raispidly removes heat from a crystallising granite and will often stall ascent. Low H_2O granites undergo later fluid saturation and have the ability to reach upper crustal levels.

A distinctive feature of the Mole Granite is its abundance of F as evidenced by magmatic and hydrothermal topaz and fluorite. Elevated F is a common feature of leucocratic A-type granites (>0.5–3 wt.%; Pichavant and Manning, 1984), and strongly effects the liquidus, viscosity, density and eutectic composition of silicate melts (Tuttle and Bowen, 1958; Manning *et al.,* 1980; Manning, 1981; Johannes and Holtz, 1996).

Manning (1981) showed that with 4 wt.% F the liquidus of silicate melts can persist to 550ºC. Tourmaline, the major boron host, is less abundant than topaz and fluorite in the Mole Granite, however boron also has the effect of lowering liquidus temperatures (Pichavant, 1981; Pollard *et al.,* 1987).

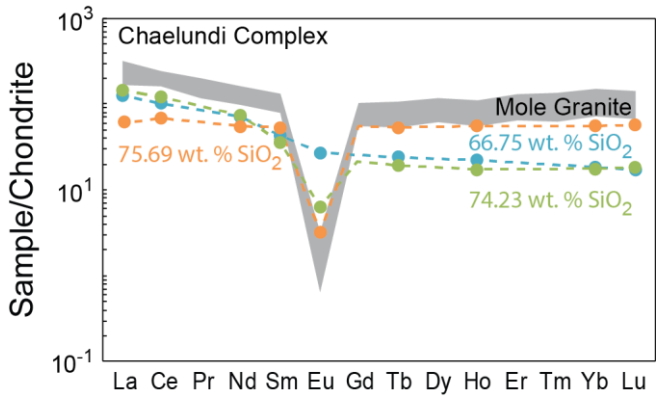

Figure 47: Chondrite normalised REE concentrations of quartz monzonite, granite and leucogranite from the A-type Chaelundi Complex of the New England Batholith determined by Landenberger and Collins (1996). Data does not include Pr, Gd, Dy, Er and Tm so these are interpolated. The Chaelundi Complex REE data are compared with the REE data of the Mole Granite presented in Laker (2017). The most fractionated unit in the Chaelundi Complex has the REE pattern similar to the Mole Granite, with slight LREE depletion. Landenberger and Collins (1996) attribute the changing REE concentrations with SiO_2 with extended fractional crystallisation, that is also proposed for the Mole Granite.

Experimental studies indicate that incorporation of F into silicate melts leads to an exponential reduction in viscosity by replacing Si–O–(Si, Al) bonds with Si–OH and Si–F respectively (Manning *et al.,* 1980; Dingwell *et al.,* 1985, 1993; Lange, 1994). At 1000ºC and 1 atmosphere pressure, the viscosity of rhyolitic melts was shown to decrease by ~1 log unit (in poise) with every additional wt.% fluorine added (Dingwell *et al.,* 1985). Similarly, addition of 2.5 wt.% F into haplogranitic melts decreases the density from ~2.29 to 2.27 g/cm^3 at 750ºC and 0.1 GPa (Dingwell *et al.,* 1993). Parental melts with low H_2O will undergo late fluid exsolution. As F partitions favourably into a fluid instead of the silicate melt, fluid exsolution will deplete F in the residual melt (Dingwell et. al., 1985).

The combined effects of lowered viscosity and density due to F and B in an originally dry magma are hypothesised allowed for a shallow emplacement in the upper crust. The depolymerised melt structure and low liquidus temperature allow for extended fractional crystallisation to occur.

Eadington and Nashar (1978) report whole-rock F concentration of 0.32 wt.% in the porphyritic phase of the Mole Granite. Audétat *et al.* (2000a) estimated a maximum F concentration in the melt of 2.5 wt.% before being buffered by precipitation of magmatic topaz. Despite high F, the major element composition of the haplogranitic Mole Granite plots between the minima in the Qz–Or–Ab system and 1 wt.% F in water saturated conditions at 0.1 GPa (Figure 35; Manning, 1981). This is likely related to the diminished effect of F in peraluminous melts on the Qz–Or–Ab eutectic due to the formation of Al–F complexes (Manning *et al.,* 1980).

Fluorine has been demonstrated to form ligands with traditionally lithophile elements such as HREE and Y (London et al., 1988; Webster et al., 1989; Keppler and Wyllie, 1990, 1991) which could account for their enrichment in the Mole SS (Figure 44B). Dostal and Chatterjee (1995) noted that F-rich fluids exsolved from cooling silicate melts will also be enriched in incompatible elements and can modify the primary composition of the granites. Fractionation of a F-rich fluid from the Mole Granite is evidenced by extensive silexite in its apical zones, containing up to 20 vol% topaz and minor fluorite. This fluid is unlikely to have effected whole-rock granite samples used in this study as there is very little variability in the REE patterns between fresh and altered samples.

Fluid fractionation

Cassiterite in the Mole Granite coprecipitated with tourmaline and continued to precipitate during mixing of magmatic and meteoric fluids (Sun and Eadington, 1987; Audétat *et al.,* 1998, 2000a; Feteke *et al.,* 2016). All tourmalines analysed here coexist with quartz that has homogenous and magmatic $\delta^{18}O$ compositions (Table 17) indicating precipitation prior to the incursion of meteoric fluids. Tourmalines of this study do not coexist with cassiterite, except in NEB016 from the McDonalds Lode, indicating that Sn concentrations in tourmaline were not significantly affected by cassiterite precipitation. Using the boiling Equation 6 outlined in Chapter 2.3, an initial water concentration of 0.5 wt.% and an $F_{(water)}$ of 0.14 will generate a fluid with 155 ppm Sn for $D_{fluid-melt} = 2$, and 310 ppm for $D_{fluid-melt} = 4$ (See section 2.3.6 for discussion on D values), which is consistent with Sn concentrations for all tourmaline samples except NEB008t

(Figure 48). These values are also broadly consistent with Sn concentration of pre-mineralising brines inferred by fluid inclusion data of the Yankee lode (55–586 ppm; Audétat *et al.,* 1998, 2000a).

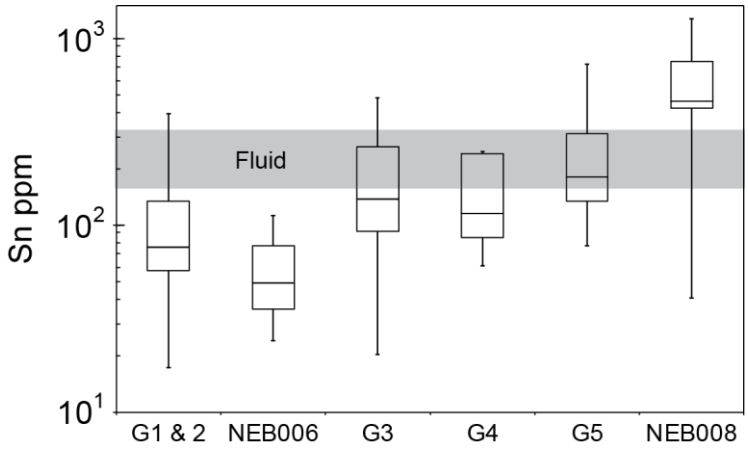

Figure 48: Box and whisker plot of Sn concentrations within tourmaline. The grey bar represents calculated compositions of a fluid generated from the Mole Granite. See section 2.3.6 for details on equations and parameters.

Fluid–rock mixing

Tourmaline not contained within the Mole Granite (groups 4 and 5) displays evidence of chemical leaching of host rocks by fluids. Chemical leaching by fluids on the host rock is most evident in Group 5 tourmalines hosted in the Bondonga Beds. Relative to the Mole Granite, the Bondonga Beds are enriched in MgO, CaO, Sc, Cu, Zn, Sr, Zr and Eu. Similarly, tourmaline of Group 5 is defined by relative enrichment of MgO, CaO, Cu, Zn, Sr and Eu relative to tourmaline of Group 1 in the Mole Granite. Major element substitution on the X site of tourmaline, between Fe and Mg, appears most sensitive to the degree of fluid leaching of the host rock, with low $Fe/(Fe+Mg)_{apfu}$ corresponding to increased leaching. Similarly, Sr shows strong correlation with $Fe/(Fe+Mg)_{apfu}$, and its concentration in tourmaline broadly correlates with the concentration of Sr in the host rock (Figure 49). Groups 1 and 2 tourmaline, hosted in the Mole Granite have the lowest range Sr (1–58 ppm), although variable. Conversely, Group 5 tourmaline, hosted in the Bondonga Beds are the most enriched in Sr of all tourmaline samples (90–386 ppm). The large difference in Sr between groups 1 and 5 is attributed to the different Sr concentration in Mole Granite (~6 ppm) and the Bondonga Beds (191 ppm). This indicates that Sr contamination of fluids from leaching of country rocks occurred. There is no significant shift in

the $^{87}Sr/^{86}Sr_{(i)}$ of hydrothermal tourmaline as the Bondonga Beds and Emmaville Volcanics have overlapping $^{87}Sr/^{86}Sr_{(i)}$ with the Mole Granite (Figure 39).

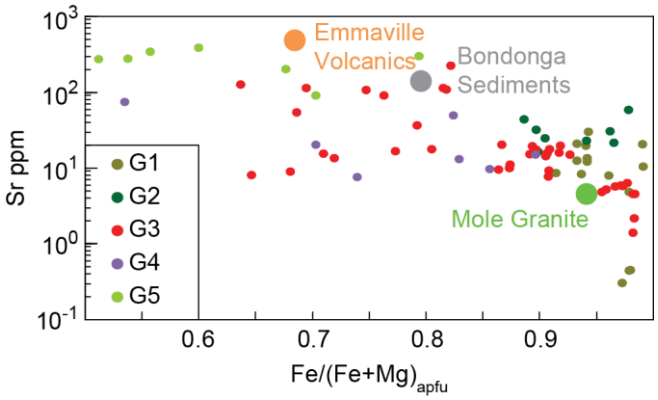

Figure 49: Increasing Sr in tourmaline associated with mixing with the host rocks. Mixing is quantified by the major element substitution between Fe and Mg on the X site in tourmaline.

The distinctive positive Eu/Eu* of NEB016t can also be attributed to fluid leaching as it is the only REE that is more enriched in the Bondonga Beds than the Mole Granite (Figure 36). Unlike at Ardlethan, Sn concentrations in tourmaline are not correlated with $Fe/(Fe+Mg)_{apfu}$, or Sr, and are interpreted to represent the composition of forming fluid or melt.

Extensive fluid leaching is evident in Group 4, hosted in the Emmaville Volcanics, directly above a buried ridge of the Mole Granite. Relative to the Mole Granite, the Emmaville Volcanics are enriched in MgO, CaO, Sr and Eu compared to the Mole Granite, and these chemical signatures are recorded in tourmaline (Figure 37 and 49).

Genesis of quartz–tourmaline nodules in the Mole Granite

The origin of tourmaline nodules is unclear, with three prevailing hypotheses; 1) boron rich vapour (bubbles) rising through the granite (Balen and Broska, 2012); 2) immiscible hydrous borosilicate melt (Drivenes *et al.,* 2015); or 3) post-magmatic boron-rich metasomatism (Dick, 1980; Le Fort, 1991; Rozendaal and Bruwer, 1995).

Textural evidence for an immiscible hydrous borosilicate melt includes a gradational increase in grain size from the Mole Granite into quartz–tourmaline nodules and biotite depletion halos indicating competition for magmatic Fe.

However, the preference for nodules to form along fracture surfaces in the granite (e.g. Figure 33A), may indicate expulsion of a melt or fluid with sub-solidus equilibration around the nucleation of tourmaline nodules.

Audétat *et al.* (2000a) suggested that B, as well Bi, Pb, Li, W, As and Mn, preferentially partition into a fluid phase instead of the silicate melt. Conversely, Rb, K and Cs preferentially partition into the melt. Tourmaline data reported here show Group 1 tourmalines are most enriched in Bi, Pb, Li, W, As Mn, Rb and K. There is no significant fractionation in Group 1 tourmaline between the fluid preference and melt preference elements as defined by Audétat *et al.* (2000a), indicating a fluid phase had not formed prior to the formation of quartz–tourmaline nodules. Increasing B within melt inclusions from the porphyritic granite (~50 ppm) to the microgranite (~650 ppm) also indicates fluid separation occurred following quartz–tourmaline nodule formation otherwise B would have been depleted from the melt by partitioning into the fluid (Audétat *et al.,* 2000a). These features preclude a fluid or vapour origin (Dick, 1980; Le Fort, 1991; Rozendaal and Bruwer, 1995, Balen and Broska, 2012) of the quartz–tourmaline nodules in the Mole Granite.

The radiogenic $^{87}Sr/^{86}Sr_{(i)}$ compositions of Group 1 tourmalines are not in equilibrium with the Mole Granite (see section 2.3.6). This disequilibrium is unlikely to result from incursion of a foreign melt or fluid with more radiogenic $^{87}Sr/^{86}Sr_{(i)}$ as there is no textural or geochemical evidence for such a fluid. Instead it is proposed here that the last pockets of melt/fluid underwent significant *in-situ* ^{87}Rb decay with elevated Rb/Sr values after the system was closed in the Mole Granite. This decay will not be corrected for in $^{87}Sr/^{86}Sr_{(i)}$ calculations of tourmaline as Rb is generally excluded from the crystal structure. However, Rb concentrations within tourmaline are the highest in nodular settings (Table 15). Whole-rock $^{87}Rb/^{86}Sr$ compositions for the Mole Granite vary between 90–300 (Table 16) and represent the minimum compositions of melt/fluid pockets. Audétat *et al.* (2000a) reported $^{87}Rb/^{86}Sr$ within highly fractionated melt inclusions of the seriate granite as ~950. Assuming the measured $^{87}Rb/^{86}Sr$ value of NEB142 whole-rock analysis (229), it would take 1.3 Ma of *in-situ* decay in the liquidus quartz–tourmaline nodules to generate the observed difference between $^{87}Sr/^{86}Sr_{(i)}$ inferred from the whole-rock

isochron for the entire Mole Granite system (0.7065) compared to the tourmaline in NEB142t (0.71064). Similarly, the observed difference between the NEB170t $^{87}Sr/^{86}Sr$ of 0.70997 and 0.7065, requires 1.1 Ma of *in-situ* decay with a $^{87}Rb/^{86}Sr$ of 229. Alternatively, a $^{87}Rb/^{86}Sr$ of ~950 in the melt/fluid pocket significantly reduces this period of *in-situ* decay to only ~310 ka for NEB142t and 260 ka for NEB170t. Extended *in-situ* decay leading to more radiogenic $^{87}Sr/^{86}Sr_{(i)}$ prior to tourmaline crystallisation will have been supported by lowered solidus due to excess B in the nodules (Manning and Pichavant, 1983).

2.3.6 Conclusions from the Mole Granite system

Magmatic to hydrothermal processes leading to sub-economic polymetallic mineralisation associated with the Mole Granite are difficult to decipher due to extended fractional crystallisation of the parental magma that disguises the magmatic source rocks, and prolonged and pervasive hydrothermal alteration that overprints magmatic-hydrothermal processes. The major, trace and isotopic composition of tourmaline from magmatic and hydrothermal environments were determined to better characterise the source composition of the Mole Granite and magmatic and hydrothermal processes. Tourmaline major, trace concentrations and Rb–Sr isotopic compositions show large compositional trends from the magmatic to hydrothermal deposits. In conjunction with whole-rock chemistry and quartz $\delta^{18}O$ compositions, five texturally distinct and chemically distinct groups of tourmaline were identified and attributed to specific processes occurring across the magmatic to hydrothermal transition.

The New England Batholith formed by the rapid accretion of isotopically juvenile rocks. Subsequently the $\varepsilon Nd_{(i)}$ and $\varepsilon Hf_{(i)}$ compositions of granites, that are commonly used to identify source rock compositions, were not significantly fractionated due to their similar partitioning coefficients of Sm and Nd, and Lu and Hf, in magmatic systems, and their long half-lives (Jeon *et al.,* 2012, 2014). In contrast, the larger range in Rb/Sr of granites and source rocks in the New England Orogen allows for greater $^{87}Sr/^{86}Sr_{(i)}$ sensitivity. Despite the extreme Rb/Sr ratios associated with the Mole Granite that require large age corrections for $^{87}Sr/^{86}Sr_{(i)}$, we present a new whole-rock isochron estimate of the $^{87}Sr/^{86}Sr_{(i)}$ composition that indicates a chemical affinity with the Uralla Supersuite and the Wandsworth Volcanics. The Mole Granite has an A-type composition due to its

high concentrations of F, Li, Rb, Sn, HFSE and U. Parental magmas of the Mole Granite which have similar compositions to the melts of the USS, have undergone continued fractional crystallisation at shallow crustal levels. Shallow emplacement and extended fractional crystallisation were facilitated by high F concentrations in the melt.

Formation of Sn deposits occurred predominantly during the formation of a chlorine-rich fluid after cooling of the silicate melt (Audétat, 1998; 2000a, 2000b). Fluid fractionation within the Mole Granite is shown by the contrasting chemistry of magmatic and hydrothermal tourmaline, and represents the major enrichment of Sn.

In the apical zones of the Mole Granite, tourmalines do not display evidence of widespread fluid leaching of the surrounding host rocks, indicating no major post-magmatic compositional changes. However, for fluids that are expelled from the Mole Granite into the country rocks, fluid leaching of those rocks is evidenced by decreasing $Fe/(Fe+Mg)_{apfu}$, $\varepsilon Nd_{(i)}$ and increasing Sr.

2.4 Tourmaline as a passive melt and fluid monitor

2.4.1 Mineral–melt partitioning in tourmaline

Mineral–melt partitioning discussed below is restricted to groups 1 and 2 tourmalines from the Ardlethan Granite and Group 1 tourmaline from the Mole Granite, as they have the strongest textural relationship with the granite. Group 1 tourmaline from the Ardlethan Granite is interstitial and anhedral between the main rock forming minerals. The major element and REE composition of group 1 and 2 tourmalines appears largely unmodified from the whole-rock compositions. Group 1 tourmaline from the Mole Granite displays both magmatic and hydrothermal textures. Magmatic textures include biotite depletion halos (Figure 33B), and inwards coarsening grain size of quartz-tourmaline nodules (Figure 33C). However, elsewhere Group 1 tourmaline of the Mole Granite is restricted to fracture surfaces (Figure 33A). Also, as noted in the Mole Granite, the Rb–Sr isotopic system remained open within the quartz–tourmaline nodules for at least 260 ka following closure of Rb–Sr in the bulk granite. Despite this, the major element and REE compositions of these tourmalines remain relatively homogenous. Mineral–melt partitioning coefficients for tourmaline cannot be determined with confidence from these nodules as the bulk chemistry of the magma and exsolved fluids may have been radically modified in these final stages of fractional crystallisation. Only the samples with the most ‘magmatic’ textures and chemistry are shown in Figure 50 after normalisation to bulk rock concentrations. The average element concentration in tourmaline normalised to the whole-rock composition for the Ardlethan Granite and Mole Granite are displayed in Table 19. Tourmaline from both the Ardlethan Granite and Mole Granite is only enriched in Sc, Zn, Ga and Sn relative to the whole-rock concentrations. Sc, Mn and Zn show increasing concentrations in the Mole Granite with SiO_2 indicating their incompatibility in enrichment in the last phases of melt (Laker, 2017). Therefore, the elevated concentrations in tourmaline may reflect late fractionation crystallisation instead of $^{i}D_{(tur/melt)}$ >1 for these elements.

Mineral–melt partitioning coefficients for tourmaline remain largely unconstrained by experimental studies. The only data are reported by van Hinsberg (2011), who obtained the data ‘serendipitously’ after a failed

experiment on Fe–Mg exchange between tourmaline and biotite (van Hinsberg and Schumacher, 2009). The $^{i}D_{(tur/melt)}$ values are shown in Table 19. The results of van Hinsberg *et al.* (2011) are not directly comparable to this study as $D_{tur–melt}$ were determined on foitite (Figure 3) and olenite (an aluminium rich tourmaline that forms a solid-substitution series with elbaite).

Van Hinsberg (2000) did not report $D_{tur–melt}$ for Sn. Sn concentrations of tourmaline presented here are 1–10 times more enriched than within the whole-rock composition for both the Ardlethan Granite and Mole Granite. Audétat *et al.* (2000a) reported increasing Sn in melt inclusions from 17 ppm in the porphyritic phase to 78 ppm in the microgranite phase of the Mole Granite, recording the final stages of fractional crystallisation (Audétat *et al.,* 2000a). However whole-rock concentrations of the Mole Granite only vary between 4–16 ppm (Figure 44). The median value within Group 1 tourmaline, within the seriate phase, is 65 ppm. If tourmaline was in equilibrium with melts of the seriate phase, then $^{Sn}D_{(tur/melt)}$ = ~ 8. If tourmaline was in equilibrium with more evolved melts, similar to those of the microgranite, then $^{Sn}D_{(tur/melt)}$ = ~1. Sn concentration of two interstitial tourmaline samples from within the Ardlethan Granite are consistent and indicate a $^{Sn}D_{(tur/melt)}$ = ~1.5. At Ardlethan Sn in tourmaline increases from 37 ppm interstitially to 73 ppm in nodular tourmaline of Group 1 due to late magmatic fractional crystallisation.

All the REE are less abundant in tourmaline compared to the whole-rock compositions of the Ardlethan Granite and Mole Granite and suggest a $^{REE}D_{(tur/melt)}$ <1. The slight positive HREE slope in tourmaline of the Mole Granite may be related to increasing compatibility of the HREE compared to the LREE (van Hinsberg 2011), however this effect is not apparent in Group 1 tourmaline of the Ardlethan Granite and groups 1 and 2 of the Mole Granite. The variable concentrations of the REE are discussed further below in relation to crystal chemical effects.

Table 19: D(Tur/melt) or concentration of elements in tourmaline relative to the whole-rock composition for the Mole Granite and Ardlethan Granite.

		Mole Granite		Ardlethan Granite	
Element	**Van Hinsberg *et al.* (2011)**	**Average**	**1SD**	**Average**	**1SD**
Sc	0.71	3.788	2.084	3.462	2.036
Cu	1.86	0.127	0.143	0.285	0.158
Zn	0.66	8.494	2.408	4.868	0.794
Ga	0.76	7.048	1.593	5.022	0.619
Rb	0.45	0.005	0.024	ND	ND
Sr	1.05	0.560	1.222	0.526	0.340
Y		0.014	0.033	0.001	0.001
Zr		0.019	0.047	0.001	0.001
Nb		0.152	0.108	0.050	0.036
Sn		1.988	1.143	8.332	5.288
La	0.5	0.118	0.138	0.027	0.015
Ce	0.57	0.081	0.082	0.021	0.011
Pr	0.36	0.063	0.063	0.018	0.009
Nd	0.51	0.049	0.063	0.010	0.005
Sm	0.64	0.043	0.082	0.004	0.003
Eu	0.84	0.169	0.163	0.162	0.100
Gd	1.10	0.029	0.063	0.001	0.001
Tb		0.020	0.043	0.001	0.001
Dy		0.017	0.036	0.001	0.001
Ho		0.018	0.034	0.002	0.002
Er		0.018	0.033	0.003	0.005
Tm		0.017	0.034	0.006	0.010
Yb	1.85	0.014	0.030	0.010	0.016
Lu		0.022	0.034	0.017	0.027
Hf	2.44	0.026	0.050	0.002	0.004
Ta		0.544	0.307	ND	ND
Pb	0.57	0.251	0.784	0.034	0.012
Th		0.033	0.070	0.001	0.002
U	0.24	0.118	0.282	0.001	0.002

The remaining high field strength elements (HFSE: Y, Zr, Nb, HREE, Ta, Th, U) and Pb are noticeably depleted in tourmaline relative to the whole-rock compositions, in contrast to $^{HFSE}D_{(tur/melt)}$ values reported by van Hinsberg (2011). Tourmaline used in the van Hinsberg (2011) experiments was relatively enriched in TiO_2 (TiO_2 = 1.52 wt.%) compared to natural tourmaline studied here (TiO_2 < 0.64 wt.%), which could allow for substitution with the HFSE.

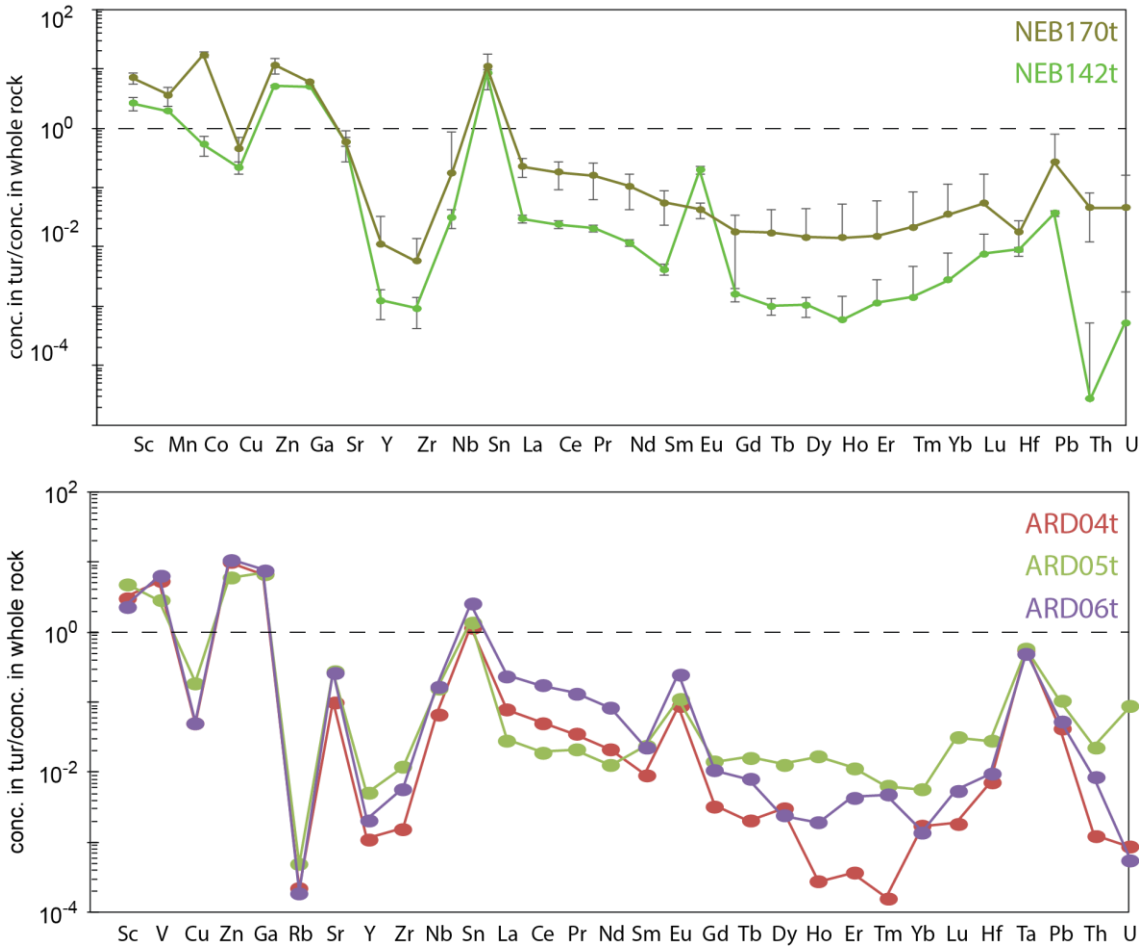

Figure 50: Trace element compositions of Group 1 tourmaline normalised to the whole-rock composition of the Mole Granite (NEB142) (top) and groups 1 and 2 tourmalines normalised to the whole-rock composition of the Ardlethan Granite (PB-ARD-07; Bodorkos et al., 2014) (bottom). Note that elements analysed vary slightly in each plot.

2.4.2 Crystal chemical effects in tourmaline

Marks *et al.* (2013) documented crystal chemical effects on the incorporation of trace elements in tourmaline. Notably the effect of major element substitution between Fe–Mg on the Y and Z sites and Na (+K)–Ca on the site X (Figure 51). These effects are difficult to assess in tourmaline from the Ardlethan Granite system as isotopic evidence indicates host rock equilibration (Chapter 2.3). Similar to Marks *et al.* (2013), X site substitutions weakly correlate with concentrations of LREE in tourmaline from the Mole Granite system. Weak correlations between X site chemistry and Nb, Ta and Sn are observed. Fe–Mg substitution shows a strong control over V and As concentration in tourmaline,

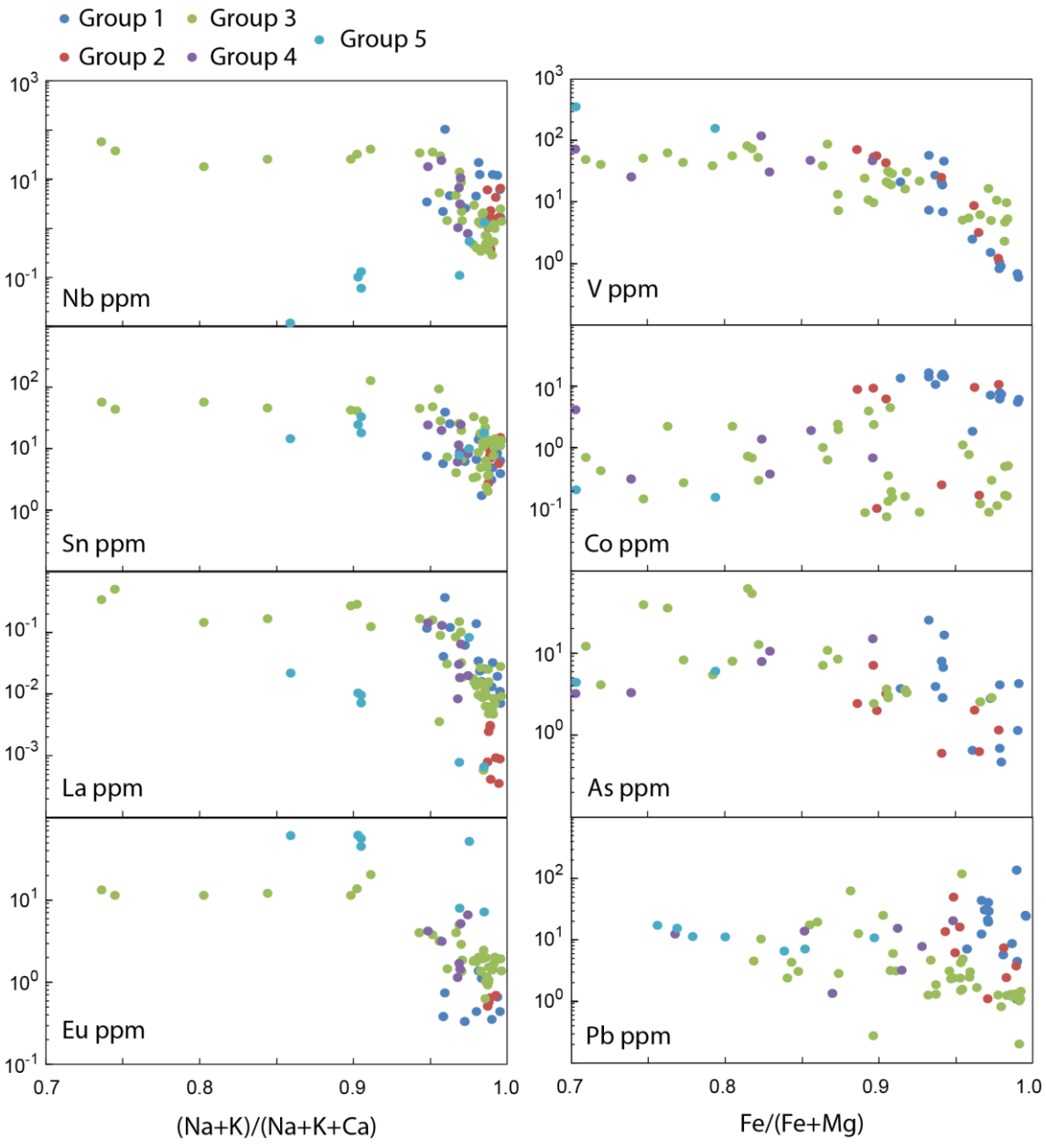

Figure 51: Trace element variation relative to major substitutions in tourmaline on site X (left) and Y and Z (right).

an effect also clear in tourmaline from the Ardlethan Granite system (Figure 52). This strong correlation indicates substitution of V for Fe on the Y site. Co in groups 1 and 2 correlates with Fe–Mg substitution, like Pb in Group 3. Unlike Marks *et al.* (2013) correlations between X site chemistry and Sr, Pb and Co were not observed. Similarly, Fe–Mg substitution does not affect concentration of Zn as presented by Marks *et al.* (2013).

The LREE concentrations are inversely correlated with Ca on the X site and indicate a substitution mechanism. Compared to the other REE, Eu is relatively enriched. Lattice strain models indicate that Eu^{2+} shows minimal strain on the X site, where as Eu^{3+} and the other REE^{3+} occur on the Y site (Van Hinsberg 2011). This results in an overall greater partitioning of Eu^{2+} over Eu^{3+} into tourmaline even when the melt is dominated by Eu^{3+} (Van Hinsberg, 2011). The ideal ionic radius for a 3+ cation on the Y site of tourmaline is ~0.68 Å, favouring the HREE (Van Hinsberg, 2011). The experimentally determined partitioning coefficient between tourmaline and melt is greater for Yb (1.85) than for La (0.5; Van Hinsberg, 2011). However as shown here, positive HREE slopes only occur in hydrothermal tourmaline from both the Ardlethan (Figure 17) and Mole (Figure 38) systems. Positive HREE slopes in tourmaline are unlikely to be due to elevated fluorine in hydrothermal systems, a ligand that favours HREE over the LREE (e.g. Duc-Tin *et al.,* 2007), as fluorine concentrations are most elevated in magmatic tourmaline.

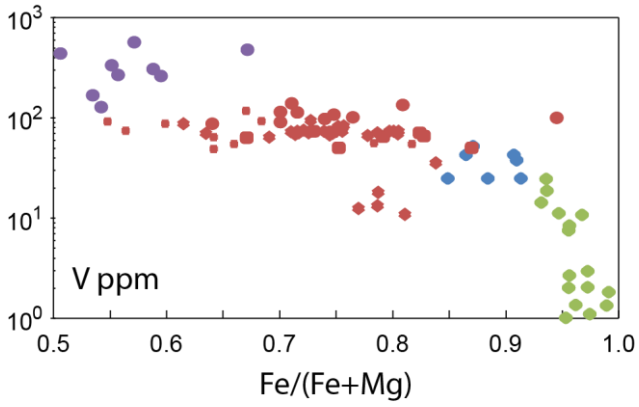

Figure 52: Trace element variation for Ardlethan tourmaline relative to major substitutions on the Y and Z sites (right).

2.5 Contributions to genetic models for Sn mineralisation

2.5.1 Sources and geodynamic setting of Sn granites

The composition of the source rocks of highly evolved Sn granites is often difficult to decipher due to their highly evolved eutectic major element compositions. Determining $^{87}Sr/^{86}Sr_{(i)}$ of the parental magmas as a provenance indicator is difficult due to the extreme $^{87}Rb/^{86}Sr$ ratios that requires large age corrections. The $\varepsilon Nd_{(i)}$ and $\varepsilon Hf_{(i)}$ of zircon can provide estimates of melt compositions without the need for age corrections. However, as shown in Chapter 2.3, the $^{87}Rb/^{86}Sr$ are more readily fractionated during magmatic processes leading to more varied $^{87}Sr/^{86}Sr_{(i)}$ that can be used to define granite provenance. As shown in Chapter 2, both the Ardlethan Granite and Mole Granite have whole-rock $^{87}Sr/^{86}Sr_{(i)}$, $\varepsilon Nd_{(i)}$ and $\delta^{18}O$, and zircon $\varepsilon Hf_{(i)}$ and $\delta^{18}O$ isotopic compositions that are intermediate between the I-type and S-type granites of the Lachlan and New England orogens, respectively, and indicate a heterogenous source or multiple sources. In Chapter 2.2, we modelled the $^{87}Sr/^{86}Sr_{(i)}$ and $\varepsilon Nd_{(i)}$ compositions of the parental melts of the Ardlethan Granite as derived from melting of an oceanic crust source followed by extended assimilation of sedimentary rocks and fractional crystallisation. In Chapter 2.4, the Mole Granite is shown to have evolved through fractional crystallisation from parental melts similar to those that formed the Uralla Supersuite. The Uralla Supersuite has intermediate I- and S-type compositions that is thought to be derived from melting an interface region between igneous and sedimentary rocks (Shaw and Flood, 1981; Bryant *et al.,* 2004), or mantle-derived magmas mixing with S-type magmas (Phillips *et al.,* 2011). The Ardlethan Granite and Mole Granite do not require Sn-rich source rocks to explain their association with Sn deposits as suggested by numerous authors for other Sn deposits (Schuiling, 1967; Romer and Kromer, 2015).

The Ardlethan Granite and Mole Granite were emplaced during two post-orogenic extension events in the Tasmanides. A schematic diagram showing the evolution of the tectonic setting of the Lachlan Orogen from convergent margin to post-orogenic setting is shown in Figure 53. The *ca* 430 Ma Koetong Supersuite of the Lachlan Orogen, and the *ca* 256 Ma Moonbi Supersuite

represent crustal anatexis in a thickened continental crust (Kemp *et al.,* 2009; Phillips *et al.,* 2011), where melting is focussed in the lower crust. In the Lachlan Orogen the Koetong Supersuite was emplaced after melting of the isotopically evolved Ordovician sediments (McCulloch and Woodhead, 1993). In the New England Orogen, the Moonbi Supersuite was emplaced after lower crustal melting of a relatively juvenile island arc shoshonite or calc-alkaline source rock, potentially a basaltic underplate emplaced during prior subduction (Shaw and Flood, 1981; Bryant *et al.,* 2004; Phillips *et al.,* 2011). Thickened continental crust prevents large scale migration of mantle-derived melts into the upper crust (Phillips *et al.,* 2011). Following the emplacement of the Koetong (Lachlan Orogen) and Moonbi supersuites (New England Orogen), new magmas in both orogens become increasingly juvenile in their isotopic compositions, including whole-rock $\varepsilon Nd_{(i)}$ and $^{87}Sr/^{86}Sr_{(i)}$ (Kemp *et al.,* 2009), and zircon $\varepsilon Hf_{(i)}$ (Kemp *et al.,* 2009; Phillips *et al.,* 2011; Laker, 2017). In both orogens this increasingly juvenile isotopic composition of granites is attributed to post orogenic extension initiated by slab retreat and extension (Kemp *et al.,* 2005, 2009; Phillips *et al.,* 2011). Alternatively, extension can be driven by a collapse of thickened crustal roots that are triggered by thinning of the underlying lithospheric mantle (through convective thinning or delamination), and partial melting and lithospheric mantle melts entering the crust (Turner *et al.,* 1992; Hawkesworth *et al.,* 1996; Turner *et al.,* 1996). Extension thins the previously thickened crust, and can produce low angle, asthenospheric piercing faults that allow for intrusion of mantle-derived magmas into the upper crust (Kemp *et al.,* 2005). During post-orogenic extension the temperature at the base of the crust will be elevated due to the advection of the underlying mantle and can promote melting or remelting of lower crustal rocks (Romer and Kroner, 2016).

For the highly evolved Sn granites of eastern Australia it is not necessary to invoke melting of Sn enriched source rocks, as suggested by numerous authors (Schuiling, 1967; Romer *et al.,* 2014, 2016; Wolf *et al.,* 2018). Whole-rock and zircon $\delta^{18}O$ isotopic compositions for both the Ardlethan Granite and Mole Granite indicate a weathered component within the source region. Romer and Kroner (2015) suggest that intense surficial weathering will enrich rocks in Sn due to its refractory behaviour. Whole-rock Sn concentrations of the Ordovician

sediments of the Lachlan Orogen vary between 1–10 ppm, with the majority of samples ~4 ppm (Blevin 2002). For the Ardlethan Granite system, partial melting and AFC processes enriched the concentration of Sn from ~1.5 ppm in the oceanic crustal source rock, to ~50 ppm in the granite with assimilation of the weathered Ordovician sediments. The very last fractions of melt were enriched to ~300 ppm (Ren *et al.,* 1995). Modelling of this enrichment assuming Sn $D_{mineral–melt}$ = 0, broadly agrees with the remaining melt fraction required as determined by Monte-Carlo modelling of the $\varepsilon Nd_{(i)}$ and $^{87}Sr/^{86}Sr_{(i)}$ of the parental melts of the Ardlethan Granite. The model allows for small variations in the Sn concentration of the assimilant (e.g. through intense surface weathering; Romer and Kroner, 2016; or lower temperature partial melting; Wolf *et al.,* 2018).

The Mole Granite, although highly fractionated, does not show the same enrichment of Sn through magmatic processes (Figure 44). Instead magmatism associated with the USS (~4 ppm) is slightly above average continental compositions. This is a result of high degree partial melting that generated the voluminous USS (Shaw and Flood 1981). The major enrichment of Sn within this system occurs at the magmatic-hydrothermal transition due to low liquidus temperatures and late fluid fractionation of saline fluids.

Several authors have implicated the role of mantle melts or fluids with Sn mineralisation (Sillitoe, 1974; Zhao *et al.,* 1995; Walshe *et al.,* 2011; Goodenough, 2014). As shown in Chapter 2.2 and Figure 22, Monte-Carlo modelling of AFC from a mantle source for melts of the Ardlethan Granite does not reconcile the highly evolved composition (low F) with $^{87}Sr/^{86}Sr_{(i)}$, $\varepsilon Nd_{(i)}$ and ASI compositions. Instead a buried oceanic crustal source is preferred as it requires high degrees of fractionation crystallisation (F = 0.15), with minor sediment assimilation (r = 0.09). The simultaneous emplacement of the Ardlethan Granite and Mine Porphyry that has ‘mantle-like’ $\varepsilon Nd_{(i)}$ and $^{87}Sr/^{86}Sr_{(i)}$, however, indicates that mantle-derived melts or fluids were reaching upper crust levels at this time (Walshe *et al.,* 1995, 2011). A mantle component is recognised in the USS from mantle $\varepsilon Hf_{(i)}$ in zircon (Phillips *et al.,* 2011). The thinning crust in this post-orogenic setting allowed for hot, mantle-derived melts to assimilate sedimentary crustal rocks in the middle and upper crust and lead

to the elevate $^{87}Sr/^{86}Sr_{(i)}$ and $\delta^{18}O$ compositions (Kemp *et al.,* 2009; Phillips *et al.,* 2011).

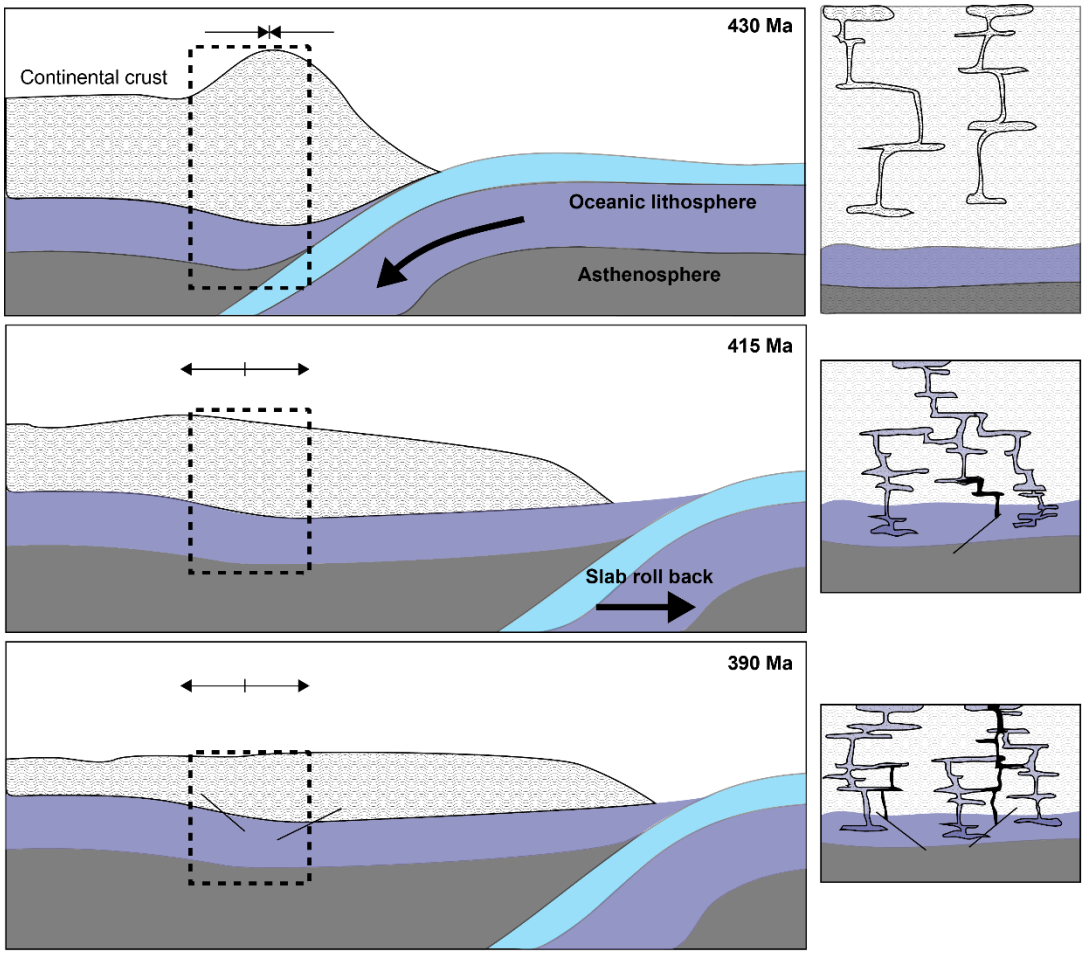

Figure 53: Geodynamic setting of the Lachlan Orogen during S-type magmatism (430 Ma; top panel), emplacement of the Ardlethan Granite (415 Ma; middle panel) and I-type magmatism (390 Ma; bottom panel). Melting regions for each period are shown to the right.

2.5.2 Volcano-plutonic relationships of highly evolved Sn granites

Emplacement of the Ardlethan Granite and Mole Granite at shallow crustal levels occurred <3 Ma following eruption of large crystal-rich volcanic units. In both cases, these volcanic units show strong geochemical affinities with the younger granites. For example, in section 2.2.6, we show that the isotopic composition of the Ardlethan Granite can be explained by small degrees of AFC from the composition of the slightly older and extrusive GQFP.

Furthermore both volcanic units were originally classified as plutonic due to their crystal-supported structure..

The prevailing model for coeval extrusive and intrusive magmatic units as proposed by Bachman *et al.* (2007), suggests that extrusive units represent the escaped melt from the intrusive crystal-rich units. This model does not fit the highly evolved Sn systems of eastern Australia because the volcanic units are 1) emplaced prior to the intrusive units, 2) less evolved than the intrusive units, and 3) crystal rich. Therefore, on the assumption that the Ardlethan Granite and Mole Granite are derived from the same parental magmas as their volcanic equivalents, a new model for volcano-plutonic relationships is required.

Cheng *et al.* (2018) proposed a model for the highly fractionated granites of the Herberton Sn–W–Mo mineral field of Queensland to account for these characteristics. In their model, highly evolved Sn granites are generated when magmatic pathways to the surface are disconnected and large silicic magma reservoirs accumulate volatiles and undergo extreme fractional crystallisation at shallow crustal depths. Cheng *et al.* (2018) suggest that surface connectivity is obstructed during regional compressional tectonics, and H_2O-poor magmas stall in the upper crust. Magma stalling creates a closed system that continues to undergo fractional crystallisation and enrich volatile components (e.g. fluorine) and incompatible elements (e.g. Sn).

Ren *et al.* (1998) inferred the GQFP was a fractionated end-member, or carapace phase, of the Ardlethan Granite, and share a gradational boundary. However, volcanic or volcaniclastic textures have been identified, and the unit has recently been reclassified as a crystal-rich ignimbrite (Bodorkos *et al.,* 2014; Bull *et al.,* 2017). U–Pb zircon ages from the GQFP are contemporaneous with the Gurragong Volcanics to the north (Black, 2005; Colquhoun *et al.*, 2005; Bodorkos *et al.,* 2014). U–Pb zircon ages of the GQFP (417.8 ± 2.3 Ma) are within error of the Ardlethan Granite (414.7 ± 2.3 Ma). The GQFP and Ardlethan Granite have similar whole-rock $^{87}Sr/^{86}Sr_{(i)}$ and $\varepsilon Nd_{(i)}$ compositions that are unique to the Lachlan Orogen, zircon $\varepsilon Hf_{(i)}$ and $\delta^{18}O$ (Blevin *et al.,* 2017) and REE abundances (Chapter 2). However, the Ardlethan Granite has undergone extended assimilation and fractional crystallisation leading to significantly more

evolved compositions including high SiO_2, Rb/Sr and low K/Rb relative to the GQFP. Parental melts of the Ardlethan Granite became disconnected from the surface following emplacement of the GQFP. A unresolved, but <3 Ma age difference between the GQFP represents the time in which the melts continued to undergo fractional crystallisation towards eutectic compositions.

The porphyritic quartz, feldspar, hornblende and pyroxene bearing Dundee Rhyodacite occurs at the top of the Wandsworth Volcanic Group and immediately preceding and adjacent to the emplacement of the Mole Granite. The Dundee Rhyodacite was originally referred to as the Dundee 'Adamellite Porphyrite' or 'Blue Granite' due to it being thick (3–4 km), crystal rich and typically weathering to form tors (Barnes *et al.,* 1989; Henley *et al.,* 2001). The Dundee Rhyodacite has a high precision TIMS U–Pb date from the zircon at 254.34 ± 0.34 Ma (Brownlow and Cross, 2010), distinguishably older than the Mole Granite, of which the oldest reported U–Pb zircon age is 249.8 ± 1.5 Ma (Chisholm *et al.,* 2014). In Chapter 2, geochemical similarities between the Mole Granite and the Wandsworth Volcanics are shown, including whole-rock $\delta^{18}O$ and $^{87}Sr/^{86}Sr_{(i)}$. The Mole Granite is a highly evolved eutectic melt compared to the intermediate to felsic composition of the Dundee Rhyodacite. The time between emplacement of the Dundee Rhyodacite and the Mole Granite (*ca* 3 Ma) represents magma stalling in the upper crust and continued fractional crystallisation. High fluorine concentrations in the parental melts of the Mole Granite allowed for increased efficiency fractional crystallisation (i.e. removal of crystals from melt) by reduced viscosity, and to lower temperatures (i.e. lower solidus).

Crystal-rich volcanics associated with 'tin' granites are also recognised elsewhere including in South China (Xu, 2008), Bolivia, South East Asia (Mitchell, 1979) and Erzeibirge of central Europe (Breiter *et al.,* 1999). Highly evolved tin granites and associated volcanics were recently identified in the Herberton Mineral Field of North Queensland, also within the Tasmanides (Cheng *et al.,* 2018). The O'Briens Creek Supersuite includes I-type leucogranites that have clear spatial and temporal associations with rich Sn mineralisation and was preceded by the crystal rich, moderately evolved Old

Feather Bed Volcanic (Blevin and Chappell, 1992; Champion and Chappell, 1992; Champion and Bultitude, 2013; Cheng *et al.,* 2018).

Two key features presented in Chapter 2 allow for modification of the Cheng *et al.* (2018) model. Firstly, as discussed above, the Ardlethan Granite and Mole Granite were emplaced in extensional tectonic regimes. Secondly, significant assimilation of host rocks occurs between emplacement of the volcanic and intrusive units. $^{87}Sr/^{86}Sr_{(i)}$ and ASI compositions are higher in the Mole Granite (0.7065; 1.04, respectively) compared to the Emmaville Volcanics (0.70501; 0.95). A similar trend is observed in the Ardlethan Granite (0.71458; 1.19) compared to the GQFP (0.71149; 1.08). This would imply that much of the assimilation of the sedimentary rocks occurred during upper crustal magma stagnation.

Cheng *et al.* (2018) suggest that stalling of magmas in the upper crust occurred due to regional compression. Instead of compression, stalling magmas in the upper crust could be attributed to: 1) lowered drive due to extensional regime, 2) voluminous assimilation of host rocks, 3) slow magmatic recharge after voluminous output.

2.6 Conclusions of tourmaline geochemistry

In this Chapter, the geochemical composition of tourmaline from magmatic and hydrothermal environments of magmatic-hydrothermal Sn deposits were presented to determine the composition of melts and hydrothermal fluids. A new method is presented for the digestion, chemical purification by ion-exchange chromatography, and analysis of Rb–Sr and Sm–Nd isotopes within tourmaline. In conjunction with major and trace element concentrations of tourmaline, these data show large compositional changes across the magmatic-hydrothermal transition. Tourmaline provides more robust estimates of $^{87}Sr/^{86}Sr_{(i)}$ because of its low $^{87}Rb/^{86}Sr$, and these data were used to determine the isotopic compositions of the Ardlethan Granite and model AFC processes. However, as shown for the Mole Granite, extreme fractional crystallisation can significantly change these $^{87}Sr/^{86}Sr_{(i)}$ compositions due to *in-situ* decay in high $^{87}Rb/^{86}Sr$ environments, and caution must be taken when interpreting these data.

This thesis focused on two magmatic-hydrothermal deposits in eastern Australia. The new tourmaline data were collected within a framework of new and published geochemical analyses by traditional methods (e.g. whole-rock Rb–Sr and Sm–Nd compositions). Tourmaline geochemistry provides new constraints on genetic models for ‘tin’ granites, including melting during post-orogenic extension, and upper crustal stalling and differentiation of magmas.

Chapter 3 Cassiterite geochronology – Absolute age and duration of magmatic to hydrothermal Sn systems in eastern Australia

3.1 Geochronology of magmatic-hydrothermal deposits

The absolute timing and duration of mineralising events is fundamental to the understanding of ore formation and a powerful exploration tool. Initially, our understanding of the timing and duration of mineralising events in general was poor due to a lack of suitable minerals for dating. Conventional approaches typically involve dating minerals assumed to be co-genetic with alteration and mineralisation (e.g. muscovite, xenotime or allanite). Significant progress has been made in the direct dating of ore minerals, for example Rb–Sr dating of sphalerite (e.g. Christensen *et al.,* 1995) and pyrite (e.g. Yang & Zhou, 2001); Sm–Nd dating of scheelite (e.g. Kempe *et al.,* 2001), chalcopyrite (Maas *et al.,* 1986), galena, sphalerite and pyrrhotite (Jiang *et al.,* 2000); and Re–Os dating of molybdenite, pyrite, chalcopyrite, sphalerite (e.g. Stein *et al.* 1998) and wolframite (Chen *et al.,* 2006), and U–Pb dating of cassiterite (e.g. Gulson and Jones, 1992; Yuan *et al.,* 2008; Li *et al.,* 2016; Neymark *et al.,* 2018).

Magmatic-hydrothermal Sn systems can display protracted histories of formation, from the emplacement of the granite and cooling of hydrothermal fluids (e.g. Halliday, 1980; Chesley *et al.,* 1993; Chen *et al.,* 1993; McNaughton *et al.,* 1993). Hypotheses for the drivers of extended periods of hydrothermal activity include sustained thermal flux from either a high heat-producing granite (enriched in the radiogenic elements K, U and Th; e.g. Tischendorf, 1977) or repeated minor intrusions over a long period (e.g. Chesley *et al.,* 1993). Granites associated with Sn deposits commonly form in convergent margin settings, with voluminous and extended episodes of granite emplacement (e.g. Taylor, 1979; Lehmann, 1990; Pirajno, 2016; Chapter 2). Individual plutons can be emplaced over timescales of 10^4–10^6 years through incremental magma accumulation (Clemens & Mawer, 1992; Petford *et al.,* 2000; Coleman *et al.,* 2004; Glazner *et al.,* 2004; Annen *et al.,* 2005; Miller *et al.,* 2007; Michel *et al.,*

2008; de Saint Blanquat *et al.,* 2011; Caricchi *et al.,* 2012; Leuthold *et al.,* 2012; Floess and Baumgartner, 2015). The timing and duration of hydrothermal fluid circulation and cassiterite precipitation during incremental magma accumulation appears is highly variable, partly due to the wide variety of minerals used in dating studies. Schlattegger *et al.* (2005) suggest cassiterite mineralisation in quartz-veins of the Yankee deposit occurred immediately after emplacement of the Mole Granite and synchronous with hydrothermal xenotime, that they dated by ID-TIMS. Chesley *et al.* (1993) utilised U–Pb dating of monazite and xenotime, and $^{39}Ar/^{40}Ar$ dating of muscovite to suggest that cassiterite mineralisation associated with the Cornubian Batholith occurred synchronously with repeated granite emplacement over a period of 6.7 Ma. Conversely, Halliday (1980) used K–Ar and Rb–Sr of mica and feldspar to indicate that cassiterite mineralisation occurred up to 60 Ma after emplacement of the main granite mass due to persistent hydrothermal circulations driven by the hot, radioactive granite. In the extreme, McNaughton *et al.* (1993) used Pb–Pb ages of granites and galena to infer cassiterite mineralisation at Zaaiplaats deposit associated with the Bushveld Granite occurred 1 billion years after granite emplacement, again due to persisting hydrothermal circulations driven by the hot granite.

Cassiterite is a potentially useful geochronometer for its ability to date Sn mineralisation directly. Cassiterite commonly incorporates moderate amounts of U and tends to exclude initial Pb (Zagruzina *et al.,* 1987), which makes it amenable to dating using the U–Pb isotopic decay systems (e.g. Gulson and Jones, 1992, Yuan *et al.*, 2008, 2011; Li *et al.*, 2016). This primary geochronological information is then readily preserved in the geological record as cassiterite is resistant to chemical and physical abrasion and can survive hydrothermal overprinting events and is commonly concentrated in detrital deposits. Pb diffusion in cassiterite is estimated to be insignificant in magmatic to hydrothermal settings. Zhang *et al.* (2011) showed that a 10 µm cassiterite grain can preserve its primary U–Pb composition for 25 Ma at 600^{o}C and a 1 mm grain for 40 Ma at 800^{o}C. However, diffusion can occur more rapidly in dissolution–reprecipitation zones of minerals (e.g. Villa, 2016), which occur in cassiterite, which can be avoided with CL imaging.

Cassiterite geochronology can also be used in a variety other metal deposits where it can be a common accessory mineral, e.g. the Wodgina Nb–Ta pegmatite district of Pilbara Craton (e.g. Sweetapple *et al.,* 2002), intrusion-related Au deposit of Kidston, Queensland (e.g. Baker and Tullemans, 1990) and polymetallic Cu–Pb–Zn deposits of the Mole Granite, NSW (Audétat *et al.* 2000a, 2000b).

3.2 Development of U–Pb age dating of cassiterite

Gulson and Jones (1992) first published a method for U–Pb age dating of cassiterite from a range of samples and ages by ID-TIMS. Further use of this method, however, was hampered by the extreme difficulty in dissolving cassiterite for solution work (Gulson and Jones, 1992). Other published ID-TIMS U–Pb data of cassiterite are few and commonly note residues with solutions after incomplete acid dissolution (Yuan *et al.,* 2008, 2011; Tu *et al.,* 2016). In Appendix 2, we present a new method for cassiterite dissolution in concentrated HBr that allows complete dissolution without residues.

Currently, U–Pb dating of cassiterite is predominantly by *in-situ* LA-(MC)-ICP-MS methods because of the rapid sample preparation and analysis and ability to determine to internal heterogeneity. Carr *et al.* (2017) (Appendix 1) presented the first SIMS cassiterite data for the Yankee deposit studied here and showed relative $^{206}Pb/^{238}U$ heterogeneity to be <1.9%. LA-ICP-MS and SIMS require a matrix-matched reference cassiterite of known U–Pb isotopic composition to account for ionisation differences of U and Pb and matrix effects (ablation and ionisation efficiency and downhole fractionation for LA-ICP-MS; Eggins *et al.* 1998; ionisation efficiency in SIMS; e.g. Ickert *et al.,* 2008). Most LA-(MC)-ICP-MS studies (Zhang *et al.,* 2014; Chen *et al.,* 2014; Du *et al.,* 2015; Zhang *et al.,* 2015; Li *et al.,* 2016; Yan *et al.,* 2016; Cao *et al.,* 2017; Deng *et al.,* 2017; Wang *et al.,* 2017; Zhang *et al.,* 2017a, 2017b) utilise two reference cassiterite samples (Lbiao and AY-4 cassiterite) whose isotopic composition was measure by ID-TIMS (Yuan *et al.,* 2008, 2011). However, in Appendix 2, new ID-TIMS data for AY-4 indicates possible heterogeneity within this reference material. In Carr *et al.* (2017), prior to the ID-TIMS study (Appendix 2), we used ideal U–Pb compositions of the reference Yankee cassiterite calculated assuming an age

243 Ma based on Rb–Sr isotopic data of coexisting micas (Kleeman *et al.,* 1997). In Appendix 2, the ID-TIMS age data from the cassiterite indicates that the Rb–Sr age is approximately 3 Ma younger than the cassiterite age, which will introduce a systematic bias in age calculations of unknown samples. Neymark *et al.* (2018) reported a method for "*In-situ* LA-ICPMS U–Pb dating of cassiterite without a known-age matrix-matched reference material". In this method U–Th–Pb isotopic compositions of cassiterite samples are determined with the NIST612 glass as a non-matrix-matched standard. The method, however, does require a 1.54 Ga cassiterite reference material with a well-defined Pb–Pb age that does not require U–Pb ionisation fractionation information. The difference between the NIST612 age of the 1.54 Ga cassiterite reference material and its Pb–Pb age provides a U/Pb fractionation factor for the unknown cassiterite samples.

3.2.1 Common Pb correction for U–Pb age dating of cassiterite

Non-radiogenic Pb incorporated into cassiterite during initial crystallisation or during a later event affects the age calculation because, for example, in the $^{238}U/^{206}Pb$ system:

$$^{206}Pb_m = {}^{206}Pb_c + {}^{206}Pb_r = {}^{206}Pb_c + {}^{238}U\,(e^{\lambda 238 t} - 1) \qquad \text{Equation 7}$$

where $^{206}Pb_m$ is the measured value (in moles), $^{206}Pb_c$ is the non-radiogenic or common Pb, and $^{206}Pb_r$ is the radiogenic component of Pb. λ^{238} is the decay constant for the ^{238}U system, and t represents the time since closure of the U–Pb system within the cassiterite.

The fraction (ƒ) of $^{206}Pb_c$ in the total Pb is ideally calculated through normalisation of $^{206}Pb_m$ to the only non-radiogenic isotope, ^{204}Pb, with an assumed composition ($^{206}Pb/^{204}Pb_c$), according to the formula (Williams, 1998):

$$ƒ = \frac{^{206}Pb/^{204}Pb_m}{^{206}Pb/^{204}Pb_c} \qquad \text{Equation 8}$$

The assumed composition ($^{206}Pb/^{204}Pb_c$) is derived either from age-specific Pb evolution model for the Earth (Cummings and Richards, 1975; Stacey and Kramers, 1975) or measured from a coexisting low U mineral such as galena or pyrite.

The radiogenic $^{206}Pb/^{238}U$ ($^{206}Pb^*/^{238}U$) used for age calculations can then be determined by:

$$\frac{^{206}Pb^*}{^{238}U} = (1 - ƒ)(\frac{^{206}Pb}{^{238}U}_m) \quad \text{Equation 9}$$

The 204-correction method is difficult to achieve with LA-ICP-MS analysis due to the low abundance of ^{204}Pb in cassiterite and a mass interference with ^{204}Hg, which is a common contaminant in the carrier gas of LA-ICP-MS systems. Corrections for this contamination using ^{202}Hg are further complicated by a potential mass inference with $^{186}W^{16}O$, which can be enriched in cassiterite by over 1 wt.% (Carr *et al.,* 2017), and uncertainties in the instrumental mass bias for $^{202}Hg/^{204}Hg$. Common Pb corrections for U–Pb cassiterite geochronology by *in-situ* methods typically rely on either 207- and 208-correction methods, where the radiogenic Pb component is defined by:

$$^{206}Pb_r = {}^{206}Pb_m * \frac{\left(\frac{^{206}Pb}{^{208}Pb}\right)_m - \left(\frac{^{206}Pb}{^{208}Pb}\right)_c}{\left(\frac{^{206}Pb}{^{208}Pb}\right)_m} \quad \text{Equation 10}$$

for the 208-correction method and,

$$^{207}Pb_r = {}^{207}Pb_m * \frac{\left(\frac{^{207}Pb}{^{208}Pb}\right)_m - \left(\frac{^{207}Pb}{^{208}Pb}\right)_c}{\left(\frac{^{207}Pb}{^{208}Pb}\right)_m} \quad \text{Equation 11}$$

for the 207-correction method. Again, the composition of the common Pb component is assumed. An important inference in this study is the apparently unusually evolved common Pb isotopic composition of the Yankee cassiterite determined by ID-TIMS ($^{206}Pb/^{204}Pb$ = 21.28 ± 0.4 and $^{207}Pb/^{204}Pb$ = 15.759 ± 0.0.4; Figure 54; Appendix 2**)**. Common Pb compositions were determined by a new method outlined in Appendix 2 that requires small sample sizes (<0.5 mg),

minimal handling and produces very low Pb blanks compared to previously published methods (Gulson et al. 1992; Yuan et al. 2008; 2011). The ID-TIMS common Pb isotopic composition of the Yankee cassiterite is significantly different from those predicted by age specific terrestrial evolution Pb models (e.g. $^{206}Pb/^{204}Pb$ = 18.31 ± 0.8 and $^{207}Pb/^{204}Pb$ = 15.61 ± 0.32 at 250 Ma; Stacey and Kramers, 1975) and from low U minerals in the Mole System. For example, the initial Pb composition of K-feldspar within the Mole Granite is $^{206}Pb/^{204}Pb$ = 18.53, $^{207}Pb/^{204}Pb$ = 15.63 and $^{208}Pb/^{204}Pb$ = 38.47 (G. R. Carr unpubl) and for hydrothermal galena associated with the Mole Granite is $^{206}Pb/^{204}Pb$ = 18.46 (SD = 0.01), $^{207}Pb/^{204}Pb$ = 15.59 (0.01) and $^{208}Pb/^{204}Pb$ = 38.35 (0.04) (n = 26; Huston *et al.,* 2017). Other ID-TIMS cassiterite studies do not publish enough data or discuss common Pb compositions (Gulson and Jones, 1992; Yuan *et al.,* 2008, 2011) and so it is unclear whether the Yankee cassiterite is unique in its highly evolved common Pb composition.

The 208-correction method is particularly popular for U–Pb dating of cassiterite for two reasons: Th is ubiquitously in low abundance or undetected in cassiterite indicating all measured ^{208}Pb is not from the decay of ^{232}Th (Carr *et al.,* 2017; Neymark *et al.,* 2018b), and ^{208}Pb is ~2.5 times more abundant than ^{207}Pb in terrestrial common Pb, which provides greater sensitivity during analysis. Others have utilised the 207-correction method on the assumption that due to the relatively low U concentrations for U–Pb dating, the radiogenic ^{207}Pb component is insignificant (Deng *et al.,* 2017; Wang *et al.,* 2017). The 207-correction method also assumes perfect concordance between the $^{206}Pb/^{238}U$ and $^{207}Pb/^{235}U$ systems.

In this Chapter, the U–Pb isotopic compositions and age estimations of cassiterite determined from the Ardlethan Granite and Mole Granite Sn systems are determined by LA-ICP-MS. Instrument bias introduced into analysis (e.g. ionisation efficiency and downhole fractionation) are corrected using by bracketing unknown samples with the Yankee reference cassiterite. We test the effectiveness of the 207- and 208-common Pb correction methods outlined above, and different initial Pb isotopic compositions and compare them with isochron data that do not carry the same assumptions. Finally, these data are compared with more ‘traditional’ geochronological methods from the literature

and obtained during this study (e.g. U–Pb in zircon, Rb–Sr isochrons in granites), to constrain the absolute timing and duration of magmatic-hydrothermal Sn systems in eastern Australia.

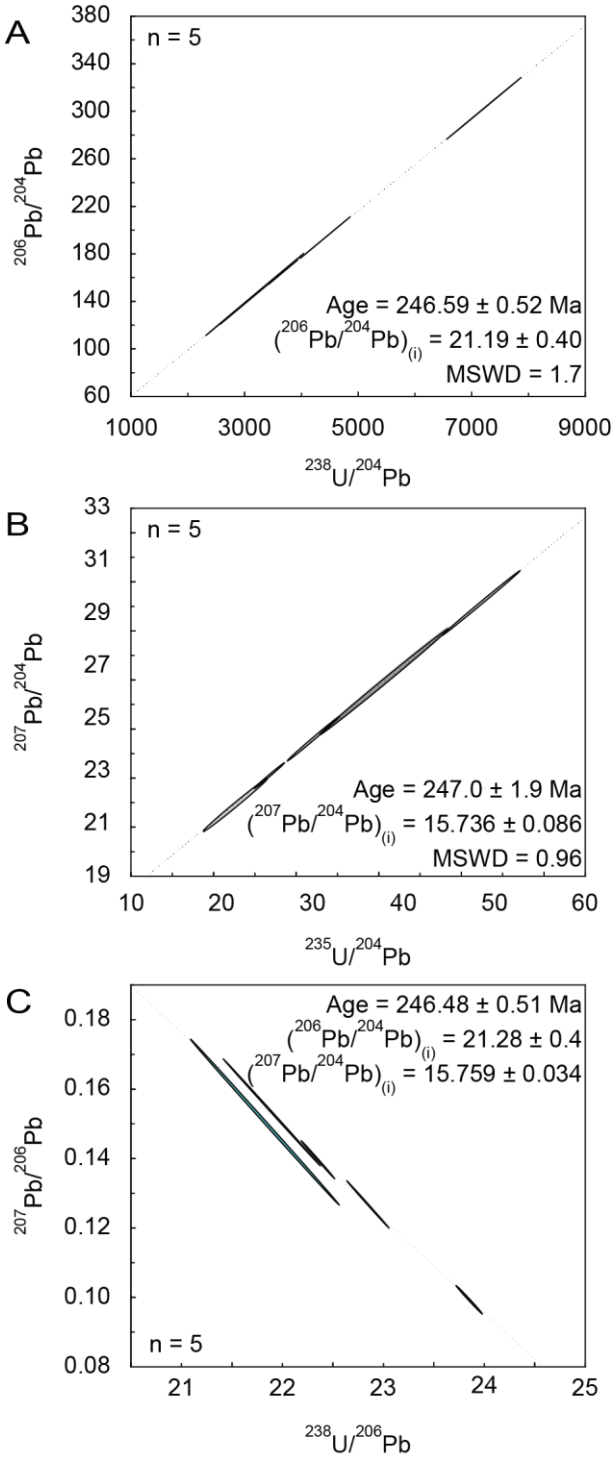

Figure 54: ID-TIMS U–Pb isochron data for the Yankee cassiterite as presented in Appendix 2.

3.3 Ardlethan Granite tin deposits

The geological context of the Ardlethan Sn system is documented in Chapter 2. A summary of the geochronological constraints is presented here. The geological map and cross section of the region, with the location of samples in this study are shown in Figure 55. Igneous activity in the Ardlethan region begins with synchronous intrusion of the S-type Mine Granite and Microgranitic dykes at 428.1 ± 2.8 Ma and 428.3 ± 1.7 Ma, respectively (SHRIMP U–Pb zircon age dating; Bodorkos *et al.,* 2013). This is contemporaneous with widespread S-type granite emplacement of the Koetong Supersuite in central Lachlan Orogen (Chappell *et al.,* 1988; Bodorkos *et al.,* 2013, 2016).

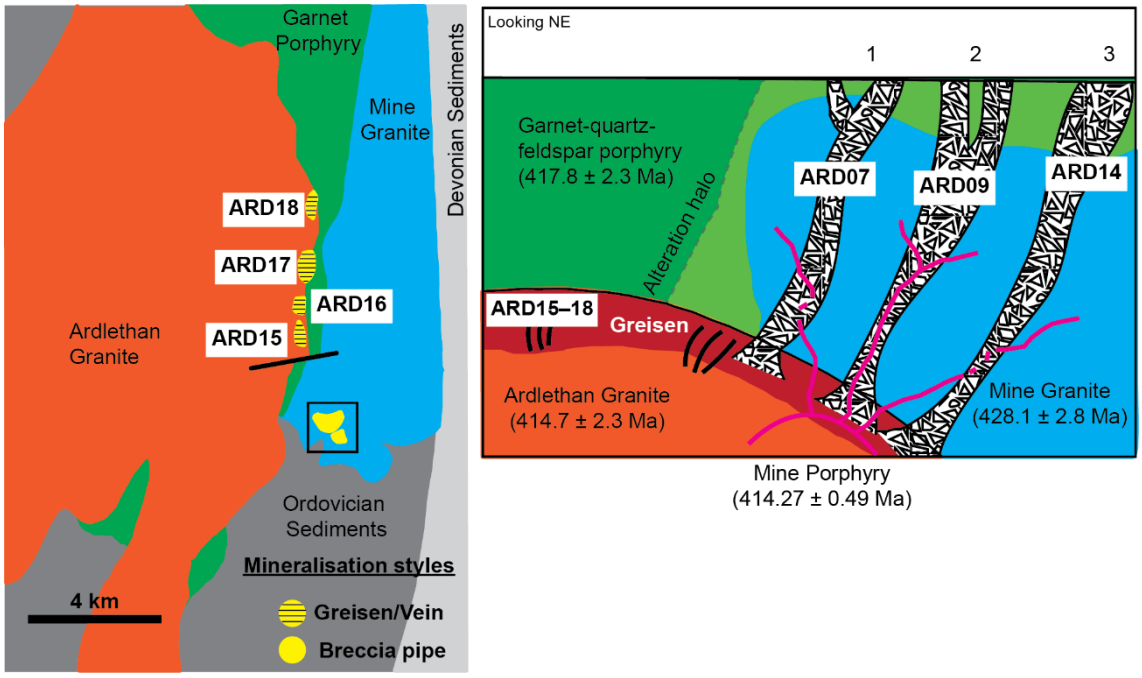

Figure 55: Geological map (left) and schematic cross-section of the Ardlethan region Sample locations are shown on the left, and their general location vertically on the right. The outlined region in the geological map indicates the location of the cross-section. U–Pb zircon ages for the igneous units are from Bodorkos et al. (2013) and Blevin (pers comm). The left and right panels have been modified from images presented in Ren et al. (1989).

The garnet–quartz–feldspar porphyry (GQFP) was originally defined as an intrusive unit with a transitional boundary with the Ardlethan Granite (Ren *et al.,* 1995). Recently the GQFP was reclassified as a quartz-rich ignimbrite that overlies the Ardlethan Granite (Bull *et al.,* 2017). SHRIMP U–Pb zircon dating indicates emplacement at 417.8 ± 2.3 Ma, contemporaneous with Gurragong Volcanics further north (Colquhoun *et al.,* 2005; Bodorkos *et al.,* 2013). The Ardlethan Granite yields a SHRIMP U–Pb zircon age of 414.7 ± 2.3 Ma (Bodorkos *et al.,* 2013).

SHRIMP U–Pb zircon dates of the Mine Porphyry indicate emplacement at 412 ± 1.9 Ma (Bodorkos *et al.,* 2013). This is confirmed by more precise TIMS dating on eight zircon grains that yield a weighted mean $^{206}Pb/^{238}U$ date of 414.27 ± 0.11 Ma (MSWD = 1.7, probability of fit = 0.11) (Blevin pers comm). Ren *et al.* (1995) described multiple stages of brecciation. In places the Mine Porphyry as cross-cut by brecciated zones, and elsewhere it cross-cuts brecciated zones, indicating synchronous emplacement (Ren *et al.,* 1995)

Despite synchronous emplacement ages, the Ardlethan Granite and Mine Porphyry have radically different $\varepsilon Nd_{(i)}$ compositions and inferred source rocks (See Chapter 2). The chemistry of tourmaline occurring with cassiterite indicates that cassiterite mineralisation originates from fluids derived from the Ardlethan Granite. Contrary to the interpretation of Walshe *et al.* (2011), this indicates that fluids derived from the Mine Porphyry were not related to cassiterite mineralisation at Ardlethan (Chapter 2).

Cassiterite mineralisation associated with the Ardlethan Granite occurs in three geological environments: 1) greisen alteration in the apical zones of the Ardlethan Granite (Scott and Rampe, 1984), 2) within veins associated with greisen zones of the Ardlethan Granite (Scott and Rampe, 1984), and 3) as breccia infill within pipes within the Mine Granite but converge on the Ardlethan Granite contact (Ren *et al.,* 1995) (Figure 55).

3.2.1 Cassiterite samples from Ardlethan

Three cassiterite samples were collected from the breccia pipes surrounding the Ardlethan Granite, and four samples from veins and greisen altered rock within the Ardlethan Granite. The location of these samples is shown in Figure 55 and images and descriptions of the hand samples are provided in Chapter 2. ARD07c, ARD15c, ARD16c and ARD18c are directly associated with tourmaline analysed in Chapter 2. ARD09c originates from a different sample from the same deposit where cassiterite and tourmaline appear to have coprecipitated. ARD14c precipitated prior to ARD14t as discussed in Chapter 2.

The internal structure of cassiterite grains were imaged on an EMP with a CL detector using the methods documented by Carr *et al.* (2017) and are shown in Figures 56–58. Luminescence in cassiterite is most sensitive to substitution of Ti, Fe and W for Sn (Hall and Ribbe, 1971; Farmer *et al.*, 1991), The three samples of breccia-hosted cassiterite include concentric and oscillating zoning of predominantly weak (quenched) features (Figure 56), interrupted by thin, sharp light bands that appear parallel to crystal faces. Banding is predominantly thin, <5 µm, and can be either defined (ARD07c and ARD09c) and in places diffuse (ARD14c). Most grains show straight-edge banding related to the crystal structure (e.g. Figures 56A, B, and 57B, C), and more rarely other grains show curved banding (Figures 56C and 57A). Secondary alteration of cassiterite occurs along grain boundaries or fractures within grains and is characterised by overexposed features in Figures 56 and 57. Mineral inclusions are rare and are predominantly quartz and mica (Figure 56B).

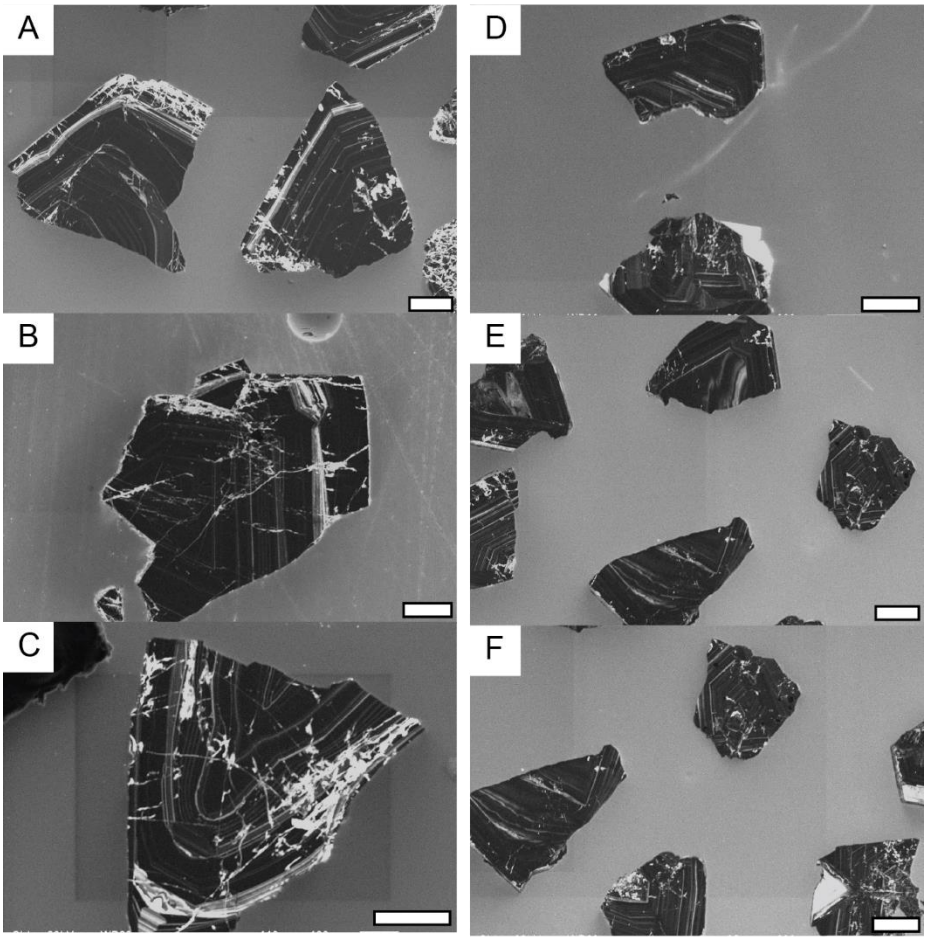

Figure 56: CL images of breccia-hosted cassiterite at Ardlethan. Samples originate from the Mine Breccia Pipe (ARD07c; A–C) and the Carpathia Breccia Pipe (ARD09c: D–E). The scale bar = 100 µm.

Four samples were collected from veins and greisen altered rocks of the Ardlethan Granite and the CL images are shown in Figure 58. Unlike breccia-hosted cassiterite, cassiterite from within the Ardlethan Granite is dominated by strong and weak luminescing features, with predominantly concentric zoning. Diffuse banding is more common (e.g. Figure 58B, D). Banding is commonly cross-cut by banding with different orientation that Carr *et al.* (2017) attributed to changing crystallographic orientation and indicating intergrown crystals. Banding is predominantly straight, although curved banding occurs rarely (Figure 58L). Core–mantle–rim relationships, similar to that of zircon, occur rarely and indicate multiple generations of cassiterite growth in changing fluid compositions (Figure 58J). Mineral inclusions are common, including micas (Figure 58G) and quartz (Figure 58L). Secondary features are more common in vein and greisen altered rock samples compared to breccia-hosted samples, in particular in samples ARD15 and ARD16 (Figure 58G–L).

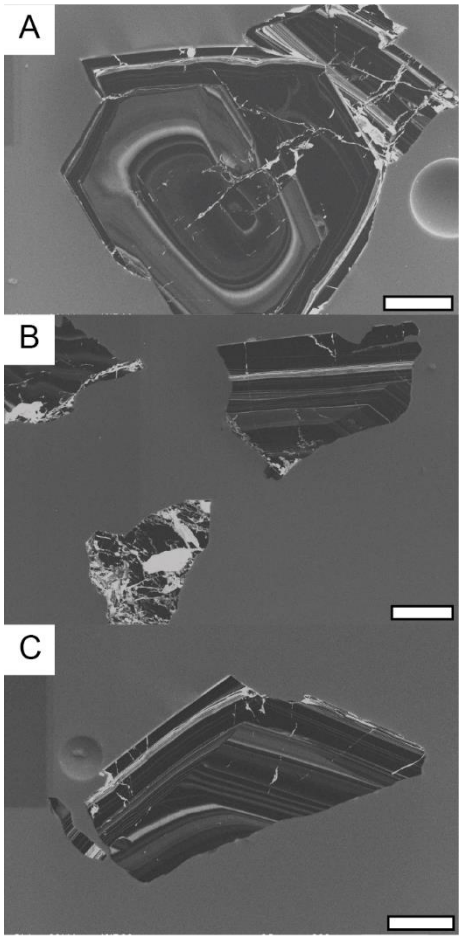

Figure 57: CL images of breccia-hosted cassiterite within the White Crystal Breccia Pipe at Ardlethan. The scale bar = 100µm.

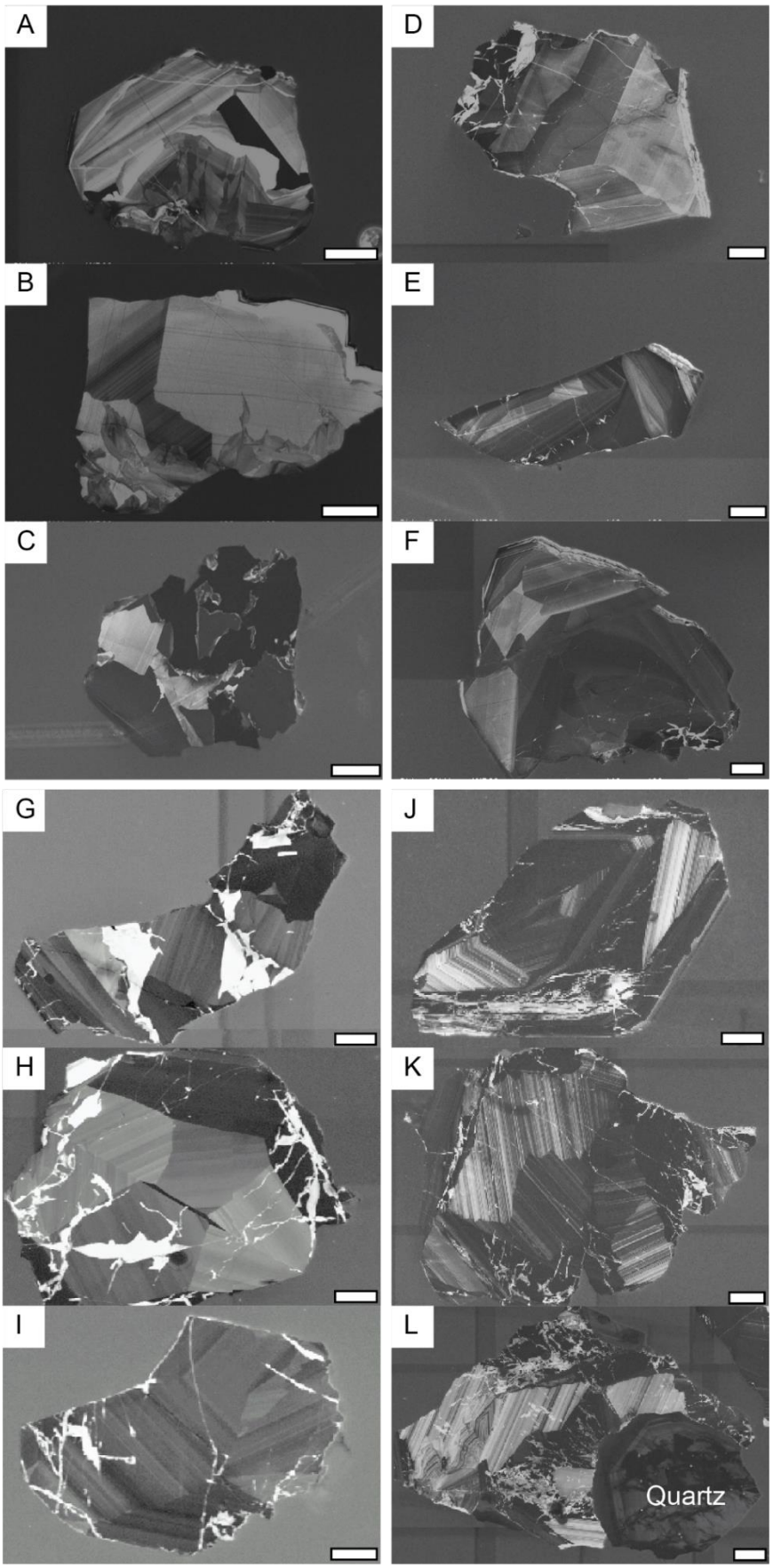

Figure 58: CL images of cassiterite from vein and greisen altered rock within the Ardlethan Granite. ARD18; A–C, ARD17; D–F, ARD16; G–I ARD15: J–L. The scale bar = 100 µm.

3.4 Mole Granite

The geological context of the Mole Granite Sn system is documented in Chapter 2. The geological map and cross section of the region, with the location of samples in this study are shown in Figure 59. A summary of the geochronological constraints is presented here. SHRIMP U–Pb zircon ages from the seriate and porphyrtic phases of the Mole Granite (Figure 59) are indistinguishable at 247.2 ± 2.2 Ma (Laker, 2017) and 249.8 ± 1.5 Ma (Chisholm *et al.,* 2014), respectively. A single sample from the microgranite phase has an age of 248.6 ± 5.8 Ma, indistinguishable from the main mass of the Mole Granite (Laker, 2017). Schlattegger *et al.* (2005) reported U–Th–Pb ages for magmatic zircon and monazite by ID-TIMS at 247.6 ± 0.4 Ma and 247.7 ± 0.5 Ma, respectively. Kleeman *et al.* (1997) reported a whole-rock Rb–Sr isochron age for the Mole Granite at 246 ± 2 Ma. Inclusion of whole-rock data included in Chapter 2 and using the new ^{87}Rb decay constant of Villa *et al.* (2015) this age becomes 247.1 ± 4.1Ma (MSWD = 0.44, n=9) (Figure 42 in Chapter 2).

^{40}Ar/^{39}Ar and K/Ar ages of muscovite and biotite within sheeted vein deposits and fluorite veins range between 247 ± 2 Ma and 245 ± 1 Ma (Kleeman *et al.,* 1997). Hydrothermal xenotime within quartz–cassiterite veins of the Yankee deposit yields a U–Th–Pb age of 246.2 ± 0.2 Ma (Schlattegger *et al.,* 2005). Cassiterite from a different sample, but within the Yankee deposit yields a similar ID-TIMS U–Pb age of 246.48 ± 0.51 Ma and indicates simultaneous mineralisation with hydrothermal xenotime (Appendix 2).

Monazite with a U–Th–Pb age of 244.4 ± 1.4 Ma indicates either prolonged hydrothermal circulation following the Mole Granite emplacement, or the arrival of a new intrusion (Schlattegger *et al.,* 2005). ^{40}Ar/^{39}Ar and K/Ar ages from muscovite and biotite show the silexite and associated veining continue to 241 ± 2 Ma (Kleeman *et al.,* 1997).

There are two hypotheses regarding the absolute age and duration of mineralisation associated with the Mole Granite: 1) emplacement of the Mole Granite at 246 ± 2 Ma followed by sustained hydrothermal activity and cassiterite mineralisation for 3–5 Ma until 241 Ma (Kleeman *et al.,* 1997), and 2)

shallow emplacement of the Mole Granite at 246.2 ± 0.5 Ma and instantaneous rapid cassiterite mineralisation within method precision (Pettke *et al.,* 2005; Schlattegger *et al.,* 2005). The authors of the second hypothesis infer that zircon (247.6 ± 0.4 Ma) and monazite (247.7 ± 0.5 Ma) saturation in the parental magma occurred early in magmatic crystallisation and differentiation at lower crustal levels or during ascent. Emplacement of the granite in upper crustal levels occurred immediately prior to hydrothermal xenotime formation at 246.2 ± 0.2 Ma (Schlattegger *et al.,* 2005).

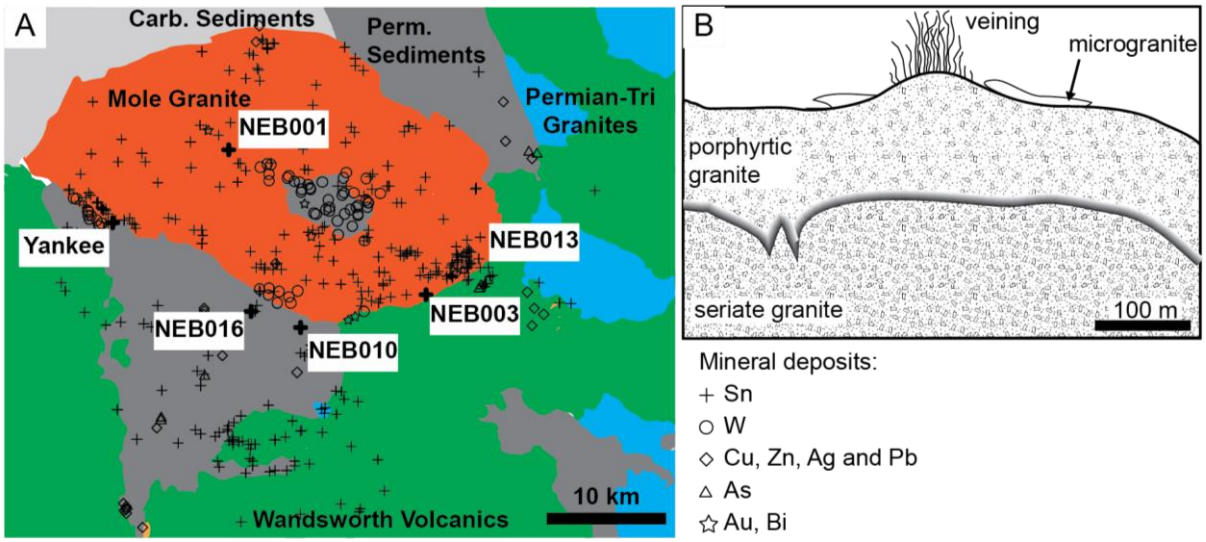

Figure 59: A) Geological Map of the Mole Granite with the locations of small to large mineral deposits, and samples of this study. B) A schematic cross section through the Mole Granite showing the relationships between key textural phases of the granite. Figure modified Audétat et al., 2000b.

3.4.1 Cassiterite samples from the Mole Granite

Cathodoluminescence and secondary electron images for cassiterite of the Mole system are presented in Figures 61–63. Images and descriptions of the samples of which cassiterite concentrates were derived are provided in Chapter 2. NEB001c and NEB003c coprecipitated with quartz with $\delta^{18}O$ values presented in Chapter 2. NEB010c was not included in Chapter 2. The sample originates from the De Milhous deposit to the south of the Mole Granite within the Bondonga Beds (Figure 59). It includes quartz veins with cassiterite and in places beryl (Figure 60). Cassiterite and beryl are euhedral, the former crystallising as grains up to 5 mm in diameter. NEB013c and NEB016c coprecipitate with tourmaline (NEB013t and NEB016t) presented in Chapter 2.

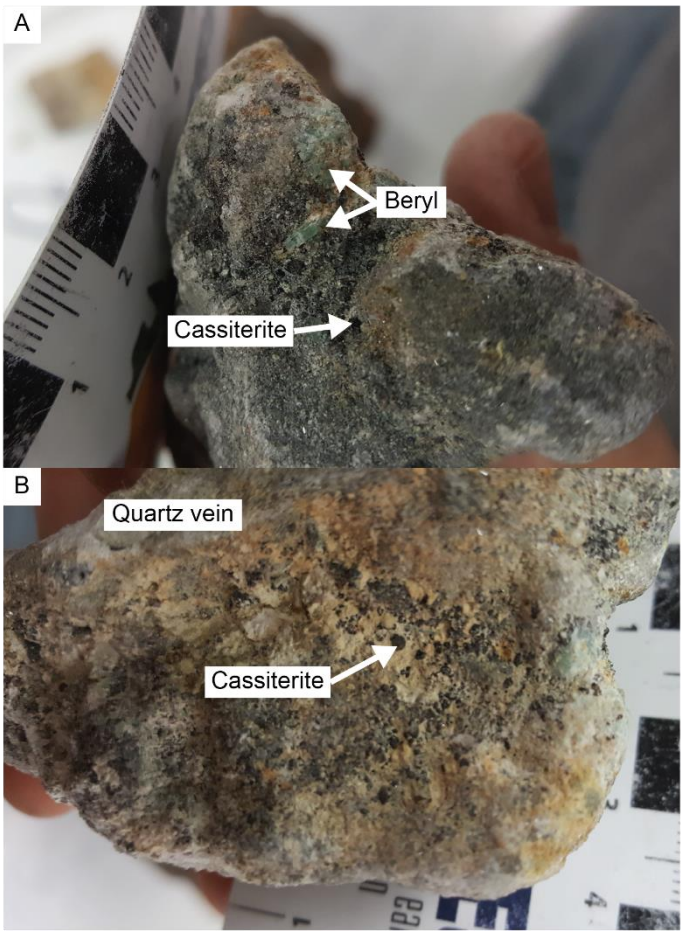

Figure 60: Hand sample image of NEB010 from a quartz–cassiterite–beryl vein in the De Milhous deposit (See Figure 59 for location). See text for description.

3.4.2 Cassiterite and zircon from the Yankee deposit

The Yankee deposit occurs within the southern margin of the Mole Granite (Figure 59). Cassiterite mineralisation is associated with quartz veining and tourmaline. The deposit has been subject to significant research on hydrothermal processes (Audétat *et al.,* 1998, 2000a, 2008; Mavrogenes *et al.,* 2002; Cauzid *et al.,* 2007; Schlattegger *et al.,* 2005; Pettke *et al.,* 2005; Feteke *et al.,* 2016; Carr *et al.,* 2017). Two samples from within the Yankee deposit (Figure 59) contain cassiterite and molybdenite associated with vuggy quartz veins. Zircon was also discovered in heavy mineral separates after processing of the samples using gravimetric and magnetic concentration methods (described below).

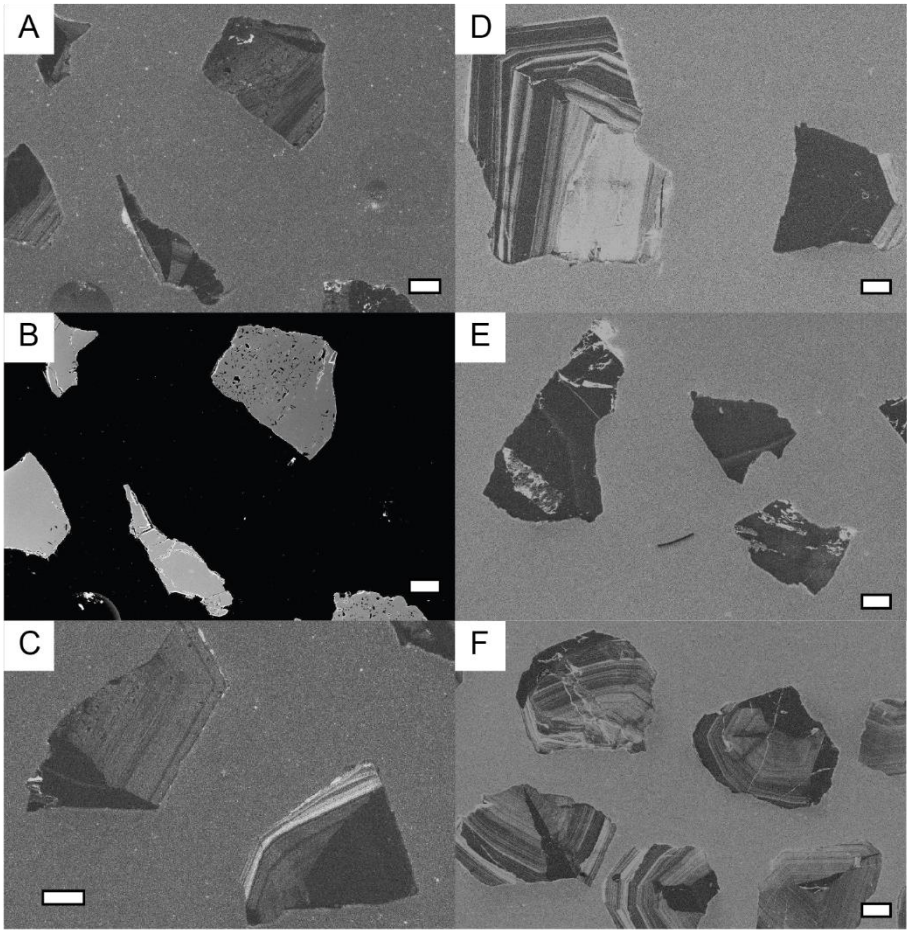

Figure 61: CL images and SEI (B) images of cassiterite from the Yankee deposit. NEB001c is included in A–C, NEB003c is in D–E, and NEB013c in F. The scale bar = 100 µm.

Cathodoluminescence images of cassiterite from NEB100c and NEB101c are displayed in Figure 63. Cassiterite from this deposit is also described by Carr *et al.* (2017) and in Appendix 2. Cassiterite from the Yankee deposit collected in this study includes two dominant textures; sector zoning defined by weak luminescence (e.g. Figure 63B), and the more common oscillatory zoning defined by thin, straight edge laminations. Carr *et al.* (2017) showed that orientation changes in laminations are commonly, but not ubiquitously associated with changes in crystal structure of cassiterite, indicating intergrown crystals in each grain. Strong variations in luminescence can be observed in single grains (e.g. Figure 63B, E). In Figure 63A, cassiterite has coprecipitated with quartz. Weak luminescent features penetrate through oscillatory laminations in Figure 63F, indicating secondary disturbance of primary layering. Strong CL material regularly infiltrates cassiterite grains along cracks (e.g. Figure 63A, B), and in places is associated with recrystallisation within the grain (e.g. Figure 63D).

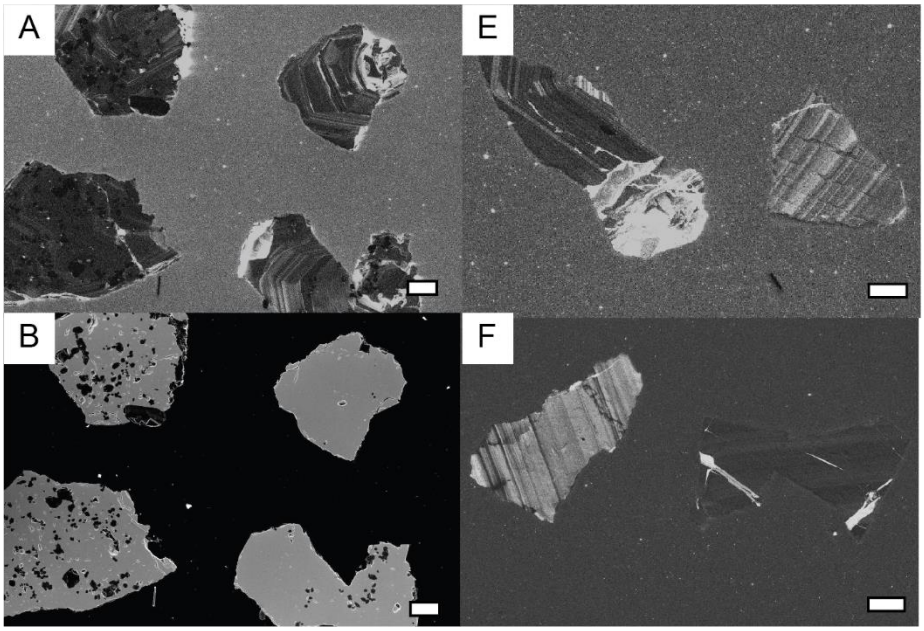

Figure 62: CL and SEI images of cassiterite hosted with the country rocks surrounding the Mole Granite. NEB010c is shown in A and B, NEB016c is shown in E and F. The scale bar = 100µm.

The internal chemical structure of zircon was imaged on an SEM with a CL detector and shown in Figure 64 (A, B) for NEB100z and (C, D) for NEB101z. Zircon grains from both samples are between 200–500 µm long and predominantly euhedral to subhedral. Zircons from both samples consist of an inner strongly luminescent segment that is typically not zoned. In places these inner zones are disturbed by weak luminescent segments that cross cut crystal boundaries indicating recrystallisation of the core (e.g. grain D and G). A mantle with pronounced oscillatory zoning is present in most grains with a moderate luminescent responses (e.g. grain F). Frequently this mantle is disturbed by a non-responsive CL section that is strongly pitted in SEI images likely due to a damaged crystal structure. This can form a rim around grains (e.g. grain A or B), or completely replace the grain (e.g. grain C). Schlattegger *et al.* (2005) observed the same pitted and porous overgrowth (they labelled ‘zone C’) in zircon also from the Yankee and attributed it to a late-magmatic or hydrothermal origin.

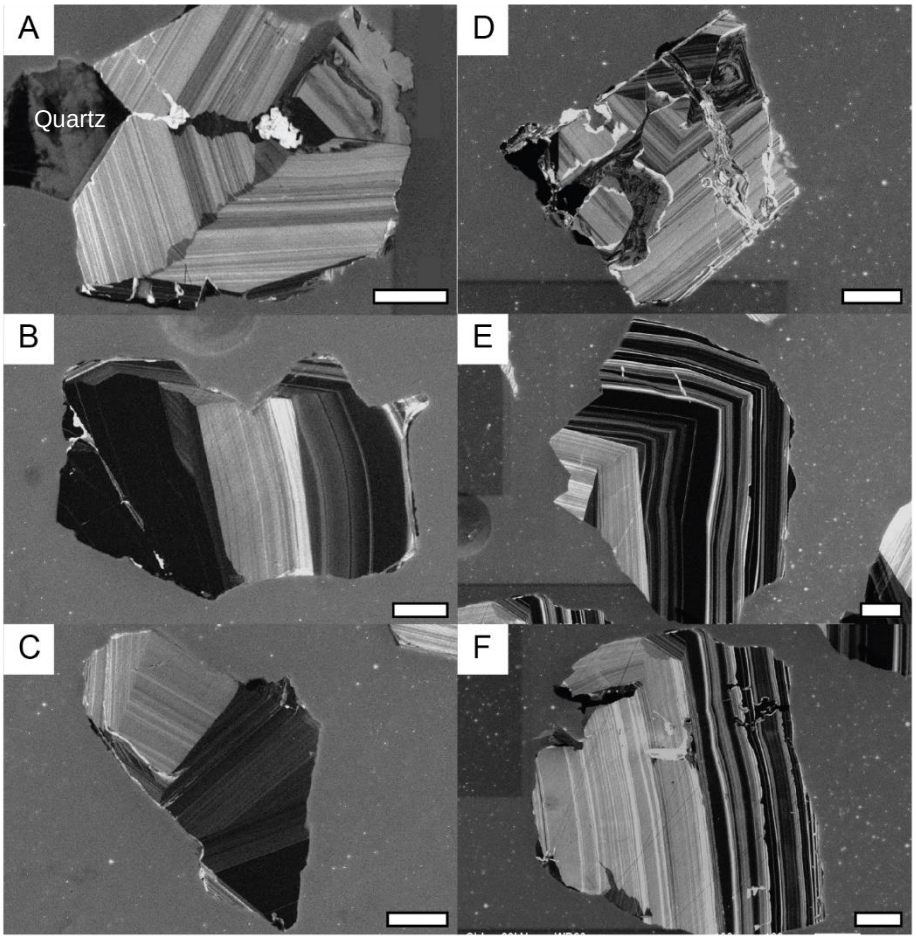

Figure 63: CL images of cassiterite within the Yankee deposit of the Mole Granite. NEB100c is shown in A–C and NEB101c is shown in D–F. The scale bar = 100 µm.

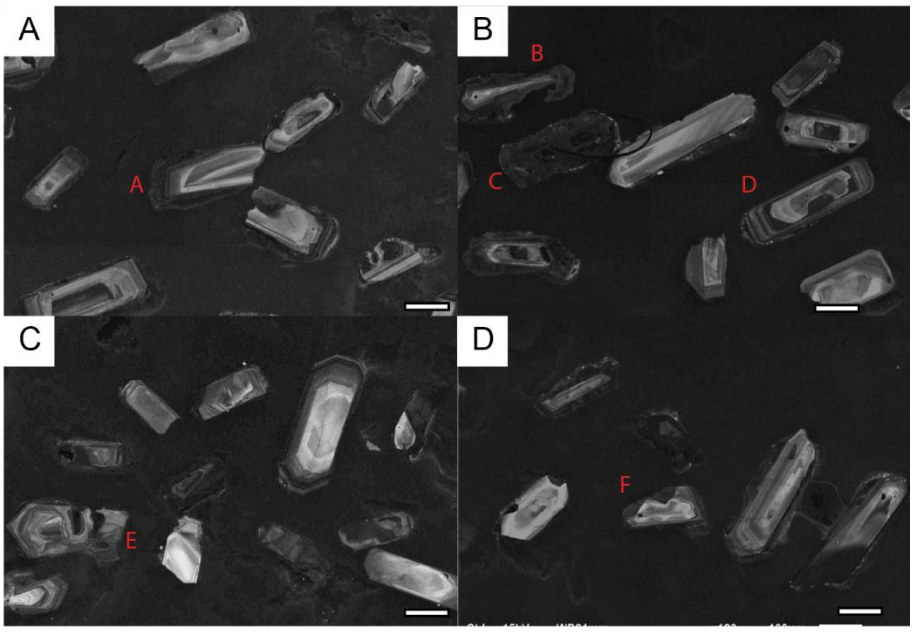

Figure 64: CL images of zircon from Yankee deposit of the Mole Granite. NEB100z is shown in A and B, and NEB101z is shown in C and D. The scale bar = 100 µm.

3.5 Methods

3.5.1 Cassiterite concentrates and imaging

Samples containing cassiterite as identified in hand specimen or thin section were crushed and sieved to >80 µm size fraction. Cassiterite was then concentrated from this fraction using gravimetric separations with TBE and MEI heavy liquids followed by magnetic separations using a Franz magnetic separator. Final purification of the cassiterite fraction was by handpicking grains under binocular microscope. Between 10 and 20 grains of cassiterite were used for each sample depending on grain size. Grains were mounted in 25 mm diameter epoxy mounts and polished initially with grit paper, and then 9 µm, 3 µm and 1 µm diamond paste until a smooth and flat surface was produced. Internal textures of cassiterite were imaged on an SEM with a CL detector using the methods of Carr *et al.* (2017).

3.5.2 U–Pb dating of cassiterite by LA-ICP-MS

U–Pb isotopic compositions of cassiterite were measured by LA-ICP-MS on an Agilent 7700 quadrupole mass spectrometer at the Research School of Earth Sciences, ANU. This system is equipped with an ArF excimer laser with a wavelength of 193 nm and a repetition rate of 5 Hz. The laser system was coupled to the mass spectrometer with a custom-built ANU 'He1Ex' two volume vortex laser ablation cell (Eggins *et al.,* 1998). Ablation was performed in a He environment and combined with an argon and hydrogen carrier gas prior to introduction to the plasma. Spot diameters of 93 and 157 µm were used depending on crystal sizes. In conjunction with ^{206}Pb, ^{207}Pb, ^{208}Pb, ^{232}Th and ^{238}U, up to 20 other isotopes were measured for trace element abundances (only U–Th–Pb concentrations are presented here). Each sample was measured over 40 seconds periods (~90 integrations) not including pre- and post-ablation rinse times of 25 seconds to allow for element signals to return to background levels between analyses. Background counts of Sn were the most problematic after ablation of cassiterite, particular for sensitivity in the NIST612 glass that has 38 ppm Sn. The data were reduced in IoLite (Paton *et al.,* 2011) using the data reduction scheme of Chew *et al.* (2014) for U–Pb and Woodhead *et al.* (2007) for trace elements. Instrument induced fractionation of U–Pb isotopes was accounted for using the Yankee lode cassiterite assuming an age

of 246.48 ± 0.51 Ma (Figure 54; Appendix 2). The Yankee cassiterite contains minor, but highly radiogenic common Pb, so the data reduction scheme of Chew *et al.* (2014), which can correct for common Pb in reference material, was used. U–Th–Pb concentrations of cassiterite were determined using the NIST612 glass (Jochum *et al.,* 2011) for normalisation and Sn as an internal standard assuming stoichiometric concentration for cassiterite (78.77 wt.%). The 208- and 207-correction methods for common Pb corrections were both tested using age appropriate compositions of Stacey and Kramers (1975), and the composition determined in the Yankee cassiterite by ID-TIMS (Appendix 2) for the Mole Granite samples.

3.5.3 U–Pb dating of zircon by SHRIMP

Zircon concentrates were derived from two samples coexisting with cassiterite in the Yankee deposit. Zircon grains were mounted in 25 mm diameter epoxy mounts with the Temora 2 and SL13 reference zircons (Black *et al.,* 2004) and polished using grit paper and 9 µm, 3 µm, 1 µm and ¼ µm diamond impregnated paste. The internal structure of zircon grains was imaged on a SEM with a CL detector using the methods of Hoskin (2000) and presented in Figure 64. After imaging, the mounts were cleaned and coated with a 30 nm gold film and dehydrated overnight in an 60^{o}C oven prior to insertion into SHRIMP II.

The U–Th–Pb isotopic composition of zircons was analysed on SHRIMP II at RSES, ANU using similar procedures to Williams (1998) and Ickert and Williams (2011). A primary ion beam of O_2^- was accelerated at 10 kV and focused to produce a 25 µm diameter spot on the zircon surface. The primary beam operated between 2 and 4 nA during the session. Mass resolution, defined by 1% peak definition, was approximately 5000. Positive secondary ions were extracted at 10 kV and then measured on a single electron multiplier cycling through U–Th–Pb isotopes of interest and ^{90}Zr as the index channel. Ionisation fractionation between U and Pb was corrected assuming a power law relationship between $^{206}Pb^+/^{238}U^+$ and $^{238}U^{16}O^+/^{238}U$ (Claoué-Long *et al.,* 1995) and normalising to the Temora 2 reference zircon (Black *et al.,* 2004). U concentrations were determined by normalisation to the SL13 reference zircon (Williams, 1998). Data were reduced in SQUID 2.5 (Ludwig, 2011). Common Pb

corrections used compositions defined be the Stacey and Kramers (1975) terrestrial Pb model for 250 Ma.

3.6 Results

3.6.1 Ardlethan Granite cassiterite U–Th–Pb data

LA-ICP-MS U–Pb isotopic analyses of cassiterite from the Ardlethan Granite are summarised in Table 20 and Figures 65 and 66. The complete dataset is included in Appendix 6. U concentrations from all samples varied between 0.2–26 ppm, and predominantly <5 ppm and Pb concentrations from all samples varied between 0.06–6.36 ppm, of which the vast majority is ^{206}Pb (0.06–6.36 ppm). Th is commonly below the detection limit (~0.005 ppm) and up to 0.2 ppm and Th/U ratios are <0.05. Wetherill (1956) (W-) and Tera and Wasserburg (1974) (TW-) concordia isochron relationships for each sample are shown in Figure 65 for breccia-hosted cassiterite, and Figure 66 for greisen-hosted cassiterite.

Table 20: U–Pb isotopic compositions determined by LA-ICP-MS on cassiterite from deposits surrounding the Ardlethan Granite. Sample locations are shown in Figure 55.

Sample	W-	±2SE	T-W-	±2SE	208 cor. ^{206}Pb/^{238}U	±2SE	207 cor. ^{206}Pb/^{238}U	±2SE
ARD07c	412.6	2.9	413.0	2.8	414.8	1.7	414.6	1.8
ARD09c	414.4	2.6	414.8	2.5	414.4	2.1	414.6	2.2
ARD14c	418.7	2.9	420.1	4.3	421.6	3.0	421.5	3.1
ARD18c	410.3	2.1	410.5	2.1	410.5	2.3	409.7	2.6
ARD17c	416.3	1.9	416.2	1.9	416.7	1.8	416.7	2.0
ARD15c	414.4	1.5	414.9	1.4	414.8	1.6	415.3	1.6
ARD16c	415.0	2.5	415.6	2.2	416.0	1.7	416.5	2.5

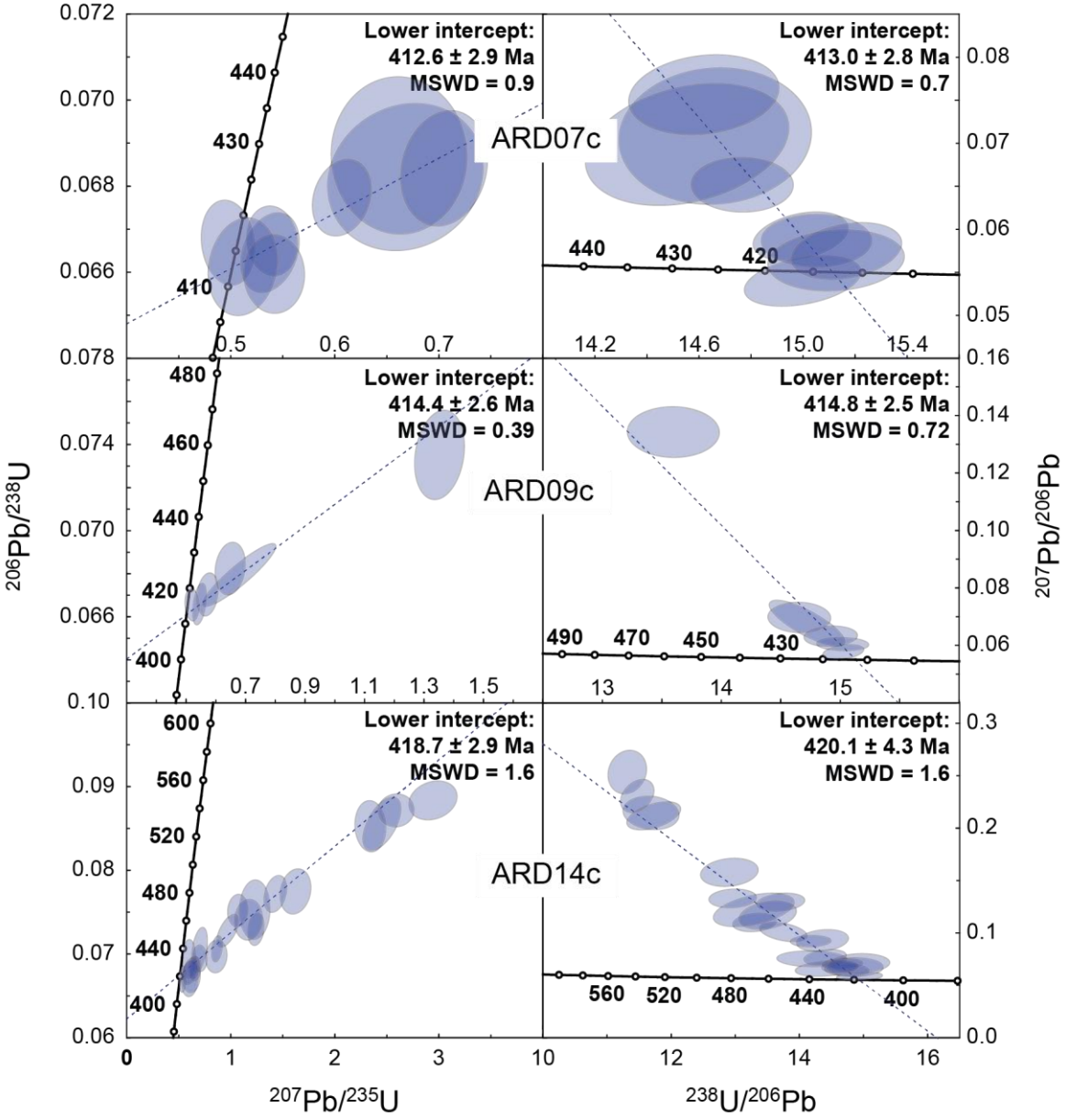

Figure 65: Wetherill (1956) (left) and Tera and Wasserburg (1975) (right) concordia diagrams for breccia-hosted cassiterite at Ardlethan.

Breccia-hosted cassiterite contains variable common Pb that defines discordance lines (Figure 65). ARD14c contains the largest common Pb component that includes four highly discordant analyses (>70%; Figure 65), which are included in age calculations. Removal of these four analyses yields lower intercept isochron ages *ca* 2 Ma younger. The W-concordia age of ARD14c is within error, although slightly younger than the TW-concordia intercept age and common Pb corrected ages (Table 20). The errors in measuring $^{207}Pb/^{238}U$ and $^{206}Pb/^{238}U$ are more strongly correlated than $^{206}Pb/^{238}U$ and $^{207}Pb/^{206}Pb$. Therefore, TW linear regression through the concordia are more poorly defined than W-concordia. The upper concordia

intercept of the TW discordia in Figure 65 indicates an initial $^{207}Pb_c/^{206}Pb_c$ composition of 0.809 ± 0.065 (2SD), which is lower than the Stacey and Kramers (1975) value at 410 Ma of 0.86 ± 0.007. Removal of the four highly discordant analyses lowers the upper concordia intercept to 0.7 ± 0.085. Despite this, the agreement between isochron intercept ages and common Pb corrected ages are within error (excepting AR14c W-concordia), indicating that the assumed common Pb compositions of Stacey and Kramers (1975) are broadly appropriate. Richards *et al.* (1982) reported Pb isotopic compositions of galena from the Ardlethan deposit that were slightly more evolved than Stacey and Kramers (1975) but does not significantly change the corrected ages. Ages of the two samples from the Mine (ARD07c; 414.8 ± 1.7 Ma) and Carpathia (ARD09c; 414.4 ± 2.1 Ma) breccia pipes are within error, and yield a mean weighted 208-corrected $^{206}Pb^*/^{238}U$ age of 414.6 ± 1.3 Ma, whilst the sample from White Crystal breccia pipe (ARD14c), that is most distal from the Ardlethan Granite, is older at 421.6 ± 3.0 Ma (Table 20).

Three greisen-hosted cassiterites also contain variable common Pb that defines W- and TW-concordia isochron lower intercept ages within error of each other at *ca* 415 Ma, whilst ARD04c is resolvable and younger at 410.3 ± 2.1 Ma (Table 20). Isochron intercept ages and $^{206}Pb/^{238}U$ ages with 208 and 207 common Pb corrections are similar, indicating model common Pb compositions are appropriate.

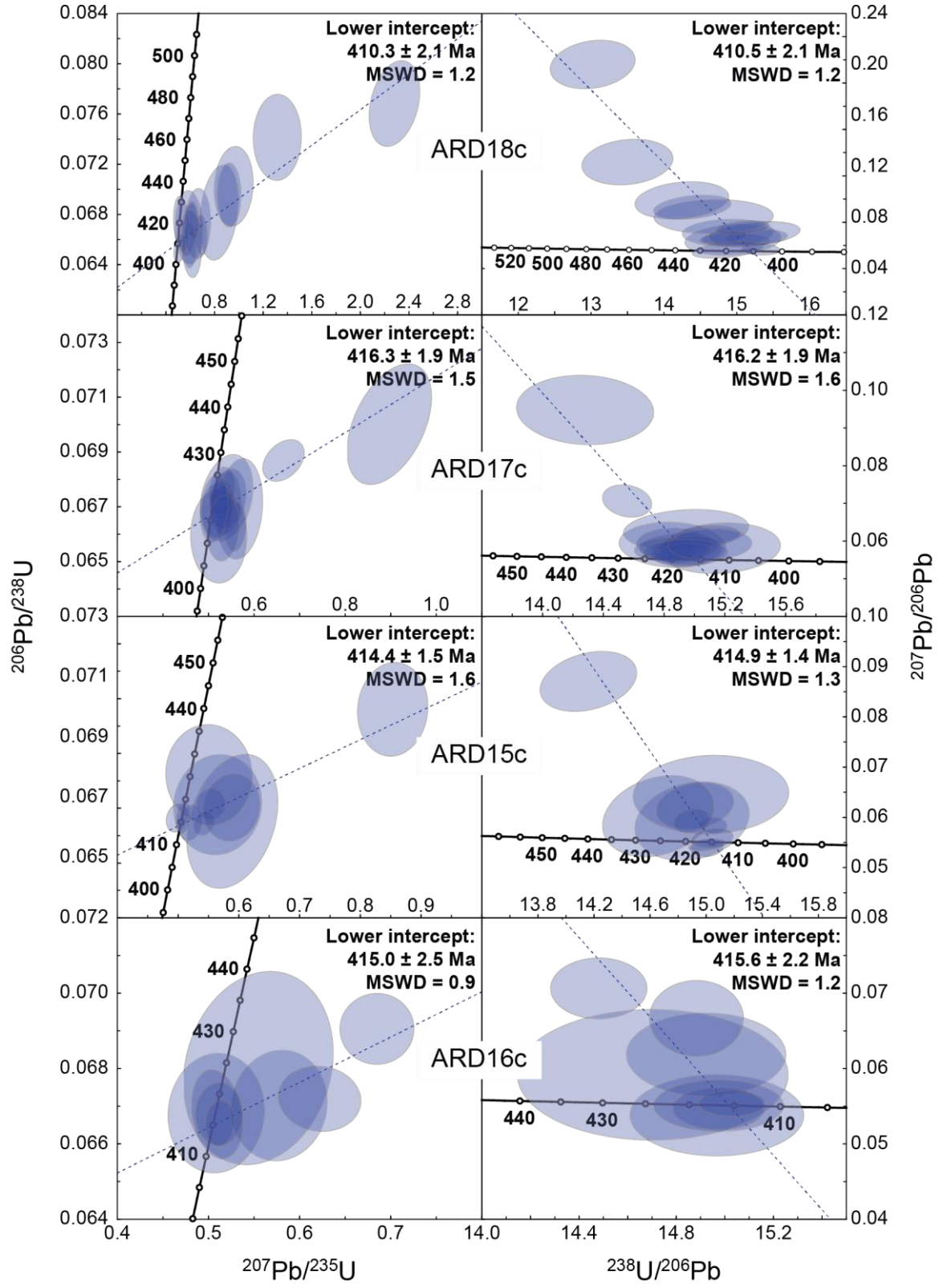

Figure 66: Wetherill (1956) (left) and Tera and Wasserburg (1975) (right) concordia diagrams for greisen-hosted cassiterite at Ardlethan.

3.6.2 Mole Granite cassiterite U–Th–Pb data

LA-ICP-MS U–Pb isotopic analyses of cassiterite from the Mole Granite are summarised in Table 21 and Figures 67 and 68. The complete dataset is included in Appendix 6. U concentrations from all samples varied between 1.17–425 ppm. Total Pb concentrations are between 0.09 and 7.15 ppm of which the vast majority (>94%) is ^{206}Pb. ^{238}U and ^{206}Pb are less abundant in cassiterite NEB001c and NEB003c occurring within the Mole Granite (^{238}U = 25.40–425 ppm; ^{206}Pb =0.09–11 ppm), compared to NEB010c and NEB016c cassiterite occurring within the country rocks (^{238}U = 1.99–49.40 ppm; ^{206}Pb = 0.3–7.2 ppm). Th is commonly below the detection limit (~0.001 ppm) and up to 0.25 ppm. W- and TW-concordia diagrams for each sample are shown in Figure 67 for cassiterite hosted within the Mole Granite, and Figure 68 for cassiterite hosted within the surrounding country rocks.

*Table 21: Summarised U–Pb cassiterite data by LA-ICP-MS of the Mole Granite system. Common Pb corrected values are from Stacey and Kramers (1975) model at 250 Ma, except for *208 cor ages that use the common Pb composition of the Yankee cassiterite as determined in Appendix 2.*

Sample	W-	±2SE	TW	±2SE	208 cor. ^{206}Pb/^{238}U	±2SE	207 cor. ^{206}Pb/^{238}U	±2SE	*208 cor. ^{206}Pb/^{238}U	±2SE
NEB001c	250.3	2.5	250.0	2.5	248.8	2.1	249.2	2.4	244.7	6.0
NEB003c	251.3	4.3	249.6	2.5	246.4	3.8	247.6	3.9	245.2	4.7
NEB013c	249.3	2.4	249.1	2.4	249.2	1.5	249.7	1.6	248.9	1.7
NEB010c	247.2	2.0	245.2	6.7	247.2	2.3	247.5	2.1	246.5	3.6
NEB016c	250.7	2.7	252	16	249.9	2.4	250.1	2.5	249.9	2.4
NEB100c	249.0	3.3	248.9	3.0	246.7	1.5	247.5	2.0	246.7	1.5
NEB101c	244.3	4.2	244.0	4.3	246.1	2.2	246.7	2.2	245.6	3.5

Cassiterite occurring within quartz veins hosted within the Mole Granite display U–Pb ages that are indistinguishable from each other (Table 21). Variable common Pb within cassiterite defines W- and TW-concordia isochron relationships that are with error of 207-corrected ^{206}Pb/^{238}U ages using Stacey and Kramers (1975) common Pb compositions. NEB001c contains the largest common Pb component and a well-defined discordia on the TW-concordia diagram (Figure 67). This discordia indicates an initial $^{207}Pb_c/^{206}Pb_c$ composition 0.86 ± 0.043 that is within the range of the Stacey and Kramers (1975) estimate for 250 Ma of 0.852 ± 0.007, but not the composition defined by ID-TIMS methods on the Yankee deposit (0.74 ± 0.015; Appendix 2). Concordia intercept ages are slightly older, but within error of 208-corrected ^{206}Pb/^{238}U ages using

Stacey and Kramers (1975) common Pb composition and the 208-corrected $^{206}Pb/^{238}U$ using the Yankee common Pb composition (Table 21).

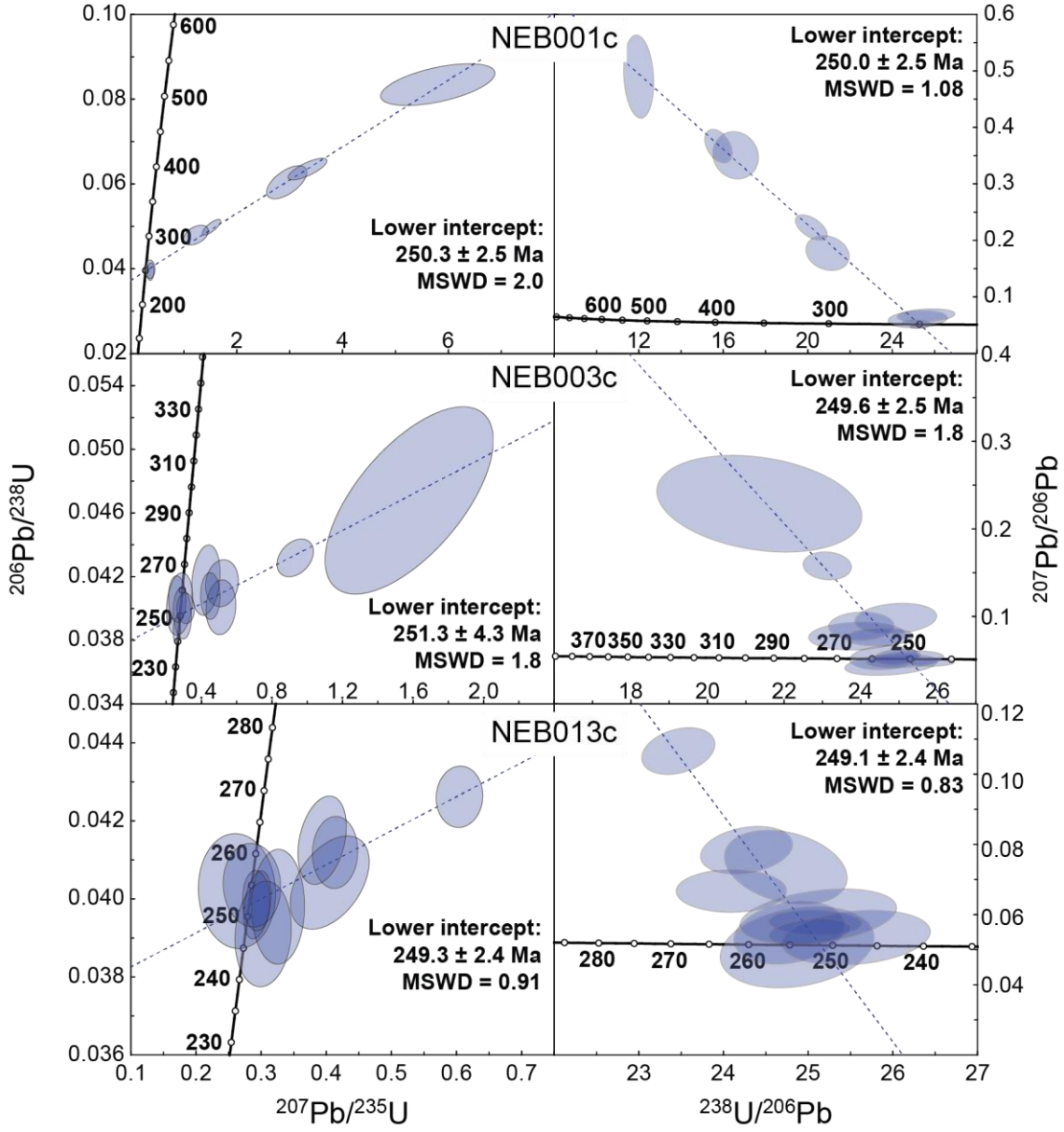

Figure 67: Wetherill (1956) (left) and Tera and Wasserburg (1975) (right) concordia diagrams for cassiterite occurring in quartz veins within the Mole Granite.

The two cassiterite samples (NEB010c and NEB016c) hosted by country rocks yield concordia intercept ages (247.2 ± 2.0 Ma and 250.7 ± 2.7 Ma respectively; Figure 68) and common Pb corrected $^{206}Pb/^{238}U$ ages (247.2 ± 2.3 Ma and 249.9 ± 2.4 Ma respectively; Table 21) marginally within error. NEB016c is relatively imprecise due to a small number of analyses with a large fraction of common Pb. Cassiterite ages of these two samples are within error of cassiterite ages from within the Mole Granite using the 208-corrected $^{206}Pb/^{238}U$

ages with Stacey and Kramers (1975) common Pb composition and the 207-corrected $^{206}Pb/^{238}U$ ages with the Yankee common Pb composition (Table 21).

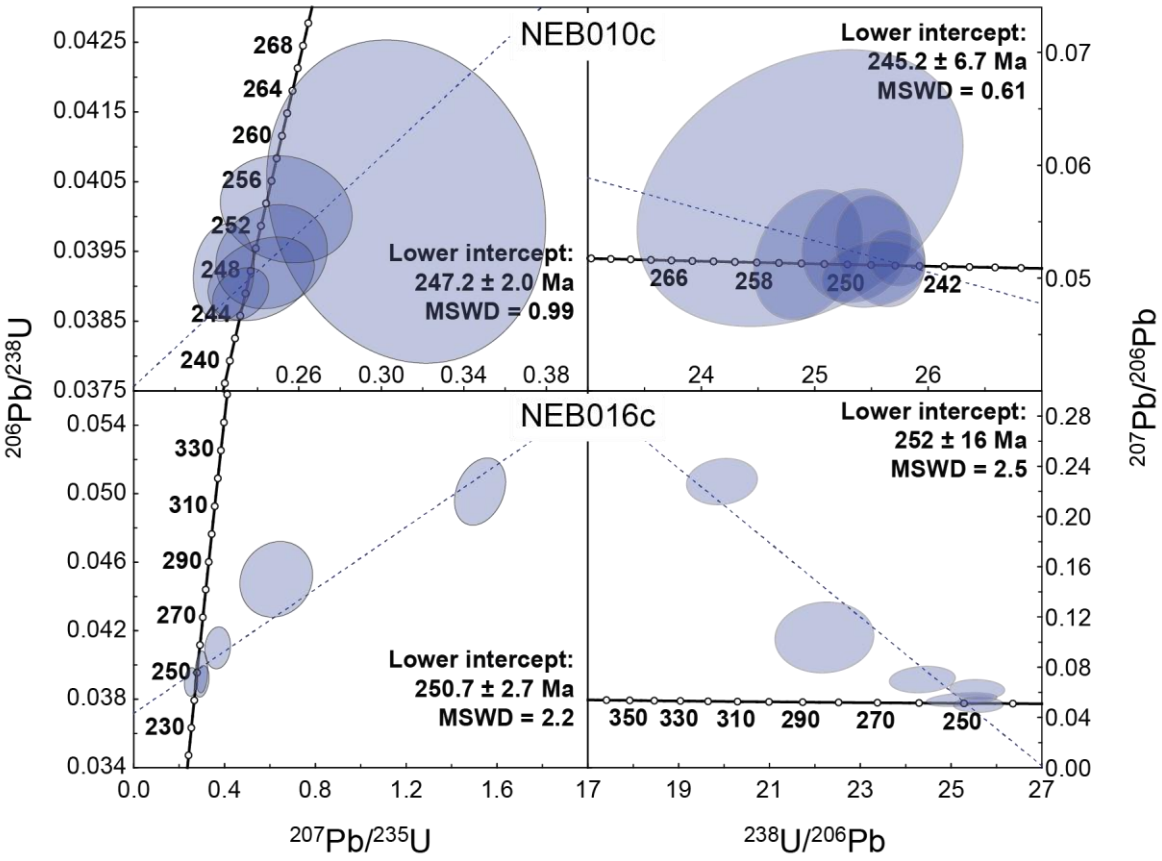

Figure 68: Wetherill (1956) (left) and Tera and Wasserburg (1975) (right) concordia diagrams for cassiterite occurring in quartz veins within the Emmaville Volcanics.

3.6.3 Cassiterite and zircon from the Yankee deposit

LA-ICP-MS U–Pb isotopic age data for cassiterite from the Yankee deposit of Mole Granite are summarised in Table 21 and Figure 69. Concentrations of U in the two samples are between 0.4–27.0 ppm. Th is predominantly below the detection limit (~0.007 ppm), however one analysis in NEB100c is 0.48 ppm and one analysis in NEB101c is 0.43 ppm. ^{206}Pb is the most abundant Pb isotope and is between 0.02 and 0.96 ppm in both samples.

NEB100c included one analyses that was highly discordant and is rejected and not included in Figure 69 or the following discussion. The remaining 16 analyses shown in Figure 69 yield lower concordia intercept ages of 249.1 ± 3.6 Ma for the W-concordia (1956) and 248.7 ± 3.0 Ma for the TW-concordia. Common Pb corrected $^{206}Pb/^{238}U$ ages using the Stacey and Kramers (1975) model for 250 Ma yield similar ages to isochron data, whilst the mean-weighted

208-corrected $^{206}Pb/^{238}U$ age using the Yankee Pb common Pb composition is younger and less precise age at 245.3 ± 2.4 Ma.

NEB101c included 21 analyses that yielded lower concordia intercept ages of 244.3 ± 4.2 Ma and 244.0 ± 4.3 Ma (Figure 70). The 208-corrected $^{206}Pb^*/^{238}U$ age is slightly older at 246.1 ± 2.2 Ma. Removal of the three most discordant analyses (>70%) improves this estimation to 246.3 ± 1.7 Ma. NEB101c contains a spread of concordant analyses with 208-corrected $^{206}Pb^*/^{238}U$ age of individual analysis between 251 ± 8.7 and 232.5 ± 7.4 Ma.

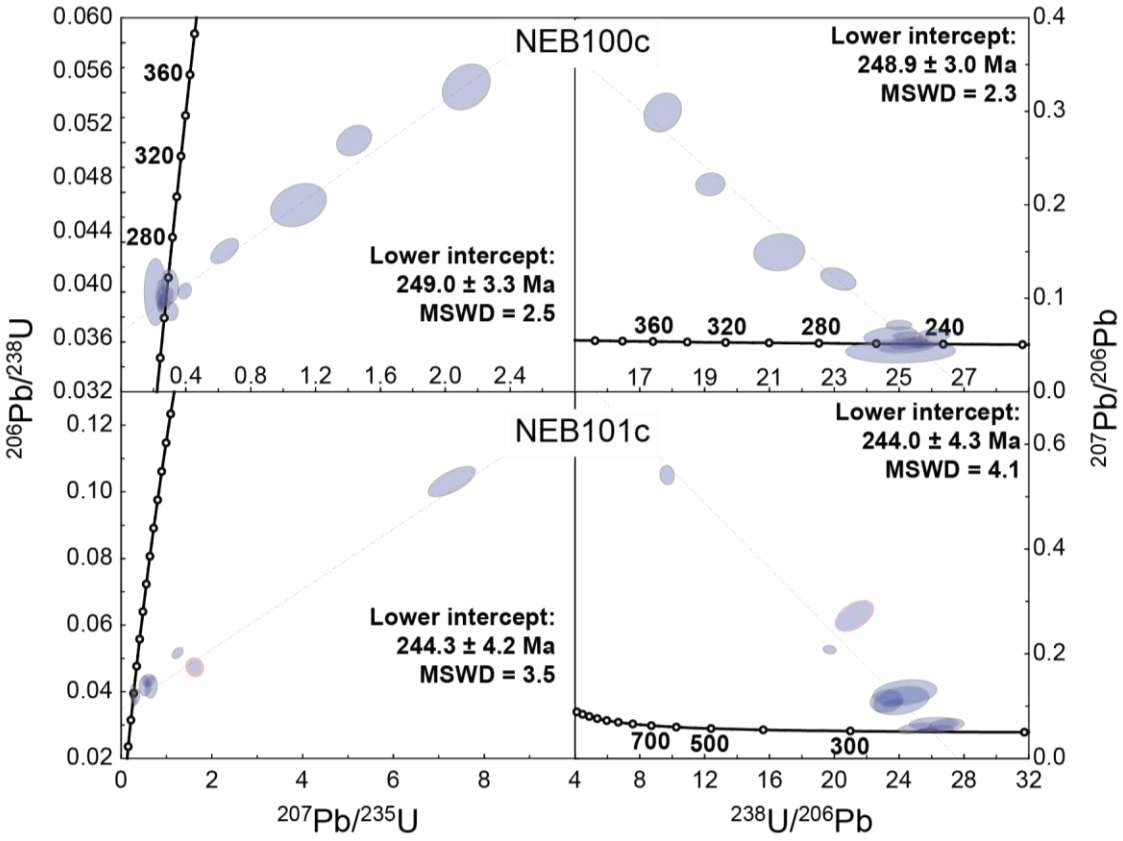

Figure 69: Wetherill (1956) (left) and Tera and Wasserburg (1975) (right) concordia diagrams for cassiterite occurring in quartz veins and zircon (data below) from the Yankee deposit within the Mole Granite.

SHRIMP U–Th–Pb isotopic compositions of the two zircon samples within the Yankee deposit are included in Appendix 6 and summarised in Figure 70. The 204, 207 and 208 correction methods using common Pb compositions of Stacey and Kramers (1975) produce $^{206}Pb/^{238}U$ ages within error of each other, however only the 208-corrected data are shown in Figure 70.

NEB100z contained one discordant analysis (Figure 70) that yields a 207-corrected $^{206}Pb/^{238}U$ age of 233 ± 3 Ma. It is the most ^{232}Th rich analysis (1278 ppm) with Th/U of 0.63. The 208-corrected $^{206}Pb/^{238}U$ age of this analysis is 244 ± 3 Ma. The remaining 22 analyses are concordant and contain between 161–4586 ppm U, 27–792 ppm Th and Th/U between 0.01 and 0.64. The weighted mean 207-corrected $^{206}Pb/^{238}U$ age for these analyses is 245.5 ± 3.1 Ma. Within these sample set there is a coherent population of 17 that defines a mean of 248.74 +2.31/–2.63 Ma (Figure 70A). This population was determined using the *TuffZirc algorithm* within Isoplot that defines a population based on a 'probability of fit' of > 0.05 for ages (Ludwig and Mundil, 2002). Six analyses were rejected from this population. A single older analysis that yields 207-corrected $^{206}Pb/^{238}U$ age of 264 ± 2 Ma, is interpreted to represent an inherited component from earlier zircon growth. The remaining four analyses, that include the discordant analyses discussed previously, define 207-corrected $^{206}Pb/^{238}U$ ages between 242 and 217 Ma. The remaining four analyses originate from strong luminescent features that cross-cut oscillatory zoning (grain E in Figure 64) or

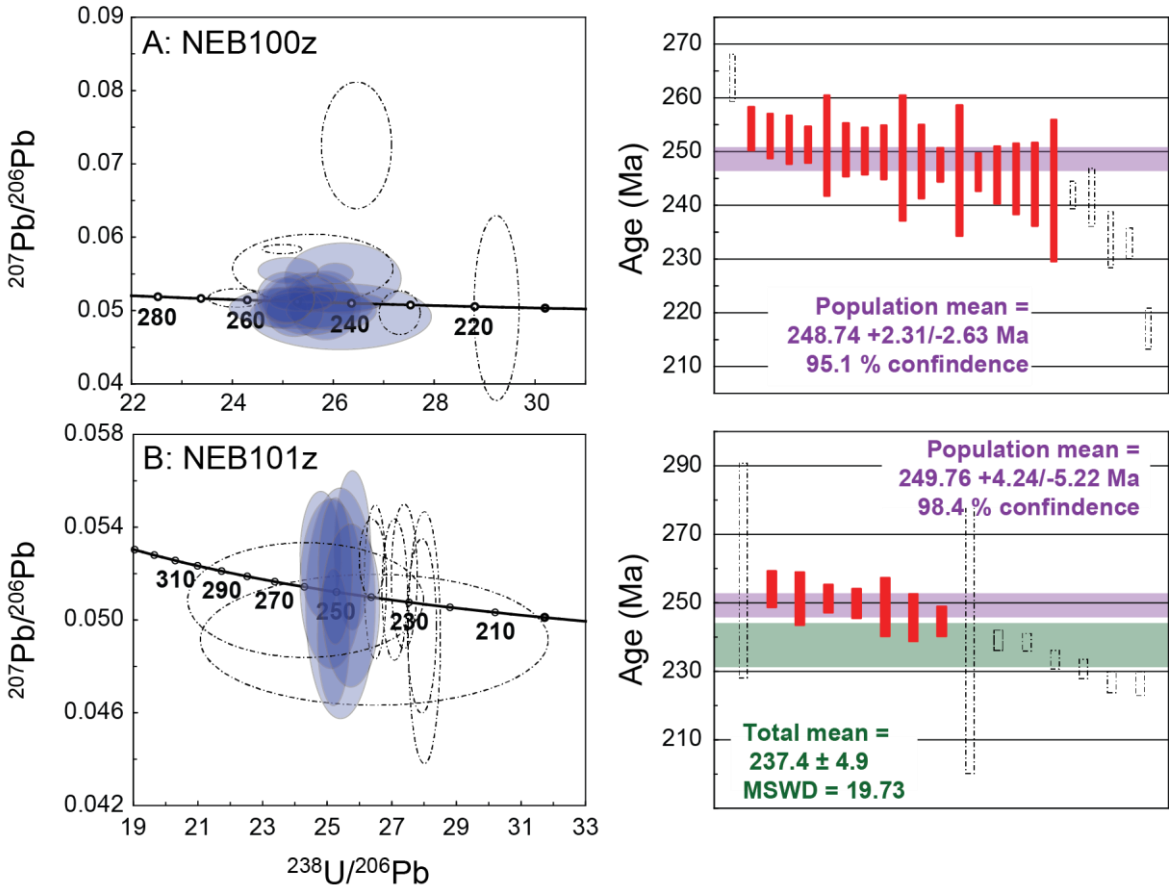

Figure 70: TW-concordia diagrams (left) for zircon from the Yankee deposit in the Mole Granite. Mean-weighted population means are shown on the right. See text for description of data.

weak features that cross-cut core textures (grain D; Figure 64), contain Th/U within the range of the entire dataset (0.17–0.64). These data are discussed below. The high Th/U analyses is the final age rejected from the population.

Zircon within NEB101z contained four highly discordant (>30%) U–Pb compositions that are characterised by high Th/U of 1.03–2.15. These analyses were rejected and not included in Figure 70 or in the following discussion. The remaining 15 analyses have U concentrations between 212–4718 ppm, Th between 86–1137 ppm and Th/U between 0.23–0.86. 207-corrected $^{206}Pb/^{238}U$ ages range between 275 and 224 Ma with a weight mean age of 237.4 ± 4.9 Ma (Figure 70). A coherent population of seven analyses has a mean of 249.76 +4.24/–5.22 (Figure 70). There is no obvious reason to reject the eight analyses, however the coherent population is closer to zircon ages in NEB100z and Yankee zircon reported in Schlattegger *et al.* (2005). The rejected analyses from this population are discussed further below.

All 207-corrected $^{206}Pb/^{238}U$ ages from NEB100z and NEB101z are compiled in Figure 71. These data yield a coherent population at 249.15 +2.06/–3.47 Ma. Young zircon ages continue to 217 Ma, younger than the 230 Ma reported by Schlattegger *et al.* (2005) from the Yankee deposit. The coherent population is considered to represent zircon saturation in the magma during emplacement of the Mole Granite. It is unclear whether young zircon ages represent new zircon growth or zircon recrystallisation, or more recent Pb loss.

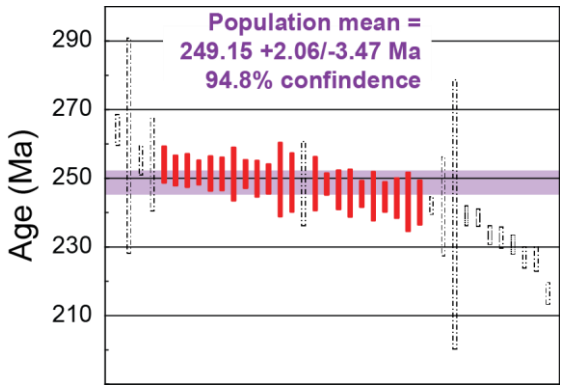

Figure 71: Mean-weighted population mean for all U–Pb SHRIMP analysis of zircon from the Yankee deposit (NEB100z and NEB101z).

3.7 Discussion

3.7.1 Age calculation and common Pb corrections for U–Pb cassiterite dating

Concordia isochron intercept ages are useful age estimations for cassiterite as they do not rely on assumptions of the common Pb composition, rather they assume concordance between the $^{207}Pb/^{235}U$ and $^{206}Pb/^{238}U$ systems. Li *et al.* (2016) and Neymark *et al.* (2018) indicate a preference for W- and TW-concordia ages for samples in their study for this reason. Several authors have utilised a derivation of these concordia, $^{238}U/^{207}Pb$ vs $^{206}Pb/^{207}Pb$ (Yuan *et al.,* 2011; Chen *et al.,* 2014; Chang *et al.,* 2014; Zhang *et al.,* 2014, 2015; Deng *et al.,* 2017; Wang *et al.,* 2017), however this method can introduce bias and underestimate the 'true age' (Li *et al.,* 2016; Neymark *et al.,* 2018). Due to the relatively low U concentration and at times high common Pb within cassiterite, precise determination of $^{207}Pb_r$ can be difficult, and will lead to errors in the estimation of $^{207}Pb/^{235}U$ and $^{207}Pb/^{206}Pb$ used in isochrons diagrams, especially for the relatively young cassiterite studied here. In this study individual analysis errors are 1.5 to 5 times larger for $^{207}Pb/^{235}U$ than for $^{206}Pb/^{238}U$. Large uncertainty associated with $^{207}Pb/^{235}U$ and $^{207}Pb/^{206}Pb$ is problematic in Precambrian cassiterite samples where, although $^{207}Pb_m$ may be in higher abundance, the ratios become increasingly sensitive towards ages, whilst $^{206}Pb/^{238}U$ behaves in the opposite sense. Concordant analyses with low common Pb are more strongly weighted in the calculation of the lower intercept age and this reduces the error associated with discordance.

Increased precision of a sample age can be achieved by correcting highly discordant grains for their common Pb component and calculating the weighted mean $^{206}Pb^*/^{238}U$ age for all analyses, as routinely done for zircon (e.g. Spencer *et al.,* 2016). This correction also allows for better assessment of age populations, or potentially multiple common Pb compositions. Li *et al.* (2016) infer that fluid and mineral inclusions within cassiterite contributed variable concentrations of common Pb and at times different common Pb compositions, which jeopardised their U–Pb dating calculations. Fortunately, fluid and or mineral inclusions are generally easily identified by sharp excursions of the signal during LA-ICP-MS analysis (Figure 72), and these analyses can be rejected. If all analyses within an inclusion-free sample originated from a single

age with a single common Pb source, weighted mean ages could provide the most precise estimation of the age. For LA-(MC)-ICP-MS and SIMS U–Pb cassiterite data, both the 207- and 208-correction methods have been applied (Carr *et al.,* 2017; Deng *et al.,* 2017; Wang *et al.,* 2017; Neymark *et al.,* 2018).

In all samples from the Ardlethan Granite and Mole Granite systems the 208-correction method produces equal or more precise weighted mean $^{206}Pb^*/^{238}U$ ages than the 207-correction method (Tables 20 and 21). The advantages of using the 208-correction method for cassiterite age dating are threefold: firstly, ^{208}Pb is the most abundant common Pb isotope in natural systems (e.g. modern initial Pb compositions are $^{208}Pb/^{204}Pb = 38.63$, $^{207}Pb/^{204}Pb = 15.63$ and $^{206}Pb/^{204}Pb = 18.7$; Stacey and Kramers, 1975) leading to the best sensitivity for direct measurement of common Pb (Figure 72). Secondly, the maximum Th/U of cassiterite is 0.002 from the Mole Granite system and 0.11 for the Ardlethan Granite system, indicating that radiogenic ^{208}Pb is insignificant in cassiterite. As shown in Figure 72, Th is also not detected in mineral inclusions. Thirdly, unlike zircon, U is in relatively low abundance in cassiterite (commonly <10 ppm), that yields extremely low radiogenic ^{207}Pb especially in these Phanerozoic deposits studied here. Low U also produces large uncertainties in calculation of ^{235}U from ^{238}U. In Figure 72, ^{207}Pb displays similar trends to ^{208}Pb, indicating the large majority is non-radiogenic, and leading to commonly inaccurate $^{207}Pb/^{235}U$ ages. $^{207}Pb^*/^{206}Pb^*$ ages for cassiterite determined here are highly inaccurate and

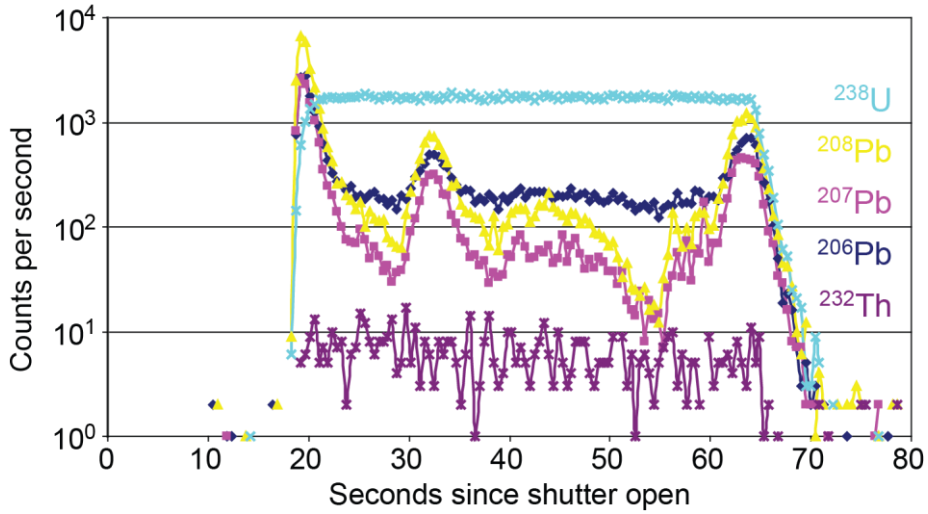

Figure 72: LA-ICP-MS signal in a cassiterite from the Yankee deposit with high common Pb occurring in micro inclusions. The non-radiogenic Pb component is accounts for the majority of the ^{208}Pb and ^{207}Pb signals and a large component of the ^{206}Pb.

imprecise for this reason, but also because the extreme small changes in $^{207}Pb/^{206}Pb$ lead to large changes in age for Phanerozoic samples. Derivation of common ^{207}Pb from the low measured ^{207}Pb signal contains a larger error than direct measurement of common Pb by ^{208}Pb. The single analysis with Th/U of 0.11 (ARD09c) yields similar 208-corrected (412.6 ± 4.6 Ma) and 207-corrected (412.9 ± 4.9 Ma) ages indicating that radiogenic ^{208}Pb does not strongly affect age calculations.

For common Pb corrections of cassiterite analysed by LA-ICP-MS or SIMS (Equations 10 and 11), the isotopic composition of the non-radiogenic component is either assumed from terrestrial evolution models (Cumming and Richards, 1975; Stacey and Kramers, 1975) or measured in low U minerals (e.g. galena) associated with cassiterite. Model compositions were similar to those obtained from low U minerals within both the Ardlethan Granite and Mole Granite systems (Richards *et al.,* 1982; Huston *et al.,* 2017; G. R. Carr unpubl). However, as shown in Figure 54, the common Pb composition of the Yankee cassiterite inferred from ID-TIMS isochron data, is significantly more evolved than predicted by models or mineral analogues. Other ID-TIMS cassiterite studies do not publish enough data or discuss common Pb compositions measured directly (Gulson and Jones, 1992; Yuan *et al.,* 2008, 2011) and so it is unclear whether the Yankee cassiterite is unique in its highly evolved common Pb composition.

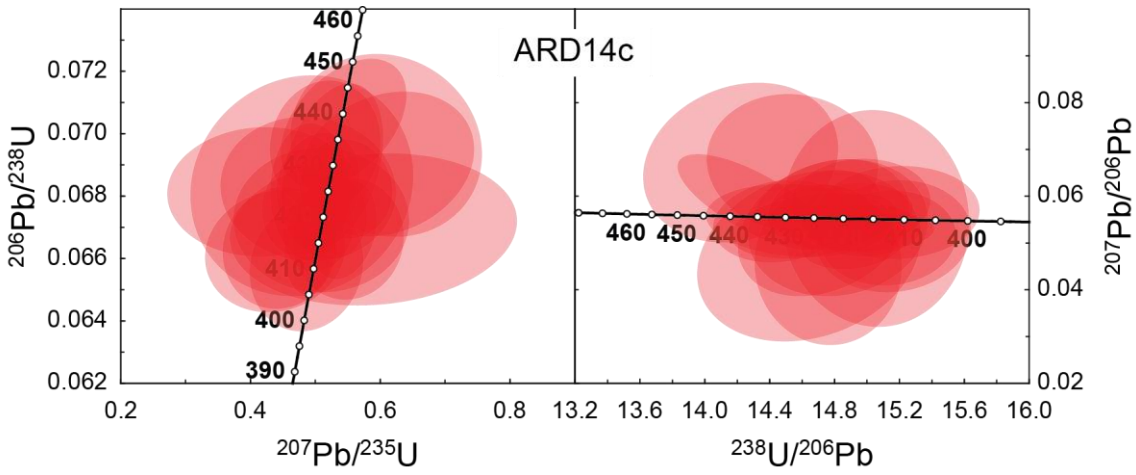

Figure 73: Wetherill (1956) and Tera and Wasserburg (1972) concordia diagrams for 208-corrected U-Pb data from ARD14c of the Ardlethan Granite system.

In this study, both the 207- and 208-common Pb correction methods were employed and compared with W- and TW- concordia isochron ages for cassiterite from the Ardlethan and Mole granite mineral systems (Tables 20 and 21; 208-corrected and W-Concordia ages are compared in Figure 74). As concordia isochron intercept ages do not rely on an assumed common Pb composition, their variance with common Pb corrected values allows for the assessment of compositions used in corrections.

Wetherwill and TW-concordia intercept ages are similar to common Pb corrected $^{206}Pb^*/^{238}U$ ages using both the 208- and 207-correction methods for cassiterite of the Ardlethan Granite system (Figure 74). The largest variance between $^{206}Pb^*/^{238}U$ and W-concordia intercept ages occurs in ARD14c, the sample with the highest common Pb component. 208-corrected $^{206}Pb^*/^{238}U$ vs $^{207}Pb^*/^{235}U$ and $^{238}U/^{206}Pb^*$ vs $^{207}Pb^*/^{206}Pb^*$ data are concordant and define an array along concordia (Figure 73). 208-corrected $^{206}Pb^*/^{238}U$ ages for individual analyses range between 438 ± 10 Ma and 410 ± 10 Ma. This range in ages may represent either cassiterite crystallisation between these dates, or multiple common Pb compositions within the cassiterite sample with a single age population. For the remaining samples, the common Pb corrected concordance, similar uncorrected isochron lower intercept ages and common Pb corrected $^{206}Pb/^{238}U$ ages, indicates that the Stacey and Kramers (1975) model at 410 Ma for the Ardlethan Granite system appropriately estimates the common Pb composition of cassiterite. The Pb isotopic composition of late-stage galena occurring within the Ardlethan Granite (Richards *et al.,* 1982) system is similar

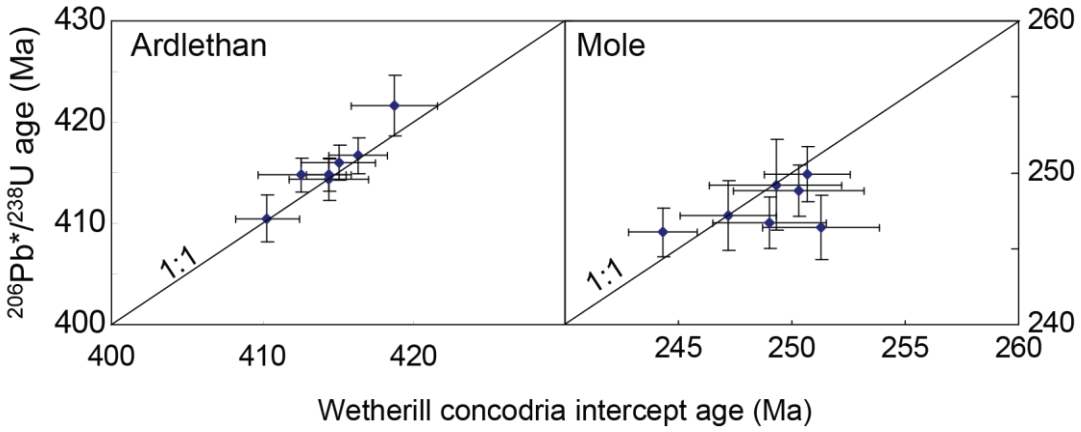

Figure 74: Comparison of $^{206}Pb^*/^{238}U$ ages after 208-correction with W-concordia intercept ages for the Ardlethan Granite (left) and Mole Granite (right) systems. Common Pb corrections used compositions of Stacey and Kramers (1975) at 410 Ma for Ardlethan and 250 Ma for the Mole. The difference between the two ages is interpreted to be related predominantly to common Pb compositions used in correction to $^{206}Pb^*/^{238}U$.

to age values used for cassiterite corrections and indicates that the common Pb composition has not evolved significantly between granite emplacement and hydrothermal cooling, as was seen in the Yankee deposit.

Concordia lower intercept isochron ages of cassiterite from the Mole Granite system are also predominantly within error of common Pb corrected $^{206}Pb^{*/238}U$ ages using both the 207- and 208-correction methods and compositions defined by the Stacey and Kramers (1975) model at 250 Ma (Table 21; Figure 74). The largest variance between 208-corrected $^{206}Pb^{*/238}U$ ages and concordia lower intercept isochron ages occurs in NEB003c, but the origin of this is unknown. In this case the concordia intercept ages are preferred. Weighted mean $^{206}Pb^{*/238}U$ ages weight precision more strongly, and whilst precision is generally correlated with concordance, it is not always the case. 208-corrected $^{206}Pb/^{238}U$ ages using the common Pb composition of the Yankee cassiterite (Appendix 2) yield ages that are within error of other age estimations but are predominantly younger and more imprecise. This indicates an overcorrection of common Pb and shows that the common Pb composition inferred from the Yankee deposit is not appropriate for all cassiterite associated with the Mole Granite.

208-corrected $^{206}Pb/^{238}U$ and $^{207}Pb/^{235}U$ data from cassiterite of the Yankee deposit yield predominantly concordant data. However, the most discordant data points of uncorrected data (Figure 70) remain discordant following correction (Figure 75). This is true using both common Pb compositions of this study. Importantly, the major variation between these two corrections is the $^{207}Pb^{*}/^{235}U$ due the large $^{207}Pb_c$ component (Figure 75). Therefore, in the Yankee cassiterite in particular, but for all cassiterite in this study, $^{206}Pb^{*}/^{238}U$ ages remain robust even in samples with high common Pb.

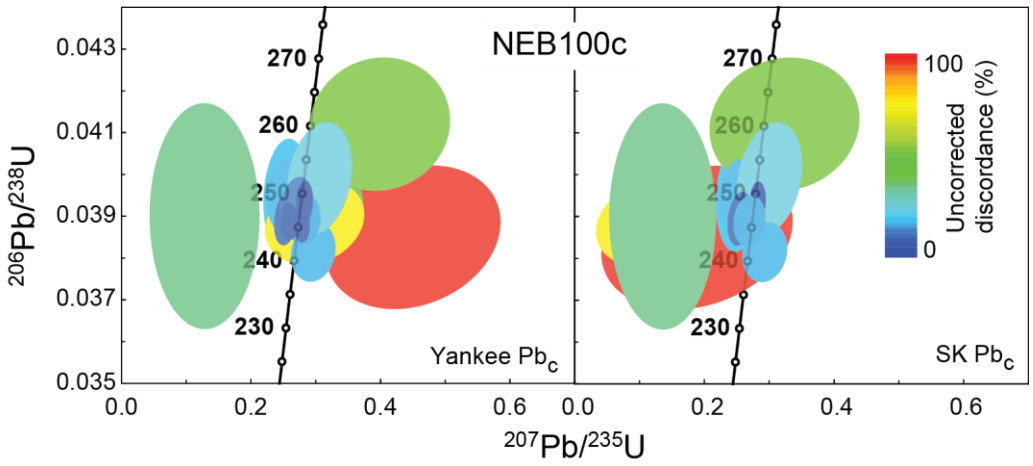

Figure 75: Wetherill (1956) concordia diagram of 208-corrected U-Pb data for cassiterite of sample NEB100c of the Yankee deposit, Mole Granite system. Two compositions for the common Pb correction were applied; (left) the composition determined in Appendix X for the Yankee cassiterite by ID-TIMS, and (right) the terrestrial model composition of Stacey and Kramers (1975) at 250 Ma.

3.7.2 Geochronology of the Ardlethan Granite system

U–Pb W-concordia intercept data for cassiterite of the Ardlethan deposit is included in Figure 76, combined with published zircon U–Pb age dates (Bodorkos *et al.,* 2013; Blevin, pers comm 2018) and Rb–Sr isochron ages of Richards *et al.* (1982).

In Chapter 2, tourmaline major and trace element concentrations, and isotopic composition from the Ardlethan deposit indicate that extended fractional crystallisation and fluid separation of Ardlethan Granite produced the fluids that resulted in cassiterite mineralisation. Cassiterite age data presented here indicate that cassiterite mineralisation occurred simultaneously with zircon crystallisation, within the precision of each method. Cassiterite precipitation continued for a maximum of 4.2 Ma. Cassiterite mineralisation is also synchronous with the GFQP (extrusive equivalent of the Ardlethan Granite) and the Mine Porphyry (Figure 76). However, the juvenile $\varepsilon Nd_{(i)}$ composition of the Mine Porphyry is not observed in tourmaline associated with cassiterite, indicating it was not involved in the generation of mineralising fluids.

Three cassiterite samples from the Mine (ARD07c), Carparthia (ARD09c) and White Crystal (ARD14c) breccia pipes are within error of the U–Pb zircon age of the Ardlethan Granite. Following zircon precipitation in the Ardlethan Granite, breccia-hosted cassiterite mineralisation occurred for a maximum of 2.7 Ma.

Although within error, cassiterite U–Pb ages seem to become progressively older with distance from the Ardlethan Granite. This may indicate that during the brecciation event, fluids most distal from the Ardlethan Granite crystallised cassiterite first either due to the increased temperature gradient or dilution of fluids. Fluid dilution was facilitated by strong wall-rock assimilation resulting in crystallisation of chlorite assemblages that lowered the Cl molarity of the fluids. The latter hypothesis is preferred as tourmaline associated with cassiterite increasingly adopts the composition of the Mine Granite with distance from the Ardlethan Granite (Figure 26). This is also indicated by the high common Pb component with ARD14c in the White Crystal deposit that displays pervasive leaching of hydrothermal fluids from the host rock (Ren, 1989; Chapter 2).

Greisen-hosted cassiterite yields 208-corrected $^{206}Pb^*/^{238}U$ ages that define 2 resolvable periods of cassiterite mineralisation: 418.5–413.2 Ma in ARD15c–17c and 410.5 ± 2.3 Ma in ARD18c. The cassiterite ages of ARD15c–17c are indistinguishable from the zircon U–Pb zircon age of the Ardlethan Granite. ARD18c, the most northerly sample in this study (Figure 55), has a cassiterite age that is also (just) within error of the Ardlethan Granite zircon age, however, it is distinguishable from the age of ARD17c and ARD16c. These data indicate that fluid fractionation and cassiterite precipitation within the Ardlethan Granite occurred shortly after zircon precipitation, within the precision of these methods. The younger age of ARD18c, however, indicates that either hydrothermal activity persisted for up to 4.2 Ma after zircon precipitation within the Ardlethan Granite, or reprecipitation of cassiterite occurred following a thermal flux initiated from a blind intrusion. Tourmaline (ARD18t) $^{87}Sr/^{86}Sr_{(i)}$ and $\varepsilon Nd_{(i)}$ isotopic compositions associated with this cassiterite (ARD18c), are similar to the Ardlethan Granite and indicate no foreign fluid input.

The Rb–Sr data of Richards *et al.* (1982) for the Ardlethan Granite system shown in Figure 76 are difficult to interpret within the overall geochronological framework. The Rb–Sr age for the Ardlethan Granite represents a single whole-rock analysis of which an isochron age is derived from an assumed initial $^{87}Sr/^{86}Sr$. This is effectively a 1-point isochron with two major assumptions: 1) the assumed initial $^{87}Sr/^{86}Sr_{(i)}$ of 0.715 composition, that in Chapter 2 is shown to be relatively accurate from $^{87}Sr/^{86}Sr_{(i)}$ of tourmaline (0.71504) within the

Ardlethan Granite, and 2) the whole-rock analysis represents a closed Rb–Sr system. No information on the degree of alteration within the whole-rock sample measured by Richards *et al.* (1982) is provided except that it occurs kilometres away from known Sn mineralisation (Richards *et al.,* 1982). The Mine Granite age is from a 2-point isochron involving a whole-rock analysis and muscovite that yields an initial $^{87}Sr/^{86}Sr_{(i)}$ of 0.7155, which is more similar to the Ardlethan Granite (0.71504) than the Mine Granite (0.71865) (Chapter 2). Richards *et al.* (1982) also present a whole-rock–biotite isochron that yields an $^{87}Sr/^{86}Sr_{(i)}$ of 0.7162 and age of 417.4 ± 4.2 Ma (^{87}Rb decay constant of Villa *et al.,* 2015). Rb–Sr isochron ages determined with the ^{87}Rb decay constant of Villa *et al.* (2015) are coeval with, although slightly earlier than zircon U–Pb ages for the Ardlethan Granite (Figure 76). Ages determined with the ^{87}Rb decay constant recommended by Steiger and Jäger (1977) would indicate the Rb–Sr system was reset following the major phase of zircon and cassiterite growth, and at the same time as ARD18c.

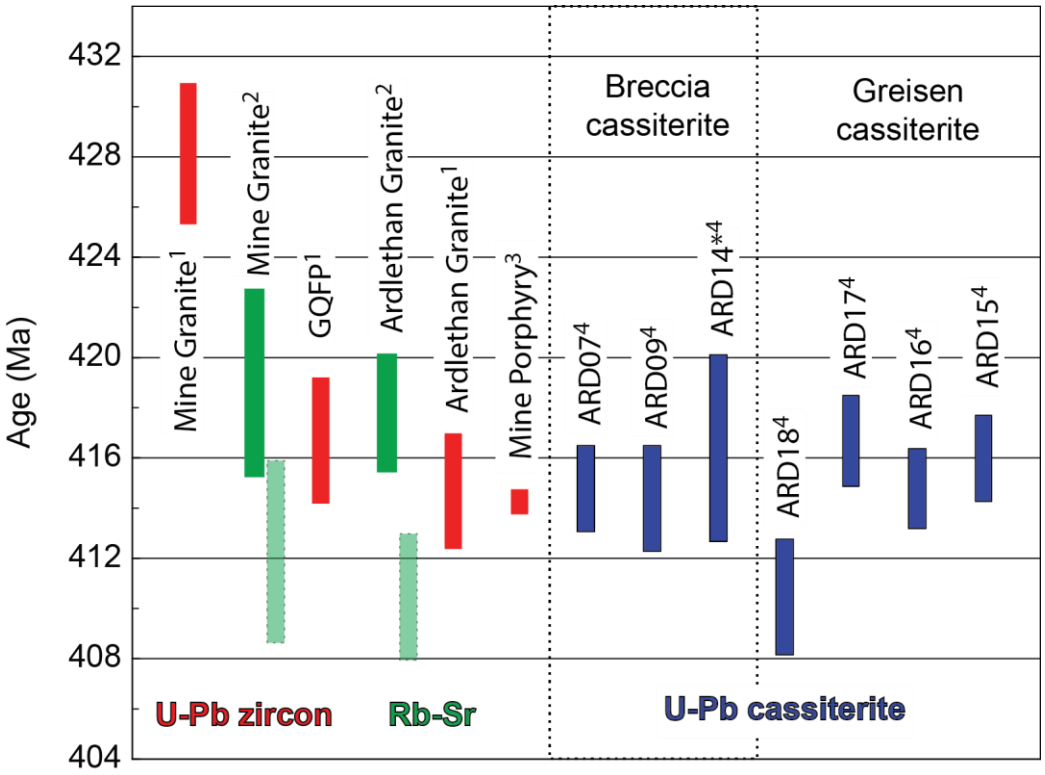

*Figure 76: Compilation of geochronological data for the Ardlethan region. Data sources include 1) U-Pb zircon weighted mean of 204 corrected 206Pb/238U age; Bodorkos et al. (2013), 2) Rb-Sr whole rock and mica isochron ages; Richards et al. (1982), shaded bar represents age using former ^{87}Rb decay constant of Steiger and Jäger (1977), 3) CA-ID-TIMS single zircon age from Blevin pers comm, and 4) 208 corrected $^{206}Pb/^{238}U$ ages of this study. * represent the concordia age due to inaccurate common Pb corrections (see text).*

3.7.3 Geochronology the Mole Granite system

U–Pb SHRIMP zircon ages presented here are similar to previously published ages by the same method (Chisholm *et al.,* 2014; Laker, 2017) and high-precision ID-TIMS zircon ages of 247.6 ± 0.4 Ma (n = 4, MSWD = 0.7; Schlattegger *et al.,* 2005). Schlattegger *et al.* (2005) presented two high-precision ID-TIMS age determinations of highly pitted zircons from the Yankee (YL2) and Breakfast Creek (Pheno) deposits that, combined with concordant data (YL1), define a Pb loss discordia with an upper intercept age of 253 ± 8 Ma (Figure 77). Even with their high-precision data, however, YL2 and Pheno still plot on the concordia and could represent younger zircon crystallisation at 230.3 ± 0.78 Ma (YL2) and 210.4 ± 0.95 Ma (Pheno). Schlattegger *et al.* (2005) interpreted these zircons to have lost Pb during a secondary event that also generated the highly pitted texture. Chisholm *et al.* (2014) indicated that ~5% of zircons from their study showed “crystal lattice damage” but did not report Pb-loss. Laker (2017) noted Pb loss commonly occurred in zircon of their study. Highly pitted zircon analysed by SHRIMP in this study (e.g. grain C; Figure 64) returned $^{206}Pb/^{238}U$ ages within the main population of Figure 71. The

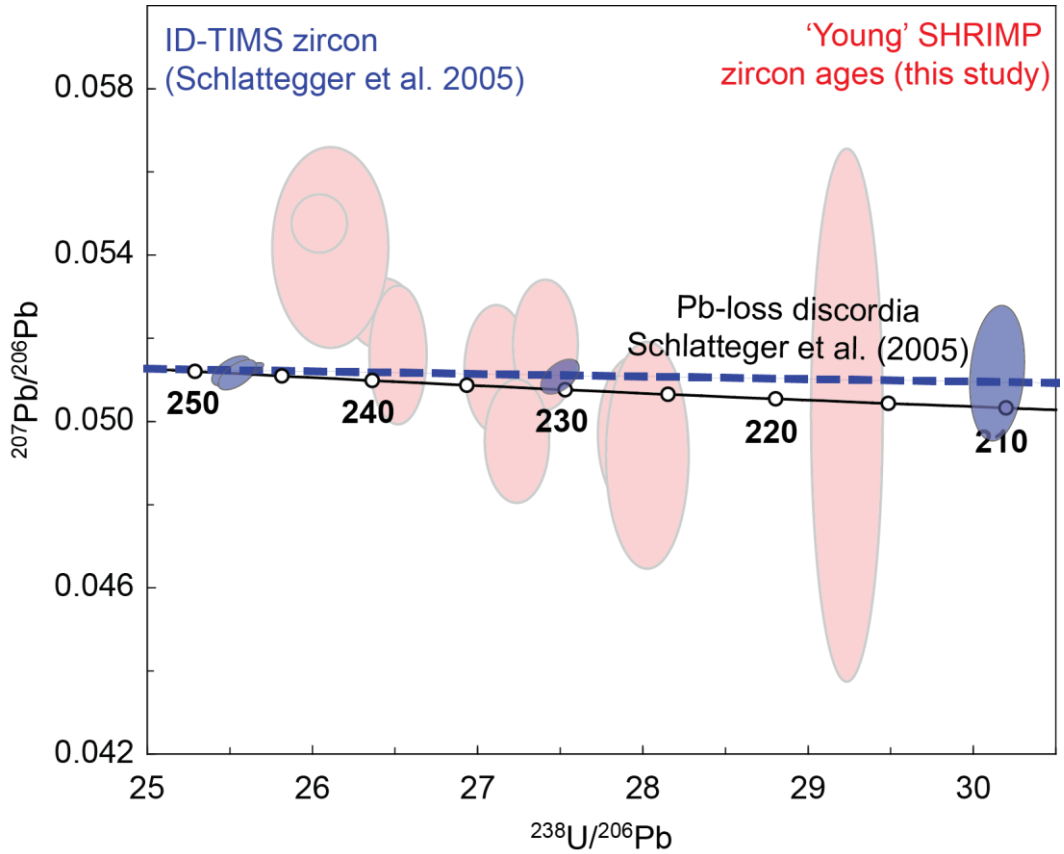

Figure 77: TW-concordia diagram of high-precision ID-TIMS zircon dating by Schlattegger et al. (2005) in the Yankee deposit. The 'young' zircon ages of this study are plotted for reference with the Pb-loss discordia of Schlattegger et al. (2005).

discordant data of Schlattegger *et al.* (2005) (Figure 77) were from analysis of entire zircons with highly pitted textures. However, as we show here, and by Laker (2017), at times this texture forms rims around concentric magmatic zoning (e.g. grain B, Figure 64) and indicates that magmatic zircon within the granite was entrained by mineralising veins. Determining Pb-loss in Phanerozoic samples is difficult due to the low angle at which the discordia meets the concordia (Figure 77). This issue is further complicated with the less precise SHRIMP data shown in Figure 77, that mostly plot on both the concordia and discordia. Therefore, these data points could represent new zircon growth or recrystallisation at their concordia intercepts, or recent Pb loss from the main magmatic population at 249.15 +2.06/–3.47 Ma. Three SHRIMP analyses from this study do not plot on either the concordia or discordia in Figure 77 and define 207-corrected $^{206}Pb/^{238}U$ ages of 242 ± 1 Ma, 241 ± 3 Ma and 239 ± 1 Ma, that are interpreted as zircon recrystallisation. These analyses occurred within high CL features that cross-cut oscillatory zoning (grain E in Figure 64) or low CL features that cross-cut core textures (grain D; Figure 64).

A compilation of SIMS U–Pb zircon ages (Chisholm *et al.,* 2014; Laker, 2017; this study), LA-ICP-MS U–Pb cassiterite ages (this study), and Rb–Sr, K–Ar and Ar–Ar whole-rock and mica ages (Kleeman *et al.,* 1997) are combined in Figure 78. High-precision ID-TIMS data of Schalegger *et al.* (2005) and this study for the Yankee deposit are shown in Figure 79.

Schlattegger *et al.* (2005) argue that zircon precipitation in the parental magmas of the Mole Granite occurred during early differentiation and ascent. In their scenario, emplacement of the Mole Granite at shallow crustal levels is marked by fluid separation and xenotime precipitation in hydrothermal veins at 246.2 ± 0.2 Ma in the Yankee and Breakfast mines on the southern edge of the granite mass (Figure 59; Schlattegger *et al.,* 2005). Zircon U–Pb data presented in Figure 78 and 79 (and references within) show an extended period of zircon precipitation and recrystallisation. Age estimations of zircon by SIMS are imprecise likely due to minor inheritance and Pb loss commonly reported (Schlattegger *et al.,* 2005; Chisholm *et al.,* 2014; Laker, 2017; this study). However, as discussed above, Pb loss is a potentially significant problem that

will yield ages younger than the true age. Therefore, the maximum interval of

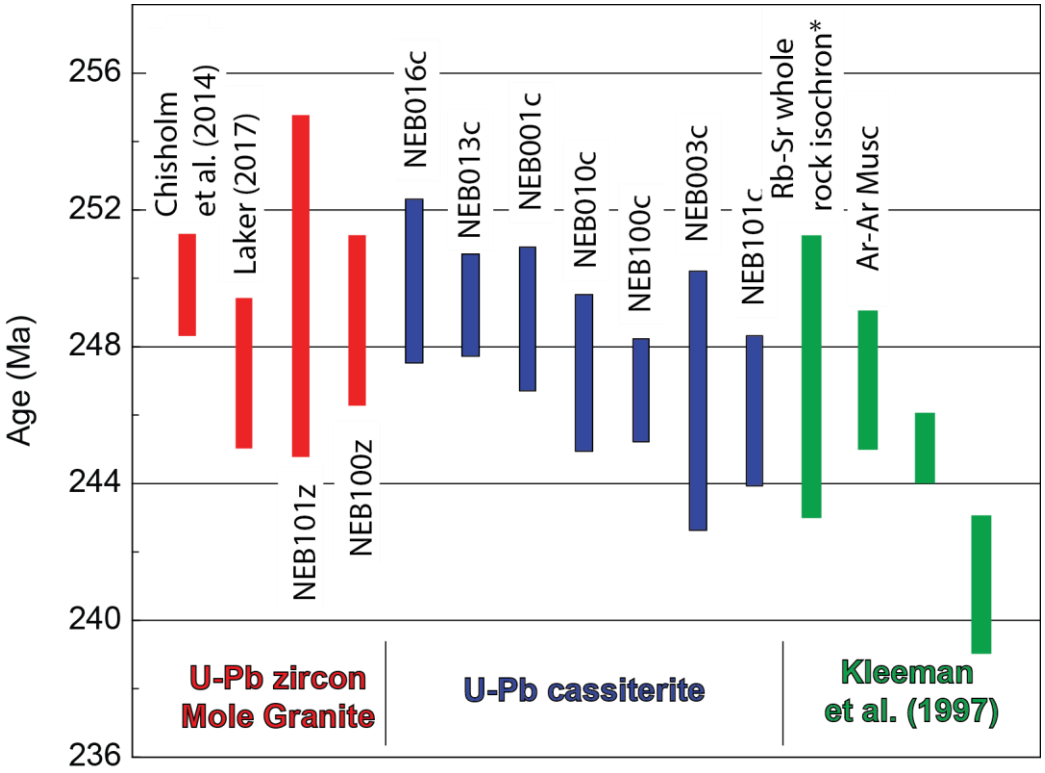

Figure 78: Geochronological data of the Mole Granite system. Bars represent weighted mean ages (2SE) of zircon (red) from Chisholm et al. (2014), Laker (2017) and this study, cassiterite (blue) from this study, and Rb-Sr and Ar-Ar data (green) of Kleeman et al. (1997).

zircon crystallisation is defined by the data of Chisholm *et al.* (2014) and Schlattegger *et al.* (2005) at 4.1 Ma. The earliest cassiterite mineralisation occurs within quartz–tourmaline veins injected into overlying Permian sediments at 250.7 ± 2.7 Ma (NEB016c). This indicates that by *ca* 250 Ma, at least part of the Mole Granite was emplaced at shallow crustal levels, contrary to Schlattegger *et al.* (2005). Zircon and monazite precipitation occurring after this, for example within the Yankee deposit, must have occurred synchronously, or immediately following early cassiterite mineralisation. This model implies an extended period of magmatic emplacement at shallow crustal depths.

High-precision ID-TIMS U–Pb data of Schlattegger *et al.* (2005) and this study (Appendix 2) from the Yankee deposit are shown in Figure 79. These data clearly distinguish the timing of cassiterite precipitation from that of magmatic zircon and monazite crystallisation, whilst SHRIMP zircon and LA-ICP-MS data do not. Quartz–cassiterite veining within the Yankee deposit occurs within the seriate granite where wall-rock alteration is minimal (Audétat *et al.,* 1998). Minimal wall-rock alteration indicates fluid incursion into the solid seriate granite

phase rather than a crystal mush, likely coincident with the microgranite phase that is commonly associated with mineralisation. High-precision geochronology of the microgranite is required to better constrain this transition.

The age difference between magmatic precipitation of zircon and hydrothermal xenotime and cassiterite in the Yankee deposit is related to the emplacement of the Mole Granite at shallow crustal depths and fluid saturation within the magma. The maximum time between zircon and cassiterite precipitation in the Yankee deposit is 2 ± 1 Ma (Schlattegger *et al.,* 2005; Appendix 2). If zircon precipitation occurred at shallow crustal levels, this would require relatively slow cooling rates. The temperature of zircon precipitation within the Mole Granite is poorly constrained, however is estimated by Ti-zircon temperatures of ~720^{o}C (Laker, 2017), and the coexistence of magmatic monazite (Schlattegger *et al.,* 2005) with an estimated closure temperature of ~750^{o}C (Copeland *et al.,* 1988). Hydrothermal xenotime in the Yankee deposit is estimated to have precipitated from initial hydrothermal fluids at 600^{o}C (Audétat *et al.,* 1998, 2000a, 2000b). Cassiterite has been shown to begin precipitating with xenotime but continued to 390 ± 25^{o}C (Audétat *et al.,* 1998; Fetekke *et al.,* 2016). From monazite to cassiterite precipitation represents a maximum temperature range of 750^{o}C to 365^{o}C over a period of over 2 ± 1 Ma (192^{o}C per Ma) within the Yankee deposit. However, if granite emplacement at shallow crustal depths occurred immediately prior to xenotime precipitation as suggested by Schlattegger *et al.* (2005), then cooling rates would have increased significantly. Radiogenic heat alone is unlikely to have sustained a thermal anomaly alone considering the thin sill-like shape of the Mole Granite (Kleeman, 1982) that would have encouraged rapid heat loss to the cool country rocks. Worster *et al.* (1990) presented a cooling model for sill-like, convecting magma chambers emplaced into country rocks initially at 0^{o}C. The model accounts for the increased cooling associated with crystallisation. Instantaneously emplacement of a $Di_{80}An_{20}$ magma into a sill 1000 m tall will be completely solid after <17 000 years, significantly faster than predicted from zircon and cassiterite U–Pb ages.

Instead, it is proposed that the Mole Granite was emplaced over an extended period (*ca* 1 Ma), through multiple magmatic injections (e.g. Clemens and Mawer, 1992). Similarly, cassiterite mineralisation occurred synchronously with

this accumulation of magmatic units leading to the spread of ages in Figure 78. The Yankee deposit represents the final stages of magmatic injection, after which fluid saturation entrained zircon and deposited in quartz–cassiterite veins. Increasing evidence from high-precision geochronology and thermal modelling of individual plutons indicates that they can be accumulated from repeated magmatic injections that occur over timescales of 10^4–10^6 years (Clemens and Mawer, 1992; Petford *et al.,* 2000; Coleman *et al.,* 2004; Glazner *et al.,* 2004; Annen *et al.,* 2006; Miller *et al.,* 2007; Michel *et al.,* 2008; Schlattegger *et al.,* 2009; de Saint Blanquat *et al.,* 2011; Caricchi *et al.,* 2012; Leuthold *et al.,* 2012; Floess and Baumgartner, 2015).

Zircon and cassiterite U–Pb ages are with error of whole-rock Rb–Sr isochron age (see Chapter 2.3) and K–Ar and Ar–Ar mica ages associated with main phase of mineralisation during assemblage of the Mole Granite (Figure 78; Kleeman *et al.,* 1997). The late hydrothermal ages from muscovite and biotite recorded by Rb–Sr and K–Ar indicate that circulation continued along major fractures in the granite (Kleeman *et al.,* 1997) and extended period of time following cassiterite mineralisation (Figure 78).

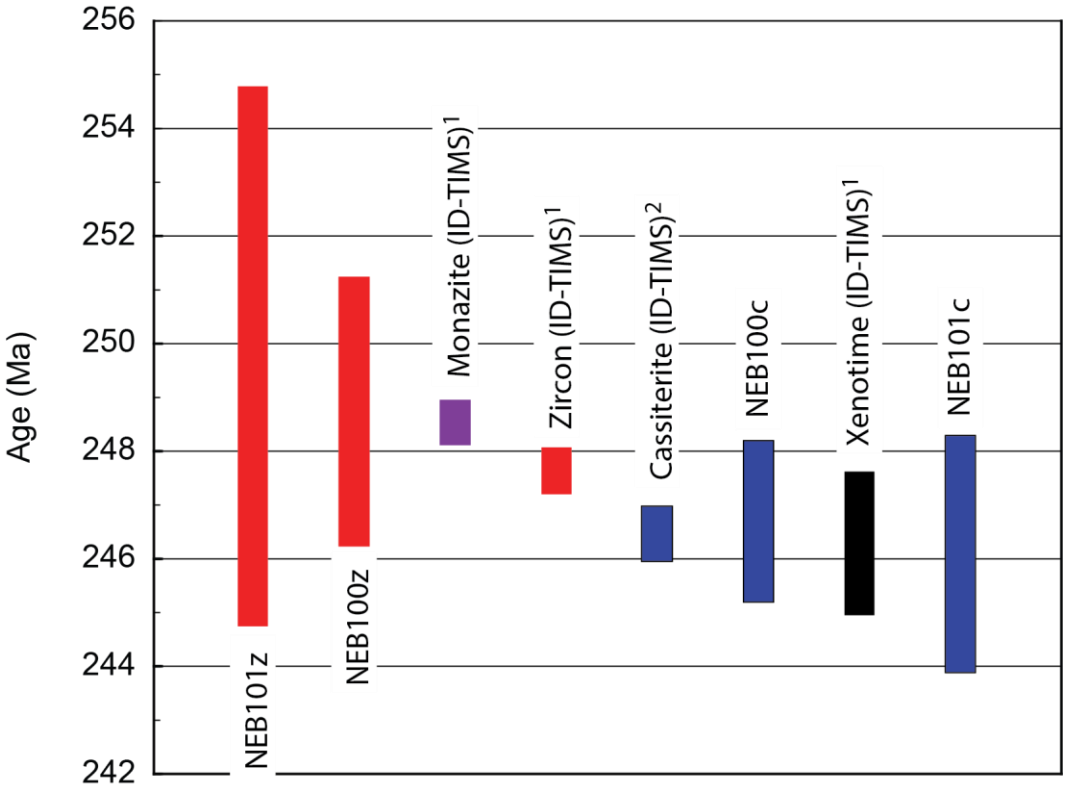

Figure 79: Geochronological data from the Yankee deposit of the Mole Granite system. Bars represent weighted mean ages (2SE). High-precision ID-TIMS data from 1) Schlattegger et al. (2005) and 2) Appendix 2 of this study. SHRIMP zircon U–Pb ages of this study shown in red and cassiterite by LA-ICP-MS in blue.

3.8 Conclusions

U–Pb geochronology of cassiterite has great potential to provide insights into the absolute age and duration of magmatic-hydrothermal mineral systems. Despite an increasing number of studies of cassiterite as a geochronometer, there remain numerous difficulties in its analysis and data interpretation. In Appendix 2, we present a new method for the precise determination of the U–Pb composition of cassiterite by ID-TIMS. This method allows for the precise characterisation of cassiterite reference material that can be used to correct for instrument induced bias inherent in more popular *in-situ* techniques (LA-ICP-MS or SIMS).

In this Chapter, the U–Pb isotopic compositions of cassiterite from the Ardlethan Granite and Mole Granite systems were determined by LA-ICP-MS. Instrument induced bias was corrected using the newly determined ID-TIMS data for the Yankee reference cassiterite, whose precise isotopic composition was determined in Appendix 2.

U–Pb isochron ages are preferred as they do not rely on assumptions of the common Pb composition within cassiterite. However, the 208-correction method is also shown to produce precise weighted mean ages, even for samples with high common Pb. The unusual common Pb composition of the Yankee cassiterite is not observed in cassiterite from the Ardlethan Granite system, or elsewhere within the Mole Granite system.

Cassiterite mineralisation associated with the Ardlethan Granite occurred synchronously with magmatic zircon within the granite. Mineralisation continued for a maximum of 4.2 Ma in breccia- and greisen-hosted mineral deposits. Cassiterite mineralisation within the Mole Granite system also occurred synchronously with zircon precipitation. Zircon U–Pb ages span an extended period of 4.1 Ma, although Pb loss is a significant problem in the interpretation of these data. A model of repeated magmatic injection accumulating in the Mole Granite mass is invoked to describe this extended period. Cassiterite ages are not adequately precise to determine the moment or moments of cassiterite mineralisation within the extended period of magma accumulation.

References

Anglin, C. D., Jonasson, I. R., Franklin, J. M., 1996. Sm–Nd dating of scheelite and tourmaline: implications for the genesis of Archean gold deposits, Val d'Or, Canada. Economic Geology, 91(8): 1372–1382.

Annen, C., Blundy, J., Sparks, R., 2005. The genesis of intermediate and silicic magmas in deep crustal hot zones. Journal of Petrology, 47(3): 505–539.

Arzi, A.A., 1978. Critical phenomena in the rheology of partially melted rocks. Tectonophysics, 44(1-4): 173-184.

Audétat, A., 1999. The magmatic-hydrothermal evolution of the Sn/W mineralized Mole Granite (Eastern Australia), ETH Zurich, Switzerland.

Audétat, A., Günther, D., Heinrich, C. A., 1998. Formation of a Magmatic-Hydrothermal Ore Deposit: Insights with LA-ICP-MS Analysis of Fluid Inclusions. Science, 279(5359): 2091–2094.

Audétat, A., Gunther, D., Heinrich, C. A., 2000a. Magmatic-hydrothermal evolution in a fractionating granite: A microchemical study of the Sn–W–F-mineralized Mole Granite (Australia). Geochimica Et Cosmochimica Acta, 64(19): 3373–3393.

Audétat, A., Günther, D., Heinrich, C. A., 2000b. Causes for Large-Scale Metal Zonation around Mineralized Plutons: Fluid Inclusion LA-ICP-MS Evidence from the Mole Granite, Australia. Economic Geology, 95(8): 1563–1581.

Audétat, A., Pettke, T., Heinrich, C. A., Bodnar, R. J., 2008. Special Paper: The Composition of Magmatic-Hydrothermal Fluids in Barren and Mineralized Intrusions. Economic Geology, 103(5): 877–908.

Baksheev, I., Prokofiev, V., Trumbull, R., Wiedenbeck, M., Yapaskurt, V., 2015. Geochemical evolution of tourmaline in the Darasun gold district, Transbaikal

region, Russia: evidence from chemical and boron isotopic compositions. Mineralium Deposita, 50(1): 125–138.

Balen, D., Broska, I., 2011. Tourmaline nodules: products of devolatilization within the final evolutionary stage of granitic melt? Geological Society, London, Special Publications, 350(1): 53–68.

Bea, F., Pereira, M. D., Stroh, A., 1994. Mineral/leucosome trace-element partitioning in a peraluminous migmatite (a laser ablation-ICP-MS study). Chemical Geology, 117(1): 291–312.

Bennett, V. C., Kennett, B. L. N., Carlson, R. W., 2002. Combined Osmium isotopic and seismic evidence for orphaned early Proterozoic mantle beneath Phanerozoic crust in the New England Fold Belt, eastern Australia. Abstracts of the Geological Society of Australia, 67: 100.

Blevin, P. L., 2002. AMIRA P515 final report: Igneous metallogenic systems of eastern Australia, final outcomes and project material, AMIRA International, Melbourne, VIC.

Blevin, P. L., 2004. Redox and compositional parameters for interpreting the granitoid metallogeny of eastern Australia: Implications for gold-rich ore systems. Resource Geology, 54(3): 241–252.

Blevin, P. L., Chappell, B. W., 1995. Chemistry, origin, and evolution of mineralized granites in the Lachlan fold belt, Australia; the metallogeny of I- and S-type granites. Economic Geology, 90(6): 1604–1619.

Blevin, P.L., Kemp, A.I.S., Williams, I.S., Bodorkos, S., 2017. Age and origins of S- and I-type magmas at the Ardlethan tin deposit, NSW. In: Vearncombe, J. (Editor), Abstracts granites2017@benalla. Australian Institute of Geoscientists, Benalla, pp. 9-10.

Bodorkos, S. et al., 2015. New SHRIMP U–Pb zircon ages from the central and eastern Lachlan Orogen, New South Wales: July 2013–June2014, Geoscience Australia and Geological Survey of NSW.

Bodorkos, S. et al., 2013. New SHRIMP U–Pb zircon ages from the Lachlan, Thomson and Delamerian orogens, New South Wales: July 2009–June 2010., Geoscience Australia, Canberra.

Bonin, B., 2007. A-type granites and related rocks: Evolution of a concept, problems and prospects. Lithos, 97(1–2): 1–29.
Bragg, W. L., 1937. Atomic Structures of Minerals. The Journal of Physical Chemistry, 41(8): 1149–1150.

Bröcker, M., Bieling, D., Hacker, B., Gans, P., 2004. High-Si phengite records the time of greenschist facies overprinting: implications for models suggesting mega-detachments in the Aegean Sea. Journal of Metamorphic Geology, 22(5): 427–442.

Bruce, M. C., Niu, Y. L., 2000. Evidence for Palaeozoic magmatism recorded in the Late Neoproterozoic Marlborough ophiolite, New England Fold Belt, central Queensland. Australian Journal of Earth Sciences, 47(6): 1065–1076.

Bryant, C. J., Arculus, R. J., Chappell, B. W., 1997. Clarence River Supersuite: 250 Ma Cordilleran Tonalitic I-type Intrusions in Eastern Australia. Journal of Petrology, 38(8): 975–1001.

Bryant, C. J., Chappell, B. W., Bennett, V. C., McCulloch, M. T., 2004. Lithium isotopic compositions of the New England Batholith: Correlations with inferred source rock compositions. Transactions of the Royal Society of Edinburgh, Earth Sciences, 95(1–2): 199–214.

Bryant, C.J., Blevin, P.L., 2017. Chappell–White Legacy: CHAPGRAN and associated resources. In: Vernacombe, J. (Editor), Granites: Crustal Evolution and Mineralisation, Perth, pp. pp 21-23.

Bull, K. F., Blevin, P. L., Fitzherbert, J. A., 2017. Felsic volcanic rocks of the Central Lachlan Orogen. In: Vearncombe, J. (Editor), granites2017@benalla. Australian Institute of Geoscientists, Benalla, Australia.

Candela, P. A., 1989. Calculation of magmatic fluid contributions to porphyry-type ore systems: Predicting fluid inclusion chemistries. Geochemical Journal, 23(6): 295–305.

Candela, P. A., 1997. A Review of Shallow, Ore-related Granites: Textures, Volatiles, and Ore Metals. Journal of Petrology, 38(12): 1619–1633.

Caricchi, L., Annen, C., Rust, A., Blundy, J., 2012. Insights into the mechanisms and timescales of pluton assembly from deformation patterns of mafic enclaves. Journal of Geophysical Research: Solid Earth, 117(B11): n/a-n/a.

Carr, G. R., Dean, J. A., Suppel, D. W., Heithersay, P. S., 1995. Precise lead isotope fingerprinting of hydrothermal activity associated with Ordovician to Carboniferous metallogenic events in the Lachlan fold belt of New South Wales. Economic Geology, 90(6): 1467–1505.

Castro, A., Gerya, T., Garcia-Casco, A., Fernandez, C., Diaz-Alvarado, J., Moreno-Ventas, I., Low, I., 2010. Melting Relations of MORB-Sediment Melanges in Underplated Mantle Wedge Plumes; Implications for the Origin of Cordilleran-type Batholiths. Journal of Petrology, 51(6): 1267-1295.

Carr, P. A., Norman, M. D., and Bennett, V. C., 2017. Assessment of crystallographic orientation effects on secondary ion mass spectrometry (SIMS) analysis of cassiterite. Chemical Geology, 467: 122–133.

Cawood, P. A., 1982. Structural relations in the subduction complex of the Paleozoic New England Fold Belt, eastern Australia. Journal of Geology, 90: 381–392.

Chappell, B. W., 1996. Compositional variation within granite suites of the Lachlan Fold Belt: its causes and implications for the physical state of granite

magma. Earth and Environmental Science Transactions of the Royal Society of Edinburgh, 87(1–2): 159–170.

Chappell, B. W., White, A. J. R., 1974. Two contrasting granite types. Pacific Geology, 8: 173–174.

Chen, Y. et al., 1993. Diachronous and Independent Histories of Plutonism and Mineralization in the Cornubian Batholith, Southwest England. Journal of the Geological Society, 150: 1183–1191.

Chen, Z. H. et al., 2006. Geological characteristics and mineralization age of the Taoxikeng tungsten deposit in Chongyi County, southern Jiangxi Province, China. Geological Bulletin of China, 25(4): 496–501.

Cheng, Y. B., Spandler, C., Chang, Z. S., Clarke, G., 2018. Volcanic–plutonic connections and metal fertility of highly evolved magma systems: A case study from the Herberton Sn–W–Mo Mineral Field, Queensland, Australia. Earth and Planetary Science Letters, 486: 84–93.

Chesley, J. T. et al., 1993. Thermochronology of the Cornubian batholith in southwest England: Implications for pluton emplacement and protracted hydrothermal mineralization. Geochimica et Cosmochimica Acta, 57(8): 1817–1835.

Chiaradia, M., Schaltegger, U., Spikings, R., Wotzlaw, J.-F., Ovtcharova, M., 2013. How accurately can we date the duration of magmatic-hydrothermal events in porphyry systems?—an invited paper. Economic Geology, 108(4): 565-584.

Christensen, J. N., Halliday, A. N., Leigh, K. E., Randell, R. N., Kesler, S. E., 1995. Direct dating of sulfides by Rb–Sr: A critical test using the Polaris Mississippi Valley-type Zn–Pb deposit. Geochimica et Cosmochimica Acta, 59(24): 5191–5197.

Clemens, J., Mawer, C., 1992. Granitic magma transport by fracture propagation. Tectonophysics, 204(3–4): 339–360.

Coleman, D. S., Gray, W., Glazner, A. F., 2004. Rethinking the emplacement and evolution of zoned plutons: Geochronologic evidence for incremental assembly of the Tuolumne Intrusive Suite, California. Geology, 32(5): 433–436.

Colquhoun, G. P. et al., 2006. CARGELLIGO, New South Wales 1:250 000 Geological Sheet SI/55-6: Explanatory Notes – 3rd. edition, Geological Survey of New South Wales.

Cox, S. F., 2007. Structural and isotopic constraints on fluid flow regimes and fluid pathways during upper crustal deformation: An example from the Taemas area of the Lachlan Orogen, SE Australia. Journal of Geophysical Research: Solid Earth, 112(B8): n/a–n/a.

Clemens, J.D., Vielzeuf, D., 1987. Constraints on Melting and Magma Production in the Crust. Earth and Planetary Science Letters, 86(2-4): 287-306.
de Saint Blanquat, M. et al., 2011. Multiscale magmatic cyclicity, duration of pluton construction, and the paradoxical relationship between tectonism and plutonism in continental arcs. Tectonophysics, 500(1–4): 20–33.

DePaolo, D. J., 1981. Trace element and isotopic effects of combined wallrock assimilation and fractional crystallization. Earth and Planetary Science Letters, 53(2): 189–202.

DePaolo, D. J., Wasserburg, G. J., 1979. Petrogenetic mixing models and Nd–Sr isotopic patterns. Geochimica et Cosmochimica Acta, 43(4): 615–627.

Desbois, G., Ingrin, J., 2007. Anisotropy of hydrogen diffusion in tourmaline. Geochimica Et Cosmochimica Acta, 71(21): 5233–5243.

Dostal, J., Chatterjee, A. K., Kontak, D. J., 2004. Chemical and isotopic (Pb, Sr) zonation in a peraluminous granite pluton: role of fluid fractionation. Contributions to Mineralogy and Petrology, 147(1): 74–90.

Drivenes, K. et al., 2015. Late-magmatic immiscibility during batholith formation: assessment of B isotopes and trace elements in tourmaline from the Land's End granite, SW England. Contributions to Mineralogy and Petrology, 169(6).

Duc-Tin, Q., Audétat, A., Keppler, H., 2007. Solubility of tin in (Cl, F)-bearing aqueous fluids at 700°C, 140MPa: A LA-ICP-MS study on synthetic fluid inclusions. Geochimica et Cosmochimica Acta, 71(13): 3323–3335.

Duncan, R. J., Buick, I. S., Kobayashi, K., Wilde, A. R., 2014. Chemical and stable isotopic characteristics of syn-tectonic tourmaline from the Western fold belt, Mount Isa inlier, Queensland, Australia. Chemical Geology, 381: 131–143.

Dutrow, B. L., Foster, C. T., Henry, D. J., 1999. Tourmaline-rich pseudomorphs in sillimanite zone metapelites: Demarcation of an infiltration front, American Mineralogist, pp. 794.

Dutrow, B. L., Henry, D. J., 2011. Tourmaline. Elements, 7(5). Mineralogical Society of America, Québec.

Dutrow, B.L., Henry, D.J., 2018. Tourmaline compositions and textures: reflections of the fluid phase. Journal of Geosciences, 63(2): 99-110.

Eadington, P. J., 1977. A study of fluid inclusions and their significance in minerals from hydrothermal ore deposits, New England, New South Wales, Univ. Newcastle.

Eadington, P. J., 1983. A fluid inclusion investigation of ore formation in a tin-mineralized granite, New England, New South Wales. Economic Geology, 78(6): 1204–1221.

Eugster, H. P., 1986. Minerals in hot water. American Mineralogist, 71: 655–673.

Fekete, S. et al., 2016. Contrasting hydrological processes of meteoric water incursion during magmatic–hydrothermal ore deposition: An oxygen isotope study by ion microprobe. Earth and Planetary Science Letters, 451: 263–271.

Floess, D., Baumgartner, L. P., 2015. Constraining magmatic fluxes through thermal modelling of contact metamorphism. Geological Society, London, Special Publications, 422(1): 41–56.

Forster, M., Lister, G., 2008. Dating movement in shear zones: The example of the South Cyclades Shear Zone, Ios, Aegean Sea, Greece. IOP Conference Series: Earth and Environmental Science, 2(1): 012004.

Fraser, G. et al., 2014. New SHRIMP U–Pb zircon ages from the Lachlan, southern Thomson and New England orogens, New South Wales, Geoscience Australia Record 2014/053.

Glazner, A. F., Bartley, J. M., Coleman, D. S., Gray, W., Taylor, R. Z., 2004. Are plutons assembled over millions of years by amalgamation from small magma chambers? GSA today, 14(4/5): 4–12.

Glen, R. A., 2005. The Tasmanides of eastern Australia. Geological Society, London, Special Publications, 246(1): 23–96.

Gonfiantini, R., Stichler, W., Rozanski, K., 1995. Standards and intercomparison materials distributed by the International Atomic Energy Agency for stable isotope measurements. IAEA-TECDOC, 825: 13–29.

Goodenough, K. M., Lusty, P. A. J., Roberts, N. M. W., Key, R. M., Garba, A., 2014. Post-collisional Pan-African granitoids and rare metal pegmatites in western Nigeria: Age, petrogenesis, and the 'pegmatite conundrum'. Lithos, 200–201(1): 22–34.

Gray, C. M., Webb, J. A., 1995. Provenance of Palaeozoic turbidites in the Lachlan Orogenic Belt: Strontium isotopic evidence. Australian Journal of Earth Sciences, 42(1): 95–105.

Griffin, W. L., Slack, J. F., Ramsden, A. R., Win, T. T., Ryan, C. G., 1996. Trace elements in tourmalines from massive sulfides deposits and tourmalinites; geochemical controls and exploration applications. Economic Geology, 91(4): 657–675.

Groves, D. I., Bierlein, F. P., 2007. Geodynamic settings of mineral deposit systems. Journal of the Geological Society, 164(1): 19–30.
Gulson, B. L., Jones, M. T., 1992. Cassiterite: Potential for direct dating of mineral deposits and a precise age for the Bushveld Complex granites. Geology, 20(4): 355–358.

Halliday, A. N., 1980. The timing of early and main stage ore mineralization in Southwest Cornwall. Economic Geology, 75(5): 752–759.

Hazarika, P., Mishra, B., Pruseth, K. L., 2015. Diverse tourmaline compositions from orogenic gold deposits in the Hutti-Maski greenstone belt, India: Implications for sources of ore-forming fluids. Economic Geology, 110(2): 337–353.

Hawthorne, F.C., Henry, D.J., 1999. Classification of the minerals of the tourmaline group. European Journal of Mineralogy, 11(2): 201-215.
Heinrich, C. A., 1990. The chemistry of hydrothermal tin(-tungsten) ore deposition. Economic Geology, 85(3): 457–481.

Heinrich, C. A., Driesner, T., Stefansson, A., Seward, T. M., 2004. Magmatic vapor contraction and the transport of gold from the porphyry environment to epithermal ore deposits. Geology, 32(9): 761–764.

Heinrich, C. A., Günther, D., Audétat, A., Ulrich, T., Frischknecht, R., 1999. Metal fractionation between magmatic brine and vapor, determined by microanalysis of fluid inclusions. Geology, 27(8): 755–758.

Heinrich, C. A., Ryan, C. G., Mernagh, T. P., Eadington, P. J., 1992. Segregation of ore metals between magmatic brine and vapor; a fluid inclusion study using PIXE microanalysis. Economic Geology, 87(6): 1566–1583.

Henley, H. F., Brown, R. E., Stroud, W. J., 1999. The Mole Granite extent of mineralisation and exploration potential. In: Flood, P. G. (Ed.), Regional Geology, Tectonics and Metallogenesis of the New England Orogen. Univ. New England, pp. 385–392.

Henry, D. J., Dutrow, B. L., 1996. Metamorphic tourmaline and its petrologic applications. Reviews in Mineralogy and Geochemistry, 33(1): 503–557.

Henry, D. J., Dutrow, B. L., 1996. Metamorphic tourmaline and its petrologic applications. Boron, 33(1): 503–557.

Henry, D. J. et al., 2011. Nomenclature of the tourmaline–supergroup minerals. American Mineralogist, 96: 895–913.

Hensel, H. D., McCulloch, M. T., Chappell, B. W., 1985. The New England Batholith: constraints on its derivation from Nd and Sr isotopic studies of granitoids and country rocks. Geochimica et Cosmochimica Acta, 49(2): 369–384.

Holtz, F., Johannes, W., 1991. Effect of Tourmaline on Melt Fraction and Composition of First Melts in Quartzofeldspathic Gneiss. European Journal of Mineralogy, 3(3): 527–536.

Holtz, F., Johannes, W., 1994. Maximum and Minimum Water Contents of Granitic Melts – Implications for Chemical and Physical-Properties of Ascending Magmas. Lithos, 32(1–2): 149–159.

Horwitz, E. P., Chiarizia, R., Dietz, M. L., Diamond, H., Nelson, D. M., 1993. Separation and preconcentration of actinides from acidic media by extraction chromatography. Analytica Chimica Acta, 281(2): 361–372.

Huang, S., Song, Y., Hou, Z., Xue, C., 2016. Chemical and stable isotopic (B, H, and O) compositions of tourmaline in the Maocaoping vein-type Cu deposit, western Yunnan, China: Constraints on fluid source and evolution. Chemical Geology, 439: 173–188.

Huyskens, M. H., Iizuka, T., Amelin, Y., 2012. Evaluation of colloidal silicagels for lead isotopic measurements using thermal ionisation mass spectrometry. Journal of Analytical Atomic Spectrometry, 27(9): 1439–1446.

Ishihara, S., 1977. The magnetite-series and ilmenite-series granitic rocks. Mining Geology, 27: 293–305.

Jeon, H., Williams, I. S., Bennett, V. C., 2014. Uncoupled O and Hf isotopic systems in zircon from the contrasting granite suites of the New England Orogen, eastern Australia: Implications for studies of Phanerozoic magma genesis. Geochimica et Cosmochimica Acta, 146: 132–149.

Jeon, H., Williams, I. S., Chappell, B. W., 2012. Magma to mud to magma: Rapid crustal recycling by Permian granite magmatism near the eastern Gondwana margin. Earth and Planetary Science Letters, 319–320: 104–117.

Jiang, S. Y., Palmer, M. R., Slack, J. F., Shaw, D. R., 1998. Paragenesis and chemistry of multistage tourmaline formation in the Sullivan Pb–Zn–Ag deposit, British Columbia. Economic Geology, 93(1): 47–67.

Jiang, S.-Y., Han, F., Shen, J.-Z., Palmer, M. R., 1999. Chemical and Rb–Sr, Sm–Nd isotopic systematics of tourmaline from the Dachang Sn-polymetallic ore deposit, Guangxi Province, P.R. China. Chemical Geology, 157(1–2): 49–67.

Jiang, S.-Y., Palmer, M. R., Yeats, C. J., 2002. Chemical and boron isotopic compositions of tourmaline from the Archean Big Bell and Mount Gibson gold deposits, Murchison Province, Yilgarn Craton, Western Australia. Chemical Geology, 188(3–4): 229–247.

Jiang, S.-Y., Slack, J. F., Palmer, M. R., 2000. Sm–Nd dating of the giant Sullivan Pb–Zn–Ag deposit, British Columbia. Geology, 28(8): 751–754.

Jiang, S.-Y., Yu, J.-M., Lu, J.-J., 2004. Trace and rare-earth element geochemistry in tourmaline and cassiterite from the Yunlong tin deposit, Yunnan, China: implication for migmatitic–hydrothermal fluid evolution and ore genesis. Chemical Geology, 209(3–4): 193–213.

Jochum, K. P. et al., 2011. Determination of Reference Values for NIST SRM 610–617 Glasses Following ISO Guidelines. Geostandards and Geoanalytical Research, 35(4): 397–429.

Keay, S., Collins, W. J., McCulloch, M. T., 1997. A three-component Sr–Nd isotopic mixing model for granitoid genesis, Lachlan fold belt, eastern Australia. Geology, 25(4): 307–310.

Kelly, J. L., Fu, B., Kita, N. T., Valley, J. W., 2007. Optically continuous silcrete quartz cements of the St. Peter Sandstone: High precision oxygen isotope analysis by ion microprobe. Geochimica et Cosmochimica Acta, 71(15): 3812–3832.

Kemp, A. I. S., Hawkesworth, C. J., Collins, W. J., Gray, C. M., Blevin, P. L., 2009. Isotopic evidence for rapid continental growth in an extensional accretionary orogen: The Tasmanides, eastern Australia. Earth and Planetary Science Letters, 284(3–4): 455–466.

Kempe, U., Belyatsky, B., Krymsky, R., Kremenetsky, A., Ivanov, P., 2001. Sm–Nd and Sr isotope systematics of scheelite from the giant Au(–W) deposit Muruntau (Uzbekistan): implications for the age and sources of Au mineralization. Mineralium Deposita, 36(5): 379–392.

Keppler, H., Wyllie, P., 1991. Partitioning of Cu, Sn, Mo, W, U, and Th between melt and aqueous fluid in the systems haplogranite–H2O−HCl and haplogranite–H2O−HF. Contributions to Mineralogy and Petrology, 109(2): 139–150.

Kerrich, R., Goldfarb, R. J., Richards, J. P., 2005. Metallogenic provinces in an evolving geodynamic framework. Economic Geology, 100(Anniversary volume): 1097–1136.
King, P. L., White, A. J. R., Chappell, B. W., Allen, C. M., 1997. Characterization and origin of aluminous A-type granites from the Lachlan Fold Belt, Southeastern Australia. Journal of Petrology, 38(3): 371–391.

Kleeman, D. J., 1982. The anatomy of a tin-mineralizing A-type granite. In: Flood, P.G., Runnegar, B. (Eds.), New England Geology. Univ. New England, pp. 327–334.

Kleeman, D. J., 1985. Origin of disseminated wolframite-bearing quartz–topaz rock at Torrington, New South Wales, Australia, High Heat Flow Production (HHP) Granites, Hydrothermal Circulation and Ore Genesis. Inst. Mining Metall., pp. 197–201.

Kleeman, J. D., Plimer, I. R., Lu, J., Foster, D. A., Davidson, R., 1997. Timing of thermal and mineralisation events associated with the Mole Granite. In: Ashley, P., Flood, P. G. (Editors), Tectonics and Metallogenesis of the New England Orogen, Special Publication 19. Geological Society of Australia, pp. 254–265.

Kovalenko, V., Ryabchikov, I. D., Antipin, V. S., 1988. Temperature dependence of the distribution coefficients for Sn, W, Pb, and Zn in magmatic systems. Geochemistry International, 25(1): 1–10.

Laker, D., 2017. Source material of the fractionated Mole Granite: whole rock and zircon analysis, Australian National University, Canberra.

Landenberger, B., Nakajima, T., Collins, W. J., Whitford, D. J., 2000. Mantle influence on the character of I-type granitoids of the New England Batholith: evidence from Sr and Nd isotopes., CSIRO, North Ryde, NSW.

Lehmann, B., 1982. Metallogeny of Tin – Magmatic Differentiation Versus Geochemical Heritage. Economic Geology, 77(1): 50–59.

Lehmann, B., 1990. Metallogeny of Tin. Lecture Notes in Earth Sciences, 32. Springer-Verlag, Berlin.
Lehmann, B., Harmanto, 1990. Large-scale tin depletion in the Tanjungpandan tin granite, Belitung Island, Indonesia. Economic Geology, 85(1): 99–111.

Leitch, E. C., 1974. The geological development of the southern part of the New England Fold Belt. Australian Journal of Earth Sciences, 21: 133–156.
Lerchbaumer, L., Audétat, A., 2012. High Cu concentrations in vapor-type fluid inclusions: An artifact? Geochimica et Cosmochimica Acta, 88 (Supplement C): 255–274.

Leuthold, J. et al., 2012. Time resolved construction of a bimodal laccolith (Torres del Paine, Patagonia). Earth and Planetary Science Letters, 325: 85–92.

Li, C. Y. et al., 2016. Dating cassiterite using laser ablation ICP-MS. Ore Geology Reviews, 72(P1): 313–322.

Li, P. F., Rosenbaum, G., Rubatto, D., 2012. Triassic asymmetric subduction rollback in the southern New England Orogen (eastern Australia): the end of the Hunter-Bowen Orogeny. Australian Journal of Earth Sciences, 59(6): 965–981.

Linnen, R. L., 1998. Depth of emplacement, fluid provenance and metallogeny in granitic terranes: a comparison of western Thailand with other tin belts. Mineralium Deposita, 33(5): 461–476.

London, D., 1996. Granitic pegmatites. Earth and Environmental Science Transactions of the Royal Society of Edinburgh, 87(1–2): 305–319.

London, D., Manning, D. A. C., 1995. Chemical variation and significance of tourmaline from Southwest England. Economic Geology, 90(3): 495–519.

Lonergan, A. D., 1971. Ore deposits in the southern half of the Mole Tableland, Univ. New England.

Longerich, H.P., Jackson, S.E., Gunther, D., 1996. Inter-laboratory note. Laser ablation inductively coupled plasma mass spectrometric transient signal data acquisition and analyte concentration calculation. Journal of Analytical Atomic Spectrometry, 11(9): 899-904.

Maas, R., McCulloch, M. T., Campbell, I. H., Goad, P. R., 1986. Sm–Nd and Rb–Sr dating of an Archean massive sulfide deposit: Kidd Creek, Ontario. Geology, 14(7): 585–588.

Marks, M. A. W. et al., 2013. Trace element systematics of tourmaline in pegmatitic and hydrothermal systems from the Variscan Schwarzwald (Germany): The importance of major element composition, sector zoning, and fluid or melt composition. Chemical Geology, 344(0): 73–90.

Marschall, H. R., Jiang, S. Y., 2011. Tourmaline Isotopes: No Element Left Behind. Elements, 7(5): 313–319.

Maruéjol, P., Cuney, M., Turpin, L., 1990. Magmatic and hydrothermal R.E.E. fractionation in the Xihuashan granites (SE China). Contributions to Mineralogy and Petrology, 104(6): 668–680.

Mavrogenes, J. A., Berry, A. J., Newville, M., Sutton, S. R., 2002. Copper speciation in vapor-phase fluid inclusions from the Mole Granite, Australia. American Mineralogist, 87(10): 1360–1364.

McCulloch, M. T., Chappell, B. W., 1982. Nd isotopic characteristics of S- and I-type granites. Earth and Planetary Science Letters, 58(1): 51–64.

McCulloch, M. T., Woodhead, J. D., 1993. Lead isotopic evidence for deep crustal-scale fluid transport during granite petrogenesis. Geochimica et Cosmochimica Acta, 57(3): 659–674.

McDonough, W. F., McCulloch, M. T., 1987. The southeast Australian lithospheric mantle: isotopic and geochemical constraints on its growth and evolution. Earth and Planetary Science Letters, 86(2–4): 327–340.

Michel, J., Baumgartner, L., Putlitz, B., Schaltegger, U., Ovtcharova, M., 2008. Incremental growth of the Patagonian Torres del Paine laccolith over 90 ky. Geology, 36(6): 459–462.

Migdisov, A.A., Williams-Jones, A.E., 2014. Hydrothermal transport and deposition of the rare earth elements by fluorine-bearing aqueous liquids. Mineralium Deposita, 49(8): 987-997.

Miller, J. S., Matzel, J. E., Miller, C. F., Burgess, S. D., Miller, R. B., 2007. Zircon growth and recycling during the assembly of large, composite arc plutons. Journal of Volcanology and Geothermal Research, 167(1–4): 282–299.

Mlynarczyk, M. S. J., Williams-Jones, A. E., 2006. Zoned tourmaline associated with cassiterite: implications for fluid evolution and tin mineralization in the San Rafael Sn–Cu deposit, southeastern Peru. The Canadian Mineralogist, 44(2): 347–365.

Mueller, A. G., de Laeter, J. R., Groves, D. I., 1991. Strontium isotope systematics of hydrothermal minerals from epigenetic Archean gold deposits in the Yilgarn Block, Western Australia. Economic Geology, 86(4): 780–809.

Mulholland, C. S. J., 1943. Torrington tin and wolfram deposits, Geological Survey of New South Wales.

Naumov, V.B., Kamenetsky, V.S., 2006. Silicate and salt melts in the genesis of the industrial'noe tin deposit: Evidence from inclusions in minerals. Geochemistry International, 44(12): 1181-1190.

Nebel, O., Mezger, K., 2008. Timing of thermal stabilization of the Zimbabwe Craton deduced from high-precision Rb–Sr chronology, Great Dyke. Precambrian Research, 164(3): 227–232.

Nekrasov, I. Y., Epel'baum, M. B., Sobolev, V. P., 1980. Partition of tin between melt and chloride fluid in the granite–SnO–SnO_2–fluid system. Dokl Earth Sci, 252;165–168.

Nekrasov, I. Y., Epel'baum, M. B., Sobolev, V. P., 1980. Tin Distribution between Melt and Chloride Fluid in the Granite–SnO (SnO_2)–Fluid. Dokl. Akad. Nauk SSSR, 252(4): 977–981.

Nelson, D. R., Crawford, A. J., McCulloch, M. T., 1984. Nd–Sr isotopic and geochemical systematics in Cambrian boninites and tholeiites from Victoria, Australia. Contributions to Mineralogy and Petrology, 88(1–2): 164–172.

Neymark, L. A., Holm-Denoma, C. S., Moscati, R. J., 2018. In situ LA-ICPMS U–Pb dating of cassiterite without a known-age matrix-matched reference material: Examples from worldwide tin deposits spanning the Proterozoic to the Tertiary. Chemical Geology.

O'Neil, J. R., Shaw, S. E., Flood, R. H., 1977. Oxygen and hydrogen isotope compositions as indicators of granite genesis in the New England Batholith, Australia. Contributions to Mineralogy and Petrology, 62(3): 313–328.

Paterson, S. R., Ducea, M. N., 2015. Arc Magmatic Tempos: Gathering the Evidence. Elements, 11(2): 91–98.

Paton, C., Hellstrom, J., Paul, B., Woodhead, J., Hergt, J., 2011. Iolite: Freeware for the visualisation and processing of mass spectrometric data. Journal of Analytical Atomic Spectrometry, 26(12): 2508–2518.

Payolla, B. L. et al., 2002. Geological evolution of the basement rocks in the east-central part of the Rondônia Tin Province, SW Amazonian craton, Brazil: U–Pb and Sm–Nd isotopic constraints. Precambrian Research, 119(1–4): 141–169.

Petford, N., Cruden, A., McCaffrey, K., Vigneresse, J.-L., 2000. Granite magma formation, transport and emplacement in the Earth's crust. Nature, 408(6813): 669.

Pettke, T., Audétat, A., Schaltegger, U., Heinrich, C. A., 2005. Magmatic-to-hydrothermal crystallization in the W–Sn mineralized Mole Granite (NSW, Australia): Part II: Evolving zircon and thorite trace element chemistry. Chemical Geology, 220(3–4): 191–213.

Phillips, G., Landenberger, B., Belousova, E. A., 2011. Building the New England Batholith, eastern Australia—Linking granite petrogenesis with geodynamic setting using Hf isotopes in zircon. Lithos, 122(1–2): 1–12.

Pirajno, F., 2016. A classification of mineral systems, overviews of plate tectonic margins and examples of ore deposits associated with convergent margins. Gondwana Research, 33: 44–62.

Plimer, I. R., Kleeman, D. J., 1985. Mineralization associated with the Mole Granite, Australia, High Heat Production Granites (HHP), Hydrothermal Circulation and Ore Genesis. Inst. Mining Metall., pp. 563–569.

Pollington, A. D. et al., 2016. Experimental calibration of silicon and oxygen isotope fractionations between quartz and water at 250°C by in situ microanalysis of experimental products and application to zoned low δ30Si quartz overgrowths. Chemical Geology, 421: 127–142.

Powell, W., O'Reilly, S. Y., 2001. Ancient mantle beneath New England, GEMOC National Key Centre for Geochemical Evolution and Metallogeny of Continents, Macquarie University, Sydney.

Rankin, A. H., Ramsey, M. H., Coles, B., Van Langevelde, F., Thomas, C. R., 1992. The composition of hypersaline, iron-rich granitic fluids based on laser-ICP and Synchrotron-XRF microprobe analysis of individual fluid inclusions in topaz, Mole granite, eastern Australia. Geochimica et Cosmochimica Acta, 56(1): 67–79.

Redler, C., Irouschek, A., Jeffries, T., Gieré, R., 2016. Origin and Formation of Tourmaline-rich Cordierite-bearing Metapelitic Rocks from Alpe Sponda, Central Alps (Switzerland). Journal of Petrology, 57(2): 277–308.

Ren, S. K., 1989. The Ardlethan tin field, New South Wales: Breccia pipes and mineralisation, Australian National University, Canberra, 266 pp.

Ren, S. K., Walshe, J. L., Paterson, R. G., Both, R. A., Andrew, A., 1995. Magmatic and hydrothermal history of the porphyry-style deposits of the Ardlethan tin field, New South Wales, Australia. Economic Geology, 90(6): 1620–1645.

Richards, J. R., Compston, W., Paterson, R. G., 1982. Isotopic information on the Ardlethan tinfield, New South Wales. Proceedings of the Australasian Institute of Mining & Metallurgy, 284: 11–16.

Romer, R. L., Kroner, U., 2016. Phanerozoic tin and tungsten mineralization – Tectonic controls on the distribution of enriched protoliths and heat sources for crustal melting. Gondwana Research, 31: 60–95.

Rozendaal, A., Bruwer, L., 1995. Tourmaline nodules: indicators of hydrothermal alteration and Sn–Zn–(W) mineralization in the Cape Granite Suite, South Africa. Journal of African Earth Sciences, 21(1): 141–155.

Rudnick, R. L., Gao, S., 2003. 3.01 – Composition of the Continental Crust A2 – Holland, Heinrich D. In: Turekian, K.K. (Ed.), Treatise on Geochemistry. Pergamon, Oxford, pp. 1–64.

Salters, V. J. M., Stracke, A., 2004. Composition of the depleted mantle. Geochemistry, Geophysics, Geosystems, 5(5): n/a–n/a.

Salvi, S., Williams-Jones, A. E., 1996. The role of hydrothermal processes in concentrating high-field strength elements in the Strange Lake peralkaline

complex, northeastern Canada. Geochimica et Cosmochimica Acta, 60(11): 1917–1932.

Sawyer, E.W., 2001. Melt segregation in the continental crust: distribution and movement of melt in anatectic rocks. Journal of Metamorphic Geology, 19(3): 291-309.

Schaltegger, U., Pettke, T., Audétat, A., Reusser, E., Heinrich, C. A., 2005. Magmatic-to-hydrothermal crystallization in the W–Sn mineralized Mole Granite (NSW, Australia): Part I: Crystallization of zircon and REE-phosphates over three million years—a geochemical and U–Pb geochronological study. Chemical Geology, 220(3–4): 215–235.

Schmidt, C., 2018. Formation of hydrothermal tin deposits: Raman spectroscopic evidence for an important role of aqueous Sn(IV) species. Geochimica et Cosmochimica Acta, 220: 499–511.

Schuiling, R. D., 1967. Tin belts on the continents around the Atlantic Ocean. Economic Geology, 62(4): 540–550.

Shaw, S. E., Flood, R. H., 1981. The New England Batholith, Eastern Australia – Geochemical Variations in Time and Space. Journal of Geophysical Research, 86(Nb11): 530–544.

Shibata, S.-N., Tanaka, T., Yamamoto, K., 2006. Crystal structure control of the dissolution of rare earth elements in water–mineral interactions. Geochemical Journal, 40: 437–446.

Sillitoe, R. H., 1974. Tin mineralisation above mantle hot spots. Nature, 248(5448): 497–499.

Sillitoe, R. H., Halls, C., Grant, J. N., 1975. Porphyry tin deposits in Bolivia. Economic Geology, 70(5): 913–927.

Simons, B., Andersen, J. C. Ø., Shail, R. K., Jenner, F. E., 2017. Fractionation of Li, Be, Ga, Nb, Ta, In, Sn, Sb, W and Bi in the peraluminous Early Permian Variscan granites of the Cornubian Batholith: Precursor processes to magmatic-hydrothermal mineralisation. Lithos, 278–281(Supplement C): 491–512.

Slack, J. F., Trumbull, R. B., 2011. Tourmaline as a recorder of ore-forming processes. Elements, 7(5): 321–326.

Smith, M. P., Yardley, B. W. D., 1996. The boron isotopic composition of tourmaline as a guide to fluid processes in the southwestern England orefield: An ion microprobe study. Geochimica et Cosmochimica Acta, 60(8): 1415–1427.

Solomon, M., Groves, D.I., 2000. The geology and origin of Australia's mineral deposits. Oxford University Press.

Spencer, E.T., Wilkinson, J.J., Creaser, R.A., Seguel, J., 2015. The Distribution and Timing of Molybdenite Mineralization at the El Teniente Cu-Mo Porphyry Deposit, Chile. Economic Geology, 110(2): 387-421.

Stein, H. J., Sundblad, K., Markey, R. J., Morgan, J. W., Motuza, G., 1998. Re–Os ages for Archean molybdenite and pyrite, Kuittila-Kivisuo, Finland and Proterozoic molybdenite, Kabeliai, Lithuania: testing the chronometer in a metamorphic and metasomatic setting. Mineralium Deposita, 33(4): 329–345.

Štemprok, M., 1990. Solubility of tin, tungsten and molybdenum oxides in felsic magmas. Mineralium Deposita, 25(3): 205–212.

Sun, S.-S., Eadington, P. J., 1987. Oxygen isotope evidence for the mixing of magmatic and meteoric waters during tin mineralization in the Mole Granite, New South Wales, Australia. Economic Geology, 82(1): 43–52.

Sushchevskaya, T., Ignatiev, A., Velivetskaya, T., 2011. Magmatic Nature of Mineralizing Fluids in the Solnechnoye Sn Deposit (Russia) Deduced from

Isotopic (H, O) Compositions of Tourmaline. Resource Geology, 61(4): 407–413.

Sweetapple, M. T., Collins, P. L. F., 2002. Genetic Framework for the Classification and Distribution of Archean Rare Metal Pegmatites in the North Pilbara Craton, Western Australia. Economic Geology, 97(4): 873–895.

Taylor, R. G., 1979. Geology of Tin Deposits. Developments in Economic Geology, 11. Elsevier.

Taylor, S. R., McLennan, S. M., 1995. The geochemical evolution of the continental crust. Reviews of Geophysics, 33(2): 241–265.

Thompson, J. F. H., Sillitoe, R. H., Baker, T., Lang, J. R., Mortensen, J. K., 1999. Intrusion-related gold deposits associated with tungsten–tin provinces. Mineralium Deposita, 34(4): 323–334.

Tischendorf, G., 1977. Geochemical and petrographic characteristics of silicic magmatic rocks associated with rare-element mineralisation. In: Stemprok, M., Burnol, L., Tischendorf, G. (Eds.), Metallization associated with acid magmatism, Prague.

Tischendorf, G., Förster, H. J., 1990. Acid magmatism and related metallogenesis in the Erzgebirge. Geological Journal, 25(3–4): 443–454.

Tonarini, S., Dini, A., Pezzotta, F., Leeman, W. P., 1998. Boron isotopic composition of zoned (schorl–elbaite) tourmalines, Mt. Capanne Li–Cs pegmatites, Elba (Italy). European Journal of Mineralogy, 10(5): 941–952.

Trumbull, R. B., Krienitz, M. S., Gottesmann, B., Wiedenbeck, M., 2008. Chemical and boron-isotope variations in tourmalines from an S-type granite and its source rocks: the Erongo granite and tourmalinites in the Damara Belt, Namibia. Contributions to Mineralogy and Petrology, 155(1): 1–18.

Tuttle, O. F., Bowen, N. L., 1958. Origin of granite in the light of experimental studies in the system $NaAlSi_3O_8$–$KAlSi_3O_8$–SiO_2–H_2O. In: Tuttle, O. F., Bowen, N. L. (Eds.), Origin of Granite in the Light of Experimental Studies in the System $NaAlSi_3O_8$–$KAlSi_3O_8$–SiO_2–H_2O. Geological Society of America.

van Hinsberg, V. J., 2011. Preliminary experimental data on trace-element partitioning between tourmaline and silicate melt. The Canadian Mineralogist, 49(1): 153–163.

Vernon, R. H., Etheridge, M.A., Wall, V. J., 1988. Shape and Microstructure of Microgranitoid Enclaves – Indicators of Magma Mingling and Flow. Lithos, 22(1): 1–11.

Vigneresse, J.L., Barbey, P., Cuney, M., 1996. Rheological transitions during partial melting and crystallization with application to felsic magma segregation and transfer. Journal of Petrology, 37(6): 1579-1600.

Villa, I.M., 2016. Diffusion in mineral geochronometers: Present and absent. Chemical Geology, 420: 1–10.

Villa, I. M., De Bièvre, P., Holden, N. E., Renne, P. R., 2015. IUPAC-IUGS recommendation on the half life of ^{87}Rb. Geochimica et Cosmochimica Acta, 164(Supplement C): 382–385.

Walshe, J. L., Heithersay, P. S., Morrison, G. W., 1995. Toward an understanding of the metallogeny of the Tasman fold belt system. Economic Geology, 90(6): 1382–1401.

Walshe, J. L., Solomon, M., Whitford, D. J., Sun, S.-S., Foden, J. D., 2011. The role of the mantle in the genesis of tin deposits and tin provinces of Eastern Australia. Economic Geology, 106(2): 297–305.

Waltenberg, K., Blevin, P. L., Bodorkos, S., Cronin, D. E., 2015. New SHRIMP U–Pb zircon ages from the New England Orogen, New South Wales, Geoscience Australia, Canberra.

Wark, D. A., Miller, C. F., 1993. Accessory mineral behavior during differentiation of a granite suite: monazite, xenotime and zircon in the Sweetwater Wash pluton, southeastern California, U.S.A. Chemical Geology, 110(1): 49–67.

Whalen, J.B., Currie, K.L., Chappell, B.W., 1987. A-type granites: geochemical characteristics, discrimination and petrogenesis. Contributions to Mineralogy and Petrology, 95(4): 407-419.

White, A. J. R., 2001. Water, restite and granite mineralisation. Australian Journal of Earth Sciences, 48(4): 551–555.

Wilson, G. A., Eugster, H. P., 1990. Cassiterite solubility and tin speciation in supercritical chloride solutions. In: Spencer, R.J., Chou, I.M. (Eds.), Fluid–Mineral interactions: A tribute to H. P. Eugster. Special Publication. The Geochemical Society, pp. 179–195.

Wolf, M., Romer, R. L., Franz, L., López-Moro, F. J., 2018. Tin in granitic melts: The role of melting temperature and protolith composition. Lithos, 310–311: 20–30.

Wood, S. A., 1990. The aqueous geochemistry of the rare-earth elements and yttrium: 2. Theoretical predictions of speciation in hydrothermal solutions to 350°C at saturation water vapor pressure. Chemical Geology, 88(1): 99–125.

Yang, J.-H., Zhou, X.-H., 2001. Rb–Sr, Sm–Nd, and Pb isotope systematics of pyrite: Implications for the age and genesis of lode gold deposits. Geology, 29(8): 711–714.

Yang, S.-Y., Jiang, S.-Y., Zhao, K.-D., Dai, B.-Z., Yang, T., 2015. Tourmaline as a recorder of magmatic–hydrothermal evolution: an in situ major and trace element analysis of tourmaline from the Qitianling batholith, South China. Contributions to Mineralogy and Petrology, 170(5–6): 1–21.

Yavuz, F., Jiang, S.-Y., Karakaya, N., Karakaya, M. Ç., Yavuz, R., 2011. Trace-element, rare-earth element and boron isotopic compositions of tourmaline from a vein-type Pb–Zn–Cu ± U deposit, NE Turkey. International Geology Review, 53(1): 1–24.

Yi, W. et al., 2000. Cadmium, indium, tin, tellurium, and sulfur in oceanic basalts: Implications for chalcophile element fractionation in the Earth. Journal of Geophysical Research: Solid Earth, 105(B8): 18927–18948.

Yuan, S. et al., 2011. In situ LA-MC-ICP-MS and ID-TIMS U–Pb geochronology of cassiterite in the giant Furong tin deposit, Hunan Province, South China: New constraints on the timing of tin–polymetallic mineralization. Ore Geology Reviews, 43(1): 235–242.

Yuan, S. et al., 2008. A precise U–Pb age on cassiterite from the Xianghualing tin-polymetallic deposit (Hunan, South China). Mineralium Deposita, 43(4): 375–382.

Zachariáš, J., Žáček, V., Pudilová, M., Machovič, V., 2005. Fluid inclusions and stable isotope study of quartz–tourmaline veins associated with beryl and emerald mineralization, Kafubu area, Zambia. Chemical Geology, 223(1–3): 136–152.

Zajacz, Z., Halter, W. E., Pettke, T., Guillong, M., 2008. Determination of fluid/melt partition coefficients by LA-ICPMS analysis of co-existing fluid and silicate melt inclusions: Controls on element partitioning. Geochimica et Cosmochimica Acta, 72(8): 2169–2197.

Zagruzina, I.A., Pinskii, E.M., Savinova, I.B., 1987. Uranium in Cassiterite of Tin Deposits. International Geology Review, 29(1): 94-109.

Zeng, L., Asimow, P. D., Saleeby, J. B., 2005. Coupling of anatectic reactions and dissolution of accessory phases and the Sr and Nd isotope systematics of anatectic melts from a metasedimentary source. Geochimica et Cosmochimica Acta, 69(14): 3671–3682.

Zhang, D. L., Peng, J. T., Hu, R. Z., Yuan, S. D., Zheng, D. S., 2011. The closure of U–Pb isotope system in cassiterite and its reliability for dating. Geological Review, 57(4): 549–554.

Zhao, K., Jiang, S., Xiao, H., Ni, P., 2002. Origin of ore-forming fluids of the Dachang Sn-polymetallic ore deposit: Evidence from helium isotopes. Chinese Science Bulletin, 47(12): 1041–1045.

Zimmerman, A., Stein, H.J., Morgan, J.W., Markey, R.J., Watanabe, Y., 2014. Re–Os geochronology of the El Salvador porphyry Cu–Mo deposit, Chile: tracking analytical improvements in accuracy and precision over the past decade. Geochimica et Cosmochimica Acta, 131: 13-32.

Appendices

Appendix 1: Carr, P.A., Norman, M. D., and Bennett, V. C., 2017. Assessment of crystallographic orientation effects on secondary ion mass spectrometry (SIMS) analysis of cassiterite. Chemical Geology, 467: 122–133.

Chemical Geology 467 (2017) 122–133

Contents lists available at ScienceDirect

Chemical Geology

journal homepage: www.elsevier.com/locate/chemgeo

Assessment of crystallographic orientation effects on secondary ion mass spectrometry (SIMS) analysis of cassiterite

Patrick A. Carr*, Marc D. Norman, Vickie C. Bennett

Research School of Earth Sciences, The Australian National University, Canberra, ACT 2601, Australia

ARTICLE INFO

Keywords:
Cassiterite
SIMS
Crystallographic orientation effects
U-Pb
$\delta^{18}O$

ABSTRACT

Crystallographic orientation effects on ion microprobe analyses for U-Pb and O-isotopes have been reported for a number of oxide minerals, including rutile (TiO_2) and baddeleyite (ZrO_2). Here we evaluate the effects of crystal orientation on U-Pb and O-isotopic data measured by ion microprobe on cassiterite (SnO_2), which is isostructural with rutile. The crystallographic orientations of mounted and polished grains of cassiterite were determined by electron backscatter diffraction (EBSD). Those grains were then analysed for U-Th-Pb isotopes and $^{18}O/^{16}O$ compositions using the SHRIMP RG and SHRIMP SI ion microprobes, respectively. Based on these data, cassiterite appears to show no dependence of key measurement parameters such as UO_2/UO, Pb/UO, or $^{18}O/^{16}O$ ratios at the achieved precision with crystallographic orientation. The contrasting behaviour of isostructural cassiterite and rutile provides new insights into the mechanisms leading to crystallographic orientation effects during ion microprobe analyses with electronic structure proposed as being a significant factor.

1. Introduction

Cassiterite (SnO_2), the primary ore mineral for Sn, commonly crystallises in magmatic and magmatic-hydrothermal environments associated with highly fractionated granites (e.g. Taylor, 1979; Linnen, 1998; Blevin, 2004). Cassiterite is resistant to chemical and physical abrasion and can survive hydrothermal overprinting events and often concentrates in detrital deposits. The geochemical characteristics of cassiterite are being used increasingly to study the processes and conditions that create tin mineralisation and related ore deposits including using the oxygen isotopic compositions of cassiterite and coexisting phases for thermometry (Macey and Harris, 2006) and tracing the source of mineralising fluids (Sun and Eadington, 1987; Plimer et al., 1991; Haapala, 1997; Jiang et al., 2004; Abdalla et al., 2008). In addition, trace element concentrations within cassiterite have been used for source tracing (e.g. Plimer et al., 1991; Jiang et al., 2004), Those studies have shown that cassiterite often incorporates moderate amounts of U and tends to exclude initial Pb (Zagruzina et al., 1987), which makes it amenable to dating using U-Pb isotopic systems (Gulson and Jones, 1992; Liu et al., 2007; Yuan et al., 2008, 2011; Li et al., 2016).

Although many cassiterites have relatively simple, monogenetic growth textures, others have more complex textures that might indicate later episodes of alteration or recrystallization that could compromise or obscure analyses of bulk samples (Fig. 1). This has motivated the application of in-situ analytical techniques such as ion microprobe and laser ablation ICPMS for U-Pb dating (Yuan et al., 2011; Chen et al., 2014; Zhang et al., 2015; Li et al., 2016) and ion microprobe oxygen isotopic analysis of cassiterite as the high spatial resolution provided by these techniques allows specific textural zones to be targeted for analysis. In addition, cassiterite is a common accessory mineral in a variety of metal deposits including Nb-Ta (e.g. Sweetapple and Collins, 2002), Au (e.g. Thompson et al., 1999) and Cu-Pb-Zn (Audétat et al., 2000a, 2000b) so that techniques requiring small amounts of material are advantageous.

A number of previous studies have applied in-situ laser ablation ICPMS analyses for U-Pb dating of cassiterite (e.g., Liu et al., 2007; Yuan et al., 2008, 2011; Blevin and Norman, 2010; Li et al., 2016; Cao et al., 2016) but to our knowledge, no U-Pb or O-isotope studies of cassiterite by secondary ionisation mass spectrometry (SIMS) have been reported. Caution is warranted, however, because previous studies have demonstrated large crystallographic orientation effects on SIMS analyses of rutile (Li et al., 2010, 2011; Taylor et al., 2012; Schmitt and Zack, 2012; Shulaker et al., 2015), which is isostructural with cassiterite, as well as for other simple structured oxides and sulphides including baddeleyite (Wingate and Compston, 2000; Li et al., 2010; Schmitt et al., 2010), magnetite (Lyon et al., 1998; Huberty et al., 2010; Kita et al., 2011), sphalerite and galena (Kozdon et al., 2010).

Although crystallographic orientation effects during SIMS analysis of some materials have been well-documented, the physical processes

* Corresponding author.
E-mail address: Patrick.carr@anu.edu.au (P.A. Carr).

http://dx.doi.org/10.1016/j.chemgeo.2017.08.003
Received 8 May 2017; Received in revised form 3 August 2017; Accepted 4 August 2017
Available online 06 August 2017

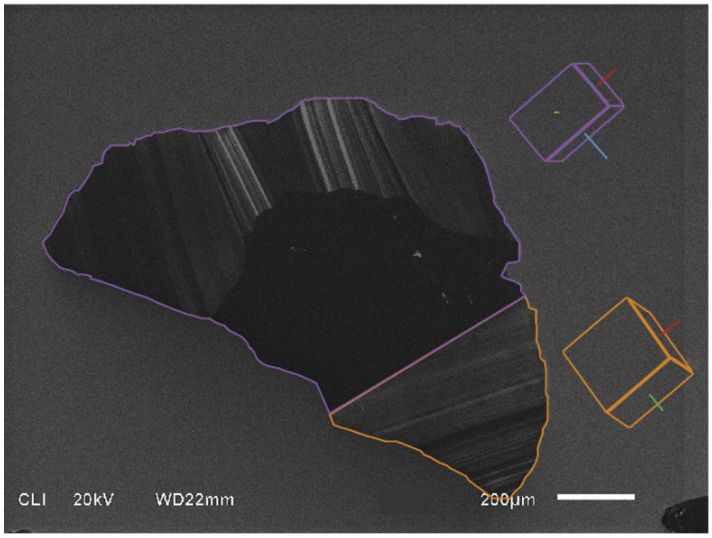

Fig. 1. Scanning Electron Microprobe (SEM) cathodoluminescence (CL) image of a Yankee cassiterite grain used in this study. The crystallographic orientation of the sectors within the grain are represented by the colour coded unit cells and major axes (red = c, green = a, blue = b). It is common in the Yankee and Elsemore cassiterite for the CL zoning to be coincident with changing crystallographic orientation. (For interpretation of the references to colour in this figure legend, the reader is referred to the web version of this article.)

that produce the effects are poorly understood (Lyon et al., 1998; Wingate and Compston, 2000; Huberty et al., 2010; Kozdon et al., 2010; Li et al., 2010, 2011; Schmitt et al., 2010; Kita et al., 2011; Taylor et al., 2012; Schmitt and Zack, 2012). The crystallographic orientation of the target mineral relative to the incoming ion beam appears to exert a control over the total sputter yield, secondary ion counts and secondary ion energies. Importantly the crystallographic orientation of some minerals can affect inter-element and isotopic fractionation, and oxide production.

Previous studies demonstrated that rutile displays some of the largest effects that have been observed so far (Li et al., 2010, 2011; Taylor et al., 2012; Schmitt and Zack, 2012; Shulaker et al., 2015). Taylor et al. (2012) showed that the crystallographic orientation of rutile affects the total signal as measured on the reference mass ($Ti_3O_3^+$), as well as the measured UO_2^+/UO^- ratio. They also showed that inaccurate estimations of the UO_2^+/UO^+ ratio can lead to 15% error in calculated ages of unknowns. Cassiterite is isostructural with rutile, being tetragonally coordinated with a 42mnm space group, although the unit cell dimensions of the two minerals differ slightly (cassiterite: a = 4.738, c = 3.118; rutile: a = 4.594, c = 2.958).

Thus knowledge of potential orientation effects is essential prior to SIMS analyses of cassiterite to determine U-Pb and O-isotopic compositions. Here we evaluate these effects using the SHRIMP RG and SHRIMP SI ion microprobes. Crystallographic orientations of the cassiterite grains and sub-grains were determined by electron backscatter diffraction (EBSD), followed by SHRIMP analyses of these grains.

2. Samples

Three cassiterite samples were used in this study. Cassiterite from the Yankee lode in the New England Orogen of eastern Australia and from near Euriowie in the Curnamona Province of central Australia were analysed for U-Pb isotopes. Cassiterite from within the Elsemore Granite in the New England Orogen was analysed for O isotopes as it appears to be relatively homogenous at the scale of ~5 mg multi-grain samples as measured by fluorination techniques (2.0 ± 0.3‰; Norman and Blevin, unpublished data obtained from GNS Science Lower Hutt, NZ).

The Yankee cassiterite occurs in veins associated with the Mole Granite, the age(s) of which are poorly defined. Kleeman et al. (1997) reported Ar and Rb–Sr isotopic data that implied emplacement of the Mole granite at 246 ± 2 Ma with hydrothermal and geothermal activity persisting in the area for about 15 Ma. They proposed cessation of widespread hydrothermal activity (~300 °C) at 243 ± 2 Ma based on a variety of fluid-related associations (see also Audétat et al., 2000a, 2000b). Recent TIMS U-Pb dating of zircon, monazite, and xenotime associated with the Mole granite system by Schaltegger et al. (2005) documents a ~3 Ma interval between the crystallisation of magmatic zircon within the granite at 247.7 ± 0.5 Ma to late-stage hydrothermal monazite at 244.4 ± 1.4 Ma. The Elsemore cassiterite occurs within a greisen hosted by the Elsemore Granite (Brown and Stroud, 1997). Like the Mole Granite, the Elsemore Granite is Middle Triassic in age but it has not been dated isotopically.

Cassiterite occurs in structurally controlled pegmatites in the Proterozoic Curnamona Province of central Australia. The age of the pegmatites and Sn mineralisation has not been measured isotopically. Anatexis prior to and during major deformation events (D_1–D_3; e.g. Fitzherbert, 2015) involved extensive partial melting and efficient melt extraction (White and Powell, 2002; White and Chappell, 2004) leading to granitic magmatism between 1597 and 1591 Ma (Page et al., 2000). Burton (2000) suggests that the pegmatites originated from late fluids derived from the undated Texas Bore Gneissic Leucogranite, which is lithologically similar to the 1591 ± 5 Ma Mundi Mundi type granites (Page et al., 2000). A minimum age constraint is provided by the Cambrian deformation associated with the Delamerian Orogeny (Burton, 2000).

3. Methods

3.1. Polishing

Whole rock samples were crushed to < 420 µm, a high density (> 3.3 g/cm^3) concentrate was prepared using heavy liquids, and the handpicked cassiterite grains were mounted randomly into epoxy discs. The mounts were polished with 1200 grade abrasive paper followed by a 9, 3 and 1 µm diamond polish. Although the mounts were suitable for most microbeam analytical techniques at this point, a further 30 min of polishing with alumina powder and approximately 2 h with colloidal silica was needed to remove the fine scratches caused by the diamond paste as these can affect measurements of crystallographic orientations as described below. Because of the extreme difference in hardness between the

cassiterite grains and epoxy resin, this process created significant surface relief, which could have affected the SIMS analyses. Thus following the grain orientation measurements by EBSD and prior to SHRIMP analysis the mount was repolished to flatness with 1 μm diamond paste.

3.2. Cathodoluminescence imaging

Internal textures within cassiterite were imaged by cathodoluminescence (CL) using a scanning electron microscope (SEM). Polished grain mounts were carbon coated and imaged using into a JEOL JSM-6610 SEM with a Robinson CL detector at the RSES, ANU with an operating voltage of 20 keV and working distance of ~20 mm.

3.3. Crystallographic orientations

Crystallographic orientations were determined for the Yankee and Elsemore grains using a Zeiss UltraPlus analytical field emission SEM with an Oxford Instruments EBSD detector at the Centre of Advanced Microscopy, ANU, using a tungsten filament with an acceleration voltage of 20 keV and spot diameter of 60 μm. Orientations were determined by spot analysis. Several grains displayed multiple crystallographic orientations which coincided with textural domains identified in CL imaging (Fig. 1). Each domain was analysed at least three times and measured backscattered patterns were compared to the match unit of Bolzan et al. (1997). All solutions had mean angular deviation (MAD) values of < 1. Data processing was completed using the Oxford Instruments Channel 5.10 software with the Mambo sub-program. The CL images were used to ensure that the same crystallographic domains analysed by EBSD were analysed by SHRIMP.

3.4. U-Th-Pb isotopes

U-Th-Pb isotopic compositions were measured on the SHRIMP RG over two sessions at the Research School of Earth Sciences, ANU. A 10 keV primary ion beam of O_2^- was focussed to a spot ~20 μm in diameter. Primary ion currents were ~4.6 nA during the first session and ~5.9 nA during the second session. Each analysis included an initial two-minute raster over the spot area to remove surficial Pb contamination. Positive sputtered ions were extracted at 10 keV and analysed at a mass resolution of ~6000, sufficient to resolve most potential isobars from the Pb and U species of interest (Fig. 2). Lead (Pb) masses were located using a mass offset from the dominant adjacent Sn peaks. The run table used for the two sessions is detailed in Appendix 1. The molecule $^{124}Sn_2{}^{16}O_2{}^+$ (AMU = 280) was used as a reference mass for estimates of concentration. During both sessions a single grain, with a single crystallographic orientation was analysed repeatedly as an internal reference. The data were reduced using SQUID 2.5 (Ludwig, 2009). Because there is no international reference material for U-Pb isotopic analysis of cassiterite, all U-Pb ages reported here were calibrated against grains of the Yankee cassiterite assuming radiogenic $^{206}Pb/^{238}U$ and $^{207}Pb/^{206}Pb$ values of 0.0384 and 0.5105, respectively, corresponding to an age of 243 Ma (Kleeman et al., 1997).

In a target with homogenous Pb/U the relative ionisation of Pb and U is proportionate to the ratio of U oxide species (typically UO_2/UO, UO/U or UO_2/U; Hinthorne et al., 1979; Compston et al., 1984). We followed procedures used previously for rutile by comparison against $UO_2{}^+/UO^+$. A mean relative sensitivity factor (RSF) is calculated for all standard analyses using the mean $UO_2{}^+/UO^+$, corresponding to the average analytical conditions for the session, using the formula:

$$Pb^+/UO^+ = RSF_{st} \times (UO_2{}^+/UO^+)^E \quad (1)$$

where E represents the slope of covariance defined by $\ln(Pb^+/UO^+)$ and $\ln(UO_2{}^+/UO^+)$ (Taylor et al., 2012; Schmitt and Zack, 2012). The true Pb/U ratios of the unknown (unk) are then calculated using the individual RSF of each unknown analysis (calculated using Eq. (1)) in the following equation:

$$(Pb/U)_{unk} = (RSF_{unk}/RSF_{st}) * (Pb/U)_{st} \quad (2)$$

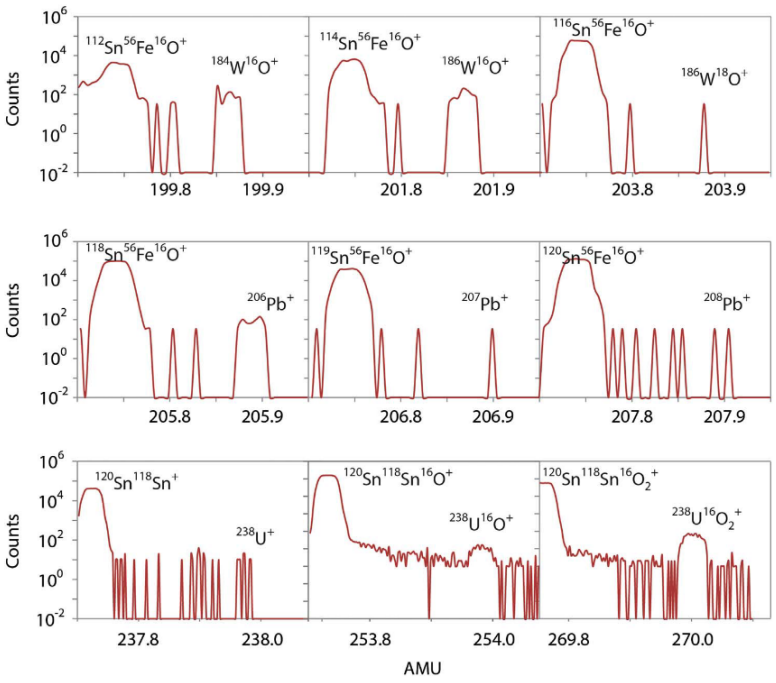

Fig. 2. SHRIMP RG mass spectra of a W-rich Yankee cassiterite grain showing A) the potential major mass interferences with ^{204}Pb) the clearly resolved ^{206}Pb peak and small to non-existent ^{207}Pb and ^{208}Pb peaks, and C) the increasing signal of U species from ^{238}U to $^{238}U^{16}O$ and $^{238}U^{16}O_2$. Ionised Sn molecules are present adjacent to all peaks and can be used to specifiy the positions of small U and Pb signals with a trim offset.

where Pb/U (st) is the true or ideal value of the standard, either assumed or measured by an independent technique.

3.5. Common Pb corrections for U-Pb SHRIMP data

Direct measurement of common Pb (monitored using ^{204}Pb) of cassiterite by SIMS is difficult due to the generally low concentrations and an isobaric interference between $^{186}W^{18}O^{+}$ and ^{204}Pb, requiring a mass resolution of ~10,000. Similarly, there is an isobaric inference between $^{120}Sn_4{}^{16}O^{++}$ and $^{232}Th^{16}O^{+}$ (see Section 4.3) that would require a mass resolution of ~12,000 to separate the two peaks. However, at 12000 mass resolution only approximately 70% of secondary ions are transmitted through the source slit, compared to approximately 90% transmission at 6000 mass resolution. Achieving the resolution required to separate these species would be at the expense of net counts, which are already low, and thus not practical.

In the Yankee and Euriowie cassiterite the highest count rates are on $^{206}Pb^{+}$ followed by $^{207}Pb^{+}$ followed by $^{208}Pb^{+}$. To correct for common Pb in age calculations we apply both the 207-method for higher count rates and the 208-method for its reliability in low Th/U minerals (Zack et al., 2011). Thorium concentrations in cassiterite are predominantly < 0.1 ppm (Gulson and Jones, 1992; Jiang et al., 2004; Li et al., 2016). Corrections were applied post-analysis using age-appropriate (243 Ma and 1585 Ma respectively) common Pb compositions from the Stacey and Kramers (1975) terrestrial model: Yankee cassiterite: $^{206}Pb/^{208}Pb = 0.474$, $^{207}Pb/^{208}Pb = 0.413$; Euriowie cassiterite: $^{206}Pb/^{208}Pb = 0.449$, $^{207}Pb/^{208}Pb = 0.431$. The reference Yankee cassiterite grain contained negligible common Pb and no corrections were required.

3.6. Oxygen isotopic compositions

Oxygen isotopic compositions ($\delta^{18}O$, where $\delta^{18}O = \left(\frac{\left(\frac{^{18}O}{^{16}O}\right)_{sample}}{\left(\frac{^{18}O}{^{16}O}\right)_{VSMOW}} - 1\right) * 1000$) of the Elsemore cassiterite were measured

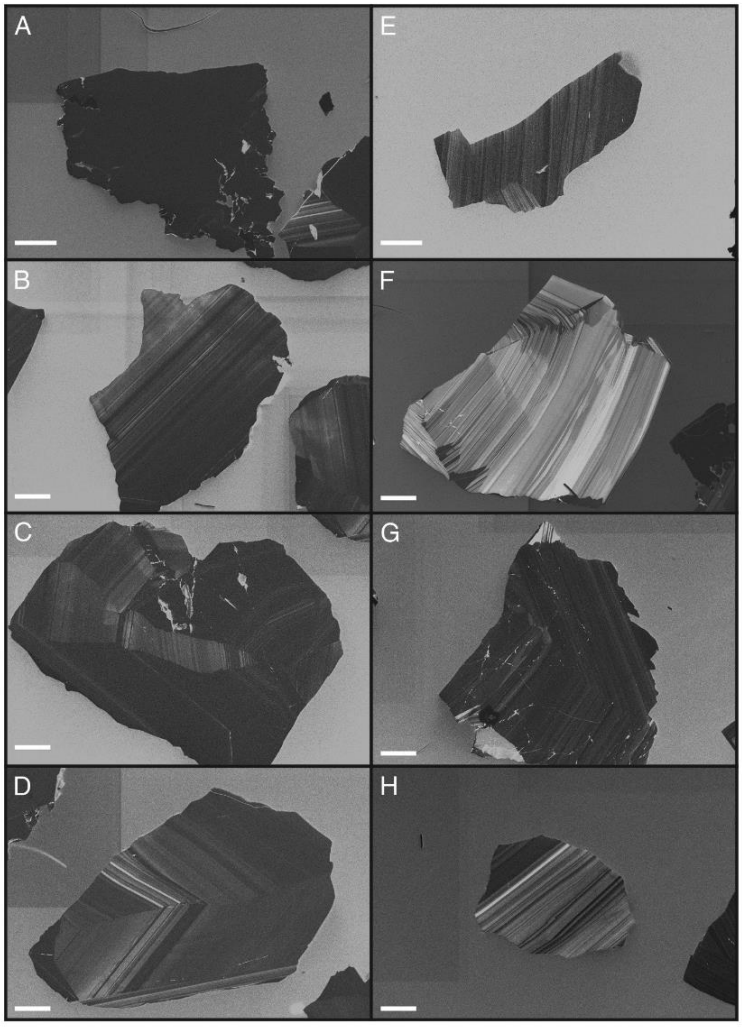

Fig. 3. SEM CL images of the Yankee cassiterite (A–D) and the Elsemore cassiterite (E–H) grains used in this study. White scale bars are 200 μm. The Yankee cassiterite commonly shows concentric zoning (B, C and D) and minor sector zoning (A and C). Secondary alterations and inclusions are rare but identified by bright CL response (e.g. A and C). The Elsemore cassiterite typically exhibits concentric zoning (*E*-F) with minor alteration along internal cracks (G) and with inclusions (E,F and G) defined by bright CL response. The bright CL inclusions are Fe- or Ti- oxides.

during a single session using the SHRIMP SI at the Research School of Earth Sciences, ANU. A primary Cs^+ beam of 12 nA was focussed to a ~ 25 μm spot. A single cassiterite crystal with one crystallographic orientation was used as a reference throughout the session, assuming a $\delta^{18}O$ value of 2.0 ± 0.3‰ based on bulk fluorination analysis of the Elsmore cassiterite (Section 2). Negative sputtered ions were extracted from the sample at 10 keV. The $^{16}O^-$ and $^{18}O^-$ isotopes were measured simultaneously with two Faraday cups (Ickert et al., 2008) at a mass resolution of 10,000 and the data were processed using the POXI in-house software. All analyses were normalised to the composition of the single orientated reference crystal.

4. Results

4.1. Cathodoluminescence imaging

Cassiterite is opaque or translucent to reddish brown in transmitted light depending on its chemical composition. Internal textures in opaque grains are difficult to identify by light microscope techniques and so cathodoluminescence (SEM–CL) imaging was used to examine internal characteristics of individual grains. The textural features revealed by CL primarily originate from the substitution of Ti, Fe and W for Sn (Hall and Ribbe 1971; Farmer et al., 1991). Titanium and W activate a bright CL response, except when in the presence of Fe which results in a quenched afterglow.

Internal textures of the Yankee and Elsemore cassiterite defined by the CL imaging are illustrated in Figs. 3 and 4. The Yankee cassiterite displays primary growth textures of concentric and sector zoning, with minor secondary alteration. Linear banding of light and dark zones, commonly concentric, is ubiquitous. Bands range between 1 and 200 μm in thickness and have both abrupt and diffuse boundaries. This banding can be both cyclic, showing repeating light to dark transitions (= Fig. 3E, F and H) and gradational from light to dark (or dark to light) (= Fig. 3B and D). Sector zoning is also common and always defined by dark features (Fig. 3A). This does not preclude chemical zoning in non-activator elements. In some grains the boundary between sector and concentric zoning is defined by a change in crystal orientation (Fig. 1) and elsewhere only by chemical composition. Mineral inclusions (mica) are common in the Elsemore cassiterite but rare in the Yankee cassiterite. Secondary features are common in both deposits and are readily identifiable by CL imaging. Generally these consist of alteration along cracks and at the boundaries that show up as extremely bright CL.

Internal textures of the Euriowie pegmatitic cassiterite grains are displayed in Fig. 4. The rhythmic banding observed in the Yankee and Elsemore cassiterite is rare in the Euriowie cassiterite (Fig. 4A). Instead textures are dominantly defined by curved, discontinuous and diffuse bands of light and dark features creating an overall mottled appearance. Single bands rarely exceed 150 μm in length and are mostly < 50 μm wide. Grains are commonly cracked and include numerous, strong luminescent (extremely bright) inclusions.

4.2. Crystallographic orientations

Crystallographic orientation data (Appendix 2) for the Yankee and Elsemore cassiterite grains are displayed in an inverse pole figure (Fig. 5A), which shows the angular differences between the sample and a reference frame (Bolzan et al., 1997). The three reference planes displayed (001), (100) and (110) represent rotations around the a, b, and c axes. Cassiterite has two major crystal faces, (100) and (110) (Fig. 5B) which are imperfect and indistinct respectively, whilst (001) is not a recognised terminal plane.

After crushing and milling, cassiterite separates generally displayed dominantly conchoidal fractured surfaces rather than the terminal growth faces shown in Fig. 5B. This is evident in Fig. 5A by a scattering of crystallographic orientations in both the Yankee and

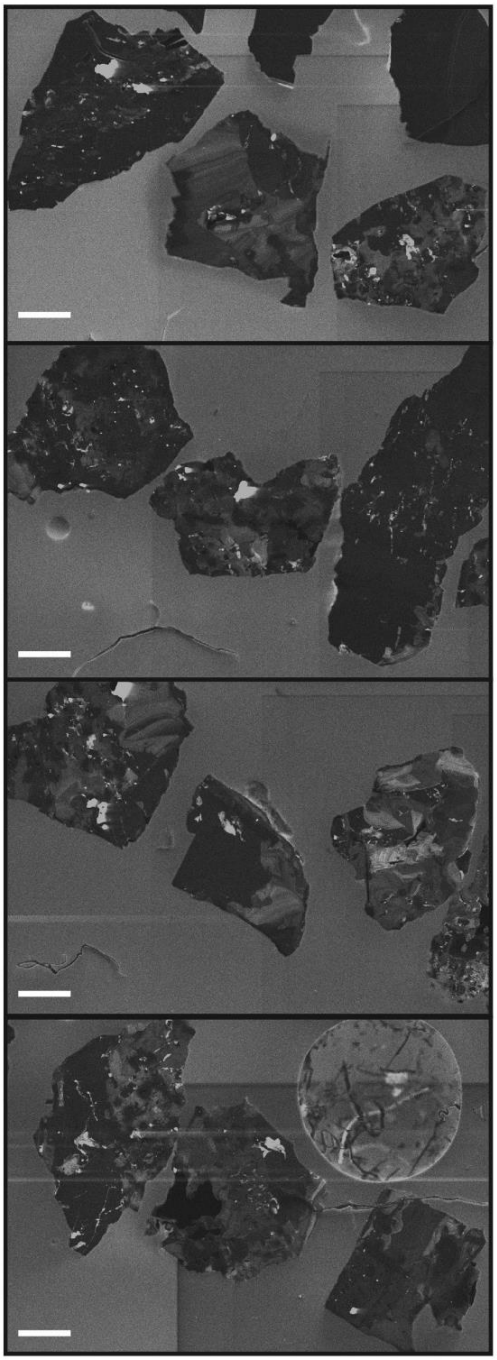

Fig. 4. SEM CL images of the Euriowie cassiterite grains used in this study. White scale bars are 200 μm. Internal textures are curved, discontinuous and diffuse bands of light and dark features creating an overall mottled appearance. Very bright oxide inclusions are common to the Euriowie Cassiterite.

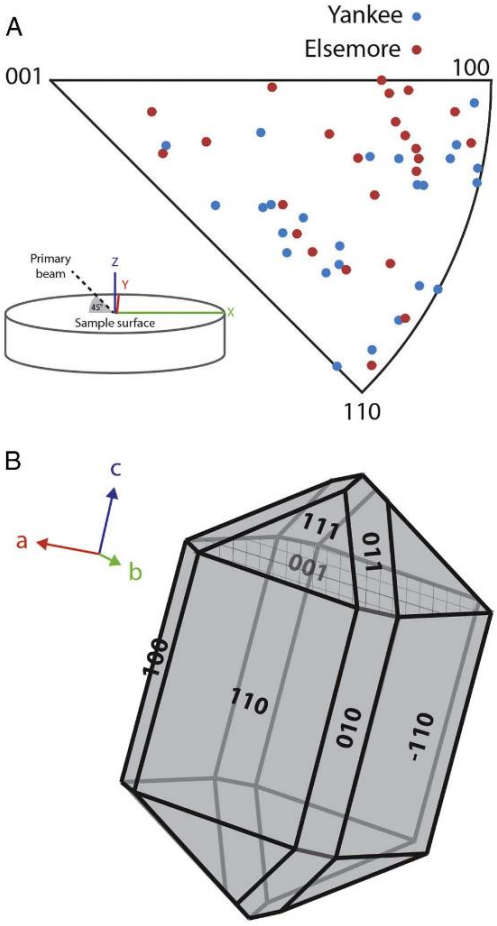

Fig. 5. (A) Inverse pole figure representation of all crystallographic orientations of the Yankee and Elsemore cassiterite used in this study. Cassiterite does not show a preferred orientation when mounted into epoxy; this is in contrast to isostructural rutile (e.g. Taylor et al., 2012) B: 3D model of cassiterite with terminating surfaces labelled.

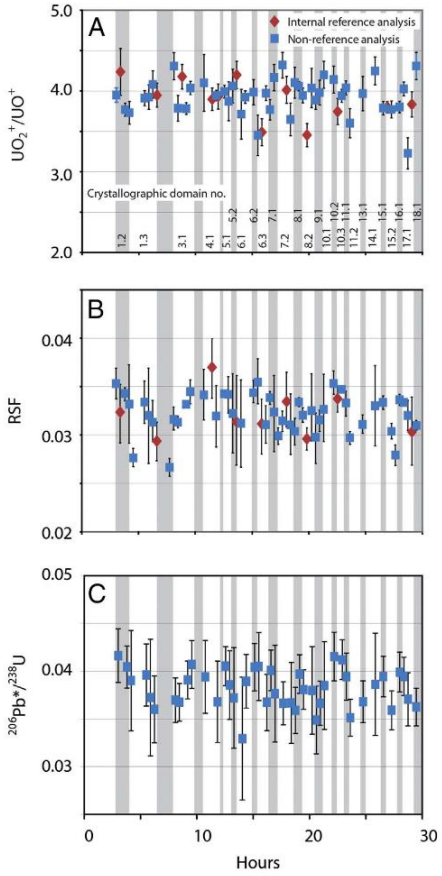

Fig. 6. Variation over time between UO_2/UO^+ (A), Relative Sensitivity Factor (B) and $^{206}Pb^*/^{238}U$ (C) for the Yankee cassiterite. Variations of these measured ratios on the single orientated crystal internal reference (red) are comparable with those 'unknown' measurements on all crystallographic orientations (blue). (For interpretation of the references to colour in this figure legend, the reader is referred to the web version of this article.)

Elsemore cassiterite. There is a scarcity of data points from both samples near to the (001) plane. The Elsemore cassiterite shows a slight preference for surfaces towards the (100) plane compared with the Yankee cassiterite.

4.3. Pb/U data and relative sensitivity calibration for SHRIMP

Sixteen of the Yankee cassiterite grains containing 26 defined crystallographic domains were analysed by SHRIMP RG. Another 10 grains of the Euriowie cassiterite with unknown crystallographic orientations were also analysed. These data are presented in Appendix 3.

All measured Pb/U ratios were corrected by normalisation to a single reference crystal of Yankee cassiterite. This single crystal displayed a restricted range in counts per second (Cts/s) on the $^{124}Sn_2{}^{16}O_2{}^+$ reference mass (11158–13,975 cts/s),$UO_2{}^+/UO^+$ (3.45–4.24) and $^{206}Pb^+/^{254}UO^+$ (0.074–0.135).

Measured $^{206}Pb^+/^{238}U^+$ values of cassiterite grains analysed as unknowns were 20–35 times higher in the Yankee cassiterite and 9–19 times larger in the Euriowie cassiterite than the ideal values calculated from the assumed ages (243 Ma and 1590 Ma respectively). Ionisation of $UO_2{}^+$, UO^+ and U^+ relative to ^{206}Pb of all crystallographic orientations displayed linear relationships in the approximate proportions 42:11:1 respectively for the Yankee cassiterite (Fig. 7A) and 23:13:1 for the Euriowie cassiterite (Fig. 7D).

The range in $UO_2{}^-/UO^+$ (3.20–4.39) and $^{206}Pb^-/^{254}UO^+$ (0.073–0.135) in the Yankee grains analysed as unknowns was slightly larger than the single crystal (Fig. 6A) The Euriowie cassiterite varied slightly more with $UO_2{}^+/UO^+$ between 1.338 and 3.131, and $^{206}Pb^+/^{254}UO^+$ between 0.224 and 0.517. Despite this variation, there is no apparent relationship between counts on the reference peak and $UO_2{}^+/UO^+$ values for either sample (Fig. 7B and D).

The covariance between Pb^+/UO^+ and $UO_2{}^-/UO^-$ in the Yankee cassiterite analyses is relatively restricted, and could be described by either a linear or a power function in order to define 'a' in Eq. (1) (Fig. 8). The Euriowie cassiterite displays a more extended array than the Yankee cassiterite in Fig. 8. A regression through these data defines a power function with a slope of 0.780.

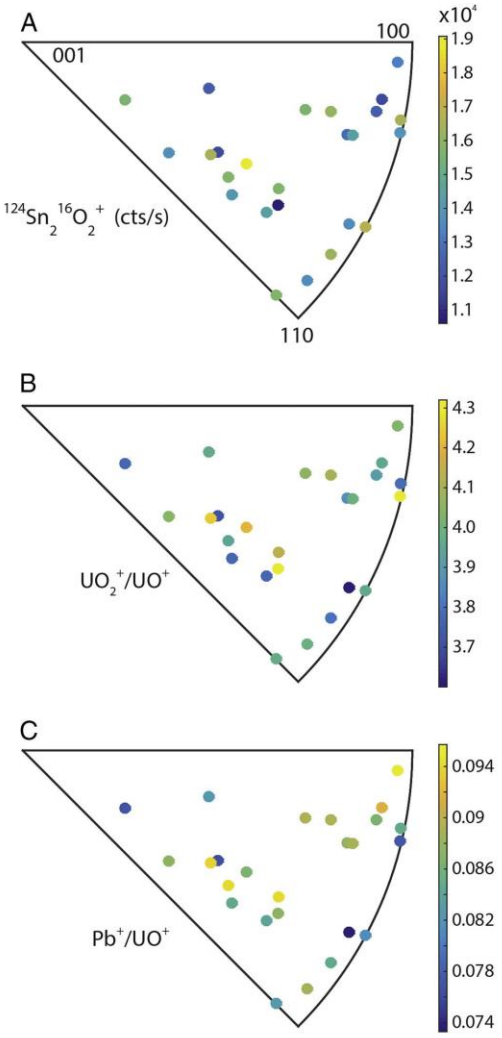

Fig. 10. Cts/s on reference peak $Sn_2O_2{}^+$ (A), UO_2/UO^+ (B) and Pb/UO^+ (C) values of the Yankee cassiterite relative to crystallographic orientation depicted in an inverse pole figure. The lack of any correlation between these parameters indicates minimal effect of orientation on SHRIMP measurements.

and 1800 total counts on the reference mass ($^{48}Ti_3{}^{16}O_3{}^+$) that co-varied with $UO_2{}^+/UO^+$ (Fig. 7F), with high total counts on the reference mass being associated with high $UO_2{}^+/UO^+$. Those authors proposed primary ion channelling – the implantation of primary ions along particular crystallographic planes – resulted in variable sputtering rates. Orientations with higher sputter rates (shallower ion implantation) consumed more O at the interface of the primary beam and sample surface than low sputtering rates (deeper ion implantation; Schmitt and Zack, 2012). Increased consumption of this O lead to the variable ionisation of UO^+ relative to $UO_2{}^+$ that affected sputtering calibrations relying on this ratio (Eq. (1)).

It is difficult to identify such effects in our data despite large variations in cts/s on the $Sn_2O_2{}^+$ reference mass (10327–19,078 cts/s). Within the single orientation domain on the reference grain (Y12), cts/s on the reference mass varied between 11,158 and 13,975. If ion channelling is occurring it appears to be insignificant relative to variations in primary beam intensity or ion yields. Measured $UO_2{}^+/UO^+$ values in the Yankee (3.20–4.39) and Euriowie cassiterite (1.34–3.13) varied slightly more than observed by Taylor et al. (2012) for rutile (0.57–1.48). However the percentage variation of $UO_2{}^+/UO^+$ in rutile is more than double that of the Yankee cassiterite. Unlike rutile there is no covariance between total counts on the reference mass and $UO_2{}^+/UO^+$ in the Yankee (Fig. 7B) and Euriowie cassiterite (Fig. 7D) and most importantly the variable ionisation of UO^+ in rutile reported by Taylor et al. (2012) (Fig. 7E) is clearly not present in cassiterite (Fig. 7A and C).

Table 2
SHRIMP 207Pb/206Pb age data for the Euriowie cassiterite.

Crystallographic domain	Uncorrected $^{207}Pb/^{206}Pb$ Age with 1σ uncertainty		208 corrected $^{207}Pb/^{206}Pb$ Age with 1σ uncertainty	
E1.1	2251	270	2128	228
E1.2	1692	125	1593	147
E2.1	1737	109	1648	123
E3.1	1687	46	1663	52
E4.1	1595	139	1509	174
E4.2	1423	158	1264	237
E4.3	1649	143	1475	183
E4.6	1645	160	1481	211
E5.1	1807	304	1202	484
E5.2	2375	289	1392	421
E5.3	2143	285	1470	370
E6.1	1633	122	1534	150
E6.2	1641	276	1107	454
E6.3	1798	24	1674	42
E6.4	1612	112	1538	138
E6.5	1644	35	1625	40
E8.1	1606	28	1547	37
E8.2	1529	48	1512	60
E8.3	1522	52	1457	68
E8.4	1610	53	1567	64
E9.2	1421	127	1306	185
E13.1	2049	185	1886	184
E13.2	1397	147	1337	211
Average	1666	51	1588	42

Calculated $^{206}Pb/^{238}U$ age estimates of the Yankee cassiterite with 26 different crystallographic orientations yielded a weighted mean error of ~5% (Table 1). In contrast, Taylor et al. (2012) highlighted potential weighted mean errors of up to 15% were possible in rutile owing to the poorly defined calibration slope. This large error is attributed to the large variation in $UO_2{}^+/UO^+$ values associated with crystallographic orientation.

5.2. δ18O variations in the Elsemore cassiterite: real or analytical uncertainty?

Cassiterite commonly forms in complex geological environments with dramatically changing temperatures and numerous fluid sources (e.g. Sun and Eadington, 1987; Ren et al., 1995) and thus the $\delta^{18}O$ values within cassiterite can be expected to vary. The two methods providing the most precise $\delta^{18}O$ determinations in a wide range of samples are fluorination, by which bulk samples (> 5 mg) are reacted with F_2 or BrF_5 to create O_2, and laser fluorination, which rapidly and efficiently heats the sample to produce O_2 and requiring > 0.3 mg of bulk separates. However in both these bulk techniques, inter- and intra-grain heterogeneities cannot be assessed. Cassiterite geothermometry by these methods, which is based on the temperature dependent fractionation of oxygen isotopes between quartz and cassiterite (e.g. Hu et al., 2005), assumes that all grains analysed are in isotopic equilibrium and are internally homogeneous.

The SHRIMP SI results reported here indicate that the $\delta^{18}O$ measured on a cassiterite crystal with a single crystallographic orientation can vary by as much as ~2‰. During SIMS analysis of oxygen isotopes the dominant source of instrumental mass fractionation is the composition of the target mineral. Therefore the ~2‰ variation observed in a

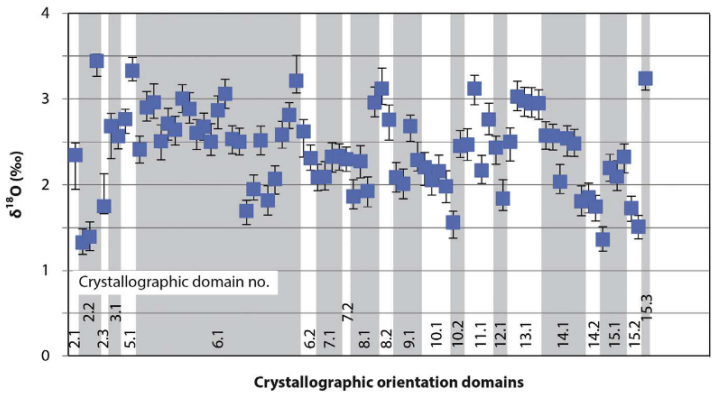

Fig. 11. All $\delta^{18}O_{VSMOW}$ Elsemore cassiterite values, normalised to a singly orientated crystal, grouped by their crystallographic orientation. Intra-grain variations for a single orientation can be as large as 1.5‰.

Table 3
SHRIMP SI δ18O average values for each crystallographic domain in the Elsemore Cassiterite. Variations reflect isotopic heterogeneity rather than orientation effects.

Crystallographic domain	No. of analyses (rejected)	Average $\delta^{18}O$	2SD
E2.1	1	2.35	0.80
E2.2	3 (1)	1.36	0.10
E2.3	1	1.75	0.17
E3.1	2	2.62	0.16
E5.1	2	3.05	1.30
E6.1	23 (1)	2.58	0.79
E6.2	2	2.46	0.44
E7.1	4	2.21	0.28
E7.2	1	2.30	0.28
E8.1	4	2.25	1.00
E8.2	2	2.94	0.51
E9.1	4	2.27	0.60
E10.1	4	2.10	0.20
E10.2	2	2.00	1.25
E11.1	4	2.63	0.82
E12.1	2	2.13	0.84
E13.1	5	2.88	0.43
E14.1	6	2.33	0.66
E14.2	2	1.80	0.15
E15.1	4	1.99	0.86
E15.2	2	1.62	0.30
E15.3	1	3.24	0.27
Average		2.40	0.97

single homogenous composition cassiterite grain is likely an approximation of the true internal O isotopic heterogeneity in that grain. Determining whether variations outside this range are real or related to differences in the crystallographic orientation is difficult. Huberty et al. (2010) reported crystallographic orientation effects in SIMS analysis of magnetite of $\delta^{18}O$ of 2–3‰, however within a single grain orientation the precision was 0.4‰ (2SD), which is more typical for O-isotopic analysis of homogeneous materials by SIMS (e.g. Ickert et al., 2008; Huberty et al., 2010). At the present, it is therefore difficult to differentiate true compositionl heterogeneity from crystallographic orientation effects in the Elsemore cassiterite at a precision < 2‰. Future work needs to identify suitably homogenous natural reference materials or develop methods to synthesize cassiterite crystals, which has proven particularly challenging (e.g. Shimada et al., 1982).

5.3. Causes of crystallographic orientation effects: cassiterite vs. rutile

The documented occurrence of large crystallographic orientation effects in rutile (Li et al., 2010, 2011; Taylor et al., 2012; Schmitt and Zack, 2012; Shulaker et al., 2015) but not the isostructural cassiterite (this study) indicates that a fundamental difference unrelated to crystallographic

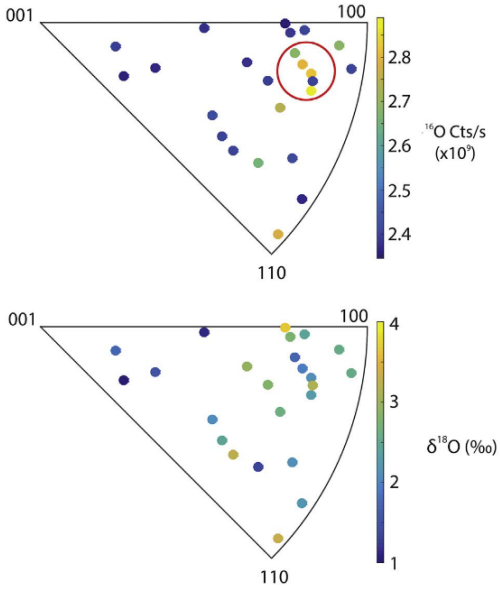

Fig. 12. Cts/s on ^{16}O (A) and $\delta^{18}O$ (B) for Elsemore cassiterite relative to crystallographic orientation depicted in an inverse pole figure. A grouping of 4 analyses (circled) ~15° from the 100 plane and ~80° from the 001 plane with high ^{16}O count rate (A) may indicate ion channelling, however it is not manifested in the U-Pb data or the $\delta^{18}O$ values.

structural parameters may contribute to crystallographic orientation effects, During SIMS analyses, the interaction between an incoming ion and a target sample is highly complex, involving numerous variables including the type of primary ion, impact angle and energy, and the composition, bond strength and structure of the sample matrix. Many models for the origin of orientation effects focus predominantly on the crystallographic structure of the target minerals (Huberty et al., 2010; Taylor et al., 2012; Schmitt and Zack, 2012). This is particularly warranted for rutile and cassiterite as Lumpkin et al. (2010) show that both minerals maintain their crystal structure and are not amorphised under ion bombardment more intense than that experienced in SIMS. Below we briefly discuss the possible mechanisms that might contribute to crystallographic orientation effects in relation to key structural and mineral physics parameters that differ between cassiterite and rutile.

Primary ion channelling is a well-documented process, describing the implantation of primary ions along particular crystallographic

planes. Primary ions entering the target mineral directed parallel to a crystallographic plane will travel deeper into the structure, whilst primary ions directed perpendicular to a crystallographic plane will interact with the top layers. Ions implanted deep into the target surface result in much less sputtered material (Benninghoven, 1994). Secondary ion focussing occurs when collisional cascades are focussed along or between crystals planes, imposing a preferred orientation on secondary ions ejected from the sample (e.g. Huberty et al., 2010). There is, however, no unifying model for crystallographic orientation effects, with primary ion channelling the preferred mechanism in U-Pb studies (Schmitt and Zack, 2012; Taylor et al., 2012) and secondary ion focussing in light stable isotopic studies (Huberty et al., 2010), despite a comparable relative mass difference (e.g. ^{18}O is 12.5% heavier than ^{16}O and ^{238}U is 15.5 % heavier than ^{206}Pb).

Taylor et al. (2012) showed that much of the variation in SIMS U-Pb analysis of rutile occurs over a ~5° rotation between the 010 and 110 cleavage planes. As in cassiterite (Fig. 6B), these planes are parallel to the major axis of the crystal and if exposed after crushing and/or milling provide an ideal surface for mounting. Crystallographic orientation effects may therefore be exaggerated in rutile due to a preference to mount in these orientations. Conversely cassiterite in this study showed a wide variety of orientations consistent with the dominant conchoidal fracture noted in the separates. As we show here the sputtering calibration equations adequately account for much of the variation seen in UO_2^+/UO^+, resulting in accurate and moderately precise Pb/U values. We thus conclude that cassiterite does not display the predominant crystallographic orientation effect documented in rutile and suggest that for cassiterite there is a compositional control on the calculated Pb/U.

How primary ion channelling leads to variations in calculated Pb/U values is unclear. Several authors have mitigated some of the effects of crystallographic orientation during U-Pb analysis by flooding the chamber with oxygen (Schuhmacher et al., 1994; Li et al., 2010; Schmitt et al., 2010; Schmitt and Zack, 2012) with the added advantage of increasing $^{206}Pb^+$ yields. In both rutile and baddeleyite this had the effect of reducing the range of UO_2^+/U^+ values and total sputter yield (Schmitt et al., 2010; Schmitt and Zack, 2012). Schmitt and Zack (2012) suggested that increased sputter rates, associated with less primary ion channelling, progressively deplete the surface layer of oxygen, resulting in a larger range in UO_x^+/U^+ values. This is in agreement with Magee et al. (2014) who showed that approximately half of the O in the secondary ion beam is sourced from the sample itself, whilst the rest comes from the primary ions or gas in the vacuum chamber. Thus the availability of introduced O can affect the production of UO_x^+.

A potential contributor to the effects of crystallographic orientation effects is the large and highly variable dielectric constant of rutile (86–170) which is related to crystallographic orientation (Diebold, 2003). Conversely the dielectric constant for cassiterite is low and restricted to between 9 and 14 (Shannon, 1993). This contrast is thought to be related to the different cell dimensions and electronic structures of the Sn and Ti oxide matrices (e.g. Kumar et al., 2011; Machesky et al., 2011). The strong and highly variable dielectric constant of rutile may locally alter the electronic field gradient, leading to a defocused or misaligned secondary beam dependent on the crystallographic orientation. Thus secondary beam optimisation should be undertaken to account for this variation by optimisation on numerous grains as suggested by Taylor et al. (2012). The variable ionisation of UO^+ relative to the reference mass and $^{206}Pb^+$ reported by Taylor et al. (2012) may thus be related to the variable secondary ion energy distribution of UO^+ relative to UO_2^+.

6. Conclusions

Crystallographically oriented grains of cassiterite were measured for U-Pb and O isotopic compositions by SHRIMP ion microprobes to assess the possible effects of orientation on U-Pb and oxygen isotopic measurements. The results indicate minimal, if any, effects of crystallographic orientation for cassiterite during SIMS analysis, in contrast to previous studies of the isostructural mineral rutile. Specifically, unlike rutile, the range in measured UO_2^+/UO^+ ratios and in reference mass cts/s is not sensitive to crystallographic orientation. Relatively large variations in apparent $\delta^{18}O$ within individual grains of the Elsemore cassiterite analysed here highlight the need for in-situ techniques, particularly for thermometry. In this study, the inferred intra-crystal heterogeneity of the cassiterite limits the identification of crystallographic orientation effects to ≤ 2‰. The physical processes leading to these crystallographic orientation effects are still unknown, although fundamental differences in the electronic structure of cassiterite compared to rutile may be influential.

Acknowledgements

The contributions of I. Williams and his assistance with all things SHRIMP throughout this project are gratefully acknowledged. P. Blevin generously provided samples, field support and discussions. H. Kokkonen is thanked for assistance with polishing samples for EBSD analysis. F. Brink and the Centre of Advance Microscopy CAM are thanked for assistance with EBSD analysis. PC was supported by an Australian Postgraduate Award. This manuscript was greatly improved by the comments of A. Schmitt and an anonymous reviewer.

Appendix A. Supplementary data

Supplementary data to this article can be found online at http://dx.doi.org/10.1016/j.chemgeo.2017.08.003.

References

Abdalla, H.M., Matsueda, H., Obeid, M.A., Takahashi, R., 2008. Chemistry of cassiterite in rare metal granitoids and the associated rocks in the Eastern Desert, Egypt. J. Mineral. Petrol. Sci. 103 (5), 318–326.
Audétat, A., Günther, D., Heinrich, C.A., 2000a. Magmatic-hydrothermal evolution in a fractionating granite: a microchemical study of the Sn-W-F-mineralized Mole Granite (Australia). Geochim. Cosmochim. Acta 64 (19), 3373–3393.
Audétat, A., Günther, D., Heinrich, C.A., 2000b. Causes for large-scale metal zonation around mineralized plutons: fluid inclusion LA-ICP-MS evidence from the Mole Granite, Australia. Econ. Geol. 95 (8), 1563–1581.
Benninghoven, A., 1994. Chemical analysis of inorganic and organic surfaces and thin films by static time-of-flight secondary ion mass spectrometry (TOF-SIMS). Angew. Chem. Int. Ed. Eng. 33 (10), 1023–1043.
Blevin, P.L., 2004. Redox and compositional parameters for interpreting the granitoid metallogeny of eastern Australia: implications for gold-rich ore systems. Resour. Geol. 54 (3), 241–252.
Blevin, P.L., Norman, M., 2010. Cassiterite; the zircon of mineral systems? A scoping study. Abstracts. J. Geol. Soc. Aust. 98, 399–400.
Bolzan, A.A., Fong, C., Kennedy, B.J., Howard, C.J., 1997. Structural studies of rutile-type metal dioxides. Acta Crystallogr. B 53 (3), 373–380.
Brown, R.E., Stroud, W.J., 1997. Inverell 1:250 000 Metallogenic map SH/56–5: Metallogenic Study and Mineral Deposit Data Sheets, Geological Survey of New South. Wales, Sydney.
Burton, G.R., 2000. Metallogenic studies of the Broken Hill and Euriowie Blocks, New South Wales. 4. Mineral deposits of the Euriowie block (including the northernmost Broken Hill block and Poolamacca inlier, bulletin). Geol. Surv. NSW 32 (4).
Cao, H.-W., Zhang, Y.-H., Pei, Q.-M., Zhang, R.-Q., Tang, L., Lin, B., Cai, G.-J., 2016. U–Pb dating of zircon and cassiterite from the early Cretaceous Jiaojiguan iron-tin polymetallic deposit, implications for magmatism and metallogeny of the Tengchong area, western Yunnan, China. Int. Geol. Rev. 59 (2), 234–258.
Chen, X.-C., Hu, R.-Z., Bi, X.-W., Li, H.-M., Lan, J.-B., Zhao, C.-H., Zhu, J.-J., 2014. Cassiterite LA-MC-ICP-MS U/Pb and muscovite 40Ar/39Ar dating of tin deposits in the Tengchong-Lianghe tin district, NW Yunnan, China. Mineral. Deposita 49 (7), 843–860.
Compston, W., Williams, I.S., Meyer, C., 1984. U-Pb geochronology of zircons from lunar breccia 73217 using a sensitive high mass-resolution ion microprobe. J. Geophys. Res. Solid Earth 89 (S02), B525–B534.
Diebold, U., 2003. The surface science of titanium dioxide. Surf. Sci. Rep. 48 (5–8), 53–229.
Farmer, C.C., Searl, A., Halls, C., 1991. Cathodoluminescence and growth of cassiterite in the composite lodes at South Crofty mine, Cornwall, England. Mineral. Mag. 55 (380), 447–458.
Fitzherbert, J., 2015. Refined peak and retrograde metamorphic isograds for the Broken Hill and Euriowie blocks, NSW. Geol. Surv. NSW 143 (1), 1–43 (Quarterly Notes).
Gulson, B.L., Jones, M.T., 1992. Cassiterite: potential for direct dating of mineral deposits

and a precise age for the Bushveld Complex granites. Geology 20 (4), 355–358.
Haapala, I., 1997. Magmatic and postmagmatic processes in tin-mineralized granites: topaz-bearing Leucogranite in the Eurajoki Rapakivi granite stock, Finland. J. Petrol. 38 (12), 1645–1659.
Hall, M.R., Ribbe, P.H., 1971. An electron microprobe study of luminscence centers in cassiterite. Am. Mineral. 56, 31–45.
Hinthorne, J.R., Andersen, C.A., Conrad, R.L., Lovering, J.F., 1979. Single-grain 207Pb/206Pb and U/Pb age determinations with a 10-μm spatial resolution using the ion microprobe mass analyzer (IMMA). Chem. Geol. 25 (4), 271–303.
Hu, G., Clayton, R.N., Polyakov, V.B., Mineev, S.D., 2005. Oxygen isotope fractionation factors involving cassiterite (SnO2): II. Determination by direct isotope exchange between cassiterite and calcite. Geochim. Cosmochim. Acta 69 (5), 1301–1305.
Huberty, J.M., Kita, N.T., Kozdon, R., Heck, P.R., Fournelle, J.H., Spicuzza, M.J., Xu, H., Valley, J.W., 2010. Crystal orientation effects in δ18O for magnetite and hematite by SIMS. Chem. Geol. 276 (3–4), 269–283.
Ickert, R.B., Hiess, J., Williams, I.S., Holden, P., Ireland, T.R., Lanc, P., Schram, N., Foster, J.J., Clement, S.W., 2008. Determining high precision, in situ, oxygen isotope ratios with a SHRIMP II: analyses of MPI-DING silicate-glass reference materials and zircon from contrasting granites. Chem. Geol. 257 (1–2), 114–128.
Jiang, S.-Y., Yu, J.-M., Lu, J.-J., 2004. Trace and rare-earth element geochemistry in tourmaline and cassiterite from the Yunlong tin deposit, Yunnan, China: implication for migmatitic–hydrothermal fluid evolution and ore genesis. Chem. Geol. 209 (3–4), 193–213.
Kita, N.T., Huberty, J.M., Kozdon, R., Beard, B.L., Valley, J.W., 2011. High-precision SIMS oxygen, sulfur and iron stable isotope analyses of geological materials: accuracy, surface topography and crystal orientation. Surf. Interface Anal. 43 (1–2), 427–431.
Kleeman, J.D., Plimer, I.R., Lu, J., Foster, D.A., Davidson, R., 1997. Timing of thermal and mineralisation events associated with the Mole Granite. In: Ashley, P., Flood, P.G. (Eds.), Tectonics and Metallogenesis of the New England Orogen, Special Publication 19. Geological Society of Australia, pp. 254–265.
Kozdon, R., Kita, N.T., Huberty, J.M., Fournelle, J.H., Johnson, C.A., Valley, J.W., 2010. In situ sulfur isotope analysis of sulfide minerals by SIMS: precision and accuracy, with application to thermometry of ~3.5 Ga Pilbara cherts. Chem. Geol. 275 (3–4), 243–253.
Kumar, N., Kent, P.R.C., Bandura, A.V., Kubicki, J.D., Wesolowski, D.J., Cole, D.R., Sofo, J.O., 2011. Faster proton transfer dynamics of water on SnO2 compared to TiO2. J. Chem. Phys. 134 (4), 044706.
Li, Q.-L., Li, X.-H., Liu, Y., Wu, F.-Y., Yang, J.-H., Mitchell, R.H., 2010. Precise U–Pb and Th–Pb age determination of kimberlitic perovskites by secondary ion mass spectrometry. Chem. Geol. 269 (3–4), 396–405.
Li, Q.-l., Lin, W., Su, W., Li, X.-H., Shi, Y.-H., Liu, Y., Tang, G.-Q., 2011. SIMS U–Pb rutile age of low-temperature eclogites from southwestern Chinese Tianshan, NW China. Lithos 122 (1–2), 76–86.
Li, C.Y., Zhang, R.Q., Ding, X., Ling, M.X., Fan, W.M., Sun, W.D., 2016. Dating cassiterite using laser ablation ICP-MS. Ore Geol. Rev. 72 (P1), 313–322.
Linnen, R.L., 1998. Depth of emplacement, fluid provenance and metallogeny in granitic terranes: a comparison of western Thailand with other tin belts. Mineral. Deposita 33 (5), 461–476.
Liu, Y., Li, Z.-X., Li, H.-M., Guo, L.-G., Xu, W., Ye, L., Li, C.-Y., Pi, D.-H., 2007. U-Pb geochronology of cassiterite and zircon from the Dulong Sn-Zn deposit: evidence for Cretaceous large-scale granitic magmatism and mineralization events in southeastern Yunnan province, China. Acta Petrol. Sin. 23 (5), 967–976.
Ludwig, K.R., 1991. ISOPLOT; a Plotting and Regression Program for Radiogenic-isotope Data; Version 2.53. USGS Open-File Report. pp. 91–445.
Ludwig, K.R., 2009. Squid 2: A User's Manual, Berkeley Geochronology Centre.
Lumpkin, G.R., Blackford, M.G., Smith, K.L., Whittle, K.R., Zaluzec, N.J., Ryan, E.A., Baldo, P., 2010. Ion irradiation of the TiO2 polymorphs and cassiterite. Am. Mineral. 95, 192–195.
Lyon, I.C., Saxton, J.M., Cornah, S.J., 1998. Isotopic fractionation during secondary ionisation mass spectrometry: crystallographic orientation effects in magnetite. Int. J. Mass Spectrom. Ion Process. 172 (1–2), 115–122.
Macey, P., Harris, C., 2006. Stable isotope and fluid inclusion evidence for the origin of the Brandberg West area Sn–W vein deposits, NW Namibia. Mineral. Deposita 41 (7), 671–690.
Machesky, M., Wesolowski, D., Rosenqvist, J., Předota, M., Vlcek, L., Ridley, M., Kohli, V., Zhang, Z., Fenter, P., Cummings, P., Lvov, S., Fedkin, M., Rodriguez-Santiago, V., Kubicki, J., Bandura, A., 2011. Comparison of cation adsorption by isostructural rutile and cassiterite. Langmuir 27 (8), 4585–4593.
Magee, C., Ferris, J., Magee, C., 2014. Effect of impact energy on SIMS U–Pb zircon geochronology. Surf. Interface Anal (n/a–n/a).
Page, R.W., Stevens, B.P.J., Gibson, G.M., Conor, C.H.H., 2000. Geochronology of WIllyama Supergroup Rocks between Olary and Broken Hill, and comparison to Northern Australia.
Plimer, I.R., Lu, J., Kleeman, J.D., 1991. Trace and rare earth elements in cassiterite – sources of components for the tin deposits of the Mole Granite, Australia. Mineral. Deposita 26 (4), 267–274.
Ren, S.K., Walshe, J.L., Paterson, R.G., Both, R.A., Andrew, A., 1995. Magmatic and hydrothermal history of the porphyry-style deposits of the Ardlethan tin field, New South Wales, Australia. Econ. Geol. 90 (6), 1620–1645.
Schaltegger, U., Pettke, T., Audétat, A., Reusser, E., Heinrich, C.A., 2005. Magmatic-to-hydrothermal crystallization in the W–Sn mineralized Mole Granite (NSW, Australia): part I: crystallization of zircon and REE-phosphates over three million years—a geochemical and U–Pb geochronological study. Chem. Geol. 220 (3–4), 215–235.
Schmitt, A.K., Zack, T., 2012. High-sensitivity U–Pb rutile dating by secondary ion mass spectrometry (SIMS) with an O2 + primary beam. Chem. Geol. 332–333 (0), 65–73.
Schmitt, A.K., Chamberlain, K.R., Swapp, S.M., Harrison, T.M., 2010. In situ U-Pb dating of micro-baddeleyite by secondary ion mass spectrometry. Chem. Geol. 269 (3–4), 386–395.
Schuhmacher, M., De Chambrost, E., McKeegan, K.D., Harrison, T.M., Migeon, H., 1994. In-situ dating of zircon with the CAMECA IMS 1270. In: Benninghoven, A., Werner, H.W., Shimizu, R., Nihei, Y. (Eds.), Secondary Ion Mass Spectrometry (SIMS IX). John Wiley & Sons, pp. 919–922.
Shannon, R.D., 1993. Dielectric polarizabilities of ions in oxides and fluorides. J. Appl. Phys. 73 (1), 348–366.
Shimada, S., Kodaira, K., Matsushita, T., 1982. Crystal growth of SnO_2 and Me_2SnO_4 (Me = Mg, Zn, Co) by flux method. J. Cryst. Growth 59 (3), 662–664.
Shulaker, D.Z., Schmitt, A.K., Zack, T., Bindeman, I., 2015. In-situ oxygen isotope and trace element geothermometry of rutilated quartz from alpine fissures. Am. Mineral. 100 (4), 915–925.
Stacey, J.S., Kramers, J.D., 1975. Approximation of terrestrial lead isotope evolution by a two-stage model. Earth Planet. Sci. Lett. 26 (2), 207–221.
Sun, S.S., Eadington, P.J., 1987. Oxygen isotope evidence for the mixing of magmatic and meteoric waters during tin mineralization in the Mole Granite, New South Wales, Australia. Econ. Geol. 82 (1), 43–52.
Sweetapple, M.T., Collins, P.L.F., 2002. Genetic framework for the classification and distribution of archean rare metal pegmatites in the North Pilbara Craton, Western Australia. Econ. Geol. 97 (4), 873–895.
Taylor, R.G., 1979. Geology of Tin Deposits. In: Developments in Economic Geology. 11 Elsevier.
Taylor, R., Clark, C., Reddy, S.M., 2012. The effect of grain orientation on secondary ion mass spectrometry (SIMS) analysis of rutile. Chem. Geol., 300–301(0): 81–87.
Thompson, J.F.H., Sillitoe, R.H., Baker, T., Lang, J.R., Mortensen, J.K., 1999. Intrusion-related gold deposits associated with tungsten-tin provinces. Mineral. Deposita 34 (4), 323–334.
White, A.J.R., Chappell, B.W., 2004. Petrographic discrimination of low- and high-temperature I-type granites. Resour. Geol. 54 (3), 215–226.
White, R.W., Powell, R., 2002. Melt loss and the preservation of granulite facies mineral assemblages. J. Metamorph. Geol. 20, 621–632.
Wingate, M.T.D., Compston, W., 2000. Crystal orientation effects during ion microprobe U–Pb analysis of baddeleyite. Chem. Geol. 168 (1–2), 75–97.
Yuan, S., Peng, J., Hu, R., Li, H., Shen, N., Zhang, D., 2008. A precise U–Pb age on cassiterite from the Xianghualing tin-polymetallic deposit (Hunan, South China). Mineral. Deposita 43 (4), 375–382.
Yuan, S., Peng, J., Hao, S., Li, H., Geng, J., Zhang, D., 2011. In situ LA-MC-ICP-MS and ID-TIMS U–Pb geochronology of cassiterite in the giant Furong tin deposit, Hunan Province, South China: new constraints on the timing of tin–polymetallic mineralization. Ore Geol. Rev. 43 (1), 235–242.
Zack, T., Stockli, D., Luvizotto, G., Barth, M., Belousova, E., Wolfe, M., Hinton, R., 2011. In situ U–Pb rutile dating by LA-ICP-MS: 208Pb correction and prospects for geological applications. Contrib. Mineral. Petrol. 162 (3), 515–530.
Zagruzina, I., Pinskii, E., Savinova, I., 1987. Uranium in cassiterite of tin deposits. Int. Geol. Rev. 29, 94–109.
Zhang, R.-Q., Lu, J.-J., Wang, R.-C., Yang, P., Zhu, J.-C., Yao, Y., Gao, J.-F., Li, C., Lei, Z.-H., Zhang, W.-L., Guo, W.-M., 2015. Constraints of in situ zircon and cassiterite U–Pb, molybdenite Re–Os and muscovite 40Ar–39Ar ages on multiple generations of granitic magmatism and related W–Sn mineralization in the Wangxianling area, Nanling Range, South China. Ore Geol. Rev. 65 (4), 1021–1042.

Appendix 2: Carr, P.A., Bennett, V.C., Norman, M.D., Zink, S., and Amelin, Y. 2019. New methods for U–Pb geochronology of cassiterite by ID-TIMS – time scales of magmatic-hydrothermal mineralisation in the Mole Granite, eastern Australia (*in prep. For Chemical Geology).*

U-Pb geochronology of cassiterite by ID-TIMS – time scales of magmatic-hydrothermal mineralisation in the Mole Granite, eastern Australia.

Patrick A. Carr[1*], Vickie C. Bennett[1], Marc D. Norman[1], Sonja Zink[1], Yuri A. Amelin[1]
Research School of Earth Sciences, The Australian National University
Canberra, ACT 2601, Australia
*Corresponding author, email: Patrick.carr@anu.edu.au

Introduction

Primary cassiterite (SnO_2) is formed in magmatic-hydrothermal environments, associated with highly evolved silicate melts (Taylor 1979; Lehman et al. 1990). Understanding the absolute timing and duration of the processes occurring during magmatic crystallisation, fluid and vapour separation, and fluid percolation are essential for genetic models and targeting of new deposits. Magmatic-hydrothermal tin systems display complex histories of variable durations, from instantaneous (Yuan et al. 2011; Schlattegger et al. 2005), over several millions of years (e.g. Kleeman et al. 1997), to tens of millions of years (Halliday et al. 1980; Chesley et al. 1993; McNaughton et al. 1993). Traditional methods to determine the age and duration of tin systems rely on geochronological information stored in minerals co-existing in cassiterite (e.g. Rb-Sr in micas, or U-Th-Pb in xenotime). These methods are compromised by the assumption of co-precipitation with cassiterite, and hydrothermal alteration of primary geochronological information in these minerals that is inherent in magmatic-hydrothermal systems.

Cassiterite is physically and chemically resistant, and its U-Pb isotopic composition is increasingly used to determine the age of tin mineralisation (e.g. Gulson and Jones 1992; Yuan et al. 2008; Chen et al. 2014; Zhang et al. 2015; Li et al. 2016; Carr et al. 2017; Neymark et. al. 2018). U-Pb age dating of cassiterite is dominantly through *in-situ* LA-(MC)-ICP-MS methods because of the rapid sample preparation and analysis and ability to determine to internal heterogeneity (e.g. Carr et al. 2017). These methods require a matrix-matched standard cassiterite of known U-Pb composition to account for ionisation differences of U and Pb and matrix effects (ablation efficiency and downhole fractionation; Eggins et al. 1998).

Cassiterite U-Pb standards do not exist. Instead, labs who produce U-Pb cassiterite data by *in-situ* methods rely on in-house reference cassiterite whose isotopic composition has been determined by isotope dilution thermal ionisation mass spectrometry (ID-TIMS)(e.g. Lbiao - Yuan et al. 2011; AY-4 – Yuan et al. 2011; Chen et al. 2014), or by age data from other methods (Yankee – Carr et al. 2017). ID-TIMS is the most precise method for U-Pb isotopic compositions in geological samples and is independent of mineral matrices. However, U-Pb cassiterite age dating by ID-TIMS has only been published by Gulson and Jones (1991) and Yuan et al. (2008; 2011) primarily because dissolution of cassiterite is extremely difficult.

For U-Pb analysis, digestion attempts have focussed on using concentrated HCl acid (Gulson and Jones 1991; Yuan et al. 2008; 2011). Other methods have proved successful however are not amenable to the extremely low Pb blanks required (Caley 1932; Yamazaki et al. 2013; Mathur et al. 2017). Digestion of cassiterite in concentrated HCl is regularly incomplete (Gulson and Jones 1992; Yuan et al. 2008; 2011) which may cause U-Pb fractionation and inaccurate ages. In these cases, undigested residues are removed from digestion bombs, pulverised again and additional acid added before further heating in pressure vessels (Gulson and Jones 1992; Yuan et al. 2008; 2011). This extra handling, increased acid volumes and the large sample sizes used in these studies inevitably leads to increases in Pb blanks and increases the potential for contamination. Gulson and Jones (1992) reported Pb blanks between 0.2–0.3 ng and Yuan et al (2008, 2011) report Pb blanks of 0.82 and 0.55 ng.

Here we present new methods for the chemical dissolution and purification of U-Pb isotopes from cassiterite. These new methods were developed to provide precise isotopic compositions on small sample sizes (<0.5 mg), with minimal handling and low Pb blanks. The combination of fast sample preparation times and relative precision of *in-situ* methods for U-Pb cassiterite dating is unparalleled. The authors envisage this method be most appropriate for precise U-Pb isotopic determination of standard or reference cassiterite grains. In this study we determine the U-Pb isotopic composition of the in-house Yankee reference cassiterite (Carr et al. 2017) and the AY-4 reference cassiterite (Yuan et al. 2011; Chen et al. 2014; Zhang et al. 2015).

The polymetallic Mole Granite system

The Mole Granite is a highly studied magmatic-hydrothermal mineral system with over 1200 strongly zoned mineral deposits (Eadington 1983; Sun and Eadington 1987; Plimer et al. 1991; Heinrich et al. 1992; Rankin et al. 1992; Audétat et. al. 1998, 2000a,b, 2008; Henley et al. 1999; Mavrogenes et al. 2002; Pettke et al. 2005; Schlategger et al. 2005; Cauzid et al. 2007; Feteke et al. 2016). The Mole Granite, part of the New England Batholith of the New England Orogen (Shaw and Flood 1981), is a shallow, sill-like intrusion into Permian sediments and volcanics (Kleeman 1982). The Mole Granite has a haplogranite composition due to extreme fractional crystallisation that lead to significant enrichment in Sn (**Audétat et al. 2000a)**. Two hypotheses of the absolute age and duration of mineralisation associated with the Mole Granite exist; 1) emplacement of the Mole Granite at 246 ± 2 Ma followed by sustained hydrothermal activity and cassiterite mineralisation for 3–5 Ma (Kleeman et al. 1997), and 2) shallow emplacement of the Mole Granite at 246.2 ± 0.5 Ma and instantaneous rapid cassiterite mineralisation within method precision (Pettke et al. 2005; Schlategger et al. 2005).

The Yankee deposit occurs within the southern boundary of the Mole Granite. The deposit is characterised by veins 10 to 40 cm thick quartz-cassiterite veins and a milky quartz selvage (Heinrich et al. 1992). Melt, fluid and vapour Inclusions within quartz of the Yankee deposit have been subject to significant research on metal speciation in magmatic to hydrothermal systems (Heinrich et al. 1992; Audétat et. al. 1998, 2000a,b, 2008; Mavrogenes et al. 2002; Cauzid et al. 2007; Feteke et al. 2016). Magmatic fluids derived from the crystallising Mole Granite became progressively diluted by meteoric fluids leading to cassiterite precipitation (Heinrich et al. 1992; Audétat et al. 1998; Feteke et al. 2016). Quartz crystals show large variations in $\delta^{18}O$ fluid compositions (10.1 – -15.4) and homogenisation temperatures (500–220^{o}C) associated with cooling and incursion these meteoric fluids (Feteke et al. 2016). Cassiterite is concentrated in vuggy zones in the centre of veins associated with large euhedral smoky quartz (Heinrich et al. 1992).

Carr et al (2017) described the petrographically features of the Yankee cassiterite. In cathodoluminescence images, the Yankee cassiterite displays two internal textures; concentric zoning defined by light and dark bands, and dark sector zones. Titanium

and W activate a bright CL response, except when in the presence of Fe which results in a quenched afterglow. Both textures contain homogenous U-Pb isotopic compositions, however the dark zones are more concentrated in U and Pb (Carr et al. 2017).

U-Pb age dating of cassiterite by ID-TIMS

Cassiterite separates were crushed in a steel mill. Fragments <80µm in diameter were handpicked to produce ultrapure concentrates. Five samples weighing less than 300µg each were produced. After sample crushing, all work was carried out in Class 10 laminar flow hoods with high purity acids and MΩ-grade water from a Millipore system at the Research School of Earth Sciences, ANU. Gulson and Jones (1992) show that preliminary washing of cassiterite concentrates removes significant amounts of common Pb, hosted in sulphides. Cassiterite was washed in MQ, ethanol, acetone, 3M HNO_3 (1 hour on hotplate @ 100^{o}C), 6.2 M HCl (overnight on hotplate at 100^{o}C), 3M HF (1 hour on hotplate at 100^{o}C), and concentrated HBr. There was no measurable reduction in the sample weight after washing.

Cassiterite digestion

After washing samples, concentrates were transferred to 3 ml Savillex beakers with 100 drops of concentrated HBr acid and ^{202}Pb-^{205}Pb-^{233}U-^{236}U tracer solution. Beakers were sealed in Parr dissolution vessels and heated at 220^{o}C for approximately 12 days. Dissolution of cassiterite concentrates was complete. Solutions were dried down and refluxed with 1mL of 6.2M HCl, twice. Following the second reflux solutions were placed back in Parr dissolution vessels overnight at 190^{o}C to break up fluorides. Solutions were dried down slowly before and taken in 300µl of 0.5M HCl for column chromatography.

U, Th and Pb purification by chromatography

Purified U, Th and Pb aliquots were produced through 3 stages of ion chromatography. The first stage used shrink Teflon columns with a column volume of 250 µl and reservoir volume of 3 ml. The top 2/3^{rds} of the column was filled with 50–100 µm TRU spec resin, and the bottom 1/3rd with an inert pre-filter resin. A fritz was secured into the base of the column. Elution curves for the Yankee cassiterite in TRU resin are shown in Figure 1. TRU spec resin Pb blanks are <0.4 pg. Pb aliquots

were contaminated by Ti, Fe and W, and U aliquots by Ta and W (Figure 1) so were each purified using HBr-anion exchange chromatography method of Amelin (2008).

Isotopic analysis by TIMS

Purified aliquots of U and Pb were dried down in 0.02N H_3PO_4 and loaded onto single zone refined Re filaments with 1µl of 0.5 % Sigma–Aldrich silica activator gel (Huyskens et al. 2012). U and Pb isotopes were measured on a Thermo Scientific Triton Plus TIMS at the Research School of Earth Sciences, ANU. Pb isotopes were measured on ^{202}Pb, ^{204}Pb, ^{205}Pb, ^{206}Pb, ^{207}Pb and ^{208}Pb between 1110–1195^{o}C on the filament and using an MasCom MC-TE-Z/17 secondary electron multiplier in peak jumping mode. U isotopes were measured on ^{233}U, ^{236}U and ^{238}U as UO_2^+ species between on 1280–1350^{o}C on the filament, using the electron multiplier and a $^{18}O/^{16}O$ of 0.0020485. Mass fractionation was corrected online in the Triton Plus software with the measured $^{202}Pb/^{205}Pb$ and $^{233}U/^{236}U$ of the tracer solution and an exponential fractionation law. Full procedural blanks are <9.09 pg with an isotopic composition of $^{206}Pb/^{204}Pb$ = 18.27, $^{207}Pb/^{204}Pb$ = 15.68 and $^{208}Pb/^{204}Pb$ = 38.23.

Results

U-Pb isotopic compositions of the Yankee and AY-4 reference cassiterite determined by ID-TIMS are listed in Table 2. Pb concentration of the Yankee cassiterite varies between 0.35–0.75 ppm, the majority being radiogenic ^{206}Pb (mol. % ^{206}Pb = 82–93.1). $^{206}Pb/^{204}Pb$ (107–266) and $^{207}Pb/^{204}Pb$ (21.9–30.2) in the Yankee cassiterite are elevated and variable and suitable for age dating.

Alpha µ ($^{206}Pb/^{204}Pb$ vs. $^{238}U/^{204}Pb$) and Beta µ ($^{207}Pb/^{204}Pb$ vs. $^{235}U/^{204}Pb$) isochron relationships for the Yankee reference cassiterite are shown in Figures 2A and 2B and define an age of 246.59 ± 0.52 Ma and 247.0 ± 1.9 Ma respectively. A 3D isochron (Ludwig 1998) that is constrained to insect the concordia provides the most precise age for the Yankee cassiterite of 246.48 ± 0.51 Ma (Figure 2C). Initial Pb compositions derived from the isochron relationships in Figure 2C are evolved ($^{206}Pb/^{204}Pb$ = 21.28 ± 0.4 and $^{207}Pb/^{204}Pb$ = 15.759 ± 0.034) relative to the terrestrial Pb model of Stacey and Kramers (1975) of 250 Ma ($^{206}Pb/^{204}Pb$ = 18.31 ± 0.8 and $^{207}Pb/^{204}Pb$ = 15.61 ± 0.32). Common Pb corrections defined by isochron relationship in Figure 2C produces concordant Wetherill (1956) and Tera and Wasserburg (1972)

concordia plots (Figure 3) and weighted 204-corrected $^{206}Pb/^{238}U$ and $^{207}Pb/^{235}U$ ages of 246.70 ± 0.29Ma (MSWD = 0.86), and 246.38 ± 0.92 (MSWD = 0.77) respectively. Stacey and Kramers (1975) model initial Pb yields discordant Wetherill (1956) and Tera and Wasserburg (1972) concordia plots (Figure 3) and distinguishably older weighted 204-corrected $^{206}Pb/^{238}U$ and $^{207}Pb/^{235}U$ ages of 250.4 ± 1.9 Ma (MSWD = 51), and 249.59 ± 0.96 (MSWD = 1.08) respectively. Isochron relationships are preferred here as they require no assumptions of the common Pb composition and yield concordant $^{238}U/^{206}Pb$ and $^{235}U/^{207}Pb$ values. This is discussed further in Section 4.2.

Three aliquots of the AY-4 reference cassiterite from the Anyuan skarn-type tin deposit of the Furong tin ore field in the middle Nanling Range (Yuan et al. 2008; 2011) yield isochron ages for Alpha-Mu = 152 ± 1.5 Ma (MSWD = 2.3), Beta-Nu = 151.4 ± 3.7 Ma (MSWD = 0.48), linear 3D concordia-constrained 151.9 ± 2.2 Ma (MSWD = 5.1). Common Pb estimates from the 3D relationship are elevated ($^{206}Pb/^{204}Pb$ = 19.9 ± 1.6 and $^{207}Pb/^{204}Pb$ = 15.75 ± 0.15), but within error of the Stacey and Kramers (1975) model for that age. The weighted 204-corrected $^{206}Pb/^{238}U$ age is 153.7 ± 1.2 Ma and $^{207}Pb/^{235}U$ is 154.9 ± 1.4 Ma using Stacey and Kramers (1975) Pb compositions slightly higher, but within error of the 3D isochron age, and may indicate that the common Pb component is more evolved than predicted by terrestrial models. like within the Yankee cassiterite. These ages are significantly younger than 158.2 ± 0.4 Ma published by Yuan et al. (2011). AY-4 analysed in this study was provided by R-Q Zhang in 2017. The precise provenance of this sample is unknown. Isochron data that includes other cassiterite samples from the deposit yields a crystallisation age of 157 ± 6 Ma (Yuan et al. 2008), within error of both our estimation and Yuan et al. (2011) and indicates U-Pb heterogeneity in the Anyuan skarn-type tin deposit.

Discussion

Geochronological history of the Mole Granite and its deposits

The geochronological history of the emplacement of the Mole Granite and the associated hydrothermal system have previously been discussed by Kleeman et al. (1997) and Schlattegger et al. (2005). Kleeman et al. (1997), using K–Ar, ^{40}Ar–^{39}Ar and Rb-Sr isotope constraints in micas and whole rock samples, inferred granite

emplacement at 246 ± 2 Ma, cassiterite mineralisation at 243 ± 2 Ma, and low temperature hydrothermal activity ceasing by 232 ± 2 Ma. Rb-Sr isochron ages were calculated using the ^{87}Rb decay constant of Steiger and Jäger (1975)($\lambda = 1.42 \times 10^{-11} y^{-1}$), and have been recalculated here with the new constant of Villa et al. (2015)($\lambda = 1.3972 \times 10^{-11} y^{-1}$). Schlattegger et al (2005) measured the U-Th-Pb isotopic compositions of magmatic and hydrothermal zircon, monazite and xenotime and infer granite emplacement and rapid cooling and mineralisation at 246.2 ± 0.5 Ma, with persistent low temperature hydrothermal activity until 243.8 ± 0.5 Ma. The Kleeman et al. (1997) model indicates 3 ± 4 Ma between granite emplacement and cassiterite mineralisation, whilst the Schlattegger et al. (2005) infer instantaneous emplacement and mineralisation within the precision of their methods. Figure 4 summaries the available geochronological data for the Mole Granite.

Schlattegger et al. (2005) infer early zircon and monazite U-Pb ages at 247.7 ± 0.5 Ma, including 249 ± 1.5 Ma (Chisholm et al. 2014), represent magmatic crystallisation at lower crustal depths or during magmatic ascent. The emplacement age of the Mole Granite is inferred from high temperature hydrothermal xenotime with a U-Pb age of 246.2 ± 0.2 Ma in quartz-cassiterite veins of the Yankee deposit. Recalculated **w**hole rock Rb-Sr data for the Mole Granite yield a relative imprecise isochron age of 247.1 ± 4.1Ma (MSWD = 0.44, n=9; Kleeman et al. 1997). U-Pb isochron cassiterite ages presented here for the Yankee deposit, 246.48 ± 0.51 Ma, indicate simultaneous mineralisation with hydrothermal xenotime. 204-corrected $^{206}Pb/^{238}Pb$ cassiterite ages using Stacey and Kramers (1975) common Pb yield a mean weighted average age 250.4 ± 1.9 that is older, although within error of, magmatic zircon and monazite and hydrothermal xenotime. Recalculation of U-Pb SHRIMP data of Carr et al. (2017) for the Yankee cassiterite using the new radiogenic and common Pb composition defined by isochron relationships here yields a mean weighted 207-corrected age of 247.3 ± 3.2 Ma (n = 39; MSWD =1.39). This period corresponds to ^{40}Ar-^{39}Ar and Rb-Sr mica ages of 246 ± 2 Ma in other sheeted-vein mineral deposits of the Mole Granite (Kleeman et al. 1997). Assuming magmatic emplacement simultaneously with hydrothermal xenotime and cassiterite precipitation, these indicate cooling from ~800ºC–<600ºC from almost instantaneously to a maximum period of 430 ka, and 2.4 Ma to 300ºC in the sheeted-

vein systems. Interpreting early zircon U-Pb ages as emplacement ages extends this period to 210ka–2.23 Ma, or to 4.2 Ma in the sheeted-veins. Closure temperature of xenotime and cassiterite are poorly constrained. Xenotime is considered comparable with monazite at >700oC (Copeland et al. 1998; Braun et al., 1998), however lower temperature examples occur (e.g. Schärer et al. 1999). Zhang et al. (2011) indicated U-Pb closure in a 10 µm cassiterite grain at 600oC for 25 Ma, and in a 1 mm grain at 800oC for 40 Ma. These data indicate rapid cooling and cassiterite mineralisation in the Yankee deposit (Figure 4). Heat loss is facilitated by the thin-sill like shape to the Mole Granite (Kleeman 1982) and the incursion of cool meteoric fluids (Sun and Eadington 1987; Audetat et al. 2000a,b).

Common Pb composition of the Yankee reference cassiterite

Cassiterite has relatively low $^{206}Pb/^{204}Pb$ ratios compared to zircon (>500), indicating are larger common Pb component. Common Pb corrections are a large area of uncertainty in age calculations of cassiterite (e.g. Neymark et al. 2018). ID-TIMS U-Pb isochron cassiterite data for the Yankee cassiterite, that makes no common Pb composition assumptions but assumes concordance between $^{238}U/^{206}Pb$ and $^{235}U/^{207}Pb$, indicates extremely evolved initial $^{206}Pb/^{204}Pb$ and $^{207}Pb/^{204}Pb$, but normal $^{208}Pb/^{204}Pb$ initial compositions relative to that predicted by terrestrial Pb evolution models (Cumming and Richards 1975; Stacey and Kramers 1975).

Mu (µ)($^{238}U/^{204}Pb$) for the New England Orogen vary between 10.0–10.7 (Huston et al. 2016; Huston et al. 2017). The initial Pb composition of K-feldspar within the Mole Granite is $^{206}Pb/^{204}Pb$ = 18.53, $^{207}Pb/^{204}Pb$ = 15.63 and $^{208}Pb/^{204}Pb$ = 38.47 (G. Carr unpubl) and for hydrothermal galena associated with the Mole Granite is $^{206}Pb/^{204}Pb$ = 18.46 (SD = 0.01), $^{207}Pb/^{204}Pb$ = 15.59 (0.01) and $^{208}Pb/^{204}Pb$ = 38.35 (0.04)(n = 26; Huston et al. 2017). These initial Pb isotopic compositions are comparable to both the Stacey and Kramers (1975) and Cummings and Richards (1975) models for 250 Ma, but the $^{206}Pb/^{204}Pb$ and $^{207}Pb/^{204}Pb$ are significantly lower than observed in Yankee cassiterite. These data indicate a high µ source to fluids associated with the Yankee cassiterite. Assuming 430 ka between emplacement of the Mole Granite and cassiterite in the Yankee deposit, the fluid would require a µ of 41,360 ± 3000. This fluid chemistry is hypothesised to be generated from either 1) separation of a U rich,

Pb poor fluid that underwent *in-situ* decay, and 2) dissolution of U rich minerals with already evolved Pb isotopic compositions.

The Mole Granite has undergone extensive fractional crystallisation leading to high U (20 ± 11 ppm) and Th (52 ± 7 ppm) concentrations (Audétat et al. 2000a). Partition coefficients of U, Th and Pb between evolved silicate melts and aqueous fluids (e.g. concentration of Pb in melt/Pb in fluid = $D_{Pb}^{fluid/melt}$) have been described after experimental studies of Keppler and Wyllie (1990, 1991), Keppler (1996), Bureau et al. (2007) and Kawamoto et al. (2014). The concentration of $D_{U}^{fluid/melt}$ and $D_{Th}^{fluid/melt}$ are low (<0.002 and <0.003 respectively) in systems where H_2O is the only volatile component but increase dramatically with HF and HCl. Increasing CO_2 has the significantly smaller effect of increasing only $D_{U}^{fluid/melt}$ (Keppler et al. 1990; 1991). The authors assumed U was dominantly in oxidised states (4+ and 5+). $D_{Pb}^{fluid/melt}$ is also increased with pressure and chlorinity (Keppler 1996; Kawamoto et al. 2014). Kawamoto et al. (2014) report $D_{Pb}^{fluid/melt}$ of <0.4 in the presence of water and 2.6 in the presence of 5M (Na,K)Cl. The preference of Pb to partition in the fluid is documented in the Yankee deposit with an several orders of magnitude increase in Pb concentration from melt inclusions (29.2 ppm), to fluid inclusions (324–2604 ppm)(Audétat et al. 2000a). Conversely high U (21 ± 4 ppm) and Th (46 ± 4 ppm) in melt inclusions decrease to below detection limits (not reported) in fluid inclusions (Audétat et al. 2000a). Both Sn and Pb strongly partition into a fluid phase over a vapour phase in the Yankee deposit (Audétat et al. 1998). Although U concentrations were elevated in the magma, the Pb-rich fluids derived exsolved from the cooling Mole Granite likely had low μ values and could not generate the Pb isotopic compositions of the Yankee cassiterite.

Accessory magmatic minerals in the Mole Granite that contain significant U-Th-Pb budgets include zircon, apatite, thorite, monazite, xenotime. Dissolution of these phases into a low Pb fluid could derive the evolved common Pb composition of the Yankee cassiterite. Hydrothermal zircon, monazite and xenotime in the Yankee deposit may indicate remobilisation of the same magmatic phases in U-Th rich fluids (Pettke et al. 2005; Schlattegger et al. 2005). Schlattegger et al. (2005) describe

three internal textures defined by CL imaging in zircon from the Mole Granite. The first two (type A and B of Schlattegger et al. 2005) represent a core and oscillatory zoned case rim of magmatic origin. On occasion both textures are disturbed, and recrystallised by a third texture, interpreted as hydrothermal in origin (type C)(Pettke et al. 2005; Schlattegger et al. 2005). Type C zircon has 'spongy' texture indicative of radiation damage due to high U and or Th. This spongy texture is common to hydrothermal zircons and is commonly associated with Pb loss (e.g. Schmidt et al. 2006). Mechanisms for zircon dissolution by aqueous fluids are summarised by Geisler et al. (2007). Zircon solubility is increased with increasing aqueous silica, hydroxl (Ayers et al. 2012) and F (Rubin et al. 1989). Fluorine is highly elevated within the Mole Granite system, with large silexite deposits in its apical zones (refs). Derivation of the evolved common Pb signature for the Yankee cassiterite from the zircon, xenotime and apatite would require a selective fluid such that the regional Pb signature was not incorporated.

Although not identified within the Mole Granite, minor dissolution of uraninite will generate highly evolved Pb compositions and does not require a specifically selective fluid due to its high instability. Uraninite can form as a late magmatic phase due to extended fractional crystallisation when melt Th/U is low (Cuney 2014) or when in hydrothermal environments when oxidised by fluids or host rocks (e.g. Cuney et al. 2014; Ballouard et al. 2017). Uranium leaching from uraninite by fluids was proposed for the leucogranites of Hercynian Guérande granite in the Armorican Massif, France (Ballouard et al. 2017).

Conclusions

High precision U-Pb ID-TIMS age dating of cassiterite requires new methods for complete dissolution of cassiterite grains and low Pb blanks. In this study a new method is proposed and compared to previously published methods (Gulson et al. 1992; Yuan et al. 2008; 2011) requires small sample sizes (<0.5 mg), minimal handling and produces very low Pb blanks. This method involves concentrated HBr dissolution followed by U,Th and Pb purification by column chromatography has provided new and precise age constraints of the Yankee cassiterite reference material. The most precise estimation of the cassiterite is 246.48 ± 0.51 Ma, derived from a 3D isochron that is constrained to insect the concordia (Ludwig 1998). These

new data indicate rapid cooling of magmatic derived fluids from the Mole Granite following granitic emplacement for a maximum period of 430 Ka and rejects previous theories of extended hydrothermal activity or protracted magmatic pulses (Kleeman et al. 1997).

Common Pb corrections remain a large uncertainty in cassiterite U-Pb dating. Typically, corrections assume ‘normal’ initial compositions determined by terrestrial evolution models of either Stacey and Kramers (1975) or Cummings and Richards (1975). However, the Yankee cassiterite contains extremely evolved common Pb values, of which the origin remains unclear. Using terrestrial common Pb for age corrections yields cassiterite ages that pre-date the inferred emplacement of the granite. Simplistic common Pb corrections to cassiterite data could yield erroneous results. Parental fluids to the Yankee cassiterite require an extremely elevated μ, that may have been derived from fluid exsolved from the crystallising Mole Granite, or after the dissolution of high μ minerals such as zircon, apatite and xenotime.

Table 22: Elution scheme for U-Pb cassiterite dating

Step	Eluent	Volume
Resin cleaning	0.5M HNO_3; 0.1M HCl-0.3MHF; 0.5M HCl	3 ml
Resin conditioning	0.5M HCl	1 ml
Load sample and collect Pb	0.5M HCl	1 ml
Rinse Sn	0.5M HNO_3	6 ml
Rinse REE	3M HCl	2 ml
Collect Th	3M HCl	2 ml
Collect U	0.1M HCl-0.3M HF	4 ml

Table 23: ID-TIMS U-Pb data from the Yankee and AY-4 cassiterite.

		Compositional Parameters									Radiogenic Isotope Ratios							
Sample	Wt. mg	U ppm	Th U	Pb ppm	206Pb* x10-13 mol	mol % 206Pb*	Pb* Pbc	Pbc (pg)	206Pb 204Pb	208Pb 204Pb	208Pb 206Pb	207Pb 206Pb	% err	207Pb 235U	% err	206Pb 238U	% err	corr. coef.
	(a)	(b)	(c)	(d)	(c)	(e)	(e)	(e)	(e)	(f)	(f)	(g)	(g)	(h)	(g)	(h)	(g)	(h)	
Yankee 1	0.3	12.01	0.00	0.55	5.86	0.92	3	37	266.1	38.30	0.001	0.05110	0.6	0.27472	0.6	0.03901	0.2	0.292
Yankee 2	0.3	6.74	0.00	0.35	3.29	0.88	2	35	169.6	38.35	0.001	0.05131	0.9	0.27586	1.0	0.03901	0.3	0.299
Yankee 3	0.3	8.06	0.01	0.44	3.93	0.86	2	48	150.4	38.43	0.002	0.05103	1.0	0.27439	1.0	0.03902	0.3	0.246
Yankee 4	0.24	6.68	0.00	0.41	2.60	0.82	1	43	115.6	38.12	-0.001	0.05071	1.7	0.27190	1.8	0.03891	0.5	0.304
Yankee 5	0.09	11.55	0.00	0.75	1.70	0.81	1	31	107.1	38.17	0.000	0.05023	2.4	0.27129	2.5	0.03919	0.6	0.351
AY4 1	0.3	9.54	0.00	0.32	2.83	0.86	2	34	151.9	38.25	0.000	0.04919	1.3	0.16073	1.4	0.02371	0.4	0.258
AY4 2	0.3	9.28	0.02	0.39	2.73	0.78	1	57	96.2	38.57	0.005	0.04950	1.9	0.16049	1.9	0.02353	0.5	0.211
AY4 3	0.3	10.91	0.01	0.42	3.21	0.81	1	58	107.7	38.53	0.004	0.04979	1.6	0.16133	1.6	0.02351	0.5	0.212

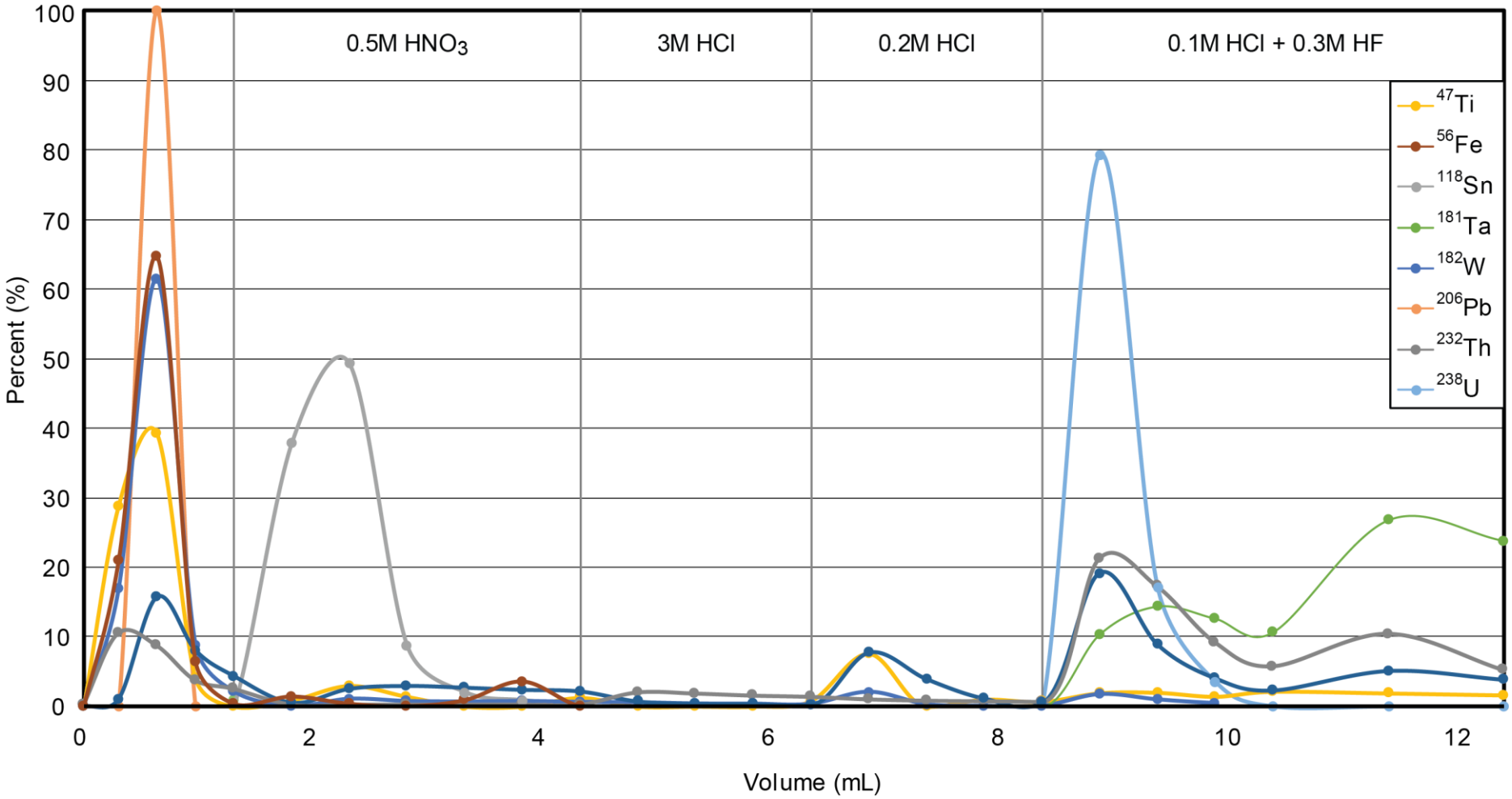

Figure 80: Elution profile for the Yankee cassiterite in TRU resin. Samples loaded in 0.5 M HCl. Aliquots collected every 0.5 mL except for during loading (0.5M HCl in 0.3mL aliquots) and the two final HCl + HF aliquots (1mL). Element yield is normalised to an untreated aliquot of the Yankee cassiterite.

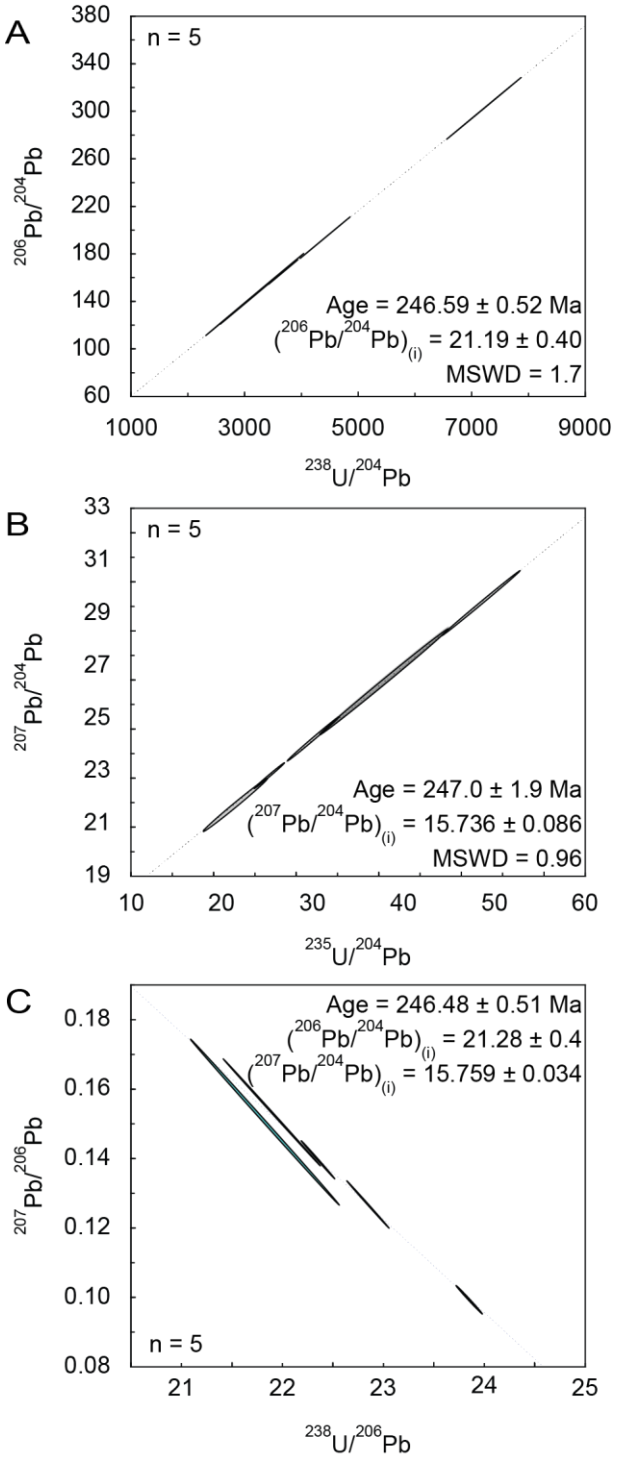

Figure 81: ID-TIMS isochron data for the Yankee cassiterite.

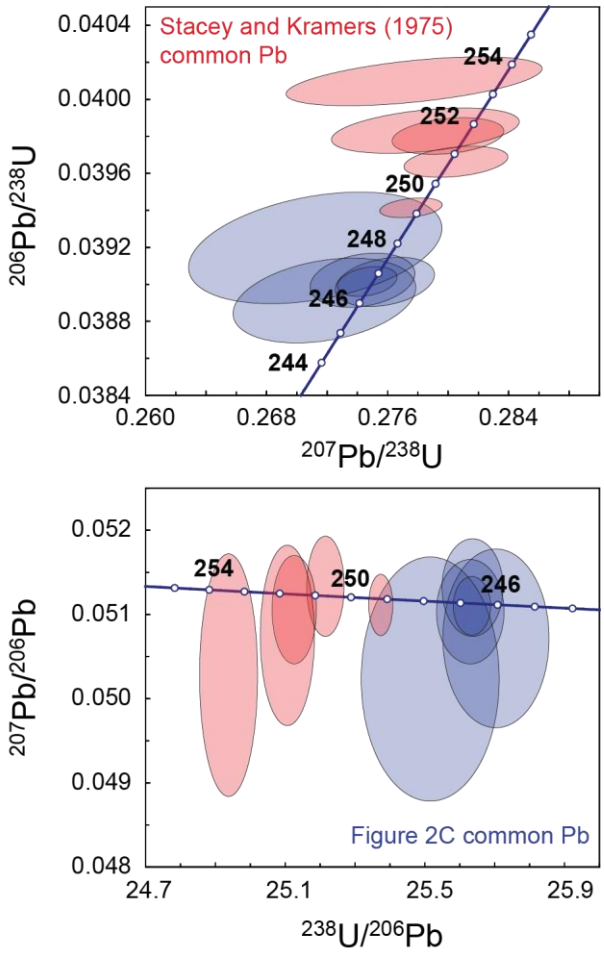

Figure 82: Common Pb corrected ID-TIMS data for the Yankee cassiterite showing the two corrections methods described in text. Stacey and Kramers (1975) corrections (red) result in discordant values in both the Wetherill (1956)(top) and Tera and Wasserburg (1972)(bottom) concordia diagrams. Common Pb corrections using values of Figure 2C yield more concordant results (blue).

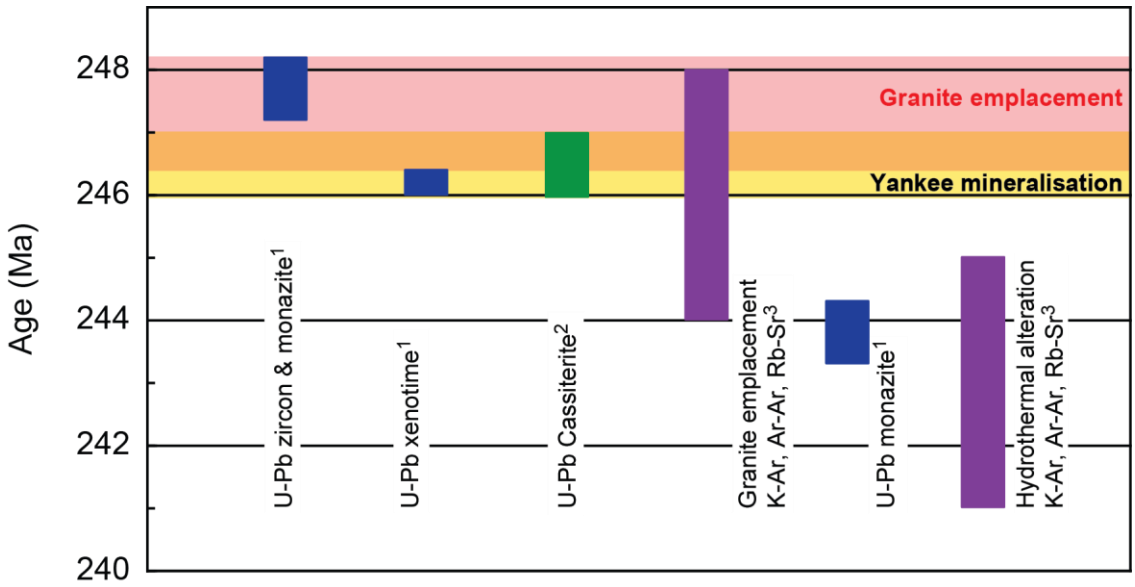

Figure 83: Summary of published geochronological data for the Mole Granite system. 1) Schlattegger et al. 2005, 2) this study, 3) Kleeman et al. 1997). Cassiterite mineralisation in the Yankee deposit occurred at maximum 430 ka after emplacement of the Mole Granite.

References

Amelin, Y., 2008. U–Pb ages of angrites. Geochimica et Cosmochimica Acta, 72(1): 221-232.

Audetat, A., Gunther, D., Heinrich, C.A., 2000a. Magmatic-hydrothermal evolution in a fractionating granite: A microchemical study of the Sn-W-F-mineralized Mole Granite (Australia). Geochimica Et Cosmochimica Acta, 64(19): 3373-3393.

Audétat, A., Günther, D., Heinrich, C.A., 1998. Formation of a Magmatic-Hydrothermal Ore Deposit: Insights with LA-ICP-MS Analysis of Fluid Inclusions. Science, 279(5359): 2091-2094.

Audétat, A., Günther, D., Heinrich, C.A., 2000b. Causes for Large-Scale Metal Zonation around Mineralized Plutons: Fluid Inclusion LA-ICP-MS Evidence from the Mole Granite, Australia. Economic Geology, 95(8): 1563-1581.

Audétat, A., Pettke, T., Heinrich, C.A., Bodnar, R.J., 2008. Special Paper: The Composition of Magmatic-Hydrothermal Fluids in Barren and Mineralized Intrusions. Economic Geology, 103(5): 877-908.

Braun, I., Montel, J.M., Nicollet, C., 1998. Electron microprobe dating of monazites from high-grade gneisses and pegmatites of the Kerala Khondalite Belt, southern India. Chemical Geology, 146(1-2): 65-85.

Bureau, H. et al., 2007. In situ mapping of high-pressure fluids using hydrothermal diamond anvil cells. High Pressure Research, 27(2): 235-247.

Caley, E.R., 1932. THE ACTION OF HYDRIODIC ACID ON STANNIC OXIDE. Journal of the American Chemical Society, 54(8): 3240-3243.

Carr, P.A., Norman, M.D., Bennett, V.C., 2017. Assessment of crystallographic orientation effects on secondary ion mass spectrometry (SIMS) analysis of cassiterite. Chemical Geology, 467: 122-133.

Cauzid, J., Philippot, P., Martinez-Criado, G., Ménez, B., Labouré, S., 2007. Contrasting Cu-complexing behaviour in vapour and liquid fluid inclusions from the Yankee Lode tin deposit, Mole Granite, Australia. Chemical Geology, 246(1–2): 39-54.

Chen, X.-C. et al., 2014. Cassiterite LA-MC-ICP-MS U/Pb and muscovite 40Ar/39Ar dating of tin deposits in the Tengchong-Lianghe tin district, NW Yunnan, China. Mineralium Deposita, 49(7): 843-860.

Chesley, J.T. et al., 1993. Thermochronology of the Cornubian batholith in southwest England: Implications for pluton emplacement and protracted hydrothermal mineralization. Geochimica et Cosmochimica Acta, 57(8): 1817-1835.
Chisholm, E.K., Blevin, P.L., Simpson, C., 2014. New SHRIMP U–Pb zircon agesfrom the New England Orogen, New South Wales: July 2012–June 2014, Geoscience Australia and Geological Survey of NSW, Canberra.
Copeland, P., Parrish, R.R., Harrison, T.M., 1988. Identification of Inherited Radiogenic Pb in Monazite and Its Implications for U-Pb Systematics. Nature, 333(6175): 760-763.
Creech, J.B., Moynier, F., Badullovich, N., 2017. Tin stable isotope analysis of geological materials by double-spike MC-ICPMS. Chemical Geology, 457: 61-67.
Cumming, G.L., Richards, J.R., 1975. Ore lead isotope ratios in a continuously changing earth. Earth and Planetary Science Letters, 28(2): 155-171.
Eggins, S.M., Kinsley, L.P.J., Shelley, J.M.G., 1998. Deposition and element fractionation processes during atmospheric pressure laser sampling for analysis by ICP-MS. Applied Surface Science, 127-129: 278-286.
Fekete, S. et al., 2016. Contrasting hydrological processes of meteoric water incursion during magmatic–hydrothermal ore deposition: An oxygen isotope study by ion microprobe. Earth and Planetary Science Letters, 451: 263-271.
Gulson, B.L., Jones, M.T., 1992. Cassiterite: Potential for direct dating of mineral deposits and a precise age for the Bushveld Complex granites. Geology, 20(4): 355-358.
Halliday, A.N., 1980. The timing of early and main stage ore mineralization in Southwest Cornwall. Economic Geology, 75(5): 752-759.
Heinrich, C.A., Ryan, C.G., Mernagh, T.P., Eadington, P.J., 1992. Segregation of ore metals between magmatic brine and vapor; a fluid inclusion study using PIXE microanalysis. Economic Geology, 87(6): 1566-1583.
Henley, H.F., Brown, R.E., Stroud, W.J., 1999. The Mole Granite extent of mineralisation and exploration potential. In: Flood, P.G. (Ed.), Regional Geology, Tectonics and Metallogenesis of the New England Orogen. Univ. New England, pp. 385–392.
Horwitz, E.P., Chiarizia, R., Dietz, M.L., Diamond, H., Nelson, D.M., 1993. Separation and preconcentration of actinides from acidic media by extraction chromatography. Analytica Chimica Acta, 281(2): 361-372.
Huston, D. et al., 2017. Spatial variations in lead isotopes, Tasman Element, eastern Australia. Geoscience Australia Record, 2017/09.
Huston, D.L. et al., 2016. Metallogenesis and geodynamics of the Lachlan Orogen: New (and old) insights from spatial and temporal variations in lead isotopes. Ore Geology Reviews, 76: 257-267.
Huyskens, M.H., Iizuka, T., Amelin, Y., 2012. Evaluation of colloidal silicagels for lead isotopic measurements using thermal ionisation mass spectrometry. Journal of Analytical Atomic Spectrometry, 27(9): 1439-1446.
Kawamoto, T. et al., 2014. Large-ion lithophile elements delivered by saline fluids to the sub-arc mantle. Earth, Planets and Space, 66(1): 61.

Keppler, H., 1996. Constraints from partitioning experiments on the composition of subduction-zone fluids. Nature, 380: 237.
Keppler, H., Wyllie, P., 1991. Partitioning of Cu, Sn, Mo, W, U, and Th between melt and aqueous fluid in the systems haplogranite-H2O−HCl and haplogranite-H2O−HF. Contributions to Mineralogy and Petrology, 109(2): 139-150.
Keppler, H., Wyllie, P.J., 1990. Role of fluids in transport and fractionation of uranium and thorium in magmatic processes. Nature, 348: 531.
Kleeman, D.J., 1982. The anatomy of a tin-mineralizing A-type granite. In: Flood, P.G., Runnegar, B. (Eds.), New England Geology. Univ. New England, pp. 327-3334.
Kleeman, J.D., Plimer, I.R., Lu, J., Foster, D.A., Davidson, R., 1997. Timing of thermal and mineralisation events associated with the Mole Granite. In: Ashley, P., Flood, P.G. (Editors), Tectonics and Metallogenesis of the New England Orogen, Special Publication 19. Geological Society of Australia, pp. 254-265.
Lehmann, B., 1990. Metallogeny of Tin. Lecture Notes in Earth Sciences, 32. Springer-Verlag, Berlin.
Li, C.Y. et al., 2016. Dating cassiterite using laser ablation ICP-MS. Ore Geology Reviews, 72(P1): 313-322.
Mathur, R. et al., 2017. Preparation and Measurement of Cassiterite for Sn Isotope Analysis. Geostandards and Geoanalytical Research, 41(4): 701-707.
McNaughton, N.J., Pollard, P.J., Groves, D.I., Taylor, R.G., 1993. A long-lived hydrothermal system in Bushveld granites at the Zaaiplaats tin mine; lead isotope evidence. Economic Geology, 88(1): 27-43.
Neymark, L.A., Holm-Denoma, C.S., Moscati, R.J., 2018. In situ LA-ICPMS U–Pb dating of cassiterite without a known-age matrix-matched reference material: Examples from worldwide tin deposits spanning the Proterozoic to the Tertiary. Chemical Geology.
Pettke, T., Audétat, A., Schaltegger, U., Heinrich, C.A., 2005. Magmatic-to-hydrothermal crystallization in the W–Sn mineralized Mole Granite (NSW, Australia): Part II: Evolving zircon and thorite trace element chemistry. Chemical Geology, 220(3–4): 191-213.
Plimer, I.R., Lu, J., Kleeman, J.D., 1991. Trace and rare earth elements in cassiterite — sources of components for the tin deposits of the Mole Granite, Australia. Mineralium Deposita, 26(4): 267-274.
Rankin, A.H., Ramsey, M.H., Coles, B., Van Langevelde, F., Thomas, C.R., 1992. The composition of hypersaline, iron-rich granitic fluids based on laser-ICP and Synchrotron-XRF microprobe analysis of individual fluid inclusions in topaz, Mole granite, eastern Australia. Geochimica et Cosmochimica Acta, 56(1): 67-79.
Schaltegger, U., Pettke, T., Audétat, A., Reusser, E., Heinrich, C.A., 2005. Magmatic-to-hydrothermal crystallization in the W–Sn mineralized Mole Granite (NSW, Australia): Part I: Crystallization of zircon and REE-phosphates over three million years—a geochemical and U–Pb geochronological study. Chemical Geology, 220(3–4): 215-235.
Scharer, U., de Parseval, P., Polve, M., de Saint Blanquat, M., 1999. Formation of the Trimouns talc-chlorite deposit (Pyrenees) from persistent hydrothermal activity between 112 and 97 Ma. Terra Nova, 11(1): 30-37.

Shaw, S.E., Flood, R.H., 1981. The New England Batholith, Eastern Australia - Geochemical Variations in Time and Space. Journal of Geophysical Research, 86(Nb11): 530-544.
Stacey, J.S., Kramers, J.D., 1975. Approximation of terrestrial lead isotope evolution by a two-stage model. Earth and Planetary Science Letters, 26(2): 207-221.
Steiger, R.H., Jäger, E., 1977. Subcommission on geochronology: Convention on the use of decay constants in geo- and cosmochronology. Earth and Planetary Science Letters, 36(3): 359-362.
Sun, S.-S., Eadington, P.J., 1987. Oxygen isotope evidence for the mixing of magmatic and meteoric waters during tin mineralization in the Mole Granite, New South Wales, Australia. Economic Geology, 82(1): 43-52.
Taylor, R.G., 1979. Geology of Tin Deposits. Developments in Economic Geology, 11. Elsevier.
Villa, I.M., De Bièvre, P., Holden, N.E., Renne, P.R., 2015. IUPAC-IUGS recommendation on the half life of 87Rb. Geochimica et Cosmochimica Acta, 164(Supplement C): 382-385.
Yamazaki, E., Nakai, S., Yokoyama, T., Ishihara, S., Tang, H.F., 2013. Tin isotope analysis of cassiterites from Southeastern and Eastern Asia. Geochemical Journal, 47(1): 21-35.
Yuan, S. et al., 2011. In situ LA-MC-ICP-MS and ID-TIMS U–Pb geochronology of cassiterite in the giant Furong tin deposit, Hunan Province, South China: New constraints on the timing of tin–polymetallic mineralization. Ore Geology Reviews, 43(1): 235-242.
Yuan, S. et al., 2008. A precise U–Pb age on cassiterite from the Xianghualing tin-polymetallic deposit (Hunan, South China). Mineralium Deposita, 43(4): 375-382.
Zhang, D.L., Peng, J.T., Hu, R.Z., Yuan, S.D., Zheng, D.S., 2011. The closure of U-Pb isotope system in cassiterite and its reliability for dating. Geological Review, 57(4): 549-554.
Zhang, R.-Q. et al., 2015. Constraints of in situ zircon and cassiterite U–Pb, molybdenite Re–Os and muscovite 40Ar–39Ar ages on multiple generations of granitic magmatism and related W–Sn mineralization in the Wangxianling area, Nanling Range, South China. Ore Geology Reviews, 65, Part 4(0): 1021-1042.

Digital Appendices (Excel file)

Appendix 3: EMP and LA-ICP-MS tourmaline for Ardlethan and Mole granites including secondary standards

Appendix 4: SHRIMP $\delta^{18}O$ quartz values for Ardlethan and Mole granites including secondary standards.

Appendix 5: TIMS Rb–Sr and Sm–Nd standard data.

Appendix 6: LA-ICP-MS U–Pb cassiterite data for Ardlethan and Mole granites systems, and zircon U–Pb data for the Yankee deposit.